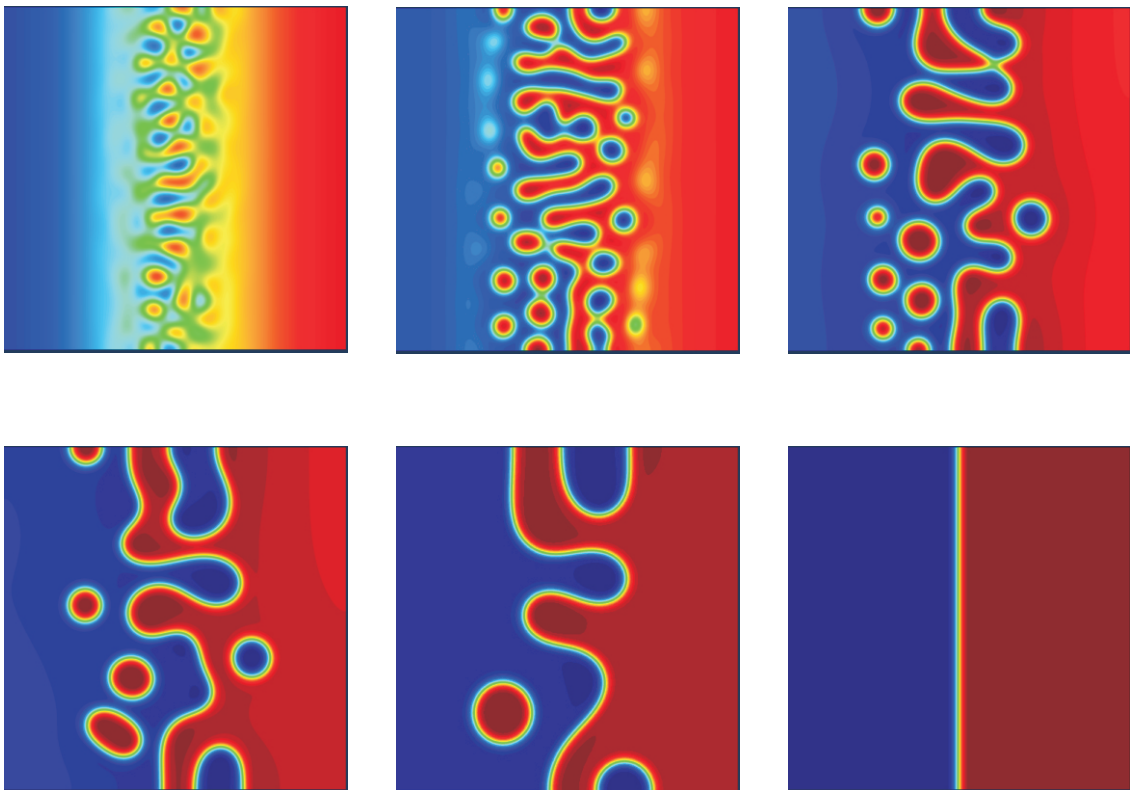Markus Kästner

Advanced Numerical Modelling of Discontinuities in Coupled Boundary Value Problems

Advanced Numerical Modelling of Discontinuities in Coupled Boundary Value Problems

*Numerische Modellierung von Diskontinuitäten
in Gekoppelten Randwertproblemen*

Von der Fakultät Maschinenwesen
der Technischen Universität Dresden
zur
Erlangung des akademischen Grades
eines habilitierten Doktoringenieurs
(Dr.-Ing. habil.)
genehmigte Habilitationsschrift
von

Dr.-Ing. Markus Kästner
geboren am 8. Februar 1980 in Rochlitz

Tag der Einreichung: 30. Juni 2015
Tag der Verteidigung: 09. Dezember 2015

Gutachter:

Prof. Dr.-Ing. habil. Volker Ulbricht
Prof. Dr. ir. René de Borst
Prof. Dr.-Ing. habil. Holm Altenbach

Preface

The present thesis compiles the results of research carried out between 2010 and 2015 when I worked as Postdoc and group leader at the Institute of Solid Mechanics, TU Dresden.

I wish to express my gratitude to Professor Volker Ulbricht for his unrestricted support of my research activities, for mentoring my personal advancement, and for providing an excellent working environment. Professor Odenbach has sparked my interest in magnetic hybrid materials and offered personal guidance which I appreciated very much. I am very thankful to Professor de Borst for hosting my research visit to the University of Glasgow and for accepting to serve as co-referee. Sincere thanks to Professor Altenbach for his interest in my work and for providing his expert opinion as co-referee. Moreover, I want to thank PD Dr. habil. Marina Grenzer and Professors Gude, Peterseim, Rohm and Wallmersperger and all co-workers for the pleasant and fruitful collaboration within several joint research projects.

During the last five years Martin Boisly, Paul Hennig, Franz Hirsch, Karl Alexander Kalina, Christian Lux, Philipp Metsch, and Sebastian Müller have been part of my research group. I would like to thank them for enriching my ideas with their profound knowledge and enthusiasm in computational mechanics. It has been a pleasure to work with all colleagues at the Institute of Solid Mechanics. In particular, I want to thank Jörg Brummund and Sebastian Müller for their friendship and the various discussions on mechanics, numerics, and beyond. Thanks also to Stefan May and Julien Vignollet for their company during my visit to Glasgow.

Eventually I want to thank my family, my wife Katja and my children – Benjamin and Konstantin – for their love, patience and orientation.

Dresden, June 2016 Markus Kästner

Abstract

Industrial development processes as well as research in physics, materials and engineering science rely on computer modelling and simulation techniques today. With increasing computer power, computations are carried out on multiple scales and involve the analysis of coupled problems. In this work, continuum modelling is therefore applied at different scales in order to facilitate a prediction of the effective material or structural behaviour based on the local morphology and the properties of the individual constituents. This provides valueable insight into the structure-property relations which are of interest for any design process.

In order to obtain reasonable predictions for the effective behaviour, numerical models which capture the essential fine scale features are required. In this context, the efficient representation of discontinuities as they arise at, e.g. material interfaces or cracks, becomes more important than in purely phenomenological macroscopic approaches. In this work, two different approaches to the modelling of discontinuities are discussed: (i) a *sharp interface* representation which requires the localisation of interfaces by the mesh topology. Since many interesting macroscopic phenomena are related to the temporal evolution of certain microscopic features, (ii) *diffuse interface* models which regularise the interface in terms of an additional field variable and therefore avoid topological mesh updates are considered as an alternative.

With the two combinations (i) Extended Finite Elemente Method (XFEM) + sharp interface model, and (ii) Isogeometric Analysis (IGA) + diffuse interface model, two fundamentally different approaches to the modelling of discontinuities are investigated in this work. XFEM reduces the continuity of the approximation by introducing suitable enrichment functions according to the discontinuity to be modelled. Instead, diffuse models regularise the interface which in many cases requires even an increased continuity that is provided by the spline-based approximation. To further increase the efficiency of isogeometric discretisations of diffuse interfaces, adaptive mesh refinement and coarsening techniques based on hierarchical splines are presented. The adaptive meshes are found to reduce the number of degrees of freedom required for a certain accuracy of the approximation significantly.

Selected discretisation techniques are applied to solve a coupled magneto-mechanical problem for particulate microstructures of Magnetorheological Elastomers (MRE). In combination with a computational homogenisation approach, these microscopic models allow for the prediction of the effective coupled magneto-mechanical response of MRE. Moreover, finite element models of generic MRE microstructures are coupled with a BEM domain that represents the surrounding free space in order to take into account finite sample geometries. The macroscopic behaviour is analysed in terms of actuation stresses, magnetostrictive deformations, and magnetorheological effects. The results obtained for different microstructures and various loadings have been found to be in qualitative agreement with experiments on MRE as well as analytical results.

Zusammenfassung

Industrielle Entwicklungsprozesse und die Forschung in Physik, Material- und Ingenieur-wissenschaft greifen in einem immer stärkeren Umfang auf rechnergestützte Modellierungs- und Simulationsverfahren zurück. Die ständig steigende Rechenleistung ermöglicht dabei auch die Analyse mehrskaliger und gekoppelter Probleme. In dieser Arbeit kommt daher ein kontinuumsmechanischer Modellierungsansatz auf verschiedenen Skalen zum Einsatz. Das Ziel der Berechnungen ist dabei die Vorhersage des effektiven Material- bzw. Strukturver-haltens auf der Grundlage der lokalen Werkstoffstruktur und der Eigenschafen der konsti-tutiven Bestandteile. Derartige Simulationen liefern interessante Aussagen zu den Struktur-Eigenschaftsbeziehungen, deren Verständnis entscheidend für das Material- und Strukturde-sign ist.

Um aussagekräftige Vorhersagen des effektiven Verhaltens zu erhalten, sind numerische Modelle erforderlich, die wesentliche Eigenschaften der lokalen Materialstruktur abbilden. Dabei kommt der effizienten Modellierung von Diskontinuitäten, beispielsweise Material-grenzen oder Rissen, eine deutlich größere Bedeutung zu als bei einer makroskopischen Betrachtung. In der vorliegenden Arbeit werden zwei unterschiedliche Modellierungsan-sätze für Unstetigkeiten diskutiert: (i) eine *scharfe* Abbildung, die üblicherweise konforme Berechnungsnetze erfordert. Da eine Evolution der Mikrostruktur bei einer derartigen Mo-dellierung eine Topologieänderung bzw. eine aufwendige Neuvernetzung nach sich zieht, werden alternativ (ii) *diffuse* Modelle, die eine zusätzliche Feldvariable zur Regularisierung der Grenzfläche verwenden, betrachtet.

Mit der Kombination von (i) Erweiterter Finite-Elemente-Methode (XFEM) + scharfem Grenzflächenmodell sowie (ii) Isogeometrischer Analyse (IGA) + diffuser Grenzflächen-modellierung werden in der vorliegenden Arbeit zwei fundamental verschiedene Zugänge zur Modellierung von Unstetigkeiten betrachtet. Bei der Diskretisierung mit XFEM wird die Kontinuität der Approximation durch eine Anreicherung der Ansatzfunktionen gemäß der abzubildenden Unstetigkeit reduziert. Demgegenüber erfolgt bei einer diffusen Gren-zflächenmodellierung eine Regularisierung. Die dazu erforderliche zusätzliche Feldvariable führt oft zu Feldgleichungen mit partiellen Ableitungen höherer Ordnung und weist in ihrem Verlauf starke Gradienten auf. Die daraus resultierenden Anforderungen an den Ansatz werden durch eine Spline-basierte Approximation erfüllt. Um die Effizienz dieser isoge-ometrischen Diskretisierung weiter zu erhöhen, werden auf der Grundlage hierarchischer Splines adaptive Verfeinerungs- und Vergröberungstechniken entwickelt.

Ausgewählte Diskretisierungsverfahren werden zur mehrskaligen Modellierung des gekop-pelten magnetomechanischen Verhaltens von Magnetorheologischen Elastomeren (MRE) angewendet. In Kombination mit numerischen Homogenisierungsverfahren, ermöglichen die Mikrostrukturmodelle eine Vorhersage des effektiven magnetomechanischen Verhaltens von MRE. Außerderm wurden Verfahren zur Kopplung von FE-Modellen der MRE-Mi-krostruktur mit einem Randelement-Modell der Umgebung vorgestellt. Mit Hilfe der en-twickelten Verfahren kann das Verhalten von MRE in Form von Aktuatorspannungen, mag-netostriktiven Deformationen und magnetischen Steifigkeitsänderungen vorhergesagt wer-den. Im Gegensatz zu zahlreichen anderen Modellierungsansätzen, stimmen die mit den hier vorgestellten Methoden für unterschiedliche Mikrostrukturen erzielten Vorhersagen sowohl mit analytischen als auch experimentellen Ergebnissen überein.

Contents

List of Figures

List of Tables

Part I

Fundamentals

1 Introduction

Multi-material lightweight designs and active devices with characteristic microscopic material structures are the key feature for the development of innovative products. The computer aided design of these sophisticated structures requires efficient numerical methods for the solution of the underlying coupled field problems. These techniques also have to take into account the multi-scale nature of the materials and components. Multi-scale modelling approaches provide valueable insight into the structure-property relations of the investigated novel materials as they predict the effective behaviour based on the local morphology and the material behaviour of the individual constituents. They also provide knowledge about the local fields within the heterogeneous material structure. In order to obtain reasonable predictions for the effective material behaviour, numerical models which capture the essential fine scale features are required. In this context, the efficient representation of discontinuities as they arise at, e.g. material interfaces or cracks, becomes more important than in purely phenomenological macroscopic approaches. Since many interesting macroscopic phenomena are related to the temporal evolution of certain microscopic features such as the decomposition and coarsening of different material phases or the initiation and propagation of cracks, modelling techniques have to capture these evolutions in a robust and efficient way.

In this work, magnetoactive polymers will be considered as an example for the large variety of active materials with a distinct local material structure. The coupled magneto-mechanical behaviour of these novel materials will be modelled on a fine scale that still allows for the application of continuum theories. Homogenisation techniques are used to analyse structure-property relations for different local material structures. The theory of the coupled magneto-mechanical boundary value problem including the used constitutive relations will be outlined in Part I. Part II is dedicated to the extended finite element modelling of the microstructure. This method facilitates the representation of material interfaces in a regular non-conforming mesh by incoporating discontinuous functions into the approximation. In Part III spline-based, so called isogeometric, approximations are introduced as an alternative discretisation approach. The numerical properties of both methods are first analysed for the coupled problem for classical sharp interface representations. Eventually, the superior regularity of the spline basis is used to discretise diffuse interface models which require a higher-order continuity of the approximation and the representation of strong gradients.

1.1 Magnetorheological Elastomers

Field-controllable functional polymers represent a new class of applied materials which exhibit a strong coupling of their response to mechanical and non-mechanical, e.g. electric or magnetic, loads. A prominent example are Magnetorheological Elastomers (MRE) [31, 46]. In the simplest case, MRE represent a two-component system in which magnetisable particles are embedded in a cross-linked non-magnetic polymer. The characteristic length of the local material structure on the *microscale* is determined by the size of the particles which is typically in the range of several microns, Fig. 1.1. On the *macroscale*, i.e. the component
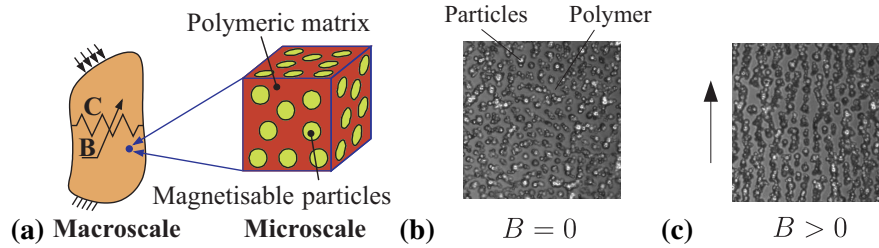
Figure 1.1: Magnetorheological elastomers: **(a)** hierarchical material structure at two distinct length scales. The effective stiffness **C** can be altered and mechanical deformations can be induced by the application of an external magnetic field **B**, **(b)** photo micrograph of randomly distributed magnetisable particles in a liquid polymer without any external magnetic induction ($|\mathbf{B}| = B = 0$), and **(c)** formation of chain-like clusters of magnetised particles aligned with the external magnetic induction $B > 0$.

level, the material is assumed to be homogeneous with characteristic magneto-mechanical coupling effects. Depending on the local morphology it can be convenient to introduce additional scales, e.g. a mesoscale where particle clusters are treated as a homogeneous medium with effective properties. Moreover, the definition of the different scales is not unique. In the physics community the particle level is often referred to as the mesoscale.

Morphology of MRE

The spatial distribution of the magnetisable particles in an MRE can be either isotropic or anisotropic [18, 85, 181, 182, 233] depending on whether the particles have been aligned by an applied magnetic field before the cross-linking of the polymer. MRE with an isotropic distribution of magnetic particles are synthesised by cross-linking of a polymer melt with well-dispersed particles without any external field ($|\mathbf{B}| = B = 0$), Fig. 1.1 (b). If a homogeneous magnetic field **B** with $B > 0$ is applied to a polymer melt with magnetisable particles, chain-like particle structures can be obtained, see Fig. 1.1 (c).

Magneto-mechanical coupling

An external magnetic field induces interactions between the magnetised particles and may even cause an evolution of the local material structure due to particle migration. As a consequence of the microscopic interactions and morphological changes, MRE feature two major magneto-mechanical coupling effects [67, 82, 200]:

- *Magnetorheological effect*, i.e. magnetically induced changes of mechanical moduli,

- *Magnetostrictive effect*, i.e. magnetically induced deformations and mechanical actuation stresses.

These features make MRE very attractive for a variety of technical implementations, especially diverse actoric devices. Since the effective coupled magneto-mechanical behaviour is of special interest in these applications, an in-depth understanding of the structure-property relations in MRE is required. A multi-scale modelling approach will be followed in this work to simulate the material behaviour of MRE because the effective response o n the macroscale is determined essentially by the MRE microstructure, i.e. the properties of the individual material phases and their geometrical arrangement in the composite, Fig. 1.1 (a). Beside MRE, the proposed modelling strategy is suitable to capture the behaviour of any magnetoactive composite [52].

1.2 Modelling of Magnetorheological Elastomers

Magnetostrictive and magnetorheological effects have been studied by two principal modelling approaches, namely discrete models which consider dipole-dipole interactions and purely phenomenological continuum formulations. Both methods are essentially based on the minimisation of a free energy functional. These functionals consist of an elastic energy accounting for the mechanical deformation of the MRE and a magnetic term that arises from interactions between the magnetisable particles placed in an external magnetic field. Discrete models have been employed to analyse the influence of the microscopic particle arrangement on the macroscopic magneto-mechanical response. Ivaneyko et al. [100, 101, 103] investigated the effect of different particle arrangements for infinite regular lattices. As a consequence of the regular particle distributions, contraction of the samples in the direction of the applied magnetic field is predicted which is rarely observed in experiments, e.g. in [40, 233] for chain-like microstructures. More commonly MRE exhibit an elongation in the direction of the magnetic field [43, 51, 233] for both isotropic and anisotropic particle structures. According to Han et al. [88] the consideration of irregular microstructures, e.g. wavy chains, is required to model this behaviour. Further interesting aspects which can affect the magneto-mechanical response of the discrete models are the influence of a finite sample size [102, 234, 235] and the required assumption on the coupling of the elastic and magnetic behaviour. In the models above affine deformations, i.e. a homogeneous deformation which neglects the underlying microstructure and the local particle-particle interactions, have been utilised. Pessot et al. [165] have demonstrated recently that this assumption leads to increasingly erroneous results if more realistic irregular particle distributions are considered. The same has to be expected for very soft, weakly crosslinked polymer matrices in which the flexibility of polymer sub-chains between cross-links allows for a considerable degree of particle motion.

The second major approach to the modelling of the magneto-mechanical behaviour are continuum models which have been used in two different ways. Firstly, they can be applied to describe the overall macroscopic behaviour of MRE. That is, models which consider microscopic features such as the orientation of particle chains in a phenomenological way can be fitted to experimental data. A recent formulation by Danas et al. [43] based on the theory developed by Kankanala and Triantafyllidis [111] accurately reproduces experimental results for small and large external magnetic fields. Further continuum theories have been presented by de Groot and Suttorp [48], Eringen and Maugin [63], Brigadnov and Dorfmann [23], Dorfmann and Ogden [55], Bustamante and Ogden [28], and Han et al. [88, 87]. On the other hand, continuum models can be used to describe the material behaviour of particles and polymers on the microscopic scale. The effective macroscopic response of the heterogeneous material can then be predicted using homogenisation techniques. To this end, relations between microscopic field variables and their effective macroscopic values are established in terms of volume averages. Suitable equivalence criteria, e.g. the energy equivalence postulated by Hill [94], are used to compute the effective behaviour taking into account the microscopic morphology as well as the material behaviour of the individual constituents. Comprehensive reviews on the method can be found in, e.g., [78, 112, 168]. Regarding the application to magneto-mechanical problems, different formulations of the field problem and boundary conditions for the homogenisation process have been presented by Chatzigeorgiou et al. [34]. In several works by Ponte Castañeda et al. [170, 171] and Galipeau et al. [73, 74, 75] analytical homogenisation schemes which are limited in terms of the material behaviour and the complexity of the local material structure have been applied.

Sharp Interface

Diffuse Interface

(a)

(b)
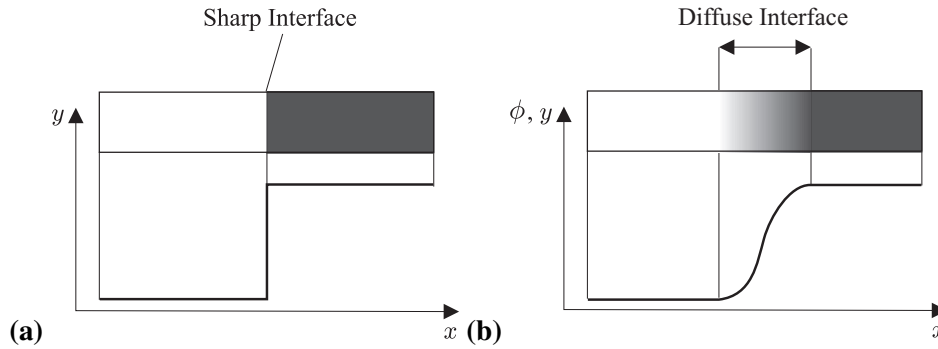
Figure 1.2: Two approaches to the modelling of interfaces: **(a)** In sharp interface models the internal boundaries have to be localised and the discontinuities of the field variables y and their derivatives have to be modelled. **(b)** Diffusive interface models regularise the discontinuity in terms of a continuously varying order parameter ϕ which represents an additional field variable. In this way an explicit localisation of interfaces can be avoided in the numerical models.

Numerical approaches

If the considered microstructure is complex and cannot be described analytically, homogenisation techniques can be combined with numerical models of the local material structure based on finite element discretisations which remove restrictions that are typical for analytic methods, e.g. regarding the particle shape and the material behaviour. Predictions for the macroscopic response are either made in terms of effective properties, characteristic curves or the computational multi-scale simulation involving a direct coupling of the numerical models of different length scales. Applications can be found in, e.g., [106, 141, 230] for magneto-mechanical and in [142, 180] for electro- and electro-magneto-mechanical field problems. This approach will be used in this work.

1.3 Numerical Modelling of Discontinuities

Discontinuities

For the computational homogenisation approach numerical models of the local material structure have to be generated. These microscale models have to account for material interfaces, cracks, or localisation phenomena which require the approximation of non-smooth fields such as the representation of discontinuities, singularities, and high gradients. With respect to MRE, in particular the modelling of material interfaces is of interest in this work, Fig. 1.2. They can be modelled by two principal approaches:

(i) *Sharp interface models:* Classical continuum theories treat internal boundaries as a sharp interface, Fig. 1.2 (a). That is, the governing equations of the field problem describe the physical behaviour in the homogeneous material phases while jump conditions state the continuity requirements between different phases in the analysis domain. In the case of material interfaces the primary field variables are required to be continuous across the interface while jumps may occur for certain components of their gradient. This is called a *weak* discontinuity. The numerical solution of sharp interface models therefore requires the localisation of the interfaces and the approximation of the discontinuous field variables. Moreover, the evolution of the microstructural features will involve topological changes of the discretisation.

(ii) *Diffuse interface models:* This approach treats interfaces in a smeared manner which is achieved through a continously varying order parameter, Fig. 1.2 (b). This additional field variable ϕ accounts for the spatial distribution of different material phases and the associated material properties, e.g. in terms of rules of mixture. Such an approach allows to fully capture the physics at the interfaces without the need to explicitly locate them. In this way topological changes are avoided in the discrete models and structured meshes can be employed. Therefore, diffuse interface representations and *phase-field* models [197] are widely used to simulate phase transformations and structural evolution processes.

The discretisation of classical continuum models and the associated sharp interface representation can be accomplished by the standard *Finite Element Method (FEM)*, Fig. 1.3 (a). It utilises approximations based on Lagrangian polynomials which provide C^0 continuity across the boundaries of individual elements. Therefore, weak discontinuities between different material phases are modelled by conforming meshes, i.e. material interfaces are represented explicitly by element edges or faces. However, for complex microstructures the process of mesh generation can be a tedious task. In order to enable a more flexible modelling of internal discontinuities and to improve the accuracy and effiency in comparison to the standard FEM, two alternative discretisation methods are in the focus of this work:

<div style="text-align: right;">Discretisation of sharp interface models</div>

(i) *Extended FEM (XFEM):* This method introduced by Belytschko et al. [9, 145] uses an enriched approximation based on Lagrangian polynomials which allow for the representation of discontinuities and singularities in non-conforming meshes, i.e. material interfaces may intersect element domains, see Fig. 1.3 (b). XFEM therefore provides an effective means for the discretisation of different particle arrangements required for the analysis of MRE.

(ii) *Isogeometric FEM (IGAFEM):* In this approach developed by Hughes et al. [99] conforming meshes and approximations based on different types of splines are utilised. The spline basis leads to a reduced overall error compared to Lagrangian basis functions. It can also provide higher-order continuity which is required for the efficient discretisation of diffuse interface models that typically involve higher than second-order spatial derivatives. However, the increased regularity results in a non-interpolatory basis, Fig. 1.3 (c).

A comparison of major features of these discretisation techniques is given in Tab. 1.1. Apart from the stated differences all approaches are essentially finite element methods. The derivation of the governing discrete equations starts from a weak form of the problem using compactly supported approximations which allow for an element point of view. In the following XFEM and IGAFEM will be briefly reviewed.

XFEM [9, 145] offers the possibility to use non-conforming meshes which do not have to be adapted to internal details, e.g. cracks or material interfaces. Instead the location of the discontinuity is located implicitly in terms of a level set [9, 159, 202, 204] and the physical behaviour is modelled by a local enrichment of the approximation. In order to handle discontinuous integrands, the element domains which are intersected by a discontinuity are divided into integration subdomains, Fig. 1.3 (b). Originally, XFEM was applied to model strong discontinuities, i.e. jumps in the primary field variables, as they occur at a crack [44, 145]. In this case XFEM enables the simulation of crack growth without remeshing as the mesh is virtually independent of the crack topology. In rapid succession the method

<div style="text-align: right;">XFEM</div>

Table 1.1: Comparison of FEM, XFEM, and IGAFEM [41]

Feature	FEM	XFEM	IGAFEM
Representation of geometry	Explicit	Implicit (Level-sets)	Explicit
Mesh	Conforming	Non-conforming	Conforming
Basis	Polynomial	Enriched, polynomial	Splines
Interpolation property	Interpolatory		Non-interpolatory
Field variables defined at	Nodes		Control points
Geometry	Approximate		Exact (in terms of CAD)
Continuity	C^0		Higher-order
Refinement	hp-refinement		hpk-refinement
Pointwise positiveness	Not guaranteed		Pointwise positive

has been used to model material interfaces [9, 114, 144, 204] which represent weak discontinuities in the mechanical boundary value problem. The combination of XFEM with cohesive zone models facilitates the modelling of interface failure [95, 115, 152]. XFEM has also been applied to non-mechanical problems, e.g. dielectric interfaces with constant values of the electric potential are modelled in [173], and the failure of electro-mechanically coupled solids is analysed by elements with embedded discontinuities in [130]. The problem of fracture in magnetoelastics is modelled by XFEM in [174]. Moreover, XFEM offers the possibility to convert CT scans into numerical analysis models [126]. Different from voxel approaches [96, 97, 118] stepped interface representations which result in oscillations of the local field variables in the vicinity of material interfaces are avoided. A comprehensive review of methodological issues of XFEM and various applications is given by Fries and Belytschko [71].

IGA

As mentioned above, spline-based discretisations are considered here because of their superior efficiency and continuity properties. However, the idea originates from the demand to remove the disjunction between geometric component models, commonly described by NURBS in Computer Aided Design (CAD) software, and FE analysis, often relying on Lagrangian polynomial approximations of geometry and field variables. Therefore, the concept of Isogeometric Analysis (IGA) was developed by Hughes et al. [99]. The central idea of IGA is to directly use CAD geometry representations to approximate field variables in the numerical model. This essentially eliminates the need for meshing of component models. Hence, the geometric discretisation errors resulting from the approximation of the geometry by Lagrangian polynomials are eliminated – the geometry used in the analysis is exactly the one defined by CAD. As a consequence, any mesh refinement required to resolve high gradients, etc. starts from the exact geometry. Isogeometric finite element analysis has been applied to a variety of problems. They include structural vibration analysis [42], fluid-structure interaction [7, 6, 8], electromagnetics [27, 212] and shape optimisation [222] as well as damage modelling [214, 215, 216] and contact problems [49, 208]. The approach has also been used with partition of unity based methods including XFEM [12, 50, 86]. Since CAD models are commonly given in terms of a NURBS-based surface description, the method is extensively applied to the analysis of shell-like structures [12, 13, 58, 120]. Throughout these different fields of application IGA has been found to allow for efficient FE formulations [7, 26]. More detailed reviews on isogeometric discretisations can be found in [41, 156].

x_2

x_3 x_1

(a)   **(b)**   **(c)**

☐☐ Standard / Isogeometric finite elements   • Nodes / Control points   ◺ Integration subdomains
◺ Elements intersected by interface   ◦ Enriched Nodes
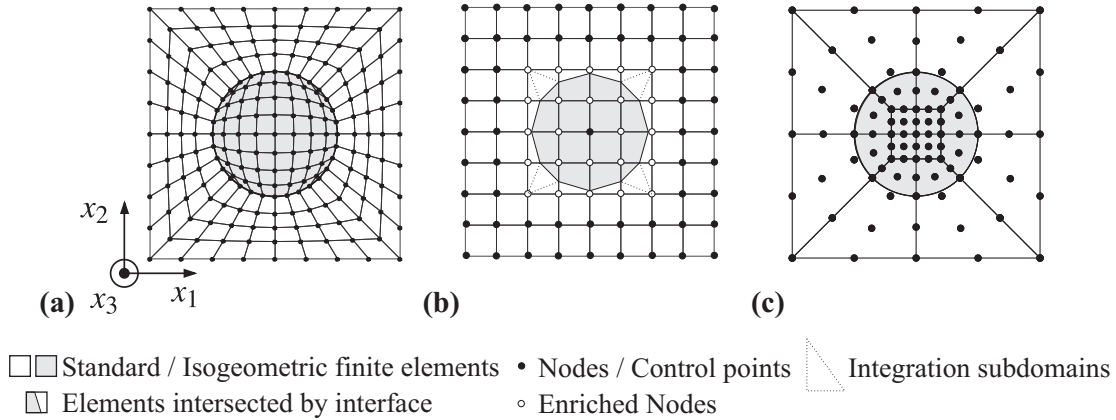
Figure 1.3: Application of the dicretisation methods considered in this work to model a bimaterial problem consisting of a circular inclusion (grey) embedded in a square domain of different material properties: **(a)** standard FEM using bilinear Lagrangian polynomials ($p = 1$) and conforming meshes, **(b)** XFEM using linear Lagrangian polynomials and non-conforming meshes. Material interfaces are modelled by an enriched approximation which requires additional degrees of freedom at nodes whose support is intersected by the discontinuity and a further subdivision of the element into integration subdomains, and **(c)** minimal IGAFEM mesh based on biquadratic NURBS ($p = 2$) shape functions which represent the geometry of the circular inclusion exactly. Due to the non-interpolatory basis, control points may not lie on element edges.

The higher-order continuity obtained from the spline basis makes isogeometric discretisations attractive for the combination with phase-field models [36, 60, 143, 197] which use a diffuse interface respresentation. In this way, the material interface still considered in XFEM is replaced or regularised by a steep gradient of the order parameter. Consequently, difficulties related to the consistent update of the interface location as well as the need for element subdivision, which actually represents a topological update, are eliminated. Since phase-field models generally involve higher than second-order partial differential operators, which impose continuity requirements that cannot be fulfilled by standard C^0-continuous Lagrangian polynomials, spline-based approximations are of special interest and facilitate a direct discretisation of the resulting weak forms [80].

Isogeometric phase-field modelling

Despite its advantages that have been demonstrated in numerous applications, isogeometric analysis faces severe mathematical and methodological challenges. Probably the most urgent have to be seen in ensuring higher-order continuity of the approximation for arbitrary geometries, and in the need for 3D solid models. That is, a suitable volume analysis mesh has to be derived from the surface representation of the structure, a task for which efficient new procedures are needed. A few attempts have been made starting from a triangulation of the boundary [136, 224, 231] or spline-based surface descriptions [232]. However, those procedures are complex and restricted to very specific model geometries and, hence, the problem remains a topic of ongoing research. An interesting alternative could be seen in the finite cell or immersed boundary approaches [57, 176, 217] which share certain common features with XFEM.

3D solid models

1.4 Outline

In the main part of this work, the numerical discretisation techniques introduced in the preceding section are combined with homogenisation techniques to predict the effective magneto-mechanical behaviour of MRE. Beyond that, ideas for the efficient modelling and simulation of structural evolution processes are discussed. The presented results have been obtained in the framework of the *European Centre for Emerging Materials and Processes (ECEMP) Dresden*, within the Priority Programme (SPP) 1681 *Field controlled particle matrix interactions: synthesis, multiscale modelling and application of magnetic hybrid materials*, and during a research visit to the University of Glasgow. In addition, first results regarding isogeometric phase-field modelling and adaptive hierarchical refinement strategies which will be further investigated in the SPP 1713 and the SPP 1748 have been included. Hence, this work is based on eight journal publications whose contents has been updated and complemented:

[HMK16] P. Hennig, S. Müller, and M. Kästner. Bézier extraction and adaptive refinement of truncated hierarchical NURBS. *Comput. Methods Appl. Mech. Engrg.*, 305:316–339, 2016.

[KMdB16] M. Kästner, P. Metsch, and R. de Borst. Isogeometric analysis of the Cahn-Hilliard equation – a convergence study. *J. Comput. Phys.*, 305:360–371, 2016.

[KMG$^+$13] M. Kästner, S. Müller, J. Goldmann, C. Spieler, J. Brummund, and V. Ulbricht. Higher-order extended FEM for weak discontinuities – level set representation, quadrature and application to magneto-mechanical problems. *Int. J. Numer. Meth. Engng*, 93:1403–1424, 2013.

[MKMU14] S. May, M. Kästner, S. Müller, and V. Ulbricht. A hybrid IGAFEM/IGABEM formulation for two-dimensional stationary magnetic and magneto-mechanical field problems. *Comput. Methods Appl. Mech. Engrg.*, 273:161–180, 2014.

[SKG$^+$13] C. Spieler, M. Kästner, J. Goldmann, J. Brummund, and V. Ulbricht. XFEM modeling and homogenization of magnetoactive composites. *Acta Mech.*, 224:2453–2469, 2013.

[SKU14] C. Spieler, M. Kästner, and V. Ulbricht. Analytic and numeric solution of a magneto-mechanical inclusion problem. *Arch. Appl. Mech.*, 2014.

[SMKU14] C. Spieler, P. Metsch, M. Kästner, and V. Ulbricht. Microscale modeling of magnetoactive composites undergoing large deformations. *Tech. Mech.*, 34:39–50, 2014.

[ZZB$^+$14] K. Zimmermann, I. Zeidis, V. Böhm, T. Kaufhold, T. Volkova, M. Krautz, A. Waske, M. Schrödner, J. Popp, M. Kästner, and C. Spieler. Mechanics of actuators based on magnetic hybrid material with applications for robotics fluid control and sensor technology. *Problems of Mechanics*, 4, 2014.

In particular the remainder of this first part which will give an introduction to the continuum formulation of the coupled magneto-mechanical boundary value problem, has been compiled from three different publications to provide a coherent statement of the underlying boundary value problems for the case of finite deformations. After a brief review of the required

foundations of continuum mechanics, the mechanical and magnetic field problems, as well as the coupling of both boundary value problems will be explained. An outline of the applied constitutive models and the presentation of two demonstration problems with available analytical solution complete this introduction.

The second part is dedicated to the XFEM modelling of magneto-mechanical boundary value problems. At first, the non-standard discretisation approach of XFEM is explained and advanced procedures for the localisation of interfaces and the quadrature of the weak form are introduced. The developed methods are verified and their numerical properties are analysed in a convergence study. The following two chapters illustrate the application of XFEM to model the microstructure in MRE. Using homogenisation techniques, the effective magneto-mechanical material behaviour is predicted for unit cell models and more complex random, isotropic and anisotropic particle distributions. The simulated magnetostrictive effect is found to be in very good agreement with experimental results.

The final part reviews isogeometric analysis and presents its application to model magneto- mechanical problems and structural evolution processes. At first, spline basis functions as well as the essential concept of Bézier extraction that allows for a seamless transition from standard FEM towards isogeometric analysis are explained. Following a numerical convergence study which demonstrates the superior numerical properties of IGA, isogeometric finite element analysis is coupled to an isogeometric boundary element method in order to analyse magnetic boundary value problems defined on open domains in an efficient way. Motivated from magnetically induced structural evolution processes observed in MRE, isogeometric discretisations of phase-field models are developed and combined with adaptive spatial discretisations based on hiearchical meshes. The described methods will be applied in future work to simulate the microstructure evolution in MRE as well as the crack propagation in heterogeneous materials.

2 Boundary Value Problems [KMG$^+$13, SKG$^+$13, SMKU14]

The modelling of the coupled magneto-mechanical behaviour on different scales is accomplished in this work by continuum theories, i.e. models that describe physical processes in terms of scalar or tensorial field variables which are functions of space and time, [1, 2, 90, 98, 211]. The atomistic structure of matter is completely disregarded. Instead, the material behaviour is taken into account by phenomenogical constitutive models which can, and to a certain extent have to, be motivated by the underlying material structure in order to produce reasonable result. Parameters of these models can be obtained either from testing of specimens or, as proposed in this work, by multi-scale modelling approaches assuming a hierarchical and heterogeneous local morphology.

The mathematical modelling in terms of a continuum approach leads to a set of governing equations which define the temporal and spatial variation of the involved field variables. Together with appropriate boundary conditions which prescribe values of the field variables on the boundary of the considered domain, they define a boundary value problem. The set of governing equations consists of general kinematic relations, balance equations and the above mentioned constitutive relations which account for the material behaviour. In this chapter the governing equations of the mechanical, the magnetic, and the coupled magneto-mechanical boundary value problems will be summarised. All equations are stated with respect to the current configuration described in terms of a Cartesian frame using mostly index notation and the Einstein summation convention.

2.1 Kinematics

A set of material particles defines a material body $\mathcal{B}$ which assumes different configurations due to deformation caused by mechanical and non-mechanical loads, Fig. 2.1. At the time $t = t_0$, the material body occupies the domain Ω_0 with volume V_0 separated from its surrounding by the boundary $\partial\Omega_0$. This state is called reference configuration. Material particles are identified by the coordinates of their position vector $\mathbf{X}$. At a time $t > t_0$, the body reaches a current configuration with domain Ω, boundary $\partial\Omega$ and volume V. The material particle $\mathbf{X} = X_K\mathbf{e}_K$ is then located at the spatial position $\mathbf{x} = x_k\mathbf{e}_k$. In the index notation, lower case indices indicate reference to the current configuration while quantities with capital indices are related to the reference configuration. The coordinates X_K are typically called material or Lagrangian coordinates, while x_k are referred to as spatial or Eulerian coordinates.

The motion of the material body defines a generally non-linear relation between both configurations. This bijective map is given by $\mathbf{x} = \boldsymbol{\chi}(\mathbf{X}, t)$, in the following abbreviated by

$$x_k = x_k(X_L, t) \,. \tag{2.1}$$

Reference configuration Ω_0 $(t = t_0)$ Current configuration Ω $(t > t_0)$
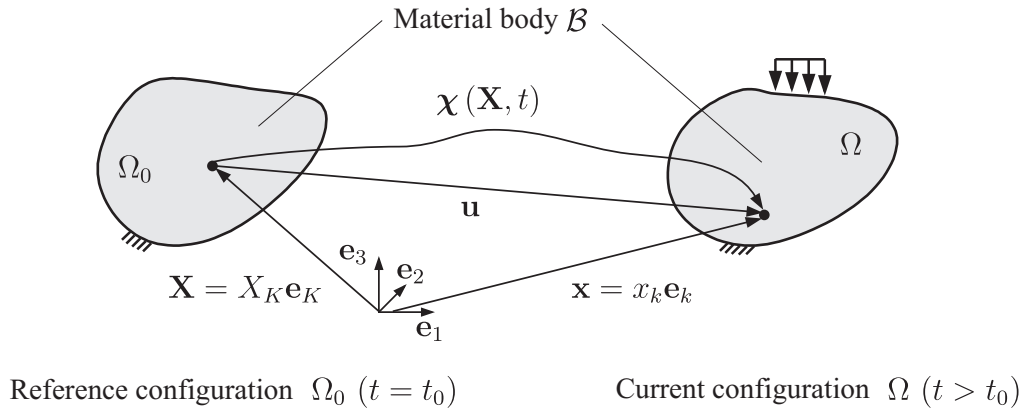
Figure 2.1: Mechanical and non-mechanial loads cause a motion χ of the material body $\mathcal{B}$. Material points identified by their position $\mathbf{X}$ in a defined reference configuration can be tracked in terms of their current spatial position $\mathbf{x}$.

If the same Cartesian frame is used for both configurations, the displacement $\mathbf{u}(\mathbf{X}, t)$ is defined as the difference between its current and original position of a material particle

$$u_K(X_L, t) = \delta_{Km} x_m(X_L, t) - X_K \ . \tag{2.2}$$

The velocity $\mathbf{v}(\mathbf{X}, t)$ is the rate of change of the position vector for a material point

$$v_K(X_L, t) = \frac{\partial u_K(X_L, t)}{\partial t} = \dot{u}_K(X_L, t) \ , \tag{2.3}$$

i.e. the time derivative of $\mathbf{u}(\mathbf{X}, t)$ with $\mathbf{X}$ held constant [10] and hence a material or total time derivative. Corresponding spatial descriptions can be obtained by exploiting the motion map (2.1), i.e.,

$$u_k(x_l, t) = \delta_{kM} u_M \left(x_l(X_N, t), t \right) \tag{2.4}$$

$$v_k(x_l, t) = \delta_{kM} v_M \left(x_l(X_N, t), t \right) . \tag{2.5}$$

Deformation gradient The partial derivative of the motion with respect to the Lagrangian coordinates

$$F_{kL} = \frac{\partial x_k(X_M, t)}{\partial X_L} = x_{k,L} \tag{2.6}$$

is defined as deformation gradient $\mathbf{F}$. From a physical point of view, the deformation gradient relates a differential line element in the current configuration to its reference state

$$dx_k = F_{kL} dX_L \ . \tag{2.7}$$

Similar transformations for infinitely small volume (dV) and surface elements $d\mathbf{S}$ are given by

$$dV = J dV_0 \tag{2.8}$$

$$dS_k = J F_{Lk}^{-1} dS_L \ . \tag{2.9}$$

These formulae involve the determinant $J = \det(F_{kL}) > 0$ of the deformation gradient $\mathbf{F}$ and its inverse

$$F_{Kl}^{-1} = \frac{\partial X_K(x_m, t)}{\partial x_l} \; . \tag{2.10}$$

Since the deformation gradient is related to the transformation of infinitesimal line elements, it enables the definition of suitable deformation measures, e.g. the left ($\mathbf{b}$) and right ($\mathbf{C}$) Cauchy-Green deformation tensors

Deformation measures

$$b_{kl} = F_{kM} F_{lM} \tag{2.11}$$
$$C_{KL} = F_{mK} F_{mL} \; . \tag{2.12}$$

Different from the deformation gradient $\mathbf{F}$ the deformation tensors do not contain contributions from rigid body rotations. Alternatively, the Euler-Almansi ($\mathbf{e}$) or Green-Lagrange ($\mathbf{E}$) strain tensors

$$e_{kl} = \frac{1}{2} \left(\delta_{kl} - b_{kl}^{-1} \right) \tag{2.13}$$

$$E_{KL} = \frac{1}{2} \left(C_{KL} - \delta_{KL} \right) \tag{2.14}$$

can be used. In the limit case of small deformations both strain tensors coincide with the infinitesimal strain tensor

$$\varepsilon_{kl} = \frac{1}{2} \left(u_{k,l} + u_{l,k} \right) \tag{2.15}$$

which is defined as the symmetric part of the displacement gradient $u_{k,l}$.

Another kinematic measure is the rate of deformation

Rate of deformation

$$D_{ij} = \frac{1}{2} \left(v_{i,j} + v_{j,i} \right) \tag{2.16}$$

computed as the symmetric part of the velocity gradient

$$L_{ij} = \frac{\partial v_i}{\partial x_j} = v_{i,j} = \dot{F}_{iK} F_{Kj}^{-1} \; . \tag{2.17}$$

2.2 Mechanical Boundary Value Problem

In this section the governing equations of the mechanical boundary value problem will be specified. The conservation of the total mass of the material body is stated in local form by

Balance of mass

$$\varrho = \frac{\varrho_0}{J} \tag{2.18}$$

where ϱ and ϱ denote the mass density with respect to the current and reference configurations, respectively.

The mechanical stress tensor $\boldsymbol{\sigma}$ has to fulfill the balances of linear momentum

Balances of momentum

$$\sigma_{kl,k} + \varrho \left(f_l - \dot{v}_l \right) = 0 \tag{2.19}$$

and angular momentum. The latter results in the symmetry of the stress tensor

$$e_{klm}\sigma_{lm} = 0. \tag{2.20}$$

In equation (2.19) $\boldsymbol{\sigma}$ is the Cauchy stress tensor, $\mathbf{e}$ represents the permutation tensor, and $\mathbf{f}$ denotes the mechanical body force density. In the case of static mechanical problems, inertia body forces $\varrho\dot{\mathbf{v}}$ are neglected.

Jump and boundary conditions

The behaviour across a material interface Γ_d is defined in terms of jump conditions which occur during the transition from the global to the local form of the balance equations. The displacement field is supposed to be continuous across an interface. The same holds for the traction vector $t_l = \sigma_{kl}n_k$ unless an additional surface traction $\mathbf{p}$ is applied.

$$[\![u_k]\!] = 0 \tag{2.21}$$

$$[\![\sigma_{kl}]\!]n_k + p_l = 0. \tag{2.22}$$

In the equations above $[\![\cdot]\!] = (\cdot)^+ - (\cdot)^-$ is the jump of a physical quantity across Γ_d with the unit normal vector $\mathbf{n}$ pointing from the subdomain Ω^- to Ω^+, Fig. 2.2 (a). Boundary conditions for the external boundary $\partial\Omega$ of the material material body are obtained from the jump conditions (2.21) and (2.22). On the part $\partial\Omega_u$ the essential condition

$$u_k = \hat{u}_k \tag{2.23}$$

holds for the k-th coordinate of the displacement vector. The natural boundary condition

$$\sigma_{kl}n_k = \hat{p}_l \tag{2.24}$$

is prescribed on $\partial\Omega_p$, where $\hat{\mathbf{p}}$ is an external surface traction. In addition, $\partial\Omega_u \cap \partial\Omega_p = \varnothing$ and $\partial\Omega_u \cup \partial\Omega_p = \partial\Omega$ hold for each coordinate.

Stress measures

As for the deformation measures, various stress tensors can be defined with respect to the reference and current configurations. These different stress tensors are of special interest for the convenient formulation of constitutive models. The Cauchy stress tensor $\boldsymbol{\sigma}$ represents the stresses in the current configuration. The weighted Cauchy stress tensor

$$\tau_{kl} = J\sigma_{kl} \tag{2.25}$$

is also known as Kirchhoff stress. The definition of further stress tensors [2, 10, 90] is based on the equivalence of infinitesimal surface forces $df_k = t_k dS = t_k^0 dS_0$ in the current and reference configuration, respectively. From the relations

$$t_k = \sigma_{lk}n_l \tag{2.26}$$

$$t_k^0 = P_{Lk}n_L \tag{2.27}$$

and the transformation (2.9), which relates the infinitesimal surface elements $dS_k = dSn_k$ and $dS_K = dS_0N_K$ in the current and reference configuration, the definition of the non-symmetric first Piola-Kirchhoff stress tensor

$$P_{Kl} = JF_{Km}^{-1}\sigma_{ml} = F_{Km}^{-1}\tau_{ml} \tag{2.28}$$

is obtained. A symmetric, purely material stress tensor is given by the second Piola-Kirchhoff
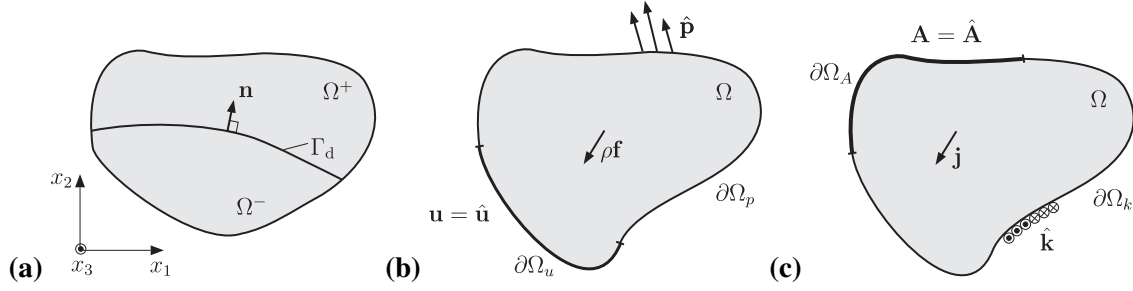
Figure 2.2: Mechanical and magnetic boundary value problems (BVP): **(a)** internal surface Γ_d with unit normal vector **n** separating the domain Ω of the material body into two domains Ω^+ and Ω^-, **(b)** mechanical BVP – prescribed displacements $\hat{\mathbf{u}}$ on $\partial\Omega_u$, surface tractions $\hat{\mathbf{p}}$ on $\partial\Omega_p$ as well as mechanical ($\varrho\mathbf{f}$) body force densities in Ω, and **(c)** magnetic BVP – prescribed vector potential $\hat{\mathbf{A}}$ on $\partial\Omega_A$, current $\hat{\mathbf{k}}$ on $\partial\Omega_k$ and current **j** in Ω.

stress

$$S_{KL} = P_{Km}F_{Lm}^{-1} = JF_{Km}^{-1}\sigma_{mn}F_{Ln}^{-1} = F_{Km}^{-1}\tau_{mn}F_{Ln}^{-1} \;. \tag{2.29}$$

Since the stress tensor can generally not be fully determined from the balances of momentum, the deformation has to be computed. The relation between the stress and deformation states are given by constitutive relations which represent the mechanical material behaviour of the body $\mathcal{B}$. The mechanical material models used in this work are specified in Section 2.6.

Constitutive relations

2.3 Stationary Magnetic Boundary Value Problem

The continuum formulation of the electro-magnetic field problem is given by the Maxwell equations [104]. They constitute a system of four coupled partial differential equations. The equations have two major variants. The atomistic set of Maxwell equations uses total charges and total currents, including those in the material at an atomic scale. From statistics and suitable averaging procedures, a macroscopic set of Maxwell equations can be derived which only considers free charges and currents. The complicated processes in the material are instead described in terms constitutive relations for the polarisation and magnetisation. More details can be found in textbooks by de Groot and Suttorp [48] as well as Eringen and Maugin [63]. In the case of stationarity, the electric and magnetic fields decouple and can therefore be treated separately. In this contribution only magnetic fields are of interest. The local form of the Maxwell equations with respect to the current configuration reads in this case

Maxwell equations

$$B_{k,k} = 0 \tag{2.30}$$

$$e_{klm}H_{m,l} = j_k \tag{2.31}$$

with the magnetic induction **B**, the magnetic field **H** and the vector of free current density **j**. The first equation is called Gauss' law and states the solenoidality of the magnetic induction, i.e. the fact that no magnetic charges or monopoles exist. Equation (2.31), typically known as Ampere's law, mathematically states the experience that magnetic fields are generated by electric currents.

Jump
conditions

At a surface of discontinuity Γ_d the jump conditions

$$[\![B_i]\!]n_i = 0 \tag{2.32}$$

$$e_{ijk}[\![H_k]\!]n_j - k_i = 0 \tag{2.33}$$

hold for the magnetic induction and field strength. Equation (2.32) represents the continuity of the normal component of the magnetic induction. If no current density **k** acts on Γ_d, the tangential components of the magnetic field strength have to be continuous according to equation (2.33). A detailed derivation of the jump conditions is presented in [25].

Magnetisation

The magnetic induction **B** is related to the magnetic field **H** by the general relation

$$B_k = \mu_0(H_k + M_k) \tag{2.34}$$

where $\mu_0 = 4\pi \times 10^{-7}\,\mathrm{N/A}^2$ is the permeability of free space. While equation (2.34) holds for any material, the choice of a constitutive relation for the magnetisation **M** defines the material behaviour of a magnetisable material. Magnetic material models used in this work will be introduced in Section 2.6.

Vector
potential

In order to solve the Maxwell equations (2.30) and (2.31), it is convenient to introduce a potential which a priori satisfies one of the equations. This potential than serves as the primary variable in an FE implementation and hence takes the role of the displacement field in a purely mechanical boundary value problem, Tab. 2.1. One possible choice is to use the magnetic vector potential **A** which is related to the magnetic induction by

$$B_k = e_{klm}A_{m,l}\,. \tag{2.35}$$

Consequently, the vector potential automatically satisfies Gauss' law (2.30) and only (2.31) has to be considered for the solution of the stationary magnetic boundary value problem. In order to fully define the vector field **A**, a gauge condition for its divergence is required for three-dimensional problems. Often the Coulomb gauge

$$A_{k,k} = 0 \tag{2.36}$$

is applied. For the two-dimensional problems considered here, equation (2.36) is automatically satisfied. At a surface of discontinuity, equation (2.35) requires the tangential component of **A** to be continuous, while the Coulomb gauge results in the continuity of the normal component. Therefore, the vector potential is continuous across Γ_d and the jump condition (2.32) is replaced by

$$[\![A_k]\!] = 0\,. \tag{2.37}$$

The boundary $\partial\Omega$ represents a special case of a surface of discontinuity. Boundary conditions can be deduced from the evaluation of the jump conditions (2.33) and (2.37). On the part $\partial\Omega_A$ of the external boundary the essential condition

$$A_k = \hat{A}_k \tag{2.38}$$

is imposed for the k-th coordinate of the vector potential. The part of $\partial\Omega$ with the natural bounadry condition

$$e_{klm}H_m n_l = -\hat{k}_k \tag{2.39}$$

is labelled $\partial\Omega_k$. The prescribed value $\hat{\mathbf{k}}$ has to represent the effects of any external magnetic field outside the domain Ω and of a surface current **k** applied on $\partial\Omega_k$. For the well-posed

definition of the boundary conditions $\partial\Omega_A \cap \partial\Omega_k = \varnothing$ and $\partial\Omega_A \cup \partial\Omega_k = \partial\Omega$ have to be valid for each coordinate direction. A detailed discussion of the influence of gauging and the choice of different boundary conditions in vector potential formulations is presented by Stark et al. [196].

Alternatively to the vector potential, the magnetic scalar potential φ defined by

$$H_k = -\varphi_{,k} \tag{2.40}$$

can be used. Equation (2.40) automatically fulfills Ampère's law (2.31) for the case of vanishing current densities. Similar to the vector potential, the scalar potential is continuous across Γ_{d}

$$[\![\varphi]\!] = 0 \tag{2.41}$$

which automatically requires the tangential component $e_{ijk}[\![H_k]\!]n_j = 0$ of the magnetic field to be continuous for vanishing surface current densities $\mathbf{k} = \mathbf{0}$ and therefore corresponds to the jump condition (2.33). From equation (2.41) and the jump condition (2.32) for the magnetic induction the following essential and natural boundary conditions can be deduced:

$$\varphi = \hat{\varphi} \quad \text{on} \quad \partial\Omega_\varphi \tag{2.42}$$

$$B_k n_k = \hat{\eta} \quad \text{on} \quad \partial\Omega_\eta \,. \tag{2.43}$$

Again, for the well-posed definition of the boundary conditions $\partial\Omega_\varphi \cap \partial\Omega_\eta = \varnothing$ and $\partial\Omega_\varphi \cup \partial\Omega_\eta = \partial\Omega$ have to be valid for each coordinate direction.

The availability of two magnetic potentials rises the question of which formulation to use. In this work the magnetic vector potential is used as it provides more flexibility for future applications, i.e. it facilitates the simulation of instationary processes and the application of current densities. In addition, the resulting magneto-mechanical problem is of minimum-minimum type which enables the use of efficient solvers whereas the magnetic scalar potential ends up in a saddle point problem which excludes the use of certain efficient solution procedures [141, 142]. On the other hand, the scalar potential naturally comes along with a reduced number of degrees of freedom compared to the vector valued formulation. This is of interest especially for large and three-dimensional models as well as during the analysis of strongly coupled magneto-mechanical problems which generally require the simultaneous analysis of the magnetic and mechanical problem. Furthermore gauging is not required.

2.4 Coupled Magneto-Mechanical Boundary Value Problem

The formulations of the two previously outlined boundary value problems can be combined to specify a strongly coupled magneto-mechanical field problem which accounts for the following bidirectional coupling:

(i) *Mechanics → Magnetics:* The influence of mechanical deformations on the current magnetic fields are modelled in terms of continuum formulations and numerical procedures suitable for finite deformations.

(ii) *Magnetics → Mechanics:* The effect of magnetic forces and couples on the deformation of the material body is accounted in terms of magnetic contributions to the total stress tensor.

(iii) *Constitutive Coupling:* Magnetorheological and -strictive effects in the individual material phases can be represented by appropriate constitutive models.

Since the individual microscopic constituents, i.e. the magnetisable particles and the polymeric matrix, do not exhibit magnetorheological or magnetostrictive coupling effects (iii), constitutive models for the representation of these effects are beyond the scope of this work. However, microscopic interactions between the magnetisable particles result in magnetically induced macroscopic stiffness changes and deformations which are predicted using a multiscale approach outlined in Chapter 4.

Magnetic body force

While the effect of mechanical deformations on the magnetic field (i) is accounted for by the evaluation of the governing equations in the current configuration, the formulation of the mechanical boundary value problem presented in Section 2.2 has to be extended in order to represent the influence of the magnetic field on the mechanical deformations (ii). This is accomplished in terms of a magnetic body force density $\mathbf{f}^{\mathrm{m}}$

$$\sigma_{kl,k} + \varrho\left(f_l - \dot{v}_l\right) + f_l^{\mathrm{m}} = 0 \tag{2.44}$$

which according de Groot and Suttorp [48] is given by

$$f_k^{\mathrm{m}} = e_{klm} j_l B_m + B_{l,k} M_l. \tag{2.45}$$

Mechanical and magnetic stress tensors

For convenience, the problems will formulated in terms of the symmetric total Cauchy stress tensor $\boldsymbol{\sigma}^{\mathrm{tot}}$ which has to fulfill the balances momentum identical to the purely mechanical case. The total stress

$$\sigma_{kl}^{\mathrm{tot}} = \sigma_{kl} + \sigma_{kl}^{\mathrm{m}} \tag{2.46}$$

can be split additively into a mechanical $\boldsymbol{\sigma}$ and magnetic stress tensor

$$\sigma_{kl}^{\mathrm{m}} = \frac{1}{\mu_0} B_k B_l - \frac{1}{2\mu_0} B_m B_m \delta_{kl} - B_k M_l + B_m M_m \delta_{kl} \tag{2.47}$$

which is in agreement with microscopic theories [48]. In the absence of any magnetisation $\boldsymbol{\sigma}^{\mathrm{m}}$ reduces to the Maxwell stress tensor. The magnetic body force and the stress tensor are related by $f_l^{\mathrm{m}} = \sigma_{kl,k}^{\mathrm{m}}$.

Balances of momentum

In the stationary coupled magneto-mechanical case, the total stress has to fulfill the balances of linear momentum

$$\sigma_{kl,k}^{\mathrm{tot}} + \varrho\left(f_l - \dot{v}_l\right) = 0 \tag{2.48}$$

and angular momentum which results in the symmetry of the total stress tensor

$$e_{klm}\sigma_{lm}^{\mathrm{tot}} = 0 \,. \tag{2.49}$$

Although the total stress tensor will always be symmetric, both mechanical and magnetic stress tensors lose their symmetry for anisotropic magnetic material behaviour. It is therefore preferable from a numerical point of view to decompose the total stress into the *symmetric* pseudo-mechanical $_{\mathrm{E}}\boldsymbol{\sigma}$ and pseudo-magnetic $\hat{\boldsymbol{\sigma}}$ stress tensors according to [63]

$$\sigma_{ij}^{\mathrm{tot}} = {_{\mathrm{E}}\sigma_{ij}} + \hat{\sigma}_{ij}, \quad {_{\mathrm{E}}\sigma_{ij}} = \sigma_{ij} + M_i B_j, \quad \hat{\sigma}_{ij} = \sigma_{ij}^{\mathrm{m}} - M_i B_j. \tag{2.50}$$

As a consequence of the introduction of the total stress tensor, the jump condition for the traction vector is formulated in terms of a total traction vector

$$\llbracket \sigma_{kl}^{\mathrm{tot}} \rrbracket n_k + p_l = 0 \, . \tag{2.51}$$

The corresponding natural boundary condition

$$\sigma_{kl}^{\mathrm{tot}} n_k = \hat{p}_l \tag{2.52}$$

is prescribed on $\partial\Omega_p$, where the effective external surface load $\hat{\mathbf{p}}$ has to account for any contribution due to mechanical $t_l = \sigma_{kl} n_k$ and magnetic tractions $t_l^{\mathrm{m}} = \sigma_{kl}^{\mathrm{m}} n_k$ from the exterior of the material body as well as an applied mechanical surface load $\mathbf{p}$. The continuity of the displacement field (2.21) also holds in the magneto-mechanical case. Hence, essential boundary conditions for the displacement are prescribed on $\partial\Omega_u$. Eventually, it can be noted that in the case of vanishing magnetic fields, the formulation of the coupled magneto-mechanical problem reduces to the mechanical field problem of Section 2.2.

In the preceding sections, the principal structure of boundary value problems that includes balance equations, kinematic relations or the definition of a magnetic potential, and constitutive equations accompanied by suitable boundary conditions was outlined. Table 2.1 compares the different sets of equations which govern the mechanical, magnetostatic and electrostatic[1] boundary value problems. In the stationary magnetic and electric cases the governing equations are given by subsets of the Maxwell equations, i.e. two equations for each problem. One of these equations is automatically satisfied by the definition of a potential. In the mechanical case the problem is usually stated by the balance of momentum and the assumed kinematics. This kinematic relation actually represents the definition of a mechanical potential, namely the displacement field. This complete analogy to the magnetic and electric case becomes obvious if the compatibility conditions are explicitly considered. They are, as in the other cases, fulfilled by the definition of strain-displacement relation.

Table 2.1: Analogies of the mechanical, magnetic, and electric boundary value problems.

Equations	Mechanical	Magnetic	Electric
Governing equations	$\sigma_{ij,i} + \varrho f_j = 0$	$e_{ijk} H_{k,j} = j_i$	$D_{i,i} = \varrho_{\mathrm{e}}$
	$e_{ijk} e_{lmn} \varepsilon_{nk,mj} = 0$	$B_{i,i} = 0$	$e_{ijk} E_{k,j} = 0$
Potential	$\varepsilon_{ij} = \frac{1}{2}\left(u_{i,j} + u_{j,i}\right)$	$B_i = e_{ijk} A_{k,j}$	$E_i = -\varphi_{,i}$
Constitutive equations	$\sigma_{ij} = \sigma_{ij}(\varepsilon_{kl})$	$H_i = H_i(B_j)$	$D_i = D_i(E_j)$
Jump conditions	$\llbracket u_i \rrbracket = 0$	$\llbracket A_i \rrbracket = 0$	$\llbracket \varphi \rrbracket = 0$
	$\llbracket \sigma_{ij} \rrbracket n_i + p_j = 0$	$e_{ijk} \llbracket H_k \rrbracket n_j = k_i$	$\llbracket D_i \rrbracket n_i = r$

2.5 Energy and Entropy Balances

In order to formulate thermodynamically consistent material models, the balances of energy

---

[1]The electric field quantities are: the dielectric displacement D_i, the eletric field strength E_i, the electric potential φ, and body ϱ_{e} as well as surface charge density r.

and entropy are considered in the following. They establish a connection between the mechanical and magnetic field variables and the energetic state of the material body. This state will change due to the transfer of mechanical and non-mechanical, i.e. magnetic, electric, or thermal power to the material body. The local form of the balance of the specific internal energy u is given by

$$\varrho\dot{u} = \sigma_{kl}v_{l,k} - M_k\dot{B}_k + j_kE_k - q_{k,k} + \varrho r \ . \tag{2.53}$$

In equation (2.53) $\mathbf{q}$ represents the heat flux vector and r is a specific heat source density. Although the electric field is not explicitly involved in the analysis of the stationary magnetic field problem outlined in Section 2.3, the product of the free current density $\mathbf{j}$ and the electric field strength $\mathbf{E}$ enters the balance of the internal energy. Since the energetic state is not considered explicitly in this work, the electric field does not have to be computed. However, the term is of importance for the discussion of the thermodynamic admissibility of constitutive equations.

Entropy balance
The entropy balance, which is also known as second principle of thermodynamics, is commonly stated in terms of an inequality for the entropy production

$$\varrho\gamma = \varrho\dot{s} + \left(\frac{1}{T}q_k\right)_{,k} - \frac{1}{T}\varrho r \geq 0 \ . \tag{2.54}$$

where γ is the specific entropy production and s is the specific entropy. Moreover, it was assumed that the entropy flux is parallel to the heat flux vector $\mathbf{q}$. Equation (2.54) expresses restrictions on the admissibility of a thermodynamic process. While the limit case of zero entropy production corresponds to an ideal, reversible process, negative entropy production is not meaningful from a physical point of view. Introducing the free Helmholtz energy $\psi = u - Ts$ and using the balance of the internal energy (2.53), the Clausius-Duhem inequality

$$\varrho T\gamma = -\varrho\left(\dot{\psi} + \dot{T}s\right)\sigma_{kl}v_{l,k} - M_k\dot{B}_k + j_kE_k - \frac{1}{T}q_kT_{,k} \geq 0 \tag{2.55}$$

is obtained. It is utilised in the following to test the thermodynamic admissibility of the constitutive relations introduced in the next section.

2.6 Constitutive Equations

Motivation
The equations discussed so far are valid irrespectively of the material in the analysis domain Ω. It is however known from experience that the deformation behaviour of a component will depend on the stiffness of the material and the presence of magnetisable matter will have an influence on any magnetic field. In the continuum formulation applied here, phenomenological constitutive models which neglect the underlying atomistic structure are used to account for the behaviour of the individual materials. From a mathematical point of view, the constitutive equations resolve the difference between the number of unknown field variables and balance equations.

2.6.1 Structure and Classification

Explicit representation
A constitutive equation relates a (tensorial) constitutively dependent variable $\mathbf{Y}$ to the history of a set of m constitutively independent variables $\mathbf{Z}_\alpha$, $\alpha = 1 \ldots m$. The most general

structure of a constitutive equation is given by the functional

$$\mathbf{Y}(t) = \underset{\tau \leq t}{\mathfrak{F}} \left[\mathbf{Z}_\alpha(\tau) \right] \tag{2.56}$$

where t is the current time and τ indicates any point of time in the process history.

Since a closed form representation cannot be stated explicitly for all classes of material models, implicit representations

$$\mathbf{Y}(t) = \mathbf{Y} \left[\mathbf{Z}_\alpha(t), \mathbf{q}_\beta(t) \right] \tag{2.57}$$
$$\dot{\mathbf{q}}_\beta(t) = \dot{\mathbf{q}}_\beta \left[\mathbf{Z}_\alpha(t), \mathbf{q}_\beta(t) \right], \tag{2.58}$$

are of special practical importance. In this formulation the history dependence, which results from, e.g., rate dependent or independent flow or magnetisation processes, is modelled by a set of n (tensorial) internal variables $\mathbf{q}_\alpha$, $\alpha = 1 \ldots n$ and the corresponding evolution equations (2.58). The equivalence to the closed form notation of equation (2.6.1) can be demonstrated by integration of the evolution equations and combination with (2.57).

In order to properly represent a material behaviour observed in experiments, a suitable material model has to be chosen and its parameters have to be identified. For special phenomena, new constitutive models have to be constructed. A guideline therefor is given by general principles of the theory of materials [211]. Moreover, the constitutive equations have to be consitent with the balance equations [179], e.g. the Clausius-Duhem inequality (2.55) places restrictions on the particular relations and the chosen parameters. For the systematic development of constitutive models and their application, it is convenient to classify the behaviour of materials and to define a set of fundamental experiments which allow for their classification. Regarding the phenomena observed in mechanical experiments, Haupt [89, 90] has suggested four categories of stress-strain behaviour as discussed in more detail in [113, 116]. This classification can also be generalised to non-mechanical phenomena. In the simplest case of material behaviour the process history has no influence on the current state $\mathbf{Y}$ and the functional (2.6.1) reduces to a function

$$\mathbf{Y}(t) = \mathbf{Y}\left(\mathbf{Z}_\alpha(t) \right) \tag{2.59}$$

of the current variables $\mathbf{Z}_\alpha(t)$. Typical mechanical and magnetic examples for this class of behaviour are all stress-strain and magnetisation curves without hysteresis as used in this work.

2.6.2 Thermodynamic Consistency

In order to obtain thermodynamically consistent material models, the Clausius-Duhem inequality (2.55) which imposes restrictions on the constitutive relations has to be examined. Assuming that the material behaviour depends on the mechanical deformation, the magnetic field and the temperature, i.e. $\psi = \psi(\mathbf{Z}_\alpha) = \psi(F_{lM}, B_K, T)$, equation (2.55) can be stated in the form

$$-\varrho \left[\frac{\partial \psi}{\partial F_{lM}} \dot{F}_{lM} + \frac{\partial \psi}{\partial B_K} \dot{B}_K + \frac{\partial \psi}{\partial T} \dot{T} + \dot{T} s \right] + \left(\sigma_{kl} + M_k B_l \dot{F}_{lM} \right) F_{Mk}^{-1} - \frac{1}{J} M_K \dot{B}_K \geq 0 \tag{2.60}$$

where the definition of the velocity gradient $v_{k,l}$ (2.17) has been utilised. The postulated independence of the material behaviour from the electric field and the temperature gradient results in the residual inequality

$$j_k E_k - \frac{q_k}{T} T_{,k} \geq 0 \ . \tag{2.61}$$

According to the procedure of Coleman and Noll [39] the general constitutive relations

$$_\text{E}\sigma_{kl} = \varrho F_{kM} \frac{\partial \psi}{\partial F_{lM}} = \sigma_{kl} + M_k B_l \tag{2.62}$$

$$M_K = -\varrho_0 \frac{\partial \psi}{\partial B_K} \tag{2.63}$$

$$s = -\frac{\partial \psi}{\partial T} \tag{2.64}$$

are derived from the inequality (2.60) and therefore guarantee thermodynamic consistency. With the limitation to isothermal processes, the relations (2.61) and (2.64) are not of interest in the following and the temperature is not considered in the set of independent constitutive variables. Specific equations for stress and magnetisation are obtained from this framework by the definition of a particular Helmholtz free energy as outlined subsequently. It is noted that only for non-magnetisable materials the stress tensor $_\text{E}\boldsymbol{\sigma}$ equals the mechanical stress tensor $\boldsymbol{\sigma}$ according to (2.62).

Helmholtz free energy The formulation of a free energy functional depends on the physical phenomena to be modelled. In order to conform with the principle of objectivity, field variables of the reference configuration are chosen as constitutively independent variables. The free energy $\psi = \psi(C_{KL}, B_M)$ is assumed to depend on the right Cauchy-Green deformation tensor C_{KL}, the material magnetic induction B_K. Due the representation of magneto-mechanical coupling effects, the free energy will involve mechanical and magnetic contributions. Here, an additive decomposition

$$\psi(C_{KL}, B_M) = \psi^{\text{mag}}(C_{KL}, B_M) + \psi^{\text{mech}}(C_{KL}, B_M) \tag{2.65}$$

is employed. For the multi-scale approach pursued in this contribution a free energy functional for each constituent has to be specified:

(i) *Matrix:* Typical polymeric matrices (superscript *M*) of MRE have a very low stiffness and are therefore likely to undergo large deformations. The matrix is non-magnetisable and the free energy functional will be purely mechanical and does not depend on the magnetic induction

$$\psi^\text{M} = \psi^{\text{mech}}(C_{KL}) \ . \tag{2.66}$$

(ii) *Particles:* The particles (superscript *P*) are magnetisable and will deform. However, they are very stiff compared to the surrounding matrix and the deformations resulting from the loading of the MRE will be small. It is therefore assumed that the magnetic and mechanical contributions to the total free energy decouple according to

$$\psi^\text{P} = \psi^{\text{mag}}(B_K) + \psi^{\text{mech}}(C_{LM}) \ . \tag{2.67}$$

These assumptions are in line with the analytical description of rigid magnetisable inclusions in a non-magnetisable elastomer by Ponte Castañeda and Galipeau [170]. Therefore, mate-

rial models, which describe the coupled behaviour in a purely phenomenological manner, are not required to model the material behaviour of the individual constituents on the microscale. The magnetic field quantities of the reference configuration which are used during the derivation of the constitutive equations are available from a set of pull back operations [63]

$$B_K = F_{lK} B_l \tag{2.68}$$

$$H_K = J F_{Kl}^{-1} H_l \tag{2.69}$$

$$M_K = J F_{Kl}^{-1} M_l . \tag{2.70}$$

It should be mentioned that the choice of these transformations is not unique. Starting from the same constitutive relation in the Lagrangian formulation, the use of a different set of pull back transformations [111] will result in a different material behaviour in the current configuration.

2.6.3 Magnetisation Behaviour

Carbonyl iron powder, e.g. BASF CIP CC which is often used in MRE, exhibits a non-linear magnetisation behaviour dominated by saturation effects with a negligible hysteresis, Fig. 4.2. Since the experimental characterisation does not induce any relevant deformation of the magnetic specimen, the measured values represent material quantities.

Experiment

Different functions have been used in the literature to model non-linear isotropic magnetisation behaviour of the particles. Three of the most frequently used two-parameter relations are the Langevin function

Magnetisation $M(H)$

$$M_K = a_1 \left[\coth \left(a_2 H \right) - \frac{1}{a_2 H} \right] H_K , \tag{2.71}$$

the Ising relation

$$M_K = c_1 \tanh \left(c_2 H \right) H_K , \tag{2.72}$$

and the Fröhlich-Kennelly model

$$M_K = \frac{d_1}{1 + d_2 H} H_K . \tag{2.73}$$

These equations all use the magnetic field H_K as independent constitutive variable with $H = \sqrt{H_K H_K}$. The Langevin model (2.71) is applied in Chapter 4 to model the magnetisation behaviour for small deformations.

In the case of large deformations the magnetic induction B_K is preferred as constitutively independent variable according to equation (2.63). It has been found in [139] and [SMKU14] that a modified Ising relation

Modified Ising relation $M(B)$

$$M_K = M_s \tanh \left(\delta B \right) \frac{B_K}{B_0} \tag{2.74}$$

with $B_0 = \sqrt{B_K B_K}$ the norm of the material magnetic induction provides a good approximation to the experimental magnetisation curve. The parameters c_1 and c_2 have been identified as the saturation magnetisation M_s, and a scaling factor δ. A linearisation of equation

(2.74) in the vicinity of $B_0 = 0$, yields the linear relation

$$M_K = \chi_B B_K = M_s \delta B_K = \frac{\mu_r - 1}{\mu_0 \mu_r} B_K = (\mu_r - 1)\, H_K \,. \tag{2.75}$$

Magnetic free energy

Free energy functions that correspond to the expressions (2.74) and (2.75) are obtained from integration according to the constitutive relation (2.63). For the magnetically non-linear case, the potential

$$\psi^{\mathrm{mag}} = -\frac{M_s}{\varrho_0 \delta} \ln\left[\cosh\left(\delta B_0\right)\right] \tag{2.76}$$

found, while

$$\psi^{\mathrm{mag}} = -\frac{1}{2\varrho_0} \chi_B B_0^2 \tag{2.77}$$

holds for linear magnetic material behaviour, respectively. Since ϱ_0 and B_0 are quantities of the reference configuration, the derivative of ψ^{mag} with respect to the deformation gradient $\mathbf{F}$ according to (2.62) does not result in any stress contribution.

2.6.4 Mechanical Material Behaviour

Introduction

In order to capture finite deformations which can occur in MRE, a hyperelastic material model is used to represent the mechanical behaviour of the polymeric matrix. The large deformation characteristics of elastomers have been modelled by statistical models and continuum mechanics approaches. Comprehensive reviews have been presented by, e.g., Boyce and Arruda [19] and Steinmann et al. [199] who also provide a comparison of the performance of different models. In this work continuum models will be applied and according to the previous section, the pseudo-mechanical stress tensor

$$_{\mathrm{E}}\sigma_{kl} = \sigma_{kl} + M_k B_l = \varrho F_{kM} \frac{\partial \psi^{\mathrm{mech}}}{\partial F_{lM}} \tag{2.78}$$

is determined by the mechanical fraction ψ^{mech} of the free energy only. Since the material behaviour of unreinforced elastomers will be isotropic, the required free energy ψ^{mech} is formulated in terms of invariants I_k of the deformation tensors or principal stretches λ_i, respectively.

Ogden model

Here a model derived by Ogden [157, 158] is applied which is defined by the free energy function

$$\psi^{\mathrm{mech}}\left(\lambda_i\right) = \rho_0 \sum_{\alpha=1}^{N} \frac{\mu_\alpha}{c_\alpha} \left(\lambda_1^{c_\alpha} + \lambda_2^{c_\alpha} + \lambda_3^{c_\alpha} - 3\right) \tag{2.79}$$

formulated in terms of principal stretches λ_i which are the square root of the eigenvalues of the deformation tensors $\mathbf{C}$ and $\mathbf{b}$. These principal stretches allow for representation of the deformation gradient and the deformation tensors in terms of a spectral decomposition

$$F_{kL} = \sum_{i=1}^{3} \lambda_i^2 n_k^i N_L^i \,, \quad C_{KL} = \sum_{i=1}^{3} \lambda_i^2 N_K^i N_L^i \,, \quad b_{kl} = \sum_{i=1}^{3} \lambda_i^2 n_k^i n_l^i \tag{2.80}$$

with the i-th eigenvectors $\mathbf{N}_i$ of the reference and current configuration $\mathbf{n}_i$, respectively. The material parameters μ_α und c_α have to be identified from experiments. Two conditions on

the material parameters

$$\sum_{\alpha=1}^{n} \mu_\alpha c_\alpha = 2\mu \, , \quad \mu_{(\alpha)} c_{(\alpha)} > 0 \tag{2.81}$$

ensure the compatibility to the limiting case of linear elasticity for small deformation as well as polyconvexity [228].

The Ogden formulation represents a class of models formulated in principal stretches that includes the Neo-Hooke model [228]. Its free energy

<div style="text-align:right">Neo-Hooke</div>

$$\psi^{\text{mech}}(\lambda_i) = \rho_0 \frac{\mu}{2} \left(\lambda_1^2 + \lambda_2^2 + \lambda_3^2 - 3 \right) \tag{2.82}$$

follows from the general relation (2.79) for $n = 1$, $\mu_1 = \mu$ und $c_1 = c = 2$.

As mentioned above, the pseudo-mechanical stress tensor $_{\text{E}}\boldsymbol{\sigma}$ can be computed directly from the mechanical free energies (2.79) or (2.82) using relation (2.62) for the considered types of local constituents. Since rubber-like polymers are usually assumed to be incompressible which is mathematically represented by $J = \lambda_1 \lambda_2 \lambda_3 = 1$, the stress state is however not fully determined by the free energy. In addition, the hydrostatic pressure p which can be interpreted as a Lagrangian multiplyer that enforces incompressibility has to be considered

<div style="text-align:right">Incompressi-
bility</div>

$$_{\text{E}}\sigma_{kl} = -p\delta_{kl} + \varrho F_{kM} \frac{\partial \psi^{\text{mech}}}{\partial F_{lM}} \tag{2.83}$$

$$= -p\delta_{kl} + 2\varrho F_{kM} F_{lN} \frac{\partial \psi^{\text{mech}}}{\partial C_{MN}} \, . \tag{2.84}$$

A convenient way to compute the stress tensor is obtained from its spectral representation

$$_{\text{E}}\sigma_{kl} = \sum_{i=1}^{3} \sigma_i n_k^i n_l^i \, . \tag{2.85}$$

The principal stresses σ_i follow from equation (2.84) as

$$\sigma_i = -p + \lambda_{(i)} \frac{\partial \psi^{\text{mech}}}{\partial \lambda_{(i)}} \tag{2.86}$$

where relations between the deformation tensor and the principal stretches as outlined by Simo and Taylor [190] have been used.

Although incompressibility is widely assumed for elastomers, their behaviour is in reality only nearly incompressible. Accurate models will therefore have to account for non-isochoric deformations. In addition to a more accurate representation of the material behaviour, compressible formulations avoid mixed FE formulations which consider the hydrostatic pressure p as a separate field quantity. In this case the incompressibility condition is removed and the free energy function is amended by an additional term related to volumetric deformations in terms of J. Two different approaches are typically used:

<div style="text-align:right">Compressi-
bility</div>

(i) In the first approach a bulk strain energy term $\psi^{\text{b}}(J)$ is added to an existing free energy function ψ^{a} given by equations (2.79) or (2.82)

$$\psi^{\text{mech}} = \psi^{\text{a}}(\lambda_i) + \psi^{\text{b}}(J). \tag{2.87}$$

In this case, both terms contain volumetric contributions to the total free energy. Considering $J = \lambda_1\lambda_2\lambda_3$, the stress tensor is fully determined in terms of the free energy

$$_{\mathrm{E}}\sigma_{kl} = \sum_{i=1}^{3} \sigma_i n_k^i n_l^i \quad \text{with} \quad \sigma_i = \lambda_i \frac{\partial \psi^{\mathrm{mech}}}{\partial \lambda_i} \,. \tag{2.88}$$

(ii) A convenient free energy formulation for compressible material behaviour that distinguishes between purely deviatoric and volumetric contributions to the mechanical free energy

$$\psi^{\mathrm{mech}} = \psi^{\mathrm{dev}}(\tilde{\lambda}_i) + \psi^{\mathrm{vol}}(J) \tag{2.89}$$

is obtained from replacing the principal stretches λ_i in equations (2.79) or (2.82) by principal deviatoric stretches

$$\tilde{\lambda}_i = J^{-1/3}\lambda_i \,, \quad \tilde{\lambda}_1\tilde{\lambda}_2\tilde{\lambda}_3 = 1 \,. \tag{2.90}$$

A purely volumetric contribution to the free energy $\psi^{\mathrm{vol}}(J)$ accounts for volumetric changes. According to [190] the stress is given by

$$_{\mathrm{E}}\sigma_{kl} = \frac{d\psi^{\mathrm{vol}}(J)}{dJ}\delta_{kl} + \sum_{i=1}^{3} \left[\tilde{\lambda}_i \frac{\partial \psi^{\mathrm{dev}}}{\partial \tilde{\lambda}_i} - \sum_{j=1}^{3} \tilde{\lambda}_j \frac{\partial \psi^{\mathrm{dev}}}{\partial \tilde{\lambda}_j} \right] n_k^i n_l^i \,. \tag{2.91}$$

Used models All large deformation computations in Chapter 5 are carried out based on the numerical implementation [110] of a compressible Ogden model in conjunction with the volumetric free energy contribution [228]

$$\psi^{\mathrm{vol}}(J) = \frac{\kappa}{4}\left(J^2 - 2\ln J - 1\right) \tag{2.92}$$

with the compression modulus κ. As mentioned above, this implementation includes the Neo-Hooke[2] model for $n = 1$, $\mu_1 = \mu$ und $c_1 = c = 2$ and does not require further consideration. The limiting case of incompressibility is realised numerically for both models by Poisson ratios close to $\nu = 0.5$ which did not result in problems for the computations in this work. Analytical reference solutions for the incompressible case are however directly obtained from equation (2.86). All models outlined in this section recover the classical Hookean law

$$_{\mathrm{E}}\sigma_{kl} = 2\mu\varepsilon_{kl} + \Lambda\varepsilon_{mm}\delta_{kl}. \tag{2.93}$$

in the case of small deformations. Therefore, the Neo-Hooke model can also be applied to represent the elastic behaviour of the carbonyl iron particles according to equation (2.67). In the relations above the LAMÉ parameters μ and Λ have been used. These constants and the compression modulus κ are related to the engineering constants E and ν by

$$\mu = \frac{E}{2\left(1 + \nu\right)} = G \,, \quad \Lambda = \frac{E\nu}{(1+\nu)(1-2\nu)} \,, \quad \kappa = \frac{E}{3\left(1-2\nu\right)} \,. \tag{2.94}$$

---

[2]*Remark:* The same Neo-Hooke material is obtained from the first approach for
$\psi^{\mathrm{b}}(J) = \frac{\Lambda}{4}(J^2 - 2\ln J - 1) - \mu\ln J.$

2.7 Analytical Reference Solutions

For the verification and analysis of the numerical solution schemes developed in this work analytical solutions are of special interest as they allow for the computation of numerical errors and the quantification of the convergence behaviour. There are few analytical treaties of coupled magneto-mechanical boundary value problems documented the literature, e.g. [3, 63, 160]. However, none of the published solutions considers heterogeneous material structures with at least two different magnetisable constituents.

During the verification process of the implemented algorithms two problems have been utilised as reference solutions in this work:

(i) The first demonstration problem considers a magnetic field which generates a force acting on a magnetisable inclusion. Solutions for the inhomogeneous magnetic field generated by a current-carrying wire and the resulting force were derived by Engel et al. [61]. As these results were available at the beginning of this work, all XFEM procedures and the coupling of finite element and boundary element formulations are verified using this solution. The problem investigated by Engel, however, allows only for convergence analyses with respect to the magnetic field and the force acting on the cylinder which represents an integral quantity. Solutions for the mechanical fields are not available. Moreover, the singularity of the magnetic field at the location of the conducting wire can influence the convergence behaviour.

(ii) Therefore, a new reference solution for a magneto-mechanical bimaterial problem which involves mechanical deformations and magnetisation effects in both material domains has been derived [195]. Analytical results for all magnetic and mechanical field quantities facilitate comprehensive convergence studies. Being available late during the development of the numerical procedures, it is mainly employed during the comparison of the convergence behaviour of Lagrangian and spline-based approximations.

Both examples are two-dimensional (planar) settings which result from three-dimensional problems that are homogeneous in the out-of-plane direction, i.e. a circular inclusion represents a cylinder in the three-dimensional case. The magnetic and mechanical material behaviour are assumed to be linear and small deformations are presumed.

As mentioned above, the first demonstration problem considers a circular inclusion of radius R, elastic properties E^-, ν^- and relative magnetic permeability μ_{r}^-. The magnetisable inclusion is surrounded by free space, i.e. $\mu_{\mathrm{r}}^+ = 1$ holds. At a distance a from the centre of the inclusion, a conducting wire carries the current J. Both, the displacements of the centre of the cylinder and of the wire are set to zero. The complete setup is illustrated in Fig. 2.3 (a). An analytic solution in terms of the magnetic field $\mathbf{H}$ is available from [61]. The integration of their results yields the magnetic potential in the inclusion and its surrounding as presented in detail in [KMG$^+$13]. In an FE model of this problem the infinite domain Ω^∞ is replaced by a rectangular finite domain $\Omega = \Omega^+ \cup \Omega^-$. In order to avoid truncation errors, the analytic solution for the magnetic potential is prescribed to the boundary $\partial\Omega$.

The setting of the second demonstration problem is given by a circular inclusion Ω^- of radius R embedded in an infinite surrounding matrix domain Ω^+, Fig. 2.3 (b). Both material phases are characterised by constant relative permeabilities μ_{r}^+ and μ_{r}^- as well as linear elastic parameters E^+, ν^+ and E^-, ν^-. A homogeneous magnetic induction $B_1 = 0$, $B_2 =$
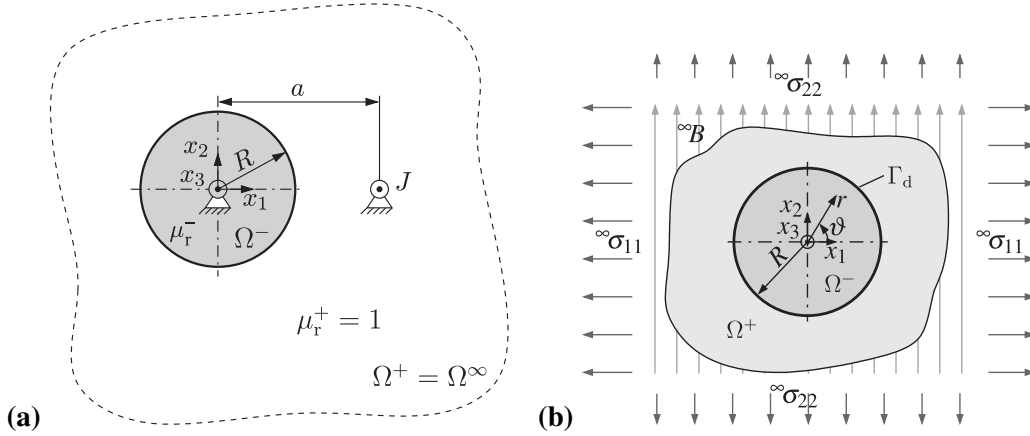
Figure 2.3: Setup of the demonstration problems with analytical solutions (homogeneous in x_3-direction): **(a)** a stiff, magnetisable circular inclusion (domain Ω^-) of radius R with relative magnetic permeability μ_r^- in free space (domain $\Omega^+ = \Omega^\infty$, $\mu_r^+ = 1$). At distance a from its centre, a conducting wire carries the current J, and **(b)** a circular inclusion (domain Ω^-, radius R, properties μ_r^-, E^-, ν^-) embedded in an infinite matrix domain Ω^+ (properties μ_r^+, E^+, ν^+) subjected to homogeneous far field loads $B_1 = 0$, $B_2 = {}^\infty B$ and $\sigma_{11} = {}^\infty \sigma_{11}$, $\sigma_{22} = {}^\infty \sigma_{22}$, $\sigma_{12} = 0$.

${}^\infty B$ and constant mechanical stresses $\sigma_{11} = {}^\infty \sigma_{11}$, $\sigma_{22} = {}^\infty \sigma_{22}$, and $\sigma_{12} = 0$ are applied in a large distance compared to the characteristic size R. While the problem of an infinite medium with a long cylindrical hole has already been considered by Paria [160] as well as Eringen and Maugin [63], the solutions for the stationary magnetic field and the coupled mechanical field problem for the bimaterial case have been derived in [195]. The solution can accomodate any combinations of mechanical and magnetic parameters, i.e. it is not limited to the typical case of a stiff magnetisable inclusion representing an iron particle embedded in a soft non-magnetisable matrix. Furthermore, it incorporates several other settings. In the case of a zero external magnetic field a purely mechanical bimaterial problem, i.e. a circular inclusion problem with the uniaxial loading ${}^\infty \sigma_{11} = p$ and ${}^\infty \sigma_{22} = 0$ as presented in [153], is obtained. If the modulus of the inclusion is set to zero, a circular hole in an infinite plane is described. Eventually, the biaxial tension problem which is applied in [204] to study the convergence of XFEM is included.

Part II

XFEM Modelling

3 Higher-Order Extended Finite Element Method [KMG$^+$13, SKG$^+$13]

In this section linear and quadratic extended finite element formulations are applied to model weak discontinuities in the magnetic and coupled magneto-mechanical boundary value problems outlined in the previous chapter. To properly resolve the location of curved interfaces and the discontinuous physical behaviour, methods for the level set representation of curved interfaces and the numerical integration of the weak form are reviewed and developed in the context of higher-order XFEM. In order to reduce the complexity of the representation of curved interfaces, an element local approach to the automated computation of the nodal level set values is proposed. In this way also the compatibility between the level set representation and the integration subdomains is improved. Integration rules for polygons and strain smoothing are applied in conjunction with quadratic elements and compared to the division into curved integration subdomains. Eventually, a coupled magneto-mechanical demonstration problem described in Section 2.7 is modelled and solved by XFEM. Errors and convergence rates are analysed for the different level set representations and numerical integration procedures as well as their dependence on the contrast of material parameters at an interface. The developed and analysed numerical procedures are employed in the following chapter to generate numerical models of random MRE particulate microstructures.

The XFEM formulation for weak discontinuities in the stationary magnetic and the coupled magneto-mechanical field problem outlined in this chapter is restricted to small deformations. This results in a one-sided coupling, i.e. the magnetic field is not influenced by the deformation but magnetic loads are considered in the solution of the mechanical problem. The location of the discontinuities is assumed to be identical for the stationary magnetic and the coupled magneto-mechanical field problem. For simplicity and demonstration purposes, only problems homogeneous in the x_3-direction will be considered. In these two-dimensional problems $A_1 = A_2 = 0$ is an appropriate choice and the vector potential $\mathbf{A}$ contains only one non-zero component $A_3 = A$. Since there are no gradients in the third direction, the Coulomb gauge (2.36) is fulfilled and does not require further consideration.

As it is not necessary to distinguish quantities of the reference and current configuration, lower case indices $(i, j, k, \ldots = 1, 2)$ are generally used in the index notation of vectors and tensors while capital indices $(I, J, K, \ldots = 1 \ldots n)$ are used to indicate vector-matrix notation where n is the length of a vector or a coloumn/row of a matrix, respectively.

3.1 Extended Finite Element Modelling of Weak Discontinuities

Generating numerical models of RVE is a problem in particular if complex local material structures are considered. In this case, the application of the standard FEM tends to result in an extensive modelling and meshing effort. XFEM [9, 145] offers the possibility to use non-conforming meshes which do not have to be adapted to internal details, e.g. cracks or

material interfaces, of the structure under consideration, Fig. 3.1 (a). Hence, it is used here to model the local heterogeneous material structure of MRE.

3.1.1 Fundamentals of the Extended Finite Element Method

Enrichment By a *local* enrichment of the FE approximation

$$\boldsymbol{\psi}^{h,\text{XFEM}} = \underbrace{\sum_I N_I \boldsymbol{\psi}_I}_{\text{FEM}} + \underbrace{\sum_{J \in \mathcal{N}^{\text{enr}}} N_J \boldsymbol{\psi}_J^* F}_{\text{Enrichment}}, \tag{3.1}$$

of the primary field variables $\boldsymbol{\psi} = \{A, \mathbf{u}\}$, where h characterises the mesh size, discontinuities can be modelled within a non-conforming mesh. The first sum over the product of shape functions N_I and the nodal vector $\boldsymbol{\psi}_I$ of ordinary degrees of freedom at node I represents the standard FE approximation. The enrichment consists of additional degrees of freedom $\boldsymbol{\psi}_J^*$ and an enrichment function F which accounts for the physical behaviour at a surface of discontinuity. By a suitable choice of the enrichment function, discontinuities in the approximated functions can be modelled. The different summation indices in equation (3.1) indicate that only those nodes $J \in \mathcal{N}^{\text{enr}}$ have additional degrees of freedom, whose support contains a discontinuity.

X-elements The implementation of XFEM is realised by the definition of special X-elements which replace the ordinary finite elements intersected by a discontinuity, Fig. 3.1 (a). It is assumed that the local enrichment can be restricted to a single element domain, so that no further elements have to be enriched, i.e. blending elements [70] are not required. This has to be ensured by the formulation of the enrichment function F.

Level set representation In order to represent surfaces of discontinuity within the non-conforming mesh, the standard XFEM procedure is to compute the signed distance

$$\varphi_I = (\mathbf{x}_I - \mathbf{x}_{\text{min}}) \cdot \mathbf{n}_{\text{min}} \tag{3.2}$$

of the node I with the position vector $\mathbf{x}_I$ to Γ_{d}, Fig. 3.1 (b), where $\mathbf{n}_{\text{min}}$ is the unit normal vector to the interface at $\mathbf{x}_{\text{min}}$ pointing in the direction of Ω^+. By interpolating the nodal values φ_I using the shape functions N_I

$$\varphi^h = \sum_I N_I \varphi_I = \begin{cases} = 0 & \text{on} \quad \Gamma_{\text{d}} \\ < 0 & \text{in} \quad \Omega^- \\ > 0 & \text{in} \quad \Omega^+ \end{cases}, \tag{3.3}$$

the values of the discretised level set function φ^h can be computed for every point in the element domain. Hence, the surface of discontinuity Γ_{d} is located by $\varphi^h = 0$. The works of Belytschko et al. [9], Sukumar et al. [204] and Stolarska et al. [202] closely link the concept of implicitly represented internal surfaces by level sets [159] to the XFEM.

Enrichment function In addition to the localisation of the interface, the approximated level set φ^h is used to formulate an enrichment function F. In both, the magnetic and the mechanical field problem, a material interface represents a surface of weak discontinuity. While the potential A and the displacement vector $\mathbf{u}$ have to be continuous in the element, jumps of the magnetic induction $\mathbf{B}$ (tangential to Γ_{d}) and the strain $\boldsymbol{\varepsilon}$ (normal to Γ_{d}) will occur and have to be modelled by
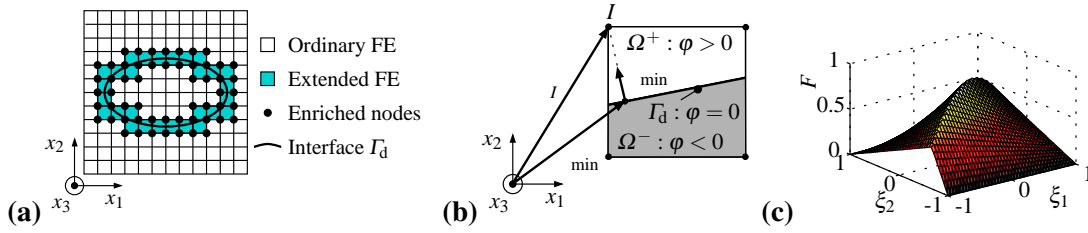
Figure 3.1: XFEM modelling of discontinuities: **(a)** intersection of a surface of discontinuity Γ_d with a regular mesh defines the location of X-elements and the nodes with additional degrees of freedom, **(b)** computation of the nodal level set values as the signed distance to the interface, and **(c)** modified abs-enrichment F according to [144] as a function of the natural element coordinates $\boldsymbol{\xi}$.

the enrichment function. Although the governing equations of both problems are different, the enrichment function

$$F = \sum_I N_I \left| \varphi_I \right| - \left| \sum_I N_I \varphi_I \right| \tag{3.4}$$

proposed by Moës [144] for modeling weak discontinuities in the mechanical field problem is also suitable for the magnetic case, Fig. 3.1 (c). Regarding the implementation of elements with enriched approximations into a commercial finite element code, this so-called modified abs-enrichment (3.4) is of special interest, as the influence of additional degrees of freedom at node I is limited to the element domain intersected by a material interface. It can be seen that $F = 0$ for all elements, whose nodal values of the signed distance satisfy $\varphi_I \varphi_J > 0, I \neq J$. As mentioned before, due to this feature of the enrichment no blending elements are required. The superior convergence of the modified abs-enrichment F over a simple abs-enrichment $\left| \varphi^h \right|$, is reported in [37, 70, 144]. From equation (3.4) it can be seen that the particular enrichment function depends on the nodal values of the level set φ_I. As a consequence, the geometry representation directly enters the approximation of the field variables. Therefore, a closer link between approximation and geometry exists than in the case of strong discontinuities.

3.1.2 Elements for Weak Discontinuities in Magneto-Mechanical Problems

Due to the considered one-sided coupling, which is limited to magnetic loads entering the mechanical equilibrium condition, the finite element analyses of both problems are performed consecutively starting with the magnetic boundary value problem. The magnetic loads are then computed from the obtained magnetic solution and applied in the mechanical pass.

Solution scheme

A weak form of the stationary magnetic boundary value problem is obtained from multiplying equation (2.31) with a weight function which can be identified as a virtual magnetic potential δA. Hence, the principle of virtual magnetic work

Weak forms

$$\int_{\Omega} H_i \delta B_i \,\mathrm{d}V - \int_{\Omega} j \delta A \,\mathrm{d}V - \int_{\partial \Omega_k} \hat{k} \delta A \,\mathrm{d}S = 0 \tag{3.5}$$

is obtained. The first term represents the internal virtual work and the latter two are the

external virtual works of the currents j and $\hat{k}$, respectively. The weak form of the mechanical equilibrium condition

$$\int_\Omega \left(_\text{E}\sigma_{ij} + \hat{\sigma}_{ij}\right) \delta\varepsilon_{ij}\,\mathrm{d}V - \int_\Omega \rho f_j \delta u_j\,\mathrm{d}V - \int_{\partial\Omega_p} \hat{p}_j \delta u_j\,\mathrm{d}S = 0 \tag{3.6}$$

is derived from equation (2.48). The involved terms can be interpreted as the internal virtual work of the pseudo-mechanical and -magnetic stresses and the external virtual work of the mechanical body forces and surface loads accounting for mechanical and magnetic contributions from the exterior of the domain Ω.

Discretisation The spatial discretisation of the domain $\Omega \approx \Omega^h = \bigcup_{I=1}^{n_\text{e}} \Omega_{I\text{e}}$ is performed by a regular mesh with n_e quadrilateral elements, both ordinary FE and X-elements with an enriched approximation, Fig. 3.1 (a). The ordinary isoparametric elements use the same shape functions $N_I(\boldsymbol{\xi})$ for mapping the element geometry from the natural $\boldsymbol{\xi}$ (with $|\xi_i| \leq 1$, $i = 1, 2$) to the physical coordinates $\mathbf{x}$ as well as for the approximation of the primary field variables $\boldsymbol{\psi} = \{A, \mathbf{u}\}$ in the element domain Ω_e.

Approximation While the mapping of the geometry is retained for the X-elements in the case of small deformations, the enriched approximation

$$\boldsymbol{\psi}^{h,\text{X-element}}(\boldsymbol{\xi}) = \sum_{I=1}^{n_\text{n}} N_I\left(\boldsymbol{\xi}\right)\left[\boldsymbol{\psi}_I + \boldsymbol{\psi}_I^* F\left(\boldsymbol{\xi}\right)\right] = \underline{\underline{\mathbf{N}}}_\psi^*\left(\boldsymbol{\xi}\right)\underline{\boldsymbol{\psi}}_\text{e}^* \tag{3.7}$$

of the field variables is used to model discontinuities within the element domain. As a consequence, all n_n nodes of the element have a vector of additional degrees of freedom $\boldsymbol{\psi}_I^*$ which results in a subparametric element formulation as far as small deformations are considered. Different from the isoparametric elements, $\underline{\underline{\mathbf{N}}}_\psi^*$ is a matrix that contains shape functions and products of shape and enrichment functions. The components of the row vector $\underline{\boldsymbol{\psi}}_\text{e}^*$ are the ordinary and additional degrees of freedom of the X-element.

Derivatives The approximations of the magnetic induction and the strain in the ordinary and the X-elements are given by

$$\underline{\mathbf{B}}^h(\boldsymbol{\xi}) = \underline{\underline{\mathbf{B}}}_A(\boldsymbol{\xi})\underline{\mathbf{A}}_\text{e}\,, \quad \underline{\mathbf{B}}^{h,\text{X-element}}(\boldsymbol{\xi}) = \underline{\underline{\mathbf{B}}}_A^*(\boldsymbol{\xi})\underline{\mathbf{A}}_\text{e}^* \tag{3.8}$$

$$\underline{\varepsilon}^h(\boldsymbol{\xi}) = \underline{\underline{\mathbf{B}}}_u(\boldsymbol{\xi})\underline{\mathbf{u}}_\text{e}\,, \quad \underline{\varepsilon}^{h,\text{X-element}}(\boldsymbol{\xi}) = \underline{\underline{\mathbf{B}}}_u^*(\boldsymbol{\xi})\underline{\mathbf{u}}_\text{e}^*\,. \tag{3.9}$$

The matrices $\underline{\underline{\mathbf{B}}}_A^*$ and $\underline{\underline{\mathbf{B}}}_u^*$ contain the partial derivatives of the shape and enrichment functions with respect to the natural coordinates and account for the mapping of the geometry.

Discrete system of equations The required element matrices and vectors of the X-elements are obtained from inserting the approximations of equations (3.7)-(3.9) into the corresponding weak forms. In vector-matrix notation are given by

$$\int_\Omega \delta\underline{\mathbf{B}}^T \underline{\mathbf{H}}\,\mathrm{d}V - \int_\Omega \delta\underline{\mathbf{A}}^T \underline{\mathbf{j}}\,\mathrm{d}V - \int_{\partial\Omega_K} \delta\underline{\mathbf{A}}^T \hat{\underline{\mathbf{k}}}\,\mathrm{d}S = 0 \tag{3.10}$$

$$\int_\Omega \delta\underline{\varepsilon}^T{}_\text{E}\underline{\boldsymbol{\sigma}}\,\mathrm{d}V - \int_\Omega \left(\delta\underline{\mathbf{u}}^T \rho\underline{\mathbf{f}} - \delta\underline{\varepsilon}^T \hat{\underline{\boldsymbol{\sigma}}}\right)\mathrm{d}V - \int_{\partial\Omega_p} \delta\underline{\mathbf{u}}^T \hat{\underline{\mathbf{p}}}\,\mathrm{d}S = 0\,. \tag{3.11}$$

The discrete formulations of the problems

$$\delta \underline{\mathbf{A}}^{*T} \left\{ \underbrace{\bigcup_{I=1}^{n_{\mathrm{e}}} \left[\int_{\Omega_{I\mathrm{e}}} \underline{\mathbf{B}}_A^{*T} \underline{\underline{\mathbf{C}}}_A \underline{\mathbf{B}}_A^* \, \mathrm{d}V \right] \underline{\mathbf{A}}^*}_{\underline{\underline{\mathbf{K}}}_A^*} - \underbrace{\bigcup_{I=1}^{n_{\mathrm{e}}} \left[\int_{\Omega_{I\mathrm{e}}} \underline{\mathbf{N}}_A^{*T} j \, \mathrm{d}V - \int_{\partial\Omega_{I\mathrm{e}}} \underline{\mathbf{N}}_A^{*T} \hat{k} \, \mathrm{d}S \right]}_{-\underline{\mathbf{P}}_A^*} - \underline{\mathbf{J}}^* \right\} = 0$$

(3.12)

$$\delta \underline{\mathbf{u}}^{*T} \left\{ \underbrace{\bigcup_{I=1}^{n_{\mathrm{e}}} \left[\int_{\Omega_{I\mathrm{e}}} \underline{\mathbf{B}}_u^{*T} \underline{\underline{\mathbf{C}}}_u \underline{\mathbf{B}}_u^* \, \mathrm{d}V \right] \underline{\mathbf{u}}_{\mathrm{e}}^*}_{\underline{\underline{\mathbf{K}}}_u^*} - \underbrace{\bigcup_{I=1}^{n_{\mathrm{e}}} \left[\int_{\Omega_{I\mathrm{e}}} \left(\underline{\mathbf{N}}_u^{*T} \rho \underline{\mathbf{f}} - \underline{\mathbf{B}}_u^{*T} \hat{\boldsymbol{\sigma}} \right) \, \mathrm{d}V - \int_{\partial\Omega_{I\mathrm{e}}} \underline{\mathbf{N}}_u^{*T} \hat{\mathbf{p}} \, \mathrm{d}S \right]}_{-\underline{\mathbf{P}}_u^*} - \underline{\mathbf{F}}^* \right\} = 0$$

(3.13)

are obtained from a standard Galerkin or Ritz approximation. The operator $\bigcup_{I=1}^{n_{\mathrm{e}}}$ indicates the assembly of contributions from all n_{e} elements $\Omega_{I\mathrm{e}}$. In the equations above, the constitutive matrices $\underline{\underline{\mathbf{C}}}_A$ and $\underline{\underline{\mathbf{C}}}_u$ are obtained from a vector-matrix representation of linear magnetic and mechanical constitutive relations according to equations (2.75) and (2.93) specified in Section 2.6. In the case of material non-linearities they have to be replaced by appropriate tangent matrices and an update algorithm for the constitutive variables is required. The vectors $\underline{\mathbf{J}}^*$ and $\underline{\mathbf{F}}^*$ account for discrete nodal loads. Eventually, the systems of discrete equations

$$\underline{\underline{\mathbf{K}}}_A^* \underline{\mathbf{A}}^* = \underline{\mathbf{P}}_A^* + \underline{\mathbf{J}}^* \quad \text{and} \quad \underline{\underline{\mathbf{K}}}_u^* \underline{\mathbf{u}}^* = \underline{\mathbf{P}}_u^* + \underline{\mathbf{F}}^*$$

(3.14)

follow from the argument of arbitrary virtual potentials and displacements.

3.2 Implicit Interface Representation by Higher-Order Level Sets

In contrast to standard isoparametric finite elements, the representation of the geometry and the approximation of the field variables can be separated, because the mesh is independent of internal details such as voids, material interfaces or cracks. In this way problems related to the meshing of complex geometries seem to be bypassed. However, these difficulties are shifted to the representation of interfaces in non-conforming meshes and the numerical integration of the weak form [11, 144]. For the evaluation of the integrals of the weak forms in an X-element the interface intersecting the element domain has to be located, i.e. the nodal values of the level set representation have to be computed. In this section two different procedures for the calculation of the nodal level set values will be outlined for linear and quadratic approximations.

Motivation

The combination of XFEM and level sets originated from linear or bilinear discretisations of the level set function. Nevertheless, curved interfaces are of major importance especially with respect to the generation of complex microstructure models and have motivated quadratic or higher-order XFEM formulations. One approach considered in the literature is to use a linear discretisation of the level set which is defined on a highly refined triangular subgrid derived from the initial mesh (background mesh) in the vicinity of the discontinuity [56, 127, 147]. In addition to the implicit representation of curved boundaries, the subgrid is used to integrate the weak form by applying standard quadrature rules. Higher-order approximations of field quantities ensure that the coarse background mesh is able to represent the solution.

Refined linear subgrids
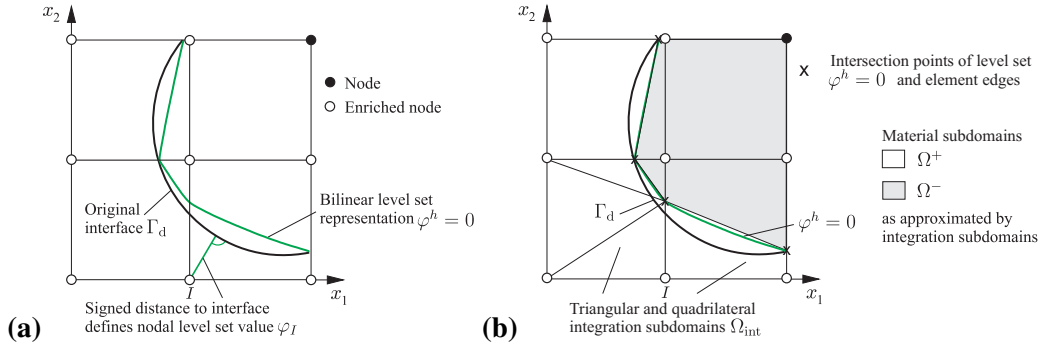
Figure 3.2: Global level set representation of a discontinuity Γ_d: **(a)** computation of global level set values φ_I at nodes, and **(b)** subdivision into integration subdomains.

Curved subdomains

As this method can be hardly combined with the modified abs-enrichment for weak discontinuities, a second technique proposed by Cheng and Fries [37] is applied in this work. In this approach higher-order level set representations of the interface corresponding to the order of the underlying finite element mesh are used in conjunction with curved integration subdomains which results in a closer link of geometry and approximation than in the previous method. However, from convergence studies in the aforementioned papers it can be concluded that the resolutions of geometry and approximation have to be balanced, i.e. the approximation mesh must be able to reproduce the fields resulting from certain geometries which is inherent to the second method.

3.2.1 Global Level Set

The standard procedure for the localisation of the discontinuity in the non-conforming mesh is to compute the nodal values φ_I of the signed distance to the interface Γ_d for each node I in the mesh as exemplarily shown in Fig. 3.2 (a) for four quadrilateral elements, three of them are intersected by a discontinuity of circular shape. The interpolation of these values over the element domains using the standard shape functions leads to an implicit representation of the interface $\varphi^h = 0$ which is slightly curved. Therefore, $\varphi^h = 0$ will generally be inconsistent with the subdivision of the element into integration subdomains with straight edges, Fig. 3.2 (b).

3.2.2 Element Local Level Set

Motivation

As analytical expressions for the geometry of interfaces are available only in special cases, e.g. for an ellipse or a sphere, the computation of the nodal level set values can be cumbersome. Efficient algorithms for complex interface geometries therefore have to be localised, i.e. the level set values have to be computed from limited information on the interface in the vicinity of the considered element. Based on this idea, an automated model generation algorithm which transforms a geometric model of the local material structure into an XFEM mesh has been developed in a previous publication [114]. Pereira et al. used similar procedures for the representation of cracks in [163].

Bilinear interface representation

In the bilinear case, Fig. 3.3, the original interface is converted into straight segments defined by the intersection points of a discontinuity Γ_d with the edges of the structured mesh. The following algorithm is applied element by element:
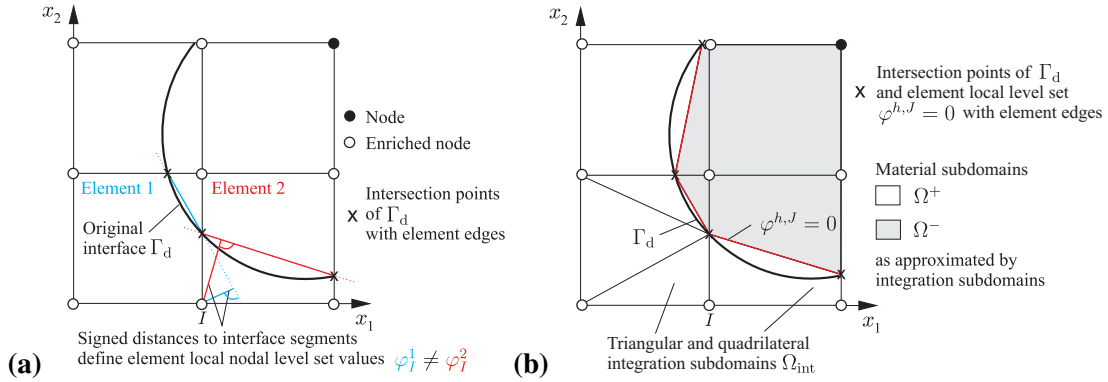
Figure 3.3: Element local level set representation of a discontinuity Γ_{d}: **(a)** approximation of the original interface by straight segments and computation of different nodal level set values for two adjacent elements, and **(b)** elementwise level set approximation $\varphi^{h,J} = 0$ and subdivision into integration subdomains.

(i) Find the points of intersection of the interface Γ_{d} with the element edges, indicated by crosses in Fig. 3.3 (a).

(ii) Obtain a linear parameter representation for the straight segment connecting the intersection points.

(iii) For each node I in element J compute the *element local* nodal level set values φ_I^J as the signed distance to the parameter function of step 2. The interface is hence implicitly represented by $\varphi^{h,J} = \sum_I N_I \varphi_I^J = 0$, Fig. 3.3 (b).

(iv) Subdivide the element domain into triangular and quadrilateral integration subdomains. The vertices of the tesselation are given by the points of intersection and the element nodes.

In this approach the interface is, irrespectively of its original shape, approximated by a straight line in each X-element. The implicit interface approximation will therefore be consistent with the subdivision of the element domain used for integration purposes, Fig. 3.3 (b). However, the element local level set is defined by two different nodal values φ_I^1 and φ_I^2, one for each of the two elements 1 and 2 in Fig. 3.3 (a). As illustrated in Fig. 3.4 (b), these different nodal values $\varphi_I^{1,2}$ in the adjacent elements cause a loss of interelement continuity of the enrichment function F, defined by equation (3.4), and hence the primary field variables. Convergence studies in Section 3.4.1 show that the error and the convergence rate in the energy norm are identical for the global and element local versions of interface approximation. But the error and convergence in the L^2 norm are deteriorated by the elementwise level set representation.

The element local level set representation is now applied higher-order elements, Fig. 3.5. It is expected that the increased variability of the higher-order basis will reduce the geometric discretisation error between the original interface Γ_{d} and its representation $\varphi^{h,J} = 0$. In addition, an improved interelement continuity of the modified abs-enrichment and the primary field variables is anticipated. The procedure is identical to the linear case except for the following changes:

Incompatibilities

Quadratic interface representation
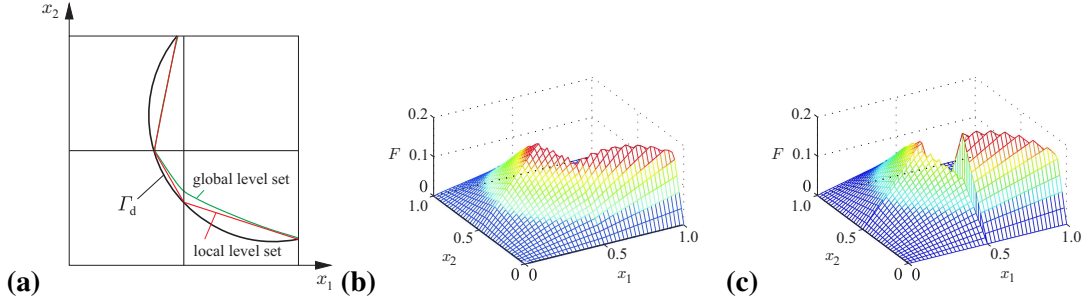
Figure 3.4: Implicit bilinear interface representation over four quadrilateral elements: **(a)** comparison of global and element local level set representation, **(b)** C^0 continuity of the modified abs-enrichment function F according to equation (3.4) for the global level set, and **(c)** C^0 discontinuity for the element local level set. The loss of interelement continuity is caused by different nodal level set values in the two adjacent elements.
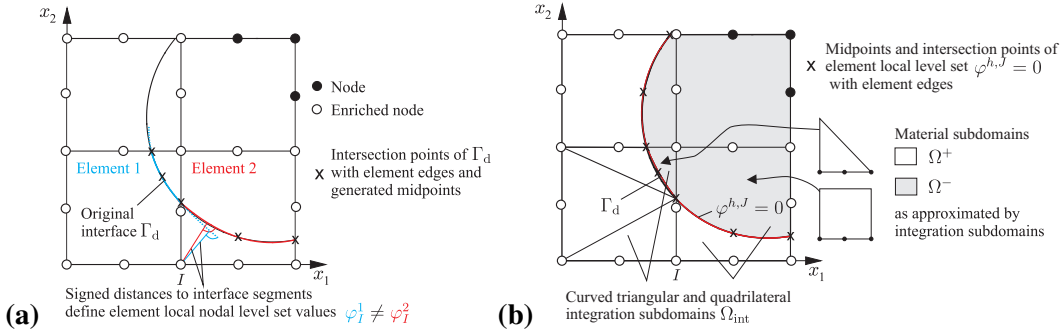
Figure 3.5: Quadratic, element local level set representation of a discontinuity Γ_d: **(a)** approximation of the original interface by quadratic segments and computation of different nodal level set values for two adjacent elements, and **(b)** elementwise level set approximation $\varphi^{h,J} = 0$ and subdivision into curved integration subdomains.

   (i) In addition to intersection points with the element edges, find a third point in the middle of the interface, Fig. 3.5 (a).

  (ii) Fit a *quadratic* parameter function through the intersection points and the midpoint.

 (iii) φ_I^J are signed distances to the quadratic parameter function of step 2, Fig. 3.3 (a).

 (iv) Obtain *curved* integration subdomains, defined by the representation $\varphi^{h,J}$ and the element edges, Fig. 3.3 (b).

From Fig. 3.6, which shows a comparison of the interface representation for global and local level sets, it can be found that both versions provide a reasonable interface approximation even for the coarse discretisation used in the four element example. The original discontinuity Γ_d and its global and element local level set representation are virtually indistinguishable. Compared to the bilinear version, Fig. 3.4, problems with interelement discontinuities in the case of the element local level set are drastically reduced. The apparently very good performance of the quadratic element local approach will be further verified and quantified in Section 3.4.1.
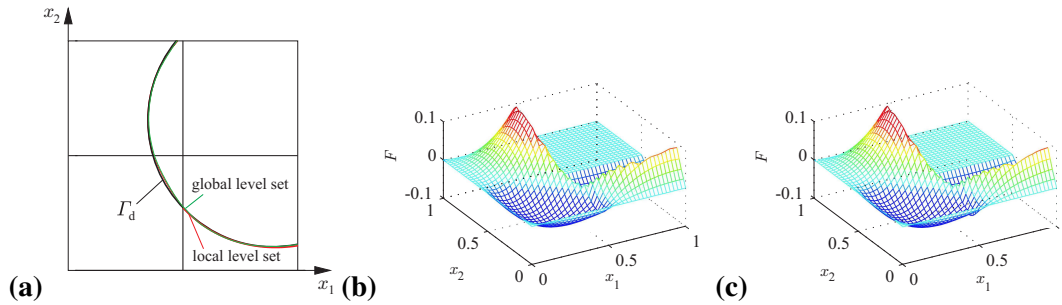
Figure 3.6: Implicit quadratic interface representation over four quadrilateral elements: **(a)** comparison of the global and the element local level set representation, **(b)** C^0 continuity of modified abs-enrichment function F for the global level set, and **(c)** improved interelement continuity for the element local level set in comparison to bilinear representations, Fig. 3.4.

3.3 Numerical Integration of Higher-Order Elements

The integrals of the element matrices will involve discontinuous kernel functions, because discontinuities are represented in a single element domain. Since Gauss quadrature rules are derived from the integration of polynomials, they will generally produce poor results when applied to non-polynomial functions. This problem is commonly handled by a subdivision of the element Ω_e into n_{int} integration subdomains Ω_{int}. The integration of the weak form $\int_{\Omega_e} \ldots \, dV = \sum_{I=1}^{n_{int}} \int_{\Omega_{int I}} \ldots \, dV$ is then performed in each of the subdomains using standard quadrature rules.

Subdivision

To avoid or at least to reduce the necessary partitioning of the element domain, other methods have been proposed to handle the numerical integration of discontinuous functions. In an earlier approach by Ventura [213] discontinuous, non-polynomial functions are replaced by equivalent continuous polynomials which can be integrated by standard quadrature rules without subdividing the element. More recent developments can be grouped into four major approaches, conformal mappings [154, 155], transformations that resolve certain singularities [148, 161], generalised quadratures for polygons [149, 150, 151] and strain smoothing techniques [15, 16, 35].

Alternatives

Natarajan et al. [154, 155] apply Schwarz-Christoffel conformal mapping techniques to integrate the discontinuous or singular weak form. The polygonal subdomains resulting from the intersection of a discontinuity with the element are mapped to unit discs where integration is carried out using midpoint or Gauss-Chebyshev quadrature rules. In this fashion, the need to further subdivide the element domain into triangular quadrature subcells is omitted. The major drawback of the method is its limitation to the two-dimensional case as it is based on mappings on the complex plane. In a similar way, accurate results can be obtained by using transformations that resolve the singularity. A generalised duffy transformation, i.e. from a triangle to a unit square, is used in [148] to integrate vertex and power singularities. Park et al. [161] developed a similar mapping method applicable to two- and three-dimensional problems with triangular and tetrahedral meshes.

Mapping techniques

Different from transformations which remove the singular integrands, Mousavi and Sukumar [151] apply adapted quadrature rules for elements with strong discontinuities based on integration over arbitrarily shaped polygons [150]. In [149] the same authors use Lasserre's

Lasserre's method

integration [124, 125] for the definition of adapted quadrature rules for convex polygons by a least square optimisation and prove its applicability to discontinuous functions. The method will be briefly outlined below and numerical results are presented in Section 3.4.2.

Strain smoothing

In order to avoid integration subdomains, Bordas et al. [16] investigated the combination of strain smoothing and XFEM. Strain smoothing was first used with meshfree methods and later in the framework of mesh based methods [131]. Convergence studies in [15] illustrate that the smoothed version of XFEM leads to comparable convergence rates and errors in the case of polynomial integrands, i.e. enrichments used for strong and weak discontinuities and linear or bilinear elements. On the other hand, singular enrichments as they are used at a crack tip deteriorate the error level while convergence rates seem to be unaffected. So far, no detailed investigations on the numerical properties exist for higher-order elements. However, the results presented in [15] for quadratic smoothed FEM formulations indicate that only a suboptimal order of convergence is obtained for quadrilateral elements in the energy norm (1.98 for FEM vs. 0.98 for smoothed FEM). Convergence studies carried out here confirm these results also for higher-order X-elements.

Used methods

In Section 3.4.2 the performance of different integration schemes for discontinuous integrands will be investigated for bilinear (Q4) and quadratic quadrilateral (Q8) elements. In particular, the subdivision of the element into curved integration subdomains [37], Lasserre's method [149] as well as strain smoothing [15] are considered. While the technique to use curved integration subdomains has already been mentioned in connection with higher-order interface representations, some details on the implementation of the latter two methods are given below. More details can be found in [KMG$^+$13].

3.3.1 Integration over Polygonal Subdomains

Concept

Lasserre's method allows for the integration of a continuous positively homogeneous function f, i.e. $f(\lambda \mathbf{x}) = \lambda^q f(\mathbf{x})$ for all $\lambda > 0$, on a convex n-dimensional polytope Ω. If f is continuously differentiable, the integration can be reduced to a weighted integration over the $(n-1)$-dimensional faces Γ_I

$$\int\limits_{\Omega} f(\mathbf{x}) d^n \mathbf{x} = \sum_{I=1}^{m} \frac{d_I}{n+q} \int\limits_{\Gamma_I} f(\mathbf{x}) d^{n-1} \mathbf{x} \tag{3.15}$$

with the algebraic distance d_I of Γ_I from the origin [124, 125]. In this way the integration of subdomains with complex shape is transferred to boundary integrals which can be evaluated by standard Gauss quadrature. That is, the triangulation of two-dimensional polygonal material subdomains is avoided. However, equation (3.15) only holds for homogeneous functions but the integration of the weak form involves linear combinations of homogeneous functions $g(\mathbf{x}) = \sum_{K=1}^{p} g_K(\mathbf{x})$. This requires the individual integration of p functions g_K. With respect to the application of the method in context of a finite element formulation g_K are usually not known explicitly which requires an extension of Lasserre's method presented by Mousavi and Sukumar [149].

Application to XFEM

In order to apply Lasserre's integration, m discrete points $\mathbf{x}_I \in \left\{ \mathbf{x} | \varphi^h(\mathbf{x}_I) = 0 \right\}$ on the level set representation of the interface are computed, Fig. 3.7. Together with element nodes and intersection points with element edges these points define a polygonal representation of the material subdomain in which Lasserre's integration can be used. Discontinuous integrands could in principle be handled by simply defining polygons on each side of the interface in
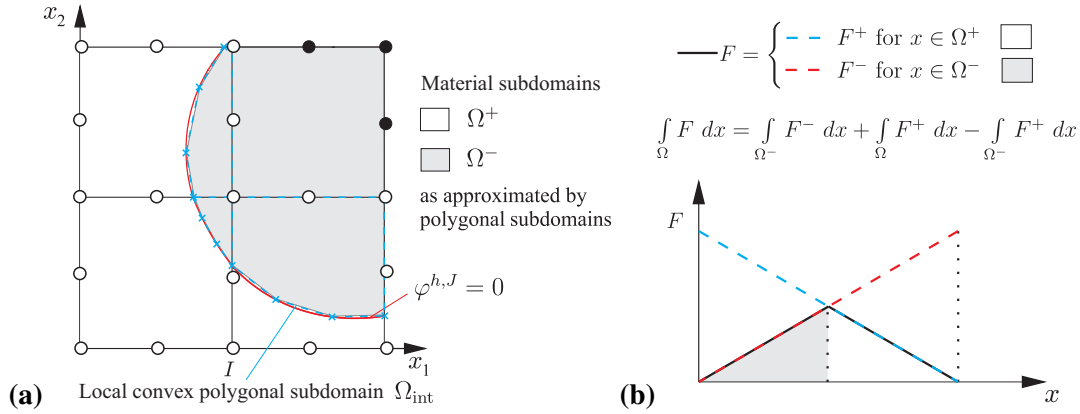
Figure 3.7: Application of Lasserre's integration method to higher-order XFEM: **(a)** polygons representing material subdomains in X-elements. Boundary integrals have to be evaluated over the edges of the convex material subdomain and the whole element, and **(b)** splitting the integration of a discontinuous function F into two integrals with continuous integrands $F^{\pm}$ (1D illustration).

which continuous polynomials can be integrated. However, considering curved interfaces, X-elements will generally be split into a convex and a concave material subdomain. Since the presented method is only applicable to convex polygons, the integration of a discontinuous function F is split into an integral over the whole element Ω_{e} and the convex subdomain Ω^{-} as illustrated for the 1D case in Fig. 3.7 (b). Lasserre's integration is applied to both, the element and subdomain integration.

3.3.2 Strain Smoothing

The basic idea of strain smoothing is to average the discretised derivatives γ^{h} of a generalised primary field variable ψ over so called smoothing cells Ω_{c}, Fig. 3.8. The integral over the subdivided element can be replaced by the integration over the boundaries of smoothing cells which also removes the influence of the Jacobian of the geometric map. Depending on the choice of the smoothing cells a reduction of the computational effort related to quadrature of the weak form can be expected.

Concept

The smoothed field of the derivatives which is constant in each cell is given by

Smoothing of derivatives

$$\bar{\gamma}_{\mathrm{c}}^{h} = \int_{\Omega} \gamma^{h}(\mathbf{x})\Phi(\mathbf{x} - \mathbf{x}_{\mathrm{c}})\, dV \quad \text{with} \quad \Phi(\mathbf{x} - \mathbf{x}_{\mathrm{c}}) = \begin{cases} 1/V_{\mathrm{c}} & \forall \quad \mathbf{x} \in \Omega_{\mathrm{c}} \\ 0 & \forall \quad \mathbf{x} \notin \Omega_{\mathrm{c}} \end{cases}, \qquad (3.16)$$

where $\mathbf{x}_{\mathrm{c}}$ is an arbitrary point in Ω_{c} and V_{c} is the volume of the cell. $\Phi(\mathbf{x} - \mathbf{x}_{\mathrm{c}})$ is the typical choice for the smoothing function satisfying $\Phi \geq 0$ and $\int_{\Omega} \Phi(\mathbf{x}) dV = 1$. With respect to the application to magneto-mechancial field problems, the generalised tensor quantity γ stands for the symmetric strain tensor ε or the vector of magnetic induction $\mathbf{B}$.

According to equations (3.8) and (3.9) the discrete enriched derivatives are given by $\gamma^{h} = \underline{\underline{\mathbf{B}}}^{*}\underline{\psi}^{*}$. Strain smoothing results in an averaged enriched matrix of partial derivatives $\underline{\underline{\mathbf{B}}}_{\mathrm{c}}$

Application to XFEM
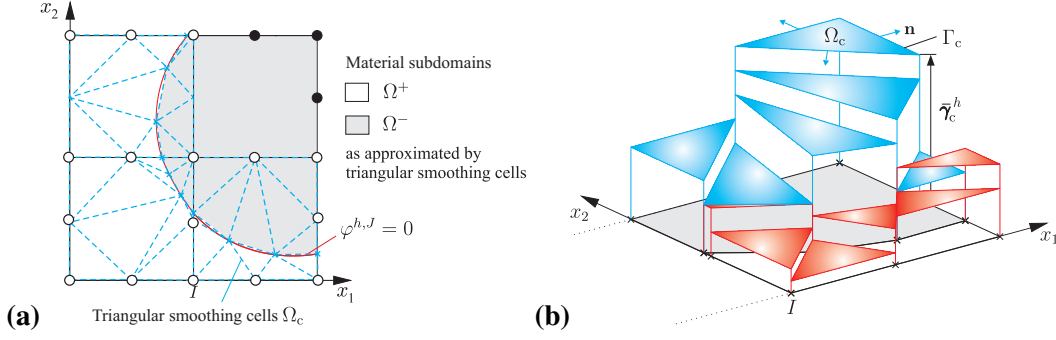
Figure 3.8: Application of strain smoothing to higher-order XFEM: **(a)** subdivision of the element domain into triangular smoothing cells Ω_c, and **(b)** smoothed generalised derivatives $\bar{\gamma}_c^h$ in smoothing cells.

being constant in each smoothing cell Ω_c

$$\bar{\gamma}_c^h = \int_\Omega \underline{\underline{\mathbf{B}}}^*(\mathbf{x})\Phi(\mathbf{x} - \mathbf{x}_c)dV \, \underline{\psi}^* = \frac{1}{V_c}\int_{\Omega_c} \underline{\underline{\mathbf{B}}}^* dV \, \underline{\psi}^* = \underline{\underline{\bar{\mathbf{B}}}}_c\underline{\psi}^*. \tag{3.17}$$

This smoothing is of interest for XFEM because the matrices $\underline{\mathbf{B}}^*$ contain terms of the form $\partial N_I/\partial x_j$ and $\partial(N_I F)/\partial x_j$. Using the divergence theorem, smoothing integrals over these partial derivatives over Ω_c

$$\int_{\Omega_c} \frac{\partial N_I}{\partial x_j}dV = \int_{\Gamma_c} N_I n_j dS \quad \text{and} \quad \int_{\Omega_c} \frac{\partial(N_I F)}{\partial x_j}dV = \int_{\Gamma_c} N_I F n_j dS \tag{3.18}$$

can be transformed into surface integrals over products of shape functions or enrichment functions with the outward unit normal vector $\mathbf{n}$ of the boundary Γ_c of smoothing cells [15, 16]. The coefficient matrices of a strain smoothed XFEM $\underline{\underline{\bar{\mathbf{K}}}}_e$ are finally obtained without explicitly computing any domain integrals from the contributions of each smoothing cell

$$\underline{\underline{\bar{\mathbf{K}}}}_e = \int_{\Omega_e} \underline{\underline{\mathbf{B}}}^T \underline{\underline{\mathbf{D}}}_I \underline{\underline{\mathbf{B}}} \, dV = \sum_{I=1}^{n_c} \int_{\Omega_{cI}} \underline{\underline{\bar{\mathbf{B}}}}_{cI}^T \underline{\underline{\mathbf{D}}}_I \underline{\underline{\bar{\mathbf{B}}}}_{cI} \, dV = \sum_{I=1}^{n_c} \underline{\underline{\bar{\mathbf{B}}}}_{cI}^T \underline{\underline{\mathbf{D}}}_I \underline{\underline{\bar{\mathbf{B}}}}_{cI} V_{cI}, \tag{3.19}$$

where $\underline{\underline{\mathbf{D}}}_I$, $\underline{\underline{\bar{\mathbf{B}}}}_{cI}$ and V_{cI} are the material matrix, the smoothed discrete matrix of partial derivatives and the volume of the Ith smoothing cell, respectively. Hence, the need to compute and integrate derivatives of shape functions including the influence of isoparametric mappings are eliminated and the methods are known to be less sensitive to mesh distortion.

Choice of smoothing cells

For X-elements with straight interfaces a single smoothing cell with straight edges per material subdomain would be sufficient to represent the topology. This would eliminate the need to further subdivide the material domains into integration triangles. Since this choice causes spurious modes similar to reduced integration, at least two smoothing cells have to be used in each subdomain [15]. In order to prevent spurious modes and to sufficiently reproduce curved material subdomains, higher-order element formulations require an even larger number of smoothing cells per subdomain. In this case, smoothing cells can be created using Delaunay triangulation based on the element nodes and discrete interface points similar
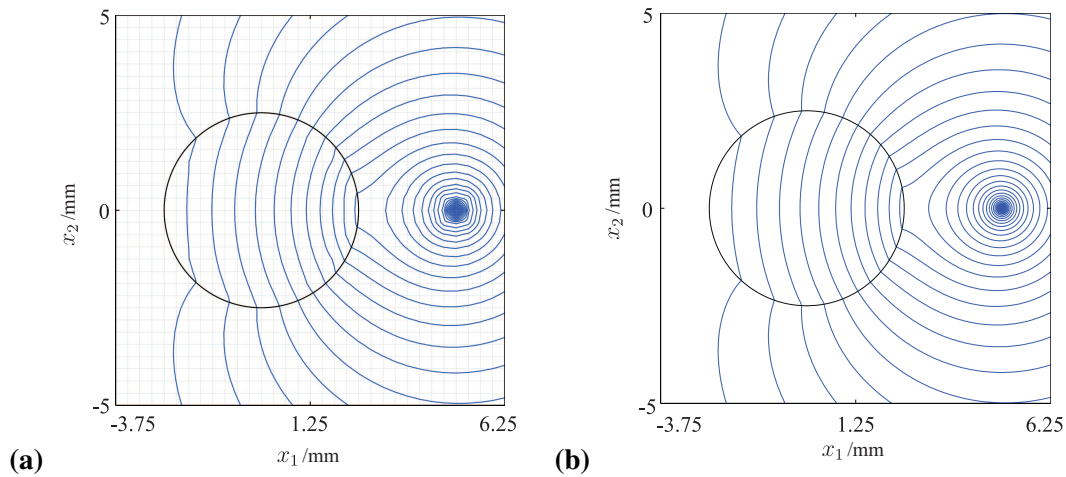
Figure 3.9: Magnetic field lines obtained from the numerical solution of the first demonstration problem outlined in Section 2.7: **(a)** solution on a mesh of 32×32 elements, and **(b)** 256×256 elements. The boundary of the inclusion is indicated by a black line. Grey lines showing the regular mesh have been omitted for the finer discretisation for clarity.

to the Lasserre's method as illustrated in Fig. 3.8 (a). However, the principal advantage of avoiding a further subdivision of the material subdomains is lost.

3.4 Convergence Analysis

In this section the applicability of XFEM to the modelling of weak discontinuities in the stationary magnetic and the coupled magneto-mechanical field problem is to be demonstrated and numerical properties are studied in terms of errors and convergence rates. The first demonstration problem outlined in Section 2.7 is used for verification purposes, Fig. 2.3 (a). Analytic and numerical results in this section have been obtained for the following set of parameters:

Parameters

$$a = 5\,\text{mm} \qquad\qquad J = 10\,\text{A} \qquad\qquad E^- = 210\,\text{GPa}$$
$$R = 2.49\,\text{mm} \qquad\qquad \mu_\text{r}^- = 1000 \qquad\qquad \nu^- = 0.3.$$

Plots of the numerical solutions obtained for the stationary magnetic boundary value problem are shown for two different discretisations of 32×32 in Fig. 3.9 (a) and 256×256 X- and ordinary finite elements in Fig. 3.9 (b). From the plots of the magnetic field lines it can be seen that even the coarse mesh of 32×32 elements is able to reproduce the principal characteristics of the solution of the stationary magnetic field problem, for instance the flux lines entering the highly permeable cylinder at an angle of approximately $90°$. Compared to the solution obtained from the fine mesh, two major sources of error can be identified. The first one is directly related to the X-elements in the vicinity of the outline of the cylinder and occurs due to the large differences in the relative magnetic permeabilities entering the element matrices by μ_r^{-1}. The error which appears through non-smooth magnetic field lines is only observable in the highly permeable cylinder. A second source of error is caused by the wire modelled by a nodal current which represents a singularity of the magnetic field problem. The error is clearly recognisable by the deviation from circularity of the magnetic field lines in the vicinity of the wire, Fig. 3.9 (a).

XFEM solution

Error norms

The order of convergence is analysed for two different measures, the L error of the magnetic potential

$$||A||_{L^2} = \left[\frac{\int_\Omega \left(A^h - A \right)^2 dV}{\int_\Omega A^2\, dV} \right]^{1/2} \tag{3.20}$$

is computed from with respect to the exact solution A stated explicitly in [KMG+13] which allows for a comparison to [37]. The normalised error of derivatives of the primary field variable

$$||A||_{\text{en}} = \left[\frac{\int_\Omega \frac{1}{\mu} \left(A^h_{,k} - A_{,k} \right)^2 dV}{\int_\Omega \frac{1}{\mu} A_{,k}{}^2 dV} \right]^{1/2} \tag{3.21}$$

is measured by the energy norm. As indicated by the name this is the average relative error of the magnetic energy in the considered domain Ω. In addition, the magneto-mechanical coupling will be assessed by the relative error

$$|\Delta F| = \left| \frac{F^h_{1\,\text{cylinder}} - F_{1\,\text{cylinder}}}{F_{1\,\text{cylinder}}} \right| \tag{3.22}$$

of the resulting force per unit length acting on the cylinder. The exact solution $F_{1\,\text{cylinder}}$ is available from [61] and [KMG+13].

3.4.1 Approximation Order and Interface Representation

Investigated cases

The convergence analysis is performed for four different cases which can be distinguished by the order of approximation and the procedure used for level set computation in the X-elements (Section 3.2):

(i) bilinear (Q4) elements and global level set values,

(ii) bilinear (Q4) elements and element local level set values,

(iii) quadratic (Q8) elements and global level set values,

(iv) quadratic (Q8) elements and element local level set values.

For each version the error measures mentioned above are computed for six discretisations of the domain Ω with $2^n \times 2^n$, $n = 4 \ldots 9$ square elements. Additionally, the errors have been calculated for three different relative permeabilities of the inclusion. The value $\mu_r^- = 10^1$ allows for a comparison with other publications like [144, 37] using a ratio of 10 in material properties. Further investigated values are $\mu_r^- = 10^3$ and $\mu_r^- = 10^6$, the latter representing an upper bound for technically possible relative permeabilities.

Results

The obtained results are plotted against the mesh size h for $\mu_r^- = 10^3$ in Fig. 3.10. The numerical values of the orders of convergence are summarised in Tab. 3.1. Since asymptotic convergence is observed only for higher resolutions, the numerical values of the convergence rates are computed using only the four finest meshes. Optimal orders of convergence in the energy norm $||A||_{\text{en}}$ are 1.0 and 2.0 for bilinear and quadratic elements, respectively. For the L^2 norm $||A||_{L^2}$ values of 2.0 and 3.0 are expected.

Bilinear elements

At first, the bilinear elements and the different versions for the computation of the level set values will be discussed. The error in the L^2 norm of the magnetic potential is clearly
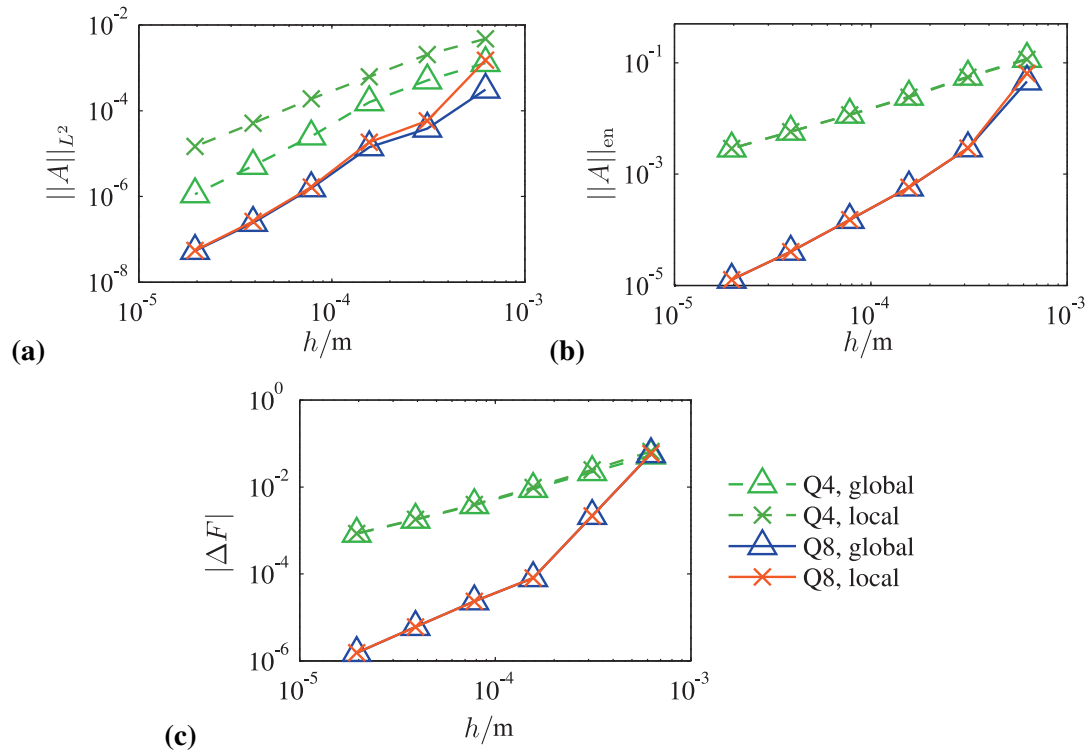
Figure 3.10: Results of the convergence analysis for different level set representations ($\mu_{\mathrm{r}}^- = 10^3$): **(a)** L^2 norm $||A||_{L^2}$ of the magnetic potential, **(b)** energy norm $||A||_{\mathrm{en}}$, and **(c)** relative error $|\Delta F|$ of the resulting force per unit length acting on the cylinder plotted over the mesh size parameter h.

Table 3.1: Convergence rates for the error measures $||A||_{L^2}$, $||A||_{\mathrm{en}}$ and $|\Delta F|$ obtained for different approximation orders, level set representations, and permeabilities.

error measure			$||A||_{L^2}$			$||A||_{\mathrm{en}}$			$|\Delta F|$		
relative permeability μ_{r}^-			10^1	10^3	10^6	10^1	10^3	10^6	10^1	10^3	10^6
(i)	Q4	global	2.00	2.37	1.63	1.02	1.03	1.03	1.16	1.14	1.14
(ii)	Q4	local	1.99	1.81	0.83	1.01	1.02	0.92	1.18	1.17	1.16
(iii)	Q8	global	2.47	2.68	2.35	1.64	1.84	1.99	1.91	1.91	1.91
(iv)	Q8	local	2.47	2.78	2.80	1.64	1.84	2.17	1.91	1.91	1.91

influenced by the used level set approach, Fig. 3.10 (a). The accuracy of the element local approach is deteriorated by the problems of interelement continuity outlined in Section 3.2. It is therefore one order of magnitude below the global level set approach. In addition, it cannot be recommended to use the bilinear elements with element local level sets for extremely high contrasts of the permeability as the order of convergence decreases significantly, Tab. 3.1. Regarding the energy norm $||A||_{en}$ it can be observed that both, the error and the orders of convergence, are virtually independent of the computation of the level set values, Fig. 3.10 (b). Optimal orders of convergence are obtained, Tab. 3.1.

Quadratic elements

For quadratic approximations a very good performance of the element local level set approach is noticed. That is, both versions produce almost identical errors and orders of convergence. However, the element local version is easier to handle due to its locality. Different from the global approach, the orders of convergence of the L^2 and energy error increase with the ratio of relative permeabilities μ_r^- / μ_r^+. The maximum and close to optimal rates are obtained for $\mu_r^- = 10^6$, Tab. 3.1.

Discussion

In summary, the use of quadratic shape functions does not yield optimal convergence rates for any of the investigated relative permeabilities, Tab. 3.1. A comparable study of a mechanical problem with a ratio of Young's moduli of 10 between inclusion and matrix, performed by Cheng and Fries [37], reports values of 2.4 and 1.4 in the L^2 and the energy norm, respectively. In this study biquadratic elements (Q9) and subdivision using four points for the interface approximation have been used which is slightly different from the present investigation. While the convergence rate for the L^2 norm observed here is in good agreement to their results, the energy norm converges more rapidly in the present study, Tab. 3.1.

Coupled problem

Because no analytic solution was available for the mechanical fields at the time of the study, the solution of the coupled field problem has to be assessed by the convergence of the relative error of the resulting force per unit length acting on the cylinder, Fig. 3.10 (c). Its computation is based on the pseudo-mechanical stress tensor $_E\boldsymbol{\sigma}$ and therefore depends on the gradient of the displacement field. However, the error is also influenced by the gradients of the magnetic field, as $\boldsymbol{\sigma}$ involves the first-order partial derivatives of A. That is why the improved approximations of the magnetic potential and the geometry will come into effect twice which results in convergence rates of $1.14 \ldots 1.18$ for the bilinear and 1.91 for the quadratic elements. As only gradients of the primary field variables are analysed, virtually no difference between the different approaches of level set approximation can be discovered. Furthermore, the convergence rates of $|\Delta F|$ are independent of the permeability.

3.4.2 Numerical Integration

Investigated cases

The convergence analysis regarding the influence of numerical integration schemes is performed for six different cases, distinguished by the order of approximation (Q4/Q8) and the integration procedure used in the X-elements:

(i) Subdivision into triangular and quadrilateral integration subdomains (IS),

(ii) Lasserre's integration (L),

(iii) Strain smoothing (SM).

It is noted that standard Gauss quadrature is applied in all ordinary finite elements. The convergence studies are performed using the same discretisations as in Section 3.4.1. Results are given for the ratio of the relative permeabilities $\mu_r^- / \mu_r^+ = 10^3$ and the use of element
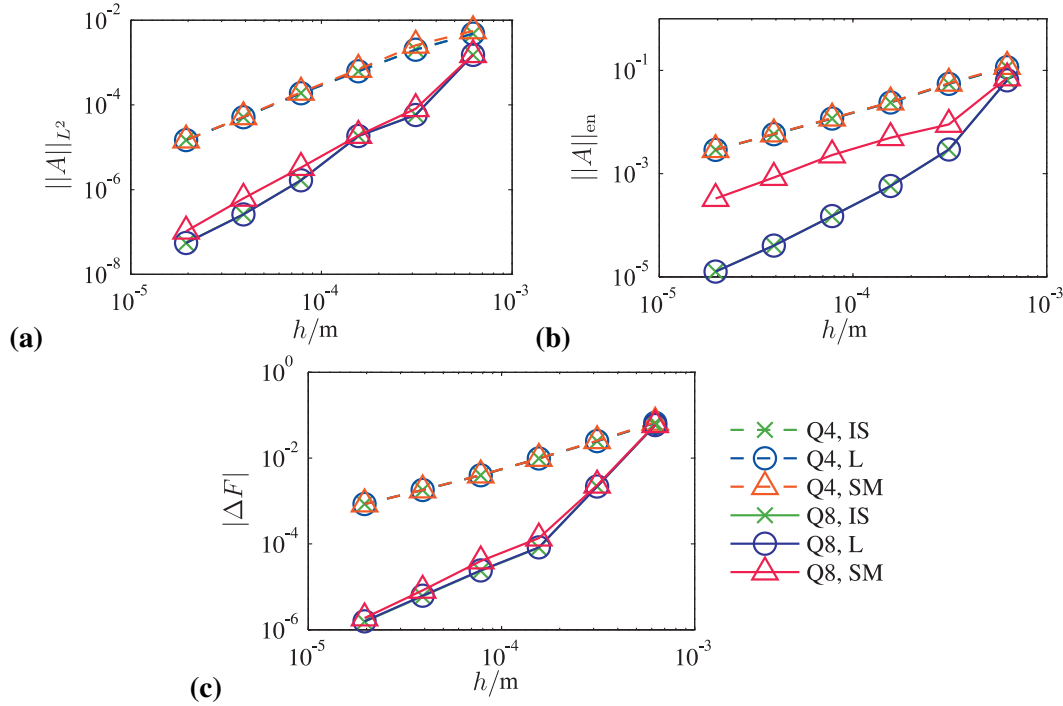
Figure 3.11: Results of the convergence analysis for different integration procedures (IS – integration subdomains, L – Lasserre's integration, SM – strain smoothing, $\mu_{\mathrm{r}}^- = 10^3$): **(a)** normalised L^2 norm $||A||_{L^2}$ of the magnetic potential, **(b)** energy norm $||A||_{\mathrm{en}}$, and **(c)** relative error $|\Delta F|$ of the resulting force per unit length acting on the cylinder plotted over the mesh size parameter h.

local level sets. In the case of Q8 elements, curved triangular and quadrilateral integration subdomains are used, Fig. 3.5 (b). For Lasserre's integration and strain smoothing the interface in the element is divided into two segments for Q4 elements. For Q8 elements with curved interfaces the required number of segments per element is chosen to ensure equivalent integration results from the polygonal approach (Lasserre's method) and the subdivision into integration subdomains. A number of 20 segments leads to identical results. However, on further numerical inspection it was found that already 5 segments per element, despite a slightly worse integration error, produce the same error and convergence behaviour with respect to L^2 and energy norm as 20 segments. In order to have comparable results the same number of interface segments is used with strain smoothing.

The obtained results are plotted against the mesh size h for $\mu_{\mathrm{r}}^- = 10^3$ in Fig. 3.11 and the convergence rates are summarised in Tab. 3.2. As in the previous section, numerical values are computed using only the four finest meshes. At first, the performance of Lasserre's method (L) will be compared to the subdivision into integration subdomains (IS). From Fig. 3.11 it can be deduced that Lasserre's method and the use of integration subdomains show equal performance regarding the error level for L^2 and energy norm as well as convergence rates for both Q4 and Q8 elements, if a fine segmentation of the interface is used. The computation time for preprocessing and integration for Lasserre's method is longer and scales with an average factor of 2.6 (5 segments per element) compared to integration subdomains. Despite the fact of being computationally more expensive, the method is advantageous from a methodic point of view since the need for a further element subdivision is eliminated which is particularly interesting for 3D implementations of higher-order methods.

Lasserre
integration vs.
subdomains

Table 3.2: Convergence rates of error measures $||A||_{L^2}$, $||A||_{en}$ and $|\Delta F|$ obtained for different integration procedures and approximation orders.

error measure		$||A||_{L^2}$		$||A||_{en}$		$|\Delta F|$	
integration procedure		Q4	Q8	Q4	Q8	Q4	Q8
(i)	Integration subdomains	1.81	2.78	1.02	1.84	1.17	1.92
(ii)	Lasserre's method	1.81	2.78	1.02	1.84	1.17	1.92
(ii)	Strain smoothing	1.86	2.49	1.02	1.32	1.17	2.08

Strain smoothing

For strain smoothing a mixed picture can be asserted. A good overall performance is observed for Q4 elements in comparison to the other methods. In addition, the results are in good agreement with [15]. For the L^2 norm Bordas et al. report an order of 1.69 ... 1.79 for the strain smoothed XFEM which is slightly less than the value of 1.86 obtained here, Tab. 3.2. The orders of convergence for the energy norm are approximately 1.3 compared to 1.02. As expected from the performance of strain smoothing with ordinary Q8 elements in [15], a loss of accuracy can be discovered for Q8 X- and ordinary elements, especially regarding the energy norm, Fig. 3.11 (b). The fairly good performance in conjunction with Q8 elements regarding the L^2 norm and the coupled problem must be assessed having in mind that strain smoothing is only applied in X-elements, while Gauss quadratures are used in standard isoparametric elements. The preprocessing and integration time of strain smoothing scales with an average factor of 1.25 compared with integration subdomains which is faster than Lasserre's method.

3.5 Conclusion

Summary

In this section one of the first applications of XFEM to non-mechanical boundary value problems has been presented. A one-sided magneto-mechanical coupling due to magnetic stresses has been considered and studied for a two-dimensional demonstration problem. Although both bilinear (Q4) and quadratic (Q8) elements are considered for comparative purposes, the major part of this chapter was devoted to the review and the development of methods for level set representation and numerical integration of the weak form for curved interfaces in higher-order XFEM formulations.

Interface representation

In order to reduce the complexity of the representation of curved interfaces, an element local approach has been developed which allows for an automated element by element computation of the level set values and also ensures the compatibility of the level set representation and the integration subdomains. For Q4 elements equal orders of convergence in the energy norm are observed while the standard approach shows a superior convergence behaviour in the L^2 norm. In the quadratic cases the results from both methods are identical for reasonable discretisations.

Quadrature

In addition to the interface representation, numerical integration procedures for curved interfaces and material subdomains have been addressed. Lasserre integration and strain smoothing have been applied in conjunction with higher-order interface representations. From the obtained results it can be concluded, that only Lasserre's method offers the possibility of avoiding the subdivision of material domains into integration subdomains. This advantage becomes particularly interesting for 3D implementations as presented in [152], even though the computational costs increase compared to the division into integration subdomains. The

application of strain smoothing to Q8 elements cannot be recommended for performance reasons and due to the fact that a fine grid of smoothing cells is required to avoid spurious modes and to properly capture a curved interface.

While mechanical problems feature typical ratios in the order of 10^1 between the stiffness properties of different materials, there are much higher ratios to be found in common magnetic applications. Therefore, the dependence of errors in XFEM on the magnitude of the jump of material properties across a discontinuity has been investigated. For ratios up to 10^6 a significant impact on the order of convergence in the L^2 and energy error norm of the magnetic field problem is found. This dependence turned out to be qualitatively different for the presented discretisations and level set procedures.

Contrast in material properties

In the following Chapter, the described methods will be applied to model the heterogeneous material structure of the magnetoactive composite material outlined in Section 1.1. XFEM models of representative volume elements are used in combination with homogenisation techniques to predict the effective magnetic and mechanical material behaviour of the composite using only geometrical and constitutive information from the micro- and mesoscale.

Application

4 Effective Response of Magnetorheological Elastomers [SKG$^+$13]

In this chapter XFEM is applied to generate numerical models of Representative Volume Elements (RVE) which are characteristic of the local material structure of a specific MRE. Based on these RVE models the effective coupled magneto-mechanical response of the composite is predicted numerically by a homogenisation procedure. The scale transition process is based on the energy equivalence condition which is satisfied by periodic boundary conditions for the primary magnetic and mechanical field variables, i.e the magnetic potential and the displacements.

4.1 Homogenisation Approach

This section presents an algorithm for the computation of the macroscopic magnetic and coupled magneto-mechanical response of MRE. The underlying microscopic structure is represented by a two-dimensional RVE of rectangular shape with two pairs of opposite boundaries $\partial\Omega^{I\pm}$, $I = 1, 2$. All nodes at the boundary of the discrete model can be grouped into node pairs which are connected by two vectors $\Delta\mathbf{x}^I$, Fig. 4.1 (a). Volume averages

$$\langle(\cdot)\rangle := \frac{1}{V_{\mathrm{RVE}}} \int\limits_{\Omega} (\cdot)\,\mathrm{d}V \tag{4.1}$$

over the RVE domain Ω with the volume V_{RVE} are used to relate the local field variables in the RVE to effective values on a larger length scale, e.g. the macroscale, which are labelled by $\bar{(\cdot)}$.

The basis of the presented scale transition process is the equivalence of the effective virtual work and an average virtual work for the heterogeneous microstructure [94]. These so-called macro-homogeneity conditions are given by

$$\bar{H}_i \delta\bar{B}_i = \langle H_i\rangle\langle\delta B_i\rangle = \langle H_i \delta B_i\rangle \tag{4.2}$$

$$\bar{\sigma}_{ij}^{\mathrm{tot}} \delta\bar{\varepsilon}_{ij} = \langle\sigma_{ij}^{\mathrm{tot}}\rangle\langle\delta\varepsilon_{ij}\rangle = \langle\sigma_{ij}^{\mathrm{tot}}\delta\varepsilon_{ij}\rangle \tag{4.3}$$

for the magnetic and coupled mechanical problem, respectively. Depending on the specific material behaviour of the local constituents, different computational homogenisation procedures based on the macro-homogeneity conditions can be used to predict the effective material behaviour:

(i) *Simulation of the effective material response*: Effective magnetisation or stress-strain curves can be simulated for different load cases based on numerical RVE models and suitable boundary conditions. This procedure gives valueable insight into structure-properties relations. In addition, the parameters of macroscopic models can be obtained from parameter fitting to the numerically predicted effective responses.
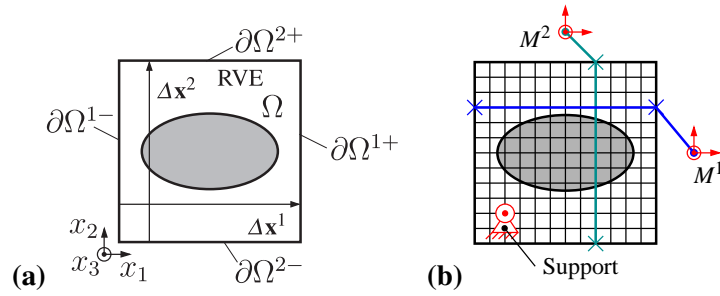
Figure 4.1: Two-dimensional representative volume element (RVE): **(a)** pairs of opposite surfaces $\partial\Omega^{I\pm}$ and characteristic vectors $\Delta\mathbf{x}^I$ with $I = 1, 2$ that define the size of the RVE, and **(b)** non-conforming regular XFEM mesh with nodal degrees of freedom coupled to two additional master nodes M^I and support to prevent rigid body motions.

(ii) *Adapted homogenisation procedures*: For certain material models, e.g. linear elastic and viscoelastic models, it is possible to directly compute effective material parameters from the simulation of the local material in the RVE for specific load cases.

(iii) *Coupled multi-scale simulations*: As effective constitutive relations will generally not be available for complex heterogeneous materials, it is possible to couple an RVE of the local material structure to macroscopic analysis models which is known as the FE^2 approach. In this method, effective material tangents and the update of the macroscopic constitutive variable are obtained from RVE models attached to the integration points of the macroscopic model, i.e. the RVE computations replace the definition and evaluation of a macroscopic material model. However, the approach comes at enormously high numerical costs which so far prevented its utilisation in realistic, large scale applications.

Boundary conditions

All three approaches are essentially based on the simulation of the local material response in an RVE which requires a set of boundary conditions. In this work the effective induction $\bar{\mathbf{B}}$ and strain $\bar{\varepsilon}$ are used as control variables, i.e. they define the effective load state of the RVE. Boundary conditions for the magnetic potential $\mathbf{A}$ and the displacement field $\mathbf{u}$ are used to prescribe the effective variables to the RVE. The effective response is then computed in terms of $\bar{\mathbf{H}}$ and $\bar{\boldsymbol{\sigma}}$. Feasible boundary conditions for the RVE problem arise from the macro-homogeneity theorem together with the balance equations (2.31) and (2.48) excluding body loads $\mathbf{j}$ and $\rho\mathbf{f}$. Here, periodic boundary conditions for the vector potential and the displacement are used. They consist of a linear term to define the macroscopic values of $\bar{\mathbf{B}}$ and $\bar{\varepsilon}$ but allow for periodic fluctuations of the potential and the displacements. The conjugated variables of the tangential magnetic field and the total traction have to be antiperiodic.

Numerical implementation

The local magneto-mechanical field problem that has to be solved in the RVE has been formulated in Chapter 2 and a numerical model is generated using XFEM as outlined in the context of Chapter 3. Fig. 4.1 (b) schematically shows the non-conforming mesh together with two additional master nodes M^I and a support to prevent rigid body motions. Following [113, 114], periodic boundary conditions are realised by prescribing the potential and the displacement to the master nodes which are coupled to node pairs on opposite edges of the RVE.

4.1.1 Effective Magnetic Response

By choosing the vector potential according to the mentioned periodic boundary conditions

$$A_3 = e_{3pq}\bar{B}_p x_q + \tilde{A}_3 \,, \tag{4.4}$$

the macro-homogeneity condition (4.2)

$$\frac{1}{V_{\text{RVE}}} \int_\Omega H_l B_l \,\mathrm{d}V = \frac{1}{V_{\text{RVE}}} \int_{\partial\Omega} H_l e_{lmn} \left(\delta_{n3} e_{3pq} \bar{B}_p x_q + \delta_{n3}\tilde{A}_3 \right) n_m \,\mathrm{d}S \tag{4.5}$$

$$= \frac{1}{V_{\text{RVE}}} \int_\Omega \left(H_l \bar{B}_l - H_3 \bar{B}_3 + H_l e_{lm3}\tilde{A}_{3,m} \right) \mathrm{d}V$$

is fulfilled. The second term on the right hand side of the equation above vanishes, because of the homogeneity in the x_3-direction $H_3 = 0$. The last term in equation (4.5) is equal to zero, if an antiperiodic surface current density $k_3^{I+} = -k_3^{I-}$ and a periodic fluctuation of the vector potential $\tilde{A}_3^{I+} = \tilde{A}_3^{I-}$ are assumed. In addition to this fluctuation term, equation (4.4) contains a linear part $e_{3pq}\bar{B}_p x_q$ required to prescribe the macroscopic value $\bar{\mathbf{B}}$ to the RVE.

The macroscopic field strength $\bar{\mathbf{H}}$ can be computed as the volume average (4.1) of the local magnetic field which simplifies to

$$\bar{H}_k = \frac{1}{V_{\text{RVE}}} \int_\Omega H_k \,\mathrm{d}V = \frac{1}{2V_{\text{RVE}}} \int_{\partial\Omega} e_{kmn} e_{qsn} H_q x_m n_s \,\mathrm{d}S = \frac{1}{A_{\text{RVE}}} \sum_{I=1,2} e_{kl3}\Delta x_l^I j_3^I \tag{4.6}$$

for the two-dimensional RVE under consideration. In equation (4.6) A_{RVE} is the area of the RVE domain, and j_3^I are the master node reaction currents which are calculated from the one-dimensional boundary integral

$$j_3^I = \int_{l^{I+}} e_{3qs} H_q n_s \,\mathrm{d}l \,. \tag{4.7}$$

The effective magnetisation $\bar{\mathbf{M}}$ is obtained from equation (2.34) and the values $\bar{\mathbf{B}}$ and $\bar{\mathbf{H}}$.

4.1.2 Effective Magneto-Mechanical Response

Similar to the magnetic relation (4.5), it can be shown that the two-dimensional displacement field

$$u_i = \bar{\varepsilon}_{ij} x_j + \tilde{u}_i \tag{4.8}$$

satisfies the Hill-Mandel lemma (4.3), together with the condition that the total traction has to be antiperiodic, i.e. $p_i^{I+} = -p_i^{I-}$. The equation above consists of a linear term $\bar{\varepsilon}_{ij} x_j$ which prescribes the macroscopic strain state to the RVE and a periodic fluctuation part $\tilde{u}_i^{I+} = \tilde{u}_i^{I-}$. Plane strain states are assumed on both, micro- and macroscale.

The effective response in terms of the mechanical stress tensor

$$\bar{\sigma}_{ij} = \frac{1}{A_{\text{RVE}}} \sum_{I=1,2} \Delta x_i^I F_j^I \tag{4.9}$$

is computed from the dyadic product of the characteristic RVE vectors $\Delta\mathbf{x}^I$ with the reaction forces divided by the area of the RVE. The mechanical master node reaction forces

$$F_j^I = \int\limits_{l^{I+}} \sigma_{ij} n_i \, \mathrm{d}l \tag{4.10}$$

are equal to the integral of the mechanical surface tractions along the positive edges of the RVE.

4.2 Unit Cell Model of an Anisotropic Microstructure

Introduction

In this section the introduced homogenisation algorithm is validated for a particular periodic microstructure. After the definition of the considered microstructure and the magnetisation behaviour of the particles which is motivated from experimental investigations, a convergence study on the effective linear magnetic and mechanical properties demonstrates the applicability of the outlined approach. Moreover, the effective anisotropic magnetisation behaviour, and the coupled response to three different magnetic loadings are analysed under the assumption of zero macroscopic deformation, $\bar{\varepsilon} = \mathbf{0}$. Despite the effective deformation state set to zero, the RVE will still deform due to periodic fluctuations.

4.2.1 Problem Definition

RVE model

The considered idealised two-dimensional microstructure is illustrated in Fig. 4.2 (a). Its internal structure is motivated by the chain-like arrangement of magnetisable particles which typcially results from the crosslinking of the polymeric matrix under an applied magnetic field, Fig. 1.1 (c). The RVE in Fig. 4.2 (a) contains three particles modelled as circular inclusions in the two-dimensional setting. All inclusions are assigned with a material behaviour representing carbonyl iron powder BASF CIP CC and have the diameter d. In the x_1-x_2-system the centers of the inclusions are located at $(3; 12)\,\mu\text{m}$, $(9; 8)\,\mu\text{m}$ and $(9; 16)\,\mu\text{m}$.

Material behaviour

Experimental results regarding the magnetisation behaviour of the BASF CIP CC material obtained by the group of S. Odenbach[1] are presented in Fig. 4.2 (b). The analysed material exhibits a non-linear, isotropic magnetisation behaviour with negligible hysteresis which can be represented in terms of the Langevin function (2.71). This function has two parameters which have to be determined from the experimental data. Results obtained for a saturation magnetisation $a_1 = M_\text{S} = 8.4 \times 10^5\,\text{A}\,\text{m}^{-1}$ and a scaling parameter $a_2 = \delta = 2.2 \times 10^{-5}\,\text{m}\,\text{A}^{-1}$ are plotted in Fig. 4.2 (b). A linearisation of equation (2.71) in the vicinity of $H = 0$ yields the constant relative permeability

$$\mu_\text{r} = \frac{M_\text{S}\delta}{3} + 1 \tag{4.11}$$

and equation (2.34) can be rewritten in the simple form $B_l = \mu_0\mu_\text{r}H_l$ representing a linear approximation to the magnetic material behaviour of the particles (superscript P). As expected, this linear approximation with $\mu_\text{r}^\text{P} = 7.2$ is only reasonable for small values of the magnetic field. The elastomeric matrix (superscript M) consists of Wacker Chemie AG Elastosil® RT 745 which is assumed to be non-magnetisable $\mu_\text{r}^\text{M} = 1$. With respect to the assumed small

---

[1]TU Dresden, Chair of Magnetofluiddynamics, Measuring and Automation Technology.
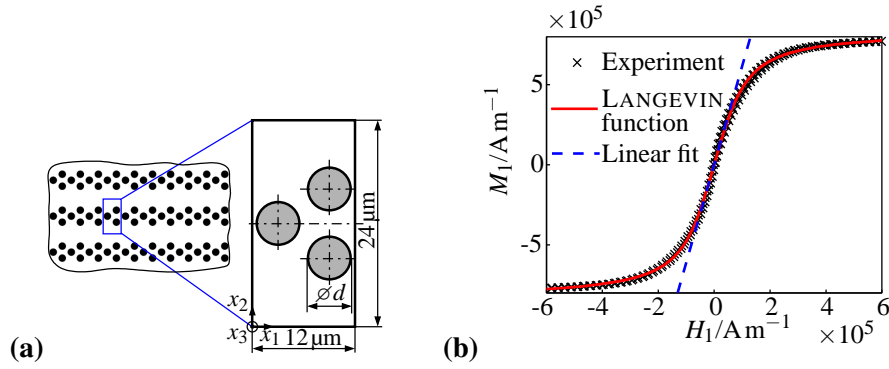
Figure 4.2: Idealised periodic microstructure: **(a)** RVE containing three circular inclusions with diameter d, and **(b)** non-linear magnetisation behaviour of BASF CIP CC powder assumed for the circular inclusions – experimental results and models according to equations (2.71) and (4.11).

deformations, both constituents are modelled as isotropic linear elastic according to equation (2.93) with the parameters $E^{\mathrm{P}} = 2.1 \times 10^5 \,\mathrm{MPa}$ and $E^{\mathrm{M}} = 0.2 \,\mathrm{MPa}$ as well as the Poisson ratios $\nu^{\mathrm{P}} = 0.3$ and $\nu^{\mathrm{M}} = 0.4$ for the particles and the matrix, respectively.

4.2.2 Convergence Study for the Effective Linear Response

In this section the convergence of the effective parameters is studied for different mesh resolutions using either linear or quadratic elements. A total number of six discretisations with 8×16, 16×32, 32×64, 64×128, 128×256 and 256×512 elements are considered, Fig. 4.3 (a). The mesh resolution is specified by the size of the element edge h. All inclusions have a diameter of $d = 3.8 \,\mu\mathrm{m}$ which results in a volume fraction of approximately $12\,\%$. | *Considered meshes*

At first, the effective magnetic behaviour is analysed. As a consequence of the geometrical arrangement of the circular inclusions, the macroscopic magnetic behaviour is anisotropic and can be described in terms of the second-order tensor of effective relative permeability $\bar{\boldsymbol{\mu}}_{\mathrm{r}}$ | *Magnetisation*

$$\bar{\mathbf{B}} = \mu_0 \bar{\boldsymbol{\mu}}_{\mathrm{r}} \bar{\mathbf{H}} \,. \tag{4.12}$$

In order to determine $\bar{\boldsymbol{\mu}}_{\mathrm{r}}$, two magnetic load cases are defined by different choices of the effective magnetic induction $\bar{\mathbf{B}}$ and solved numerically for the effective magnetic field $\bar{\mathbf{H}}$. The first considers $\bar{\mathbf{B}}$ parallel to the x_1-axis and the second a magnetic field parallel to the x_2-direction. In Fig. 4.3 (b) the convergence of $\bar{\mu}_{\mathrm{r}\,11}$ is plotted for all six meshes of linear and quadratic elements, respectively. A monotonic convergence is observed for both element types. Even with the coarsest mesh, the results obtained with the quadratic elements produce errors of less than $0.2\,\%$. All results lie in between the Reuss ($\bar{\mu}_{\mathrm{r}\,11}^{\mathrm{R}} = 1.1$) and Voigt ($\bar{\mu}_{\mathrm{r}\,11}^{\mathrm{V}} = 1.7$) bounds.

To obtain the effective stiffness $\bar{\mathbf{C}}$, a purely mechanical homogenisation ($\mathbf{B} = \mathbf{0}$) is performed under the assumption of a plane strain state. Three macroscopic deformation states, i.e. two uniaxial strain and one shear mode, are prescribed to the RVE in terms of the effective strain $\bar{\boldsymbol{\varepsilon}}$ applied by periodic displacement boundary conditions. The effective linear elastic stiffness is computed from the corresponding macroscopic stresses according to equation (4.9). The results of the convergence study in terms of $\bar{C}_{11}$ are plotted in Fig. 4.3 (c). | *Stiffness*
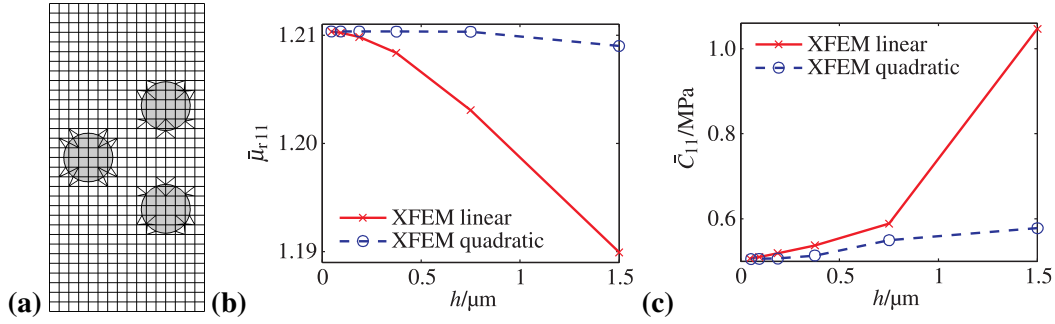
Figure 4.3: Selected results of a convergence study for the effective material behaviour using different discretisations of linear and quadratic elements: **(a)** numerical RVE model with $d = 3.8\,\mu\text{m}$ and $h = 0.75\,\mu\text{m}$ – ordinary finite elements together with triangular and quadrilateral integration subdomains of the X-elements, **(b)** relative permeability $\bar{\mu}_{\text{r}11}$, and **(c)** stiffness $\bar{C}_{11}$.

Again, significantly smaller errors are obtained for quadratics. It is noted that coarse discretisations produce higher relative errors in the mechanical case than for the effective magnetic behaviour at the same resolution. This is due to the large contrast of the elastic moduli of inclusion and matrix of almost six orders of magnitude. In comparison, the relative permeabilities of both components differ only by the factor 7.2. However, all numerical values obtained lie in between the Reuss ($\bar{C}_{11}^{\text{R}} = 0.49\,\text{MPa}$) and Voigt ($\bar{C}_{11}^{\text{V}} = 3.34 \times 10^4\,\text{MPa}$) bounds. Since the matrix is very soft and has a high volume fraction compared to the particles, the numerical results for periodic boundary conditions are close to the Reuss bound which assumes a homogeneous stress field. The magnetic and the mechanical macroscopic properties converge from different directions (Fig. 4.3 (b) and (c)), because the tensor of the relative permeability $\bar{\mu}_{\text{r}}$ has the nature of a compliance rather than a stiffness, as $\bar{\mathbf{B}}$ can be interpreted as a kinematic and $\bar{\mathbf{H}}$ as the conjugated kinetic variable.

4.2.3 Effective Magnetisation Behaviour

RVE model and loading

The effective magnetic behaviour of the MRE is now predicted in terms of macroscopic magnetisation curves $\bar{M}(\bar{H})$. All particles have a diameter of $d = 5\,\mu\text{m}$ resulting in a particle volume fraction of approximately $20\,\%$. The RVE domain is discretised by 49×98 quadratic elements. Both, non-linear (2.71) and linear (4.11) magnetisation behaviour of the inclusions will be considered. A macroscopic magnetic induction with an intensity of $2\,\text{T}$ is applied to the RVE within 20 increments for three different directions: parallel (0°), perpendicular (90°) and under an angle of $45°$ to the internal chain direction, Fig. 4.4. The application of such a high magnetic induction which is hardly achievable in experiments without losing the homogeneity of the macroscopic field is required to investigate the full range of the physical non-linearity.

Effective magnetic response

The results in Fig. 4.4 show the obtained effective magnetisation curves for the non-linear magnetic behaviour of the particles and its linear approximation. As a consequence of the internal material structure, the effective magnetic material behaviour is anisotropic. This effect decays for strong magnetic fields due to the magnetic saturation characteristics in the non-linear case. Corresponding experimental have been reported by Danas et al. [43]. For the linear material behaviour the magnetisation is anisotropic for all values of the magnetic field $\bar{H}$.
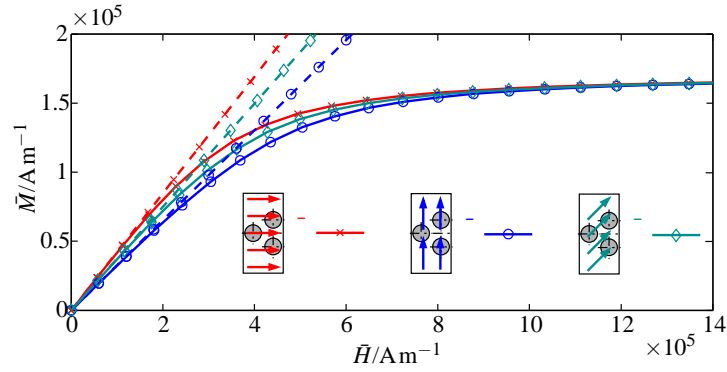
Figure 4.4: Numerically computed effective magnetisation curves for three different load cases with non-linear (solid lines) and linear (dashed lines) behaviour of the particles and a non-magnetisable matrix material.

4.2.4 Effective Magneto-Mechanical Behaviour

The effective coupled magneto-mechanical behaviour is analysed by evaluating mechanical actuation stresses according to equation (4.9). These stresses occur in the coupled magneto-mechanical problem if the macroscopic deformation is set to zero, i.e. $\bar{\varepsilon} = \mathbf{0}$, and the MRE is loaded magnetically. However, as a consequence of the periodic displacement boundary conditions (4.8), the RVE is allowed to deform locally due to the fluctuation terms. | *Actuation stresses*

At first, two load cases are considered with the effective magnetic induction either aligned with or perpendicular to the internal chain-like structure. Again, the macroscopic induction of $|\bar{\mathbf{B}}| = 2\,\mathrm{T}$ is applied to the RVE within 20 increments. Fig. 4.5 (a) shows the mechanical actuation stresses for the macroscopic magnetic induction aligned with the internal chain-like structure. The small inserted picture of the local displacement field u_2 illustrates that the two inclusions on the right attract each other. In this contour plot red corresponds to positive and blue to negative values of the local vertical displacement field u_2. Since the macroscopic deformation is set to zero, an elongation of the RVE in the x_1-direction is prevented which results in a negative actuation stress $\bar{\sigma}_{11} < 0$. In the x_2-direction the attraction of the inclusions is compensated by a tensile stress $\bar{\sigma}_{22} > 0$. The initial behaviour of the actuation stresses versus the magnetic induction is quadratic as the pseudo-magnetic stress $\hat{\boldsymbol{\sigma}}$ is a quadratic function of the magnetic field. This is in accordance to analytical results of Galipeau and Ponte Castañeda [73]. For $|\mathbf{B}| \gtrsim 0.6\,\mathrm{T}$ the saturation becomes dominant in the non-linear case, but in the linearised regime ($\mu_{\mathrm{r}}^{\mathrm{P}} = \mathrm{const.}$) the behaviour remains quadratic in $|\bar{\mathbf{B}}|$. | *0° direction*

If the macroscopic induction is applied perpendicular to the chain direction, there is a repulsive interaction which result in the actuation stresses $\bar{\sigma}_{11} > 0$ and $\bar{\sigma}_{22} < 0$, Fig. 4.5. Again, the initial dependence is quadratic in $|\bar{\mathbf{B}}|$ before saturation effects become relevant. The plotted shear stress components $\bar{\sigma}_{12}$ and $\bar{\sigma}_{21}$ are almost zero for the linear and the non-linear magnetic case and both loading directions. | *90° direction*

The results shown in Fig. 4.6 correspond to the macroscopic induction applied at an angle of $45°$. In Fig. 4.6 (a) the contour plots of the local magnetic induction on the deformed RVE are displayed. The resulting actuation stresses are qualitatively different from the stresses discussed for the parallel and the perpendicular orientations of the magnetic field, Fig. 4.6 (b). Here, the normal stress components $\bar{\sigma}_{11}$ and $\bar{\sigma}_{22}$ are smaller than the shear stresses $\bar{\sigma}_{12}$ and | *45° direction*
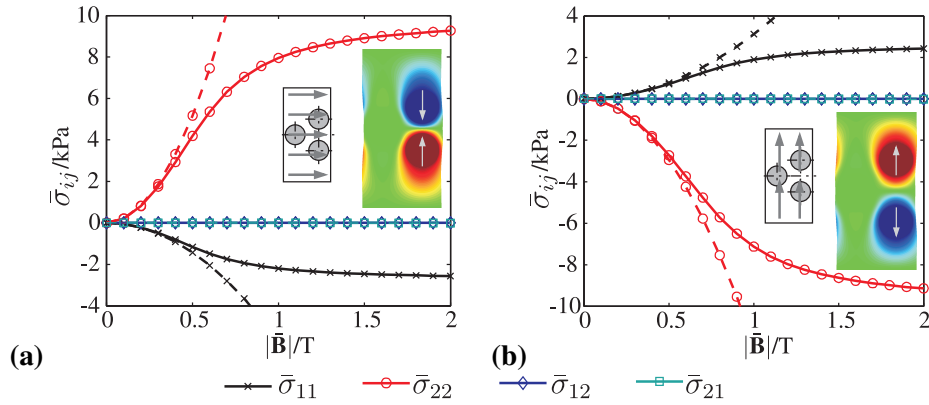
Figure 4.5: Macroscopic mechanical actuation stresses for magnetic loading $|\bar{\mathbf{B}}| = 2\,\mathrm{T}$ within 20 increments and $\bar{\varepsilon} = \mathbf{0}$: **(a)** macroscopic magnetic induction applied parallel, and **(b)** perpendicular to the internal chain-like structure. Non-linear magnetic response of the inclusions is represented by solid lines and the linear approximation with dashed lines.
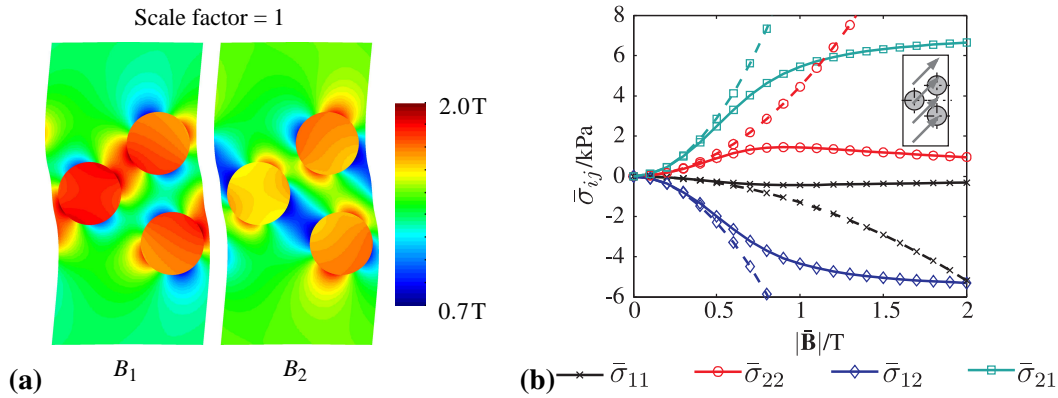
Figure 4.6: Magnetic loading $|\bar{\mathbf{B}}| = 2\,\mathrm{T}$ at an angle of $45°$ and $\bar{\varepsilon} = \mathbf{0}$: **(a)** local magnetic induction in the deformed RVE, and **(b)** macroscopic mechanical actuation stresses for the non-linear (solid lines) and linear (dashed lines) magnetic material behaviour of the inclusions.

$\bar{\sigma}_{21}$. An essential aspect of the results is that the macroscopic mechanical stress tensor is unsymmetric with $\bar{\sigma}_{12} < 0$ and $\bar{\sigma}_{21} > 0$. This is due to the anisotropic microstructure. The non-symmetric macroscopic shear components of the actuation stress equilibrate a macroscopic torque, which acts counterclockwise on the structure. Since the magnetic induction is not applied parallel to the principal axes of the composite, the internal chain-like structure of the composite, Fig. 4.2 (a), intends to rotate and align with the external magnetic field. This causes a macroscopic torque acting on the composite. Again, the initial behaviour is quadratic in $|\bar{\mathbf{B}}|$ for the non-linear magnetic model and quadratic over the whole range of $|\bar{\mathbf{B}}|$ for the linear approximation.

4.3 Random Isotropic and Anisotropic Microstructures

Generation of random RVE

In this section numerical simulations are carried out for more complex microstructures with random, polydisperse, isotropic or anisotropic particle distributions. XFEM models of these local material structures are generated by a random sequential adsorption algorithm [210]

which can be used very efficiently with the XFEM procedures for interface representation. Circularly shaped particles (radius r_I) are added sequentially to the RVE domain Ω. Intersections of the I-th particle domain with adjacent particles are avoided by testing the criterion

$$||\mathbf{x}_I - \mathbf{x}_J|| < r_I + r_J + d \tag{4.13}$$

for any particle J already added to the domain. That is, the distance of the center points of two neighbouring inclusions must be larger than the sum of their radii r_I and r_J, respectively. The parameter d is chosen to prevent numerical problems that may result from thin matrix domains. Polydisperse microstructures are defined in terms of a set of radii $\underline{r}$ and associated partial concentrations $\underline{\phi}$ which can be parametrised by experimentally obtained particle size distributions as demonstrated in Section 4.3.2. The algorithm produces random, quasi-isotropic particle distributions. To generate anisotropic arrangements, the coordinates of the particle centers $\mathbf{x}_I$ have to be constrained. As a result of the circular particle shape, the particle-matrix interface is given analytically and a level set representation of the particle boundary is defined by the center $\mathbf{x}_I$ and radius r_I of the I-th particle. All elements intersected by the material interface become X-elements and the resulting material subdomains as well as the ordinary finite elements are assigned with the corresponding properties of particle or matrix, respectively.

4.3.1 Effective Magnetostrictive Behaviour

The random adsortion algorithm has been used to generate two-dimensional RVE models of random isotropic and anisotropic particulate microstructures with particle volume fractions of $c = 0.3$ and $c = 0.08$, respectively. Particles distributions defined by three different radii $\underline{r} = \{1, 2, 3\}\mu m$ which account for $\underline{\phi} = \{20, 40, 40\}\%$ of the total particle volume fraction are used for the isotropic and anisotropic case. The mechanical behaviour of both constituents is modelled as isotropic linear elastic with the parameters $E^P = 2.1 \times 10^5\,\mathrm{MPa}$ and $E^M = 0.2\,\mathrm{MPa}$ as well as the Poisson ratios $\nu^P = 0.3$ and $\nu^M = 0.4$. Linear magnetisation behaviour ($\mu_r^P = 7.2$) is assumed for the particles while the matrix is non-magnetisable ($\mu_r^M = 1$). The assumption of linear magnetic material behaviour is reasonable for the applied magnetic inductions of $\bar{B} = 0.3\,\mathrm{T}$.

The coupled magneto-mechanical response of the random microstructures has been simulated for a macroscopic magnetic induction $\bar{B}$ which is applied to the RVE. Two different perpendicular orientations are considered according to Fig. 4.7 (a). Macroscopically traction free boundaries allow for the analysis of magnetically induced deformations $\bar{\varepsilon}$, i.e. the prediction of magnetostrictive effects, Fig. 4.7 (b). It is found that both, isotropic and anisotropic, RVE elongate ($\bar{\varepsilon} > 0$) parallel to the applied magnetic field. Lateral contraction is observed due to the Poisson effect. It has to be noted, that an ideal chain of finite length would show a contraction if the magnetic field is applied parallel to the chain. The elongation observed for the random chain-like microstructure results from the motion of the particles that try to form an ideal chain, Fig. 4.7 (a). This has been previously explained by Danas et al. [43]. Similarly, Han et al. [88] have performed microscopic finite element computations which underline the importance of a wavy chain geometry on the direction of the resulting magnetostriction. While the random particle distribution yields an isotropic effective response, the chain-like RVE shows an anisotropic behaviour with stronger magnetostrictive effects observed in the direction of the particle chain. Again, even linear magnetic and mechanical properties translate into a progressive coupling behaviour which is in line

RVE models

Discussion
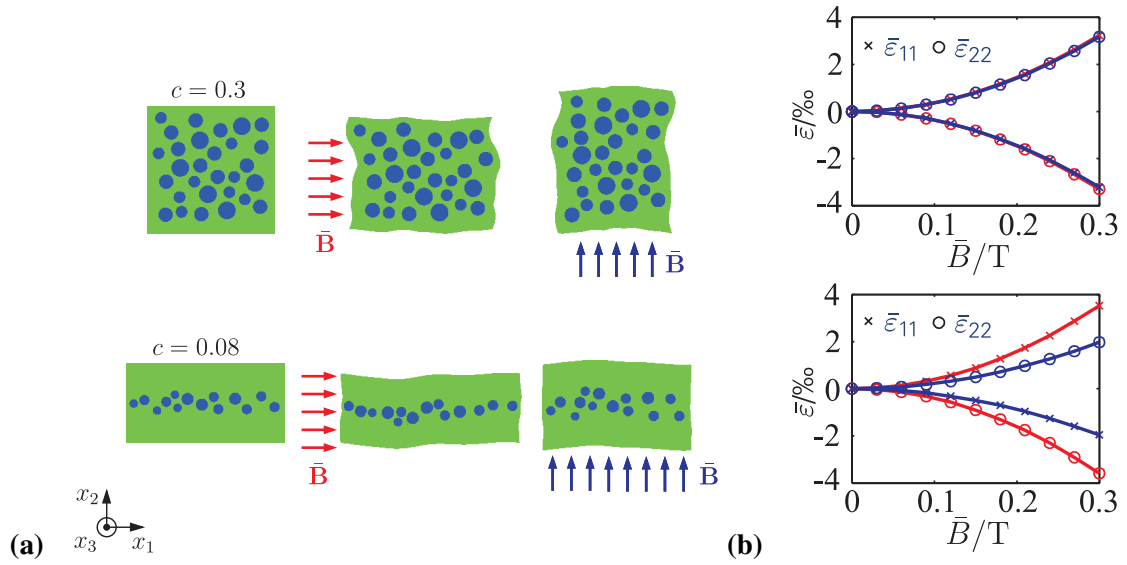
Figure 4.7: Effective magnetostrictive behaviour of isotropic and anisotropic RVE: **(a)** random isotropic microstructure of particle volume fraction $c = 0.3$ and chain-like distribution of $c = 0.08$. Two load cases for external magnetic field $\bar{B}$ are considered. The particles in the anisotropic RVE move to form a perfectly aligned chain which results in an elongation of the RVE in the direction of external magnetic field, and **(b)** macroscopic magnetostrictive strain as a function of the applied magnetic induction.

with the preceding section and theoretical results [73].

4.3.2 Experimental Validation

Problem definition

Following the comparison of numerical results for different microstructures, the predictions for RVE with random, polydisperse isotropic particle distributions are to be validated by experimental results obtained in the group of M. Schrödner[2]. Similarly to the preceding theoretical study, RVE with randomly distributed magnetisable particles (BASF CIP-SQ with properties $E^{P} = 210\,\text{GPa}$, $\nu^{P} = 0.3$, and $\mu_{r}^{P} = 7.2$) are generated. Particles with four different radii $\underline{r} = \{1,\ 2,\ 3,\ 4\}\mu\text{m}$ accounting for $\underline{\phi} = \{10,\ 40,\ 30,\ 20\}\%$ of the total particle volume fraction are embedded into the non-magnetisable ($\mu_{r}^{M} = 1.0$) polymeric matrix. The matrix material Bayer Desmopan 481 is assumed to show almost incompressible linear elastic behaviour ($E^{M} = 14.6\,\text{MPa}$, $\nu^{M} = 0.49$). The chosen radii and the corresponding volume fractions originate from a particle size distribution reported in [ZZB$^+$14]. Clusters of particles, which have been detected by a computed tomography analysis, are not included in the simulations. Examplary isotropic RVE with different total particle volume fractions c are presented in Fig. 4.8. In addition to the experimentally used volume fractions which have been derived from the mass contents of CIP-SQ, the values of $c = 23.0\%$ and $c = 33.0\%$ have been included only for the purpose of simulation.

Effective mechanical behaviour

First, the effective mechanical behaviour is to be computed and compared to analytical as well as experimental results. According to Lopez-Pamies et al. [133, 134, 135] the effective

---

[2]Thuringian Institute of Textile and Plastics Research.

$c = 9.2\%$ $c = 13.2\%$ $c = 18.6\%$ $c = 23.0\%$ $c = 26.3\%$ $c = 33.0\%$ $c = 37.8\%$
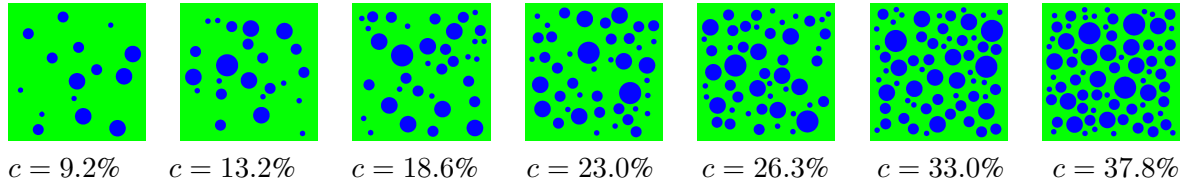
Figure 4.8: Isotropic RVE with randomly distributed particles of different volume fractions c.

(a)   **(b)**
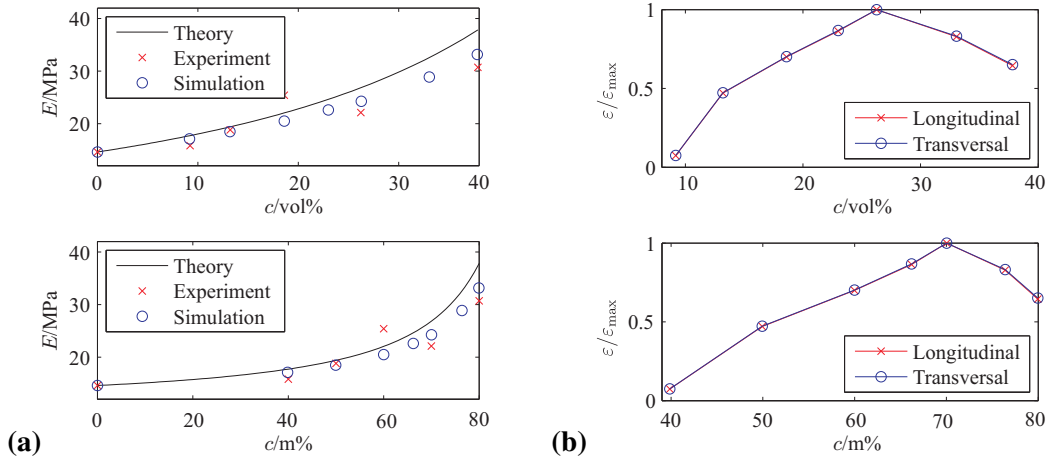
Figure 4.9: Effective magneto-mechanical behaviour of isotropic MRE – comparison of analytical, numerical and experimental results: **(a)** effective Young's modulus, and **(b)** macroscopic magnetostrictive strain, normalised by its maximum value, as a function of the particle volume fraction c.

Young's modulus is calculated from

$$\bar{E}(c) = \frac{1}{(1-c)^2} E^{\mathrm{M}} \,, \tag{4.14}$$

i.e. the effective behaviour of the isotropic RVE will be exactly the same as für the pure matrix except for a concentration dependent amplification factor, see Section 5.2.2 for further details. In order to predict the effective mechanical behaviour, XFEM models of the random particulate microstructure are loaded mechanically by a prescribed uniaxial macroscopic strain $\bar{\varepsilon}$. Figure 4.9 (a) presents experimental data and results of the multiscale XFEM simulation together with the theoretical prediction according to equation (4.14). It can be seen that the effective stiffness of the isotropic MRE in terms of the macroscopic Young's modulus $\bar{E}$ grows with increasing volume content of magnetisable particles. Both, theoretical and experimental curves predict the same characteristic dependence with the analytical approach slightly overestimating the effective stiffness.

The coupled magneto-mechanical response of the considered real MRE is analysed in terms of magnetostrictive strains, Fig. 4.9 (b). A macroscopic magnetic induction $\bar{B}$ is applied to the RVE while macroscopically traction free boundaries allow for a magnetically induced macroscopic deformation $\bar{\varepsilon}$. The resulting magneto-mechanical boundary value problem is solved numerically using quadratic standard and X-elements. Linear magnetic material behaviour is assumed for the particles as only moderate magnetic inductions of $\bar{B} = 0.3\,\mathrm{T}$ are applied. Similarly to the previous section, the RVE elongates parallel to the applied magnetic

Effective
magneto-
mechanical
behaviour

field. As it can be seen in Fig. 4.9 (b), the macroscopic magnetostrictive effect increases up to an extremal value at $c = 26.3\%$. After this maximum, the mechanical stiffening effect dominates for a further increase of the particle volume content. Actually, this value is in excellent accordance with results of Davis [46] where an optimal concentration of $c = 27\%$ is found to yield the maximum magnetorheological effect. All values in Fig. 4.9 (b) are given normalised with respect to the maximum magnetostrictive deformation.

4.4 Conclusion

Summary

In this section a computational homogenisation approach to predict the effective magnetic and coupled magneto-mechanical response of MRE has been presented. It was applied to a generic unit cell model as well as more complex random microstructures which can be modelled efficiently using XFEM. The convergence of the approach regarding the effective linear magnetic and mechanical material behaviour has been demonstrated for linear and quadratic approximations.

Effective response of MRE

For the initially analysed unit cell, actuation stresses for three different magnetic loading directions are found to be in qualitative agreement with experiments on MRE as well as analytical findings. The model predicts an elongation of the composite, if the magnetic stimulus is applied parallel to the chains of magnetisable particles. Physically sensible predictions are also obtained for isotropic and anisotropic RVE with random particle distributions that have been validated by experimental results.

Outlook

With the combination of the continuum formulation of the magneto-mechanical boundary value problem and the efficient discretisation of complex microstructures using XFEM with homogenisation techniques for the coupled problem, a modelling strategy has been proposed that enables a qualitative and quantitative analysis of the structure-property relations of MRE. The method is very flexible regarding the microstructure to be modelled and a variety of material models can be used to represent the microscopic constituents. This approach is to be further developed in order to directly convert computed tomography scans into numerical analysis models or to work with statistically similar RVE models. However, it has to be noted that discrete approaches [100, 101, 103, 165] are more efficient if a large number of particles has to be modelled. In the future it seems reasonable to combine both approaches, i.e. to use finite element simulations to thoroughly analyse particle-particle interactions and to incorporate these results into the discrete models in terms of modified potentials. In this way short-range interactions that cannot be represented with the typically used dipole-dipole model could be included.

5 Modelling of the Large Deformation Behaviour of Magnetorheological Elastomers [SMKU14]

Polymeric matrices of MRE are often designed to exhibit a very low mechanical stiffness in order to maximise the relative magnetorheological effect, i.e. the ratio of the stiffness with and without an applied magnetic field. These soft polymers may also lead to large overall deformations of the MRE especially under mechanical loads and allow for large displacements of the particles due to magnetic interactions. A first step to take these effects into account in the numerical simulations is presented in this section. An updated Lagrangian FE formulation for the magneto-mechanical BVP is developed which can accomodate a two-sided coupling according to Section 2.4, That is, the influence of mechanical deformations on the current magnetic fields is now considered in terms of a configurational update. After the derivation of the FE formulation in the following section, the numerical implementation of XFEM for large deformations will be explained and verified using results from an analytical homogenisation scheme. Eventually, first results representing a comparison with the small deformation model introduced in Chapter 3 and Chapter 4 point out the consequences of the two-sided coupling. As in the previous chapter two-dimensional problems homogeneous in the thickness direction are considered.

5.1 Finite Element Formulation

The finite element formulation for the solution of the coupled magneto-mechanical problem is to be generalised to large deformations below. After the presentation of the numerical coupling, weak forms for the stationary magnetic and coupled magneto-mechanical boundary value problems which can account for large deformations are developed. For the solution of the non-linear system of equations resulting from the FE discretisation of the weak forms the Newton-Raphson method is applied which requires a linearisation of the discrete equations.

5.1.1 Numerical Coupling Scheme

There are two different approaches to treat the two-sided coupling of field problems numerically:

(i) *Strong coupling:* In this numerical solution scheme both problems are consistently linearised. This results in a monolithic system of equations, i.e. both problems are solved at the same time and interated until a certain accuracy criterion is met.

(ii) *Weak coupling:* This numerically simpler scheme uses a staggered solution procedure with a load vector coupling similar to the case of small deformations. The magnetic problem is solved with respect to the configuration of the previous mechanical load

step. Magnetic loads from this computation are then considered in the subsequent mechanical pass to update the configuration.

Since the weak coupling approach misses the consistent linearisation of the strong coupling scheme, it is generally more susceptible to instabilities and therefore less robust. On the other hand, virtually the same implementation as for small deformations can be used and the systems of equations to be solved are smaller and feature symmetric system matrices which is not the case for the monolithic approach.

Staggered
solution
The work presented in this chapter is primarily intended to demonstrate the principal differences between small and large deformation simulations. Therefore, a staggered solution procedure is applied. This approach turned out to be suitable for the demonstration problems considered in the following. The incremental analysis using the weak coupling scheme starts from solving the magnetic field problem with respect to the undeformed reference configuration. With this solution at hand the mechanical problem is solved. After each pass of both calculations a convergence criterion is checked, i.e. the corrections of the primary field variables of the current iteration are compared to their incremental changes. If these relative changes are smaller than a given value, then the solution is assumed to be in equilibrium and the analysis continues with the next increment by increasing the magnetic load. Otherwise the configuration is updated and both field problems are solved again. To reach a converged state, at least two cycles have to be passed.

5.1.2 Weak Forms and Linearisation

Lagrangian
meshes
In this section the governing discrete equations of large deformation finite element formulations for the magnetic and magneto-mechanical field problems are developed. As it is typical for solid mechanics applications, a Lagrangian mesh is used, i.e. the analysis mesh deformes with the material body and a material point is always assigned to the same natural coordinate ξ. This is essential for the handling of inelastic constitutive equations which require an update of internal variables at an integration point level. For severe deformations this geometric map may cause numerical problems regarding the conditioning of the system of equations and remeshing can be required to recover acceptable element shapes.

Total vs.
Updated
Lagragian
Two principal Lagrangian finite element formulations result from the discretisation of the weak forms formulated with respect to the reference and current configuration, respectively:

(i) *Total Lagrangian FEM:* This formulation is based on the balance equations with respect to the undeformed reference configuration Ω_0.

(ii) *Updated Lagrangian FEM:* Here, the balance equations with respect to the deformed current configuration Ω are employed.updated during analysis.

The expressions for the discrete equations are different for both formulations and they will involve different representations of constitutive equations, etc. However, the equations can be converted into each other and the same numerical values of the coefficient matrices are obtained after integration. Both formulations will actually predict exactly the same solution. The choice of one of the formulations is merely a question of convenience. Here, the updated Lagrangian approach is used, because the structure of the underlying matrices is essentially the same as for the small deformation approach which eases implementation. Some details of the underlying non-linear FE procedures will be given in Section 5.2 including a generalisation to XFEM. For further details the textbooks of, e.g., Belytschko et al. [10], de Borst et al. [47], and Wriggers [228] are recommended.

Similarly to the case of small deformations, a weak form for the stationary magnetic field problem is obtained from mutiplying equation (2.31) with a weight or test function function, i.e. the virtual potential δA_k which fulfills $\delta A_k = 0$ on $\partial\Omega_A$. By applying integration by parts and using the relations (2.35) and (2.39), the weak form of the magnetic problem

$$\int_\Omega H_k \delta B_k \, \mathrm{d}V - \int_\Omega j_k \delta A_k \, \mathrm{d}V - \int_{\partial\Omega_k} \hat{k}_k \delta A_k \, \mathrm{d}S = 0 \qquad (5.1)$$

is obtained.

Using a standard isoparametric FE approximation with the matrix of shape functions $\underline{\underline{\mathbf{N}}}_A$ and their partial derivatives expressed by $\underline{\underline{\mathbf{B}}}_A$, the weak form (5.1) of n_e assembled elements is given by the discrete Ritz formulation

$$\delta\underline{\mathbf{A}}^T \left\{ \underbrace{\bigcup_{I=1}^{n_\mathrm{e}} \left[\int_{\Omega_{I_\mathrm{e}}} \underline{\underline{\mathbf{B}}}_A^T \underline{\mathbf{H}} \, \mathrm{d}V \right]}_{\underline{\mathbf{j}}^{\mathrm{int}}} - \underbrace{\bigcup_{I=1}^{n_\mathrm{e}} \left[\int_{\Omega_{I_\mathrm{e}}} \underline{\underline{\mathbf{N}}}_A^T \underline{\mathbf{j}} \, \mathrm{d}V - \int_{\partial\Omega_{I_\mathrm{e}}} \underline{\underline{\mathbf{N}}}_A^T \hat{\underline{\mathbf{k}}} \, \mathrm{d}S \right] - \underline{\mathbf{J}}}_{-\underline{\mathbf{j}}^{\mathrm{ext}}} \right\} = \underline{\mathbf{0}} \, . \qquad (5.2)$$

In the equation above the vector $\underline{\mathbf{J}}$ accounts for discrete nodal loads typically applied in FE analysis. From the argument of arbitrary but admissible virtual potentials $\delta\underline{\mathbf{A}}$, finally the nonlinear FE system is defined by the equilibrium of the internal and external nodal loads

$$\underline{\mathbf{j}}^{\mathrm{int}} - \underline{\mathbf{j}}^{\mathrm{ext}} = \underline{\mathbf{0}} \, . \qquad (5.3)$$

For an iterative solution of the underlying FE system, a linearisation of the discrete weak form (5.2) is required. To be consistent with the weak numerical coupling scheme, the configuration is assumed to be constant during the iteration of an increment. Furthermore, the external loads, expressed by the last two terms in the equation above, are assumed to be independent of $\mathbf{A}$. Eventually, a materially non-linear problem has to be solved on a configuration updated from increment to increment. The iterative solution within each increment using the Newton-Raphson method is based on the linearised relation

$$\underline{\underline{\mathbf{K}}}_A \Delta\underline{\mathbf{A}} = \underline{\mathbf{j}}^{\mathrm{ext}} - \underline{\mathbf{j}}^{\mathrm{int}} \, , \qquad (5.4)$$

where $\Delta\underline{\mathbf{A}}$ indicates the change of the magnetic potential during a single iteration step. The magnetic tangent stiffness matrix

$$\underline{\underline{\mathbf{K}}}_A = \bigcup_{I=1}^{n_\mathrm{e}} \left[\int_{\Omega_{I_\mathrm{e}}} \underline{\underline{\mathbf{B}}}_A^{\mathrm{T}} \underline{\underline{\mathbf{C}}}_A \underline{\underline{\mathbf{B}}}_A \mathrm{d}V \right] \qquad (5.5)$$

contains only contributions from the magnetic material tangent $\mathbf{C}_A$. After transforming the linear and non-linear magnetic constitutive relations given in section 2.6.3 to the current configuration by applying the transformations (2.68) and (2.69), $\mathbf{C}_A$ can be calculated using the chain rule of differentiation. For linear magnetisation behaviour according to equation

(2.75) the coefficients of $\mathbf{C}_A$ read

$$\frac{\partial H_k}{\partial B_l} = \frac{1}{\mu_0}\delta_{kl} - \frac{1}{J}\chi_B b_{kl} \;. \tag{5.6}$$

For the non-linear case of equation (2.74) the elements of $\mathbf{C}_A$ are given by

$$\frac{\partial H_k}{\partial B_l} = \frac{1}{\mu_0}\delta_{kl} - \frac{M_{\mathrm{s}}}{JB_0}\tanh(\delta B_0)b_{kl} + \frac{M_{\mathrm{s}}}{JB_0^2}\left[\frac{\tanh(\delta B_0)}{B_0} - \frac{\delta}{\cosh^2(\delta B_0)}\right]b_{km}b_{lq}B_m B_q \;. \tag{5.7}$$

Mechanical problem

The weak form of the coupled mechanical subsystem

$$\int_\Omega \delta v_{k,l\mathrm{E}}\sigma_{kl}\,\mathrm{d}V - \int_\Omega \left(\varrho f_k \delta v_k - \delta v_{k,l}\hat{\sigma}_{kl}\right)\mathrm{d}V - \int_{\partial\Omega_p} \hat{p}_k \delta v_k \,\mathrm{d}S = 0 \tag{5.8}$$

is obtained from multiplying the balance of momentum (2.48) by a weight function and integrating over the domain Ω which represents the current configuration of the material body. If the weight function is said to be a virtual velocity field δv_k satisfying $\delta v_k = 0$ on $\partial\Omega_u$, equation (5.8) represents the principal of virtual power. In addition, the split of the total stress tensor according to (2.50) and the boundary condition (2.52) have been used in the derivation.

Discretisation

The approximation and FE discretisation with the matrices of shape functions $\underline{\underline{\mathbf{N}}}_u$ and their partial derivatives included in $\underline{\underline{\mathbf{B}}}_u$ yields a discrete representation

$$\delta\underline{\mathbf{v}}^{\mathrm{T}}\left\{\underbrace{\bigcup_{I=1}^{n_{\mathrm{e}}}\left[\int_{\Omega_{I\mathrm{e}}}\underline{\underline{\mathbf{B}}}_u^T{}_{\mathrm{E}}\boldsymbol{\sigma}\,\mathrm{d}V\right]}_{\underline{\mathbf{f}}^{\mathrm{int}}} - \underbrace{\bigcup_{I=1}^{n_{\mathrm{e}}}\left[\int_{\Omega_{I\mathrm{e}}}\left(\underline{\underline{\mathbf{N}}}_u^T\varrho\underline{\mathbf{f}} - \underline{\underline{\mathbf{B}}}_u^T\hat{\boldsymbol{\sigma}}\right)\mathrm{d}V - \int_{\partial\Omega_{I\mathrm{e}}}\underline{\underline{\mathbf{N}}}_u^T\hat{\underline{\mathbf{p}}}\,\mathrm{d}S\right)}_{-\underline{\mathbf{f}}^{\mathrm{ext}}} - \underline{\mathbf{F}}\right\} = \underline{\mathbf{0}} \tag{5.9}$$

for the weak form (5.8) of the coupled mechanical subsystem. The non-linear discrete system of equations states the equilibrium of internal and external nodal forces

$$\underline{\mathbf{f}}^{\mathrm{int}} - \underline{\mathbf{f}}^{\mathrm{ext}} = \underline{\mathbf{0}} \;. \tag{5.10}$$

Consistency with the weak coupling requires the magnetic contribution to the external load vector to be constant during the iteration of one increment. As no other external forces are present in the demonstration problems of this section, the external force vector is assumed to be constant and can be excluded from the linearisation process.

Linearisation

As the mechanical consitutive model proposed in section 2.6.4 is formulated for the pseudo-mechanical stress tensor ${}_{\mathrm{E}}\boldsymbol{\sigma}$, standard linearisation procedures [10] can be applied to the internal nodal force vector which results in two contributions to the tangent stiffness matrix

$$\left[\underline{\underline{\mathbf{K}}}^{\mathrm{mat}} + \underline{\underline{\mathbf{K}}}^{\mathrm{geo}}\right]\Delta\underline{\mathbf{u}} = \underline{\mathbf{f}}^{\mathrm{ext}} - \underline{\mathbf{f}}^{\mathrm{int}} \;, \tag{5.11}$$

a material part $\underline{\underline{\mathbf{K}}}^{\mathrm{mat}}$ which accounts for the non-linearity of the material behaviour and a geometrical part $\underline{\underline{\mathbf{K}}}^{\mathrm{geo}}$ representing the effects of deformation on the existing stresses. The

material tangent stiffness results from the linearisation of the constitutive equations

$$\underline{\underline{\mathbf{K}}}^{\text{mat}} = \bigcup_{I=1}^{n_{\text{e}}} \left[\int_{\Omega_{I\text{e}}} \underline{\underline{\mathbf{B}}}_u^T \underline{\underline{\mathbf{C}}}_u \underline{\underline{\mathbf{B}}}_u \, \mathrm{d}V \right] \tag{5.12}$$

with $\underline{\underline{\mathbf{C}}}_u$ the material tangent stiffness matrix. For Neo-Hooke material and two-dimensional plane strain problems $\underline{\underline{\mathbf{C}}}_u$ is given by

$$\underline{\underline{\mathbf{C}}}_u = \frac{1}{J} \begin{bmatrix} 2\mu + \lambda & \lambda J^2 & 0 \\ \lambda J^2 & 2\mu + \lambda & 0 \\ 0 & 0 & \mu - \frac{\lambda}{2}\left(J^2 - 1\right) \end{bmatrix} . \tag{5.13}$$

Submatrices of the geometrical tangent stiffness matrix $\underline{\underline{\mathbf{K}}}^{\text{geo}}$ are computed from the relation

$$\underline{\underline{\mathbf{K}}}^{\text{geo}}_{KL} = \bigcup_{I=1}^{n_{\text{e}}} \underline{\underline{\mathbf{I}}} H_{KL}^I \, , \tag{5.14}$$

with the two-by-two identity matrix $\underline{\underline{\mathbf{I}}}$ and the matrix

$$\underline{\underline{\mathbf{H}}}^I = \int_{\Omega_{I\text{e}}} \underline{\underline{\mathbf{B}}}^{\text{geo}^{\mathrm{T}}}{}_{\text{E}} \boldsymbol{\sigma} \, \underline{\underline{\mathbf{B}}}^{\text{geo}} \, \mathrm{d}V \, . \tag{5.15}$$

5.2 Updated Lagrangian XFEM

In this section the derivation of the updated Lagrangian formulation of the mechanical boundary value problem will be reviewed in more detail to point out differences between a standard FEM and XFEM. In addition, the structure of the matrices $\underline{\underline{\mathbf{B}}}_u$ and $\underline{\underline{\mathbf{B}}}^{\text{geo}}$ will become apparent from this derivation.

Introduction

5.2.1 Comparison of Updated Lagrangian FEM and XFEM

For brevity of the notation and without a loss of generality, a purely mechanical BVP will be considered in the following

Isoparametric
approximation

$$\int_{\Omega} \delta v_{i,j} \sigma_{ij} \, \mathrm{d}V - \int_{\Omega} \rho f_i \delta v_i \, \mathrm{d}V - \int_{\partial\Omega} p_i \delta v_i \, \mathrm{d}S = 0 \, . \tag{5.16}$$

In a standard isoparametric element formulation, the geometry $\mathbf{x}$ and the velocity fields $\mathbf{v}$, $\delta\mathbf{v}$

$$\mathbf{x}^h\left(\boldsymbol{\xi}, t\right) = N_I(\boldsymbol{\xi})\underline{\mathbf{x}}_I(t) \tag{5.17}$$

$$\mathbf{v}^h(\boldsymbol{\xi}, t) = N_I(\boldsymbol{\xi})\underline{\mathbf{v}}_I(t) \tag{5.18}$$

are approximated by shape functions $N_I(\boldsymbol{\xi})$ of the natural element coordinates $\boldsymbol{\xi}$.

The spatial velocity gradient which appears in the principal of virtual power (5.16) is expressed by

$$v_{i,j}^h = \frac{\partial v_i^h}{\partial x_j^h} = \frac{\partial v_i^h}{\partial \xi_k} \frac{\partial \xi_k}{\partial x_j^h} \, . \tag{5.19}$$

As in the case of small deformations, the partial derivatives of the natural coordinates $\boldsymbol{\xi}$ with respect to $\mathbf{x}$ can be computed from the geometrical map (5.18) which involves the Jacobian

$$F_{ij}^{\xi}(\boldsymbol{\xi}, t) = \frac{\partial x_i^h(\boldsymbol{\xi}, t)}{\partial \xi_j} = \frac{\partial N_I(\boldsymbol{\xi})}{\partial \xi_j} x_{iI}(t) \tag{5.20}$$

that depends on the current deformation state. The symbol $\mathbf{F}_\xi$ in the above equations indicates that the Jacobian can be interpreted as deformation gradient with respect to the natural element coordinates. Its determinant

$$J_\xi = \det(\mathbf{F}_\xi) \tag{5.21}$$

relates the spatial volume element $\mathrm{d}V = J_\xi \mathrm{d}V_\xi$ to an infinitesimal volume $\mathrm{d}V_\xi$ in the numerical domain.

Internal load vector

Applying the approximations defined above to discretise the weak form (5.16) yields

$$\delta v_{iI} \left[\underbrace{\int\limits_\Omega \frac{\partial N_I}{\partial x_j} \sigma_{ij} \, \mathrm{d}V}_{f_{iI}^{\text{int}}} \underbrace{- \int\limits_\Omega N_I \rho f_i \, \mathrm{d}V - \int\limits_{\partial\Omega} N_I p_i \, \mathrm{d}S}_{-f_{iI}^{\text{ext}}} \right] = 0 \tag{5.22}$$

with f_{iI}^{int} being an index notation of the nodal vector of internal forces

$$f_{iI}^{\text{int}} = \int\limits_\Omega \frac{\partial N_I}{\partial x_j} \sigma_{ij} \, \mathrm{d}V = \int\limits_\Omega \frac{\partial N_I}{\partial \xi_k} F_{kj}^{\xi \, -1} \sigma_{ij} \, \mathrm{d}V \, . \tag{5.23}$$

Matrix $\underline{\underline{\mathbf{B}}}_u$

In order to recover the vector-matrix expression of the nodal force vector in equation (5.9)

$$\underline{\mathbf{f}}^{\text{int}} = \int\limits_\Omega \underline{\underline{\mathbf{B}}}_u^T \underline{\sigma} \, \mathrm{d}V \tag{5.24}$$

which involves the matrix $\underline{\underline{\mathbf{B}}}_u$, the symmetry of the Cauchy stress tensor which also holds for the pseudo-mechanical stress tensor is exploited. Then the virtual stress power

$$\delta v_{i,j} \sigma_{ij} = \delta L_{ij} \sigma_{ij} = (\delta D_{ij} + \delta W_{ij}) \sigma_{ij} = \delta D_{ij} \sigma_{ij} \tag{5.25}$$

can be rewritten in terms of the deformation rate $\mathbf{D}$. According to equation (2.16), $\mathbf{D}$ is the symmetric part of the velocity gradient $v_{k,l}$. Due to the similarity of equation (2.16) to the infinitesimal strain-displacement relation (2.15) between $\boldsymbol{\varepsilon}$ and the displacement vector $\mathbf{u}$, the matrix $\underline{\underline{\mathbf{B}}}_u$ will be the same for the small deformation and updated Lagrangian formulation. However, as a consequence of the continuous configurational update it is now a function of the displacement field.

Matrix $\underline{\underline{\mathbf{B}}}^{\text{geo}}$

Due to the deformation dependence of $\underline{\underline{\mathbf{B}}}_u$, a linearisation of the internal load vector with respect to the displacement field will involve two contributions $\underline{\underline{\mathbf{K}}}^{\text{mat}}$ and $\underline{\underline{\mathbf{K}}}^{\text{geo}}$ as outlined in

the previous section. The first part accounts for the non-linearity of the constitutive relation while the second part results from the linearisation of $\underline{\underline{\mathbf{B}}}_u$ and yields the geometric stiffness which represents the effect of deformation on the existing stresses. All entries in the matrices $\underline{\underline{\mathbf{B}}}_u$ and $\underline{\underline{\mathbf{B}}}^{\text{geo}}$ are partial derivatives of the shape functions $\frac{\partial N_I}{x_j}$ with respect to the spatial coordinates [10] and will therefore involve the Jacobian $\mathbf{F}_\xi$ of the geometric map.

With the results of the previous derivation and knowledge on the structure of $\underline{\underline{\mathbf{B}}}_u$ and $\underline{\underline{\mathbf{B}}}^{\text{geo}}$ it is possible to identify the effect of the enriched XFEM approximation and to point out differences to a conventional updated Lagrangian FEM. As in the case of small deformations, enriching the displacement and velocity fields

Updated Lagrangian FEM vs. XFEM

$$\mathbf{u}^{h,\text{XFEM}}(\boldsymbol{\xi},t) = N_I(\boldsymbol{\xi})\underline{\mathbf{u}}_I(t) + N_I(\boldsymbol{\xi})F(\boldsymbol{\xi})\underline{\mathbf{u}}_I^*(t) = \underline{\underline{\mathbf{N}}}^*\underline{\mathbf{u}}^* \tag{5.26}$$

$$\mathbf{v}^{h,\text{XFEM}}(\boldsymbol{\xi},t) = N_I(\boldsymbol{\xi})\underline{\mathbf{v}}_I(t) + N_I(\boldsymbol{\xi})F(\boldsymbol{\xi})\underline{\mathbf{v}}_I^*(t) = \underline{\underline{\mathbf{N}}}^*\underline{\mathbf{v}}^* \tag{5.27}$$

will introduce derivatives $\frac{\partial \underline{\underline{\mathbf{N}}}^*}{x_j}$ in $\underline{\underline{\mathbf{B}}}_u^*$ and $\underline{\underline{\mathbf{B}}}^{*\text{geo}}$. While the geometric map of a small strain formulation did not involve the additional degrees of freedom, updating the geometry now yields an enriched geometry approximation

$$\begin{aligned}\mathbf{x}^{h,\text{XFEM}}(\boldsymbol{\xi},t) &= \mathbf{X}(\boldsymbol{\xi}) + \mathbf{u}^h(\boldsymbol{\xi},t) \\ &= \mathbf{X}(\boldsymbol{\xi}) + N_I(\boldsymbol{\xi})\underline{\mathbf{u}}_I(t) + N_I(\boldsymbol{\xi})F(\boldsymbol{\xi})\underline{\mathbf{u}}_I^*(t) \\ &= \mathbf{x}^h(\boldsymbol{\xi},t) + N_I(\boldsymbol{\xi})F(\boldsymbol{\xi})\underline{\mathbf{u}}_I^*(t)\end{aligned} \tag{5.28}\tag{5.29}$$

which has to be considered during the evaluation of the Jacobian

$$F_{ij}^{\xi,\text{XFEM}}(\boldsymbol{\xi},t) = F_{ij}^{\xi}(\boldsymbol{\xi},t) + \frac{\partial\left(N_I(\boldsymbol{\xi})F(\boldsymbol{\xi})\right)}{\partial\xi_j}u_{iI}^*(t) \tag{5.30}$$

and its determinant $J_\xi^{\text{XFEM}} = \det\left(F_{ij}^{\xi,\text{XFEM}}\right)$. Compared to the updated Lagrangian FEM, XFEM requires minor changes to the code structure which result from the influence of the additional degrees of freedom on the Jacobian of the isoparametric map and its determinant.

5.2.2 Verification – Large Deformation Homogenisation

As there are no analytical solutions available for large deformation problems, e.g. the displacement or stress fields of an inclusion problem, the verification of XFEM will be carried out in terms of the effective response of a particle reinforced elastomer. Recently, Lopez-Pamies et al. [133, 134, 135] have used an iterative homogenisation procedure to derive analytical estimates for the effective response of a Neo-Hookean rubber reinforced by an isotropic, polydisperse distribution of rigid particles. Essentially they predict that the macroscopic behaviour of the composite will be exactly the same as the pure matrix except for a concentration dependent amplification factor. This relation has already been applied to the small deformation case considered in the previous chapter. For large deformations, the macroscopic free energy $\bar{\psi}$ for an effective deformation state defined by the macroscopic stretches $\bar{\lambda}_i$ is related to the free energy ψ of the elastomer by

Analytical results

$$\bar{\psi}\left(\bar{\lambda}_i,c\right) = \frac{1}{(1-c)^2}\psi\left(\bar{\lambda}_i\right) \tag{5.31}$$

with c the concentration of the particles.
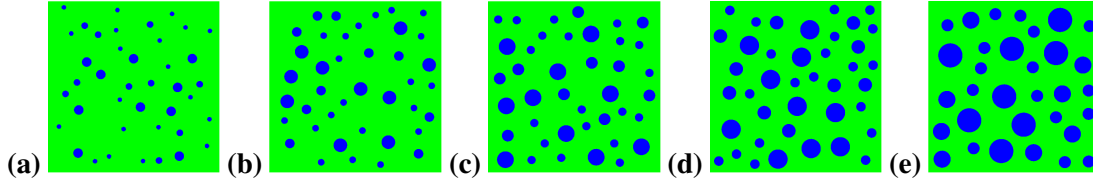
Figure 5.1: Two-dimensional RVE with random, isotropic, polydisperse particle distributions with different concentrations **(a)**–**(e)** of 5, 10, 15, 20, and 25 %.

As the analytical predictions are in excellent agreement with numerical results of Moraleda et al. [146], the effective response according to equation (5.31) will serve as a reference solution. In the following, the XFEM modelling approach outlined in the previous sections will be combined with numerical homogenisation procedures suitable for large deformations in order to compute the effective response of the reinforced elastomer. The results in terms of macroscopic stress-strain curves obtained for different concentrations of particles will be compared with the analytical predictions.

Problem description

Numerical simulations are carried out for the pure matrix material and five different particle concentrations of $\underline{c} = \{0.5, 0.10, 0.15, 0.20, 0.25\}$. The unit square RVE domain is discretised by a regular mesh of quadratic elements. Random, isotropic and polydisperse particle distributions in the RVE as illustrated in Fig. 5.1 are generated by the random sequential adsortion algorithm [210] explained in Section 4.3. Particles of three different radii $\underline{r} = R_1 \left\{ 1 \quad \frac{1}{\sqrt{2}} \quad \frac{1}{2} \right\}$ are sequentially added. The number of particles of each size are chosen such that the largest particles amount to 50% of the total volume fraction while the remainder is equally split into the medium and small size particles. Both, matrix and particles are modelled by a compressible Neo-Hooke model defined by the free energy according to equations (2.82), (2.89), and (2.92), see Section 2.6.4 for details. The particles are charaterised by an elastic modulus of $E^- = 10\,\text{GPa}$ and a Poisson ratio $\nu^- = 0.3$ while $E^+ = 1\,\text{GPa}$ and $\nu^+ = 0.45$ hold for the matrix material.

Numerical homogenisation

The macroscopic response for each RVE is computed using a large deformation homogenisation scheme as outlined in [121]. In this case the macro-homogeneity condition, cf. Chapter 4,

$$\bar{P}_{Ji}\delta\bar{F}_{iJ} = \langle P_{Ji}\rangle_0\langle\delta F_{iJ}\rangle_0 = \langle P_{Ji}\delta F_{iJ}\rangle_0, \quad \langle(\cdot)\rangle_0 = \frac{1}{|V_0|}\int_{\Omega_0}(\cdot)\mathrm{d}V_0 \quad (5.32)$$

is stated in terms of the first Piola-Kirchhoff stress tensor **P** and the deformation gradient **F** with $\langle(\cdot)\rangle_0$ indicating volume averages over the reference configuration. Similar to the small deformation case, a macroscopic deformation state $\bar{\mathbf{F}}$ is assigned to the RVE using periodic displacement boundary conditions

$$u_i = \bar{F}_{iJ}X_J + \tilde{u}_i \quad (5.33)$$

while the stresses are directly available from the reaction forces at the master nodes used to control the deformation state. Two different macroscopic deformation modes, uniaxial tension and compression, i.e. $\bar{F}_{11} = \bar{\lambda}_1$, $\bar{F}_{22} = \bar{\lambda}_2$, and $\bar{F}_{iJ} = 0$ otherwise, are considered under the assumption of plane strain $\bar{\lambda}_3 = 0$.
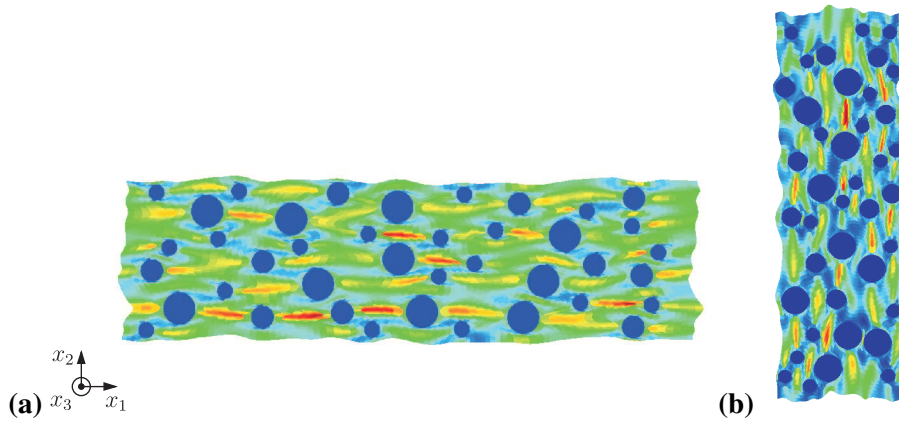
Figure 5.2: Two deformation modes of one realisation of a random, isotropic, polydisperse particle distribution ($c = 0.2$): **(a)** uniaxial tension (colors show F_{11}), and **(b)** uniaxial compression (colors show F_{22}) in the x_1 direction.

The effective stress response in terms of the Cauchy stress

$$\bar{\sigma}_{ij} = \bar{J}^{-1}\bar{F}_{iK}\bar{P}_{Kj} \neq \langle \sigma_{ij} \rangle = \frac{1}{|V|}\int_{\Omega} \sigma_{ij}\mathrm{d}V \tag{5.34}$$

is computed from the macroscopic Piola-Kirchhoff stress using the transformation (2.28). It is noted that this value is generally not equal to the average $\langle \sigma_{ij} \rangle$ of the Cauchy stress over the current RVE configuration.

The simulation of the local deformation behaviour in the generated RVE as illustrated in Fig. 5.2 allows for the computation of effective stress-strain curves. These numerical results are compared with the analytical estimates obtained from the iterative homogenisation procedure according to equation (5.31). For the considered uniaxial macroscopic stress states the principal directions coincide with the Cartesian coordinates and the effective analytical stress response

$$\begin{aligned}\bar{\sigma}_{11} = \bar{\sigma}_1 &= \frac{1}{\bar{\lambda}_1}\frac{\partial\bar{\psi}(\bar{\lambda}_i)}{\partial\bar{\lambda}_1} \\ &= \frac{1}{(1-c)^2}\frac{1}{\bar{\lambda}_1}\frac{\partial\psi(\bar{\lambda}_i)}{\partial\bar{\lambda}_1} \\ &= \frac{1}{(1-c)^2}\left[\mu\left(\bar{\lambda}_1 - 1\right) + \frac{\Lambda}{2}\left(\bar{\lambda}_1^2\bar{\lambda}_2^2 - 1\right)\right]\end{aligned} \tag{5.35}$$

is obtained from combining equations (2.88) and (5.31). The principal stretch

$$\bar{\lambda}_2 = \left[\frac{\mu + \frac{\Lambda}{2}}{\mu + \frac{\Lambda}{2}\bar{\lambda}_1^2}\right]^{\frac{1}{2}} \tag{5.36}$$

in the lateral direction follows from the condition of a uniaxial stress state $\bar{\sigma}_2 = 0$.

Both, analytical and numerical stress-strain curves, are compared in Fig. 5.3 for uniaxial tension and compression. The numerical results represent averages of five different random
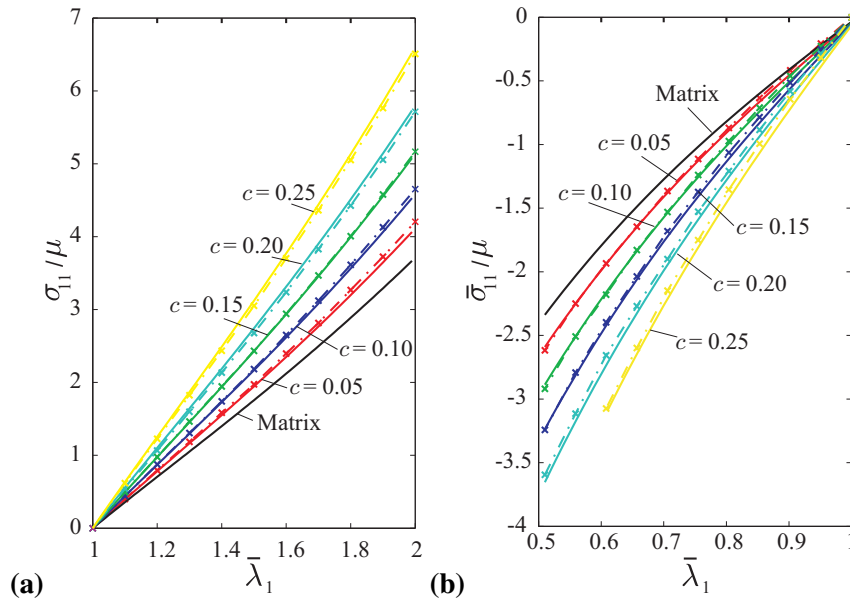
<div style="text-align: right">Results</div>

Figure 5.3: Comparison of analytical (solid lines) and numerical results (dash-dotted lines with symbols) for the effective response of Neo-Hookean rubber reinforced by random, isotropic, polydisperse particle distributions: **(a)** uniaxial tension, and **(b)** uniaxial compression.

realisation of the same particle volume fraction. However, no significant deviations between the individual random distributions have been recognised which indicates an adequate choice of the RVE. In Fig. 5.3 a very good agreement of the numerical and analytic predictions can be concluded which verifies the implementation of the homogenisation procedure as well as the updated Lagrangian XFEM formulation. The XFEM scheme will subsequently be applied to the simulation of magneto-mechanical problems.

5.3 Large Deformation Magneto-Mechanical Problems

Introduction

In the following section, the proposed modelling strategy is applied to two heterogeneous microstructural arrangements which are schematically depicted in Fig. 5.4. A comparison of selected results with the small deformation model utilised in Chapter 4 allows for an evaluation of the influence of configurational changes on the magneto-mechanical coupling for both, magnetically linear and non-linear material behaviour.

5.3.1 Two Interacting Circular Inclusions

Problem description

Motivated by chain-like particle structures observed in oriented MRE, the interaction between two circular inclusions is investigated. The domain of interest illustrated in Fig. 5.4 (a) has a size of $20\,\mu\mathrm{m}\times10\,\mu\mathrm{m}$. Both embedded circular inclusions have a radius of $2.49\,\mu\mathrm{m}$ and an initial distance of $10\,\mu\mathrm{m}$. The mechanical deformation behaviour of both constituents is assumed to be Neo-Hookean as outlined in Section 2.6.4. However, due their high stiffness the inclusions are essentially rigid compared to the soft polymer matrix. The magnetisation behaviour of the particles is modelled by the modified Ising relation (2.74) and the response is compared to a saturation free model (2.75) resulting from the linearisation of the Ising relation. The inclusions are characterised by the mechanical parameters $E^- = 210\,\mathrm{GPa}$,
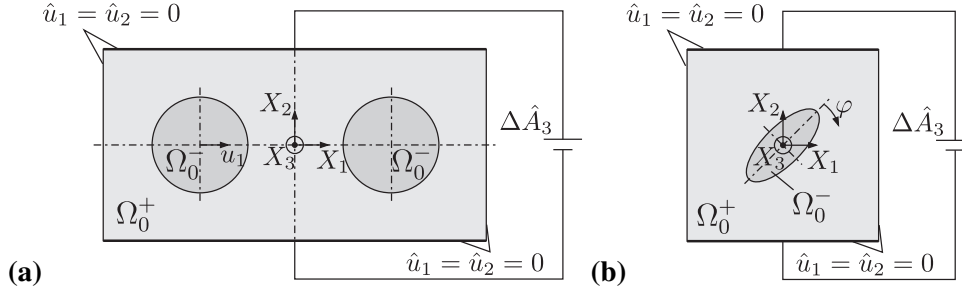
Figure 5.4: Demonstration problems for the comparison of the small and large deformation magneto-mechanical response: **(a)** two interacting circular inclusions, and **(b)** reorientation of an elliptic inclusion. The displacements of the boundary are set to zero and a vector potential varying linearly between the lower and upper boundary is applied.
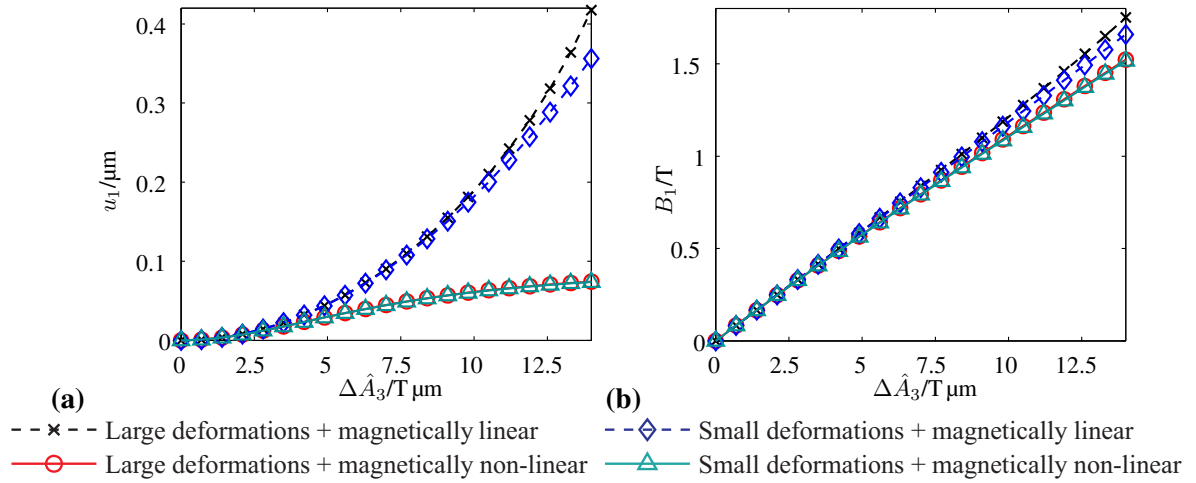
Figure 5.5: Numerical simulation results for two interacting inclusions: **(a)** horizontal displacement of the left particle's center, and **(b)** magnetic induction B_1 at the point $X_1 = X_2 = 0$

$\nu^- = 0.3$ while $M_s^- = 868\,\mathrm{kA\,m}^{-1}$, $\delta^- = 0.883\,\mathrm{T}^{-1}$ and $\chi_B^- = 767\,\mathrm{kA\,m}^{-1}\,\mathrm{T}^{-1}$ are used for the magnetically non-linear and linear case, respectively. The parameters $E^+ = 75\,\mathrm{kPa}$, $\nu^+ = 0.4$ and $\chi_B^+ = 0$ are assigned to the soft, non-magnetisable matrix material. On the boundary $\partial\Omega$ the displacement is fixed and a linear vector potential results in an effective magnetic field pointing into the X_1-direction. The difference of $\Delta\hat{A}_3 = \Delta\hat{A}$ between the upper and lower boundary defines the macroscopic magnetic field. Motivated by the range of experimental magnetisation data available for the non-linear material model, a value of $\Delta\hat{A} = 14\,\mathrm{T\,\mu m}$ has been chosen.

Being located close to each other, the inclusions become magnetised inhomogeneously. As a consequence, resultant forces act on each particle which cause their mutual attraction. Fig. 5.5 (a) shows the computed displacement u_1 of the center of the left inclusion as a function of the external magnetic field $\Delta\hat{A}$. There is a significant difference between the curves of the magnetically linear and non-linear behaviour. This material non-linearity, caused by magnetic saturation effects, limits the attractive forces and consequently the displacements of the inclusions. In the magnetically linear case the large deformation model yields larger

Results

deformations because the attractive forces are inversely proportional to the distance of the particles. This change of configuration is not incorporated in the small deformation model. However, in the magnetically non-linear case the large and small deformation model predict virtually the same displacement as the magnetic saturation limits the displacements of the particles. An impact of the different models on the magnetic field variables is analysed in terms of the magnetic induction B_1 of the point $X_1 = X_2 = 0$ and shown in Fig. 5.5 (b). Again, the influence of the saturation is obvious. If the particles approach each other, the field lines between them are more concentrated which is an effect of the present configuration dependence.

5.3.2 Reorientation of an Elliptic Inclusion

Problem
description

Beside the geometric arrangement, another important aspect of real particulate microstructures is the shape of the individual particles. To this end, the behaviour of an elliptic inclusion embedded in a soft matrix and subjected to an external magnetic field which is not aligned with the major axis of the ellipse [74, 189] is analysed below, Fig. 5.4 (b). The square analysis domain has an edge length of $2\,\mu\mathrm{m}$ while the major and minor axes of the ellipse are given by $1\,\mu\mathrm{m}$ and $0.4\,\mu\mathrm{m}$, respectively. In accordance to the previous example of section 5.3.1, the parameters $E^- = 210\,\mathrm{GPa}$, $\nu^- = 0.3$, $M_\mathrm{s}^- = 868\,\mathrm{kA\,m^{-1}}$ and $\delta^- = 0.883\,\mathrm{T^{-1}}$ or $\chi_B^- = 767\,\mathrm{kA\,m^{-1}\,T^{-1}}$ characterise the material of the inclusion. $E^+ = 1\,\mathrm{MPa}$, $\nu^+ = 0.4$ and $\chi_B^+ = 0$ are assigned to the non-magnetisable matrix. The elastic modulus of the elastic matrix was chosen to be almost two orders of magnitude larger than in the previous section to limit the deformations, because the magneto-mechanical coupling effects of the reorientation problem are significantly higher than for the previous example. Again, the boundary displacements are set to zero and a linear vector potential with a difference of $\Delta\hat{A} = 2.5\,\mathrm{T\,\mu m}$ is prescribed on the boundary.

Results

As the externally applied magnetic field is not parallel to the effective field inside the inclusion, a resultant torque occurs which tends to align the ellipse with the external magnetic field. This results in a clockwise rotation of the inclusion. The magnetic torque is equilibrated by mechanical stresses in the surrounding matrix material. The rotation of the inclusion is presented in Fig. 5.6 (a) in terms of the angle φ defined in Fig. 5.4 (b). Interestingly and different from the first example, the small deformation model predicts larger rotations than the finite deformation model for the magnetically linear cases. This is due to the proportionality of the magnetic torque to the angle between the external magnetic field and the major axis which decreases with increasing φ. In the small deformation model all calculations are performed with respect to the undeformed reference configuration. Hence, it does not account for the reduction of the torque with the rotation of the inclusion. As in the previous example, the magnetically linear behaviour results in a significant overestimation of the deformation due to the lack of saturation. Fig. 5.6 (b) shows the dependence of the magnetic induction B_1 at the point $X_1 = X_2 = 0$ on the magnetic field. The magnetisation in the X_1-direction inside the inclusion increases with the alignment and reaches a theoretical maximum at $\varphi = 45°$. However, this state is not achieved for the applied magnetic loads.

5.4 Conclusion

Large
deformations

The large deformation finite element formulation proposed in this section accounts for the influence of configurational changes on the magnetic field. It facilitates the modelling of
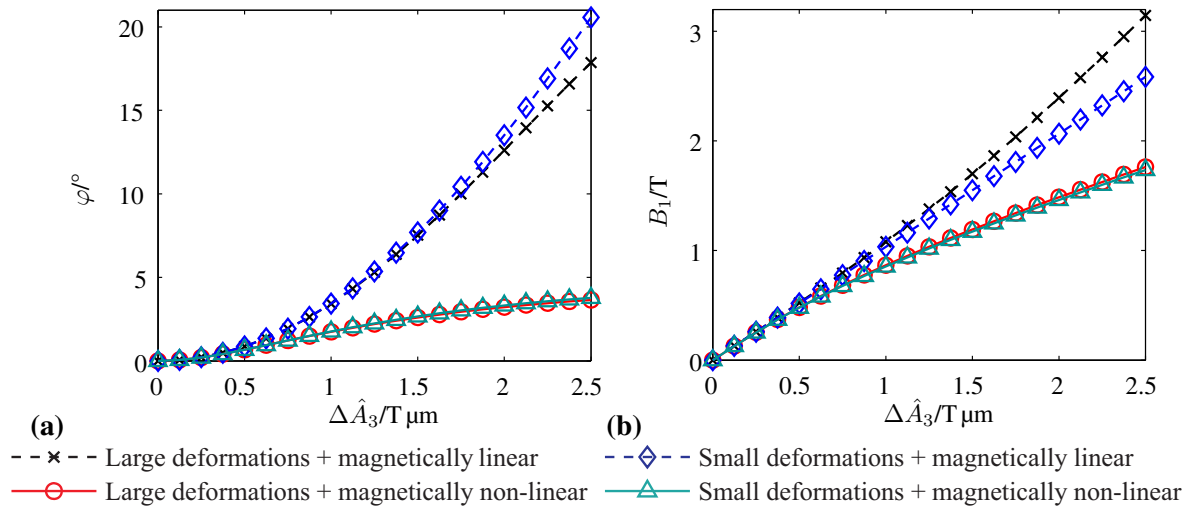
Figure 5.6: Numerical results for the reorientation of an elliptic inclusion: **(a)** rotation angle of major axis, and **(b)** magnetic induction B_1 at the point $X_1 = X_2 = 0$.

a two-side magneto-mechanical coupling. The used staggered solution scheme was appropriate for the demonstration problems considered. Recently, a monolithic approach which uses a consistent linearisation of both problems to avoid numerical stability issues for more complex settings has been implemented. With the generalisation of XFEM to the large deformation case, the procedures for interface representation developed in Chapter 3 can be applied to analyse more realistic microstructural models in the future.

The presented results show that there is no significant difference between the small and the large deformation model in particular for a realistic non-linear magnetisation behaviour. However, in many loading situations MRE can undergo finite strains, e.g. induced by mechanical loadings which cause significant changes to the internal structure. Taking into account these microstructural changes during the solution of the coupled magneto-mechanical field problem will require the application of the large deformation procedures developed in this section.

<div style="text-align: right">Small vs. large deformations</div>

Part III

Isogeometric Modelling

6 Isogeometric Analysis

The development of the second major discretisation technique considered in this work – the Isogeometric Analysis (IGA) – was motivated by the fact that the conversion of a geometrical model into a numerical one, i.e. the generation of a suitable finite element mesh, has been a tedious and sometimes cumbersome task which can be hardly automated. The disjunction between the Computer Aided Design (CAD) geometry, commonly described by Non-Uniform Rational B-Splines (NURBS), and a finite element model, based on Lagrangian polynomial approximations of the geometry and the field variables, can be overcome using the idea of IGA. In this concept, which was pioneered by Hughes et al. [99], the same functions which represent the geometry of the CAD model are used to approximate the field variables in the numerical model. As a consequence, the geometric discretisation errors that result from the approximation of the CAD geometry by Lagrangian polynomials are eliminated – the geometry used in the analysis is exactly the one defined by CAD.

6.1 Fundamentals

The essential difference between a standard and an isogeometric finite element formulation results from replacing the Lagrangian polynomial basis by spline-based approximations. B-splines and NURBS possess several features which make them attractive for analysis. According to [6] they can be summarised as:

(i) The basis functions are non-negative and form a partition-of-unity.

(ii) The support of each basis function is local.

(iii) Many relevant geometries for engineering applications can be represented exactly.

(iv) Besides standard h- and p-refinement techniques, k-refinement allows for a systematic control of the continuity properties.

However, spline-based approximations will generally be non-interpolatory, i.e. discrete control values which are an equivalent to nodal values in a standard FEM do not represent the value of the approximated field variable at its geometric location. That is way projections are required, e.g. for the application of boundary or initial conditions.

This chapter will briefly outline B-splines, NURBS, and the concept Bézier extraction introduced by Borden et al. [17] which is a unified approach to the implementation of spline-based approximations into any existing finite element framework. This short review essentially follows [17]. More details with similar notation can be found, e.g., in [17, 183, 192]. For a comprehensive review please refer to the NURBS book of Piegl and Tiller [167] as well as the textbook on IGA [41]. In the remainder of this chapter, an isogeometric finite element formulation is developed for the coupled magneto-mechanical field problem. A convergence study based on an analytic solution presented in Section 2.7 provides the basis for a comparison of XFEM and IGA in terms of errors and convergence rates.

6.1.1 Basis Functions

Bézier curves Below, all univariate functions will be introduced with respect to a dimensionless parameter coordinate ξ. Since the procedure of Bézier extraction involves Bézier curves, the review will start from there. A Bézier curve of degree p

$$\mathbf{C}(\xi) = \sum_{I=1}^{p+1} B_{I,p}(\xi)\underline{\mathbf{P}}_I \tag{6.1}$$

is defined by the linear combination of $I = 1 \ldots p + 1$ univariate Bernstein polynomials $B_{I,p}(\xi)$ of order p and the control point vectors $\underline{\mathbf{P}}_I$ according to the spatial dimension d of the problem. A corresponding vector-matrix notation is obtained from defining a vector of Bernstein basis functions $\underline{\mathbf{B}} = \{B_{I,p}\}_{I=1}^{p+1}$ and a matrix $\underline{\underline{\mathbf{P}}} = \{\underline{\mathbf{P}}_I\}_{I=1}^{p+1}$ of control points of size $[p+1 \times d]$

$$\mathbf{C}(\xi) = \underline{\underline{\mathbf{P}}}^T \underline{\mathbf{B}}(\xi). \tag{6.2}$$

For $\xi \in [-1, 1]$ the Bernstein basis functions are computed recursively from

$$B_{I,p}(\xi) = \frac{1}{2}\left[(1 - \xi)\, B_{I,p-1}(\xi) + (1 + \xi)\, B_{I-1,p-1}(\xi)\right] \tag{6.3}$$

$$B_{1,0} \equiv 1$$

$$B_{I,p} = 0 \quad \text{if} \quad I < 1 \ \vee \ I > p + 1.$$

Similar equations can be obtained for the computation of the first- and second-order derivatives

$$\frac{dB_{I,p}}{d\xi}(\xi) = \frac{1}{2}p\left(B_{I-1,p-1}(\xi) - B_{I,p-1}(\xi)\right) \tag{6.4}$$

$$\frac{d^2 B_{I,p}}{d\xi^2}(\xi) = \frac{1}{2}p\,(p-1)\left[\frac{1}{2}\left(B_{I,p-2}(\xi) + B_{I-2,p-2}(\xi)\right) - B_{I-1,p-2}(\xi)\right]. \tag{6.5}$$

B-spline curves A B-spline curve

$$\mathbf{C}(\xi) = \sum_{I=1}^{n} N_{I,p}(\xi)\underline{\mathbf{P}}_I = \underline{\underline{\mathbf{P}}}^T \underline{\mathbf{N}}(\xi) \tag{6.6}$$

is given by the univariate B-spline basis functions $\underline{\mathbf{N}} = \{N_{I,p}(\xi)\}_{I=1}^{n}$ of order p and a set of n control points $\underline{\mathbf{P}} = \{\underline{\mathbf{P}}_I\}_{I=1}^{n}$, Fig. 6.1. The basis functions are defined by a knot vector $\underline{\mathbf{\Xi}} = \{\xi_I\}_{I=1}^{m}$ which contains $I = 1 \ldots m$ non-decreasing coordinates $\xi_I, \xi \geq 0$. From the m elements of the knot vector a set of $n = m - p - 1$ B-spline basis functions can be computed according to the Cox-de Boor recursion formula

$$N_{I,p}(\xi) = \frac{\xi - \xi_I}{\xi_{I+p} - \xi_I} N_{I,p-1}(\xi) + \frac{\xi_{I+p+1} - \xi}{\xi_{I+p+1} - \xi_{I+1}} N_{I+1,p-1}(\xi) \quad \text{for} \quad p \geq 1 \tag{6.7}$$

$$N_{I,0}(\xi) = \begin{cases} 1 & \text{if } \xi_I \leq \xi < \xi_{I+1} \\ 0 & \text{otherwise} \end{cases} \quad \text{for} \quad p = 0\,.$$

As an example, a second-order B-Spline curve and the corresponding B-spline basis functions are plotted in Fig. 6.1. The curve is defined by a set of $n = 8$ control points illustrated
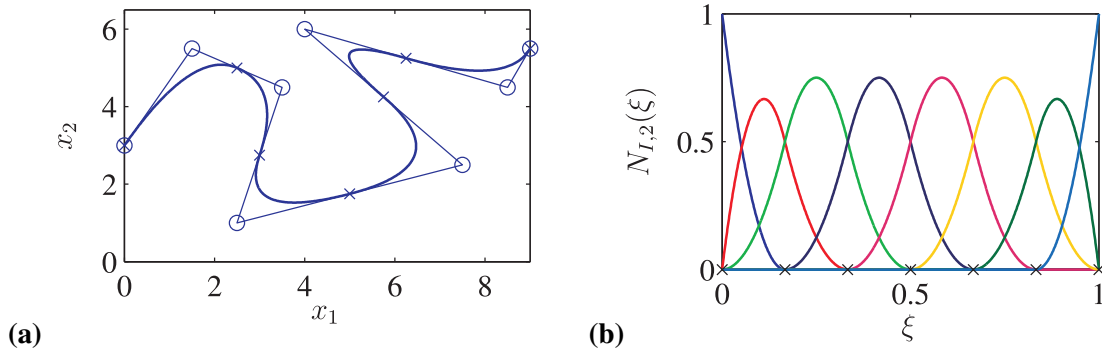
Figure 6.1: B-spline curve defined by a set of control points $\{\underline{\mathbf{P}}_I\}_{I=1}^{8}$ (symbol $\circ$), and the knot vector $\underline{\boldsymbol{\Xi}} = [0\ 0\ 0\ \frac{1}{6}\ \frac{1}{3}\ \frac{1}{2}\ \frac{2}{3}\ \frac{5}{6}\ 1\ 1\ 1]^T$ (symbol $\times$): **(a)** Plot of the curve and the associated control points in the physical x_1-x_2 domain, and **(b)** B-spline basis functions $N_{I,2}(\xi)$ in the parameter domain.

by circles in Fig. 6.1 (a) and a corresponding knot vector $\underline{\boldsymbol{\Xi}} = [0\ 0\ 0\ \frac{1}{6}\ \frac{1}{3}\ \frac{1}{2}\ \frac{2}{3}\ \frac{5}{6}\ 1\ 1\ 1]^T$ of length $m = n + p + 1 = 11$. The basis functions for the given knot vector $\underline{\boldsymbol{\Xi}}$ are non-interpolatory in the interior but interpolatory at both ends because the first and last knot are repeated $k = p + 1 = 3$ times. B-spline curves are generally C^{p-k} continuous at a knot. Therefore, the curve illustrated in Fig. 6.1 is C^{-1} continuous at the ends and C^1 continuous in the interior domain.

Since B-spline basis functions consist of polynomial functions, shapes like circles and ellipses cannot be modelled exactly. This can be achieved by geometric representations based on NURBS curves and surfaces. They are therefore commonly used in CAD and IGA has been strongly linked to NURBS. A NURBS curve of order p NURBS

$$\mathbf{C}(\xi) = \sum_{I=1}^{n} R_{I,p}(\xi)\underline{\mathbf{P}}_I = \underline{\underline{\mathbf{P}}}^T \underline{\mathbf{R}}(\xi) \tag{6.8}$$

is defined by a set of univariate NURBS basis functions $\underline{\mathbf{R}}(\xi) = \{R_{I,p}(\xi)\}_{I=1}^{n}$ which are weighted (weights w_I) rational B-spline basis functions of the same order p

$$R_{I,p}(\xi) = \frac{N_{I,p}(\xi)w_I}{\sum\limits_{J=1}^{n} N_{J,p}(\xi)w_J}. \tag{6.9}$$

In order to apply Bézier extraction to both, B-splines and NURBS, equation (6.9) can be recast into the vector-matrix representation

$$\underline{\mathbf{R}}(\xi) = \frac{1}{\underline{\mathbf{w}}^T\underline{\mathbf{N}}(\xi)}\underline{\underline{\mathbf{W}}}\,\underline{\mathbf{N}}(\xi) \tag{6.10}$$

with $\underline{\mathbf{w}} = \{w_I\}_{I=1}^{n}$ and $\underline{\underline{\mathbf{W}}} = \text{diag}\{w_I\}_{I=1}^{n}$.

In the same fashion B-spline and NURBS surfaces Surfaces

$$\mathbf{S}(\boldsymbol{\xi}) = \sum_{I=1}^{n}\sum_{J=1}^{m} N_{IJ}^{p_1,p_2}(\boldsymbol{\xi})\underline{\mathbf{P}}_{IJ} \quad,\quad \mathbf{S}(\boldsymbol{\xi}) = \sum_{I=1}^{n}\sum_{J=1}^{m} R_{IJ}^{p_1,p_2}(\boldsymbol{\xi})\underline{\mathbf{P}}_{IJ} \tag{6.11}$$
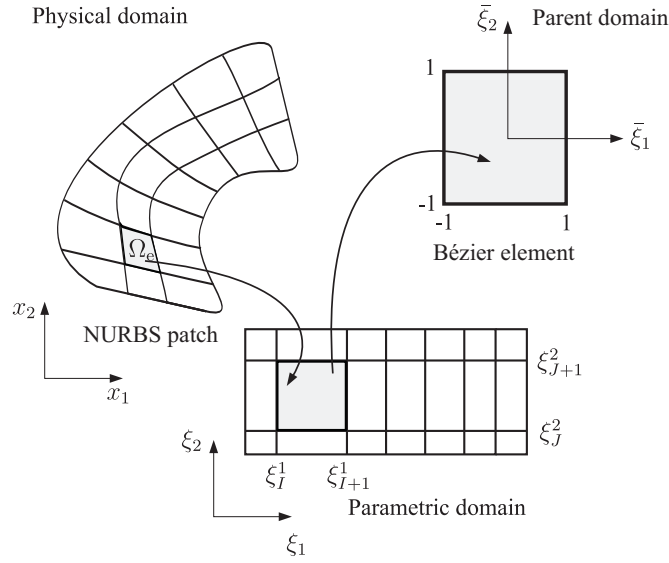
Figure 6.2: Bézier extraction: NURBS patch in the physical domain, knots in the parametric domain, Bézier element in the parent domain, and three sets of associated Cartesian coordinates.

are defined by a mesh of control points $\underline{\mathbf{P}}_{IJ}$ and bivariate B-spline $N_{I,J}^{p_1,p_2}(\boldsymbol{\xi})$ or NURBS basis functions $R_{IJ}^{p_1,p_2}(\boldsymbol{\xi})$, respectively. The bivariate basis functions are tensor products of the associated univariate basis functions of order p_1 and p_2

$$N_{IJ}^{p_1,p_2}(\boldsymbol{\xi}) = N_{I,p_1}(\xi_1)N_{J,p_2}(\xi_2) \tag{6.12}$$

$$R_{IJ}^{p_1,p_2}(\boldsymbol{\xi}) = \frac{N_{I,p_1}(\xi_1)M_{J,p_2}(\xi_2)w_{I,J}}{\displaystyle\sum_{K=1}^{n}\sum_{L=1}^{m} N_{K,p_1}(\xi_1)M_{L,p_2}(\xi_2)w_{K,L}} \tag{6.13}$$

corresponding to the knot vectors $\underline{\Xi}_1 = \{\xi_1^1, \xi_2^1, \ldots, \xi_{n+p_1+1}^1\}$ and $\underline{\Xi}_2 = \{\xi_1^2, \xi_2^2, \ldots, \xi_{m+p_2+1}^2\}$.

6.1.2 Bézier Extraction

Motivation and concept

Isogeometric analysis based on NURBS does not use elements in the classical sense but patches, Fig. 6.2. The knot vectors that define a NURBS patch or surface in the physical domain can be represented by two-dimensional rectangles in the parameter space. Although isogeometric finite element methods can be implemented directly using the previously defined B-splines and NURBS basis functions defined on patches, it is more convenient to apply Bézier extraction [17] to map the B-spline or NURBS basis onto a local, C^0-continuous, piecewise polynomial Bernstein basis. Using this transformation, the original NURBS patch is decomposed into C^0 continuous Bézier finite elements, one for each non-zero knot span $[\xi_I \; \xi_{I+1}]$ in the original knot vector $\underline{\Xi}$, Fig. 6.2. These Bézier elements can be handled in the same way as standard finite elements. That is, every existing finite element code can be enhanced with isogeometric analysis features using Bézier extraction. The only information to compute the Bézier elements for a given B-spline or NURBS is its knot vector. In the following, Bézier extraction will be outlined for the one-dimensional case. Due to the tensor product nature of the two-dimensional basis functions, all procedures can be generalised to surfaces and volumes.

Bézier extraction is essentially based on the insertion of knots which will therefore be briefly outlined in the following. A new knot at $\hat{\xi}$ can be inserted into the knot vector $\underline{\Xi}$ which is altered to $\hat{\underline{\Xi}} = \begin{bmatrix} \xi_1 & \xi_2 & \dots & \xi_I & \hat{\xi} & \xi_{I+1} & \dots & \xi_{n+p+1} \end{bmatrix}^T$, $(I > p)$. This results in a set of new basis functions that are computed from equation (6.7). If a new knot is inserted at the location of an existing one, the continuity of the basis is reduced by one at this position. In order to retain the shape and the continuity of the geometry, namely the curve $\mathbf{C}(\xi)$, while changing the continuity of the basis functions, the position of control points has to be adjusted according to

$$\hat{\underline{\mathbf{P}}}_J = \begin{cases} \underline{\mathbf{P}}_1 & J = 1 \\ \alpha_J \underline{\mathbf{P}}_J + (1 - \alpha_J)\underline{\mathbf{P}}_{J-1} & 1 < J < m \\ \underline{\mathbf{P}}_m & J = m \end{cases}, \qquad (6.14)$$

$$\alpha_J = \begin{cases} 1 & 1 \leq J \leq I - p \\ \frac{\hat{\xi}-\xi_J}{\xi_{J+p}-\xi_J} & k - p + 1 \leq J \leq I \\ 0 & J \geq I + 1 \end{cases}. \qquad (6.15)$$

Bézier extraction is actually accomplished by repeated knot insertion. For every inserted knot ξ_J, $J = 1 \dots m$ a new matrix of control points $\hat{\underline{\mathbf{P}}}_{J+1} = \left(\underline{\underline{\mathbf{C}}}_J\right)^T \hat{\underline{\mathbf{P}}}_J$ with $\hat{\underline{\mathbf{P}}}_1 = \underline{\mathbf{P}}$ has to be computed. The operator $\underline{\underline{\mathbf{C}}}_J$ follows directly from equations (6.14) and (6.15), see [17] for details. Repeating all interior knots of the given knot vector to a multiplicity of p results in a set of Bézier control points

$$\underline{\underline{\mathbf{Q}}} = \hat{\underline{\mathbf{P}}}_{m+1} = \left(\underline{\underline{\mathbf{C}}}_m\right)^T \left(\underline{\underline{\mathbf{C}}}_{m-1}\right)^T \dots \left(\underline{\underline{\mathbf{C}}}_1\right)^T \underline{\mathbf{P}} = \underline{\underline{\mathbf{C}}}^T \underline{\mathbf{P}}. \qquad (6.16)$$

The matrix $\underline{\underline{\mathbf{C}}}$ is called *Bézier extraction operator*. It relates the B-spline control points to their Bézier counterparts. Due to the one-to-one correspondence of control points and basis functions, the B-spline basis

$$\underline{\mathbf{N}}\left(\bar{\xi}\right) = \underline{\underline{\mathbf{C}}}\underline{\mathbf{B}}\left(\bar{\xi}\right) \qquad (6.17)$$

can now be expressed in terms of the Bernstein polynomial basis[1] which is C^0 continuous at each knot. This leads to the representation

$$\mathbf{C}\left(\bar{\xi}\right) = \underline{\underline{\mathbf{Q}}}^T \underline{\mathbf{B}}\left(\bar{\xi}\right) = \left(\underline{\underline{\mathbf{C}}}^T \underline{\mathbf{P}}\right)^T \underline{\mathbf{B}}\left(\bar{\xi}\right) = \underline{\mathbf{P}}^T \underline{\underline{\mathbf{C}}}\underline{\mathbf{B}}\left(\bar{\xi}\right) \qquad (6.18)$$

for any univariate B-spline geometry or approximation.

As an example, the B-spline curve according to Fig. 6.1 is now represented in terms of Bernstein basis functions, Fig. 6.3. Bézier extraction converts the B-spline functions that are active over a Bézier element domain into $p + 1$ Bernstein shape functions. Different colours indicate the domains and shape functions of the associated Bézier elements. It can be seen from Fig. 6.3 (a) that the approximation is interpolatory at the element boundaries with identical Bézier control points of adjacent elements. While the B-spline or NURBS basis functions will in general be different for each knot span, Fig. 6.1 (b), the same Bernstein polynomials are used in each knot interval $[\xi_I \ \xi_{I+1}]$, Fig. 6.3 (b). They therefore take the

---

[1]To facilitate numerical integration of the weak form over each element domain, the Bernstein shape functions according to equation (6.3) have been defined for the interval $\bar{\xi} \in [-1, 1]$ that spans a single Bézier element.

(a)

(b)
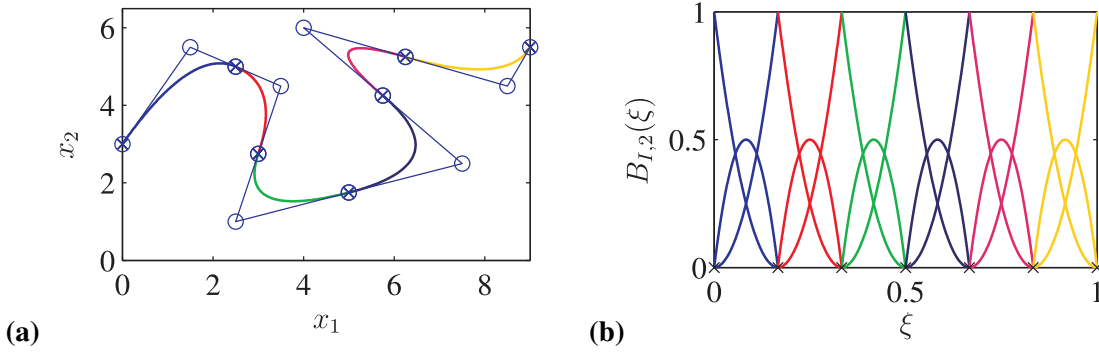
Figure 6.3: Bézier extraction for the B-spline curve according to Fig. 6.1: **(a)** Plot of the curve and the associated Bézier control points $\underline{\underline{\mathbf{Q}}}$ (symbols ○) in the physical x_1-x_2 domain, and **(b)** Bernstein basis functions $B_{I,2}(\xi)$ in the parameter domain. Colors in both figures indicate different Bézier elements.

role of a classical shape function in each Bézier element.

NURBS Bézier extraction

Since the NURBS basis functions consist of weighted B-splines, Bézier extraction can be directly applied to equation (6.10) using the results of the preceding paragraph and of [17]

$$\underline{\mathbf{R}}(\xi) = \frac{1}{\underline{\mathbf{w}}^T \underline{\underline{\mathbf{C}}} \mathbf{B}(\bar{\xi})} \underline{\underline{\mathbf{W}}}\, \underline{\underline{\mathbf{C}}} \mathbf{B}(\bar{\xi}) = \underline{\underline{\mathbf{W}}}\, \underline{\underline{\mathbf{C}}} \frac{\mathbf{B}(\bar{\xi})}{W(\bar{\xi})} \ . \tag{6.19}$$

From the denominator of the equation above it follows that the weights corresponding to the Bézier basis functions are $\underline{\mathbf{w}}_Q = \underline{\underline{\mathbf{C}}}^T \underline{\mathbf{w}}$. Using a diagonal matrix representation $\underline{\underline{\mathbf{W}}}_Q = \mathrm{diag}\underline{\mathbf{w}}_Q$ as shown in [17], the required set of Bézier control points for NURBS are computed as

$$\underline{\underline{\mathbf{Q}}} = \underline{\underline{\mathbf{W}}}_Q^{-1} \underline{\underline{\mathbf{C}}}^T \underline{\underline{\mathbf{W}}}\mathbf{P} \ . \tag{6.20}$$

6.2 Isogeometric Discretisation of the Magneto-Mechanical Boundary Value Problem

Introduction

In this section IGA will be applied to model the coupled magneto-mechanical boundary value problem assuming small deformations and hence a one-sided coupling. Only two-dimensional problems homogeneous in the x_3-direction will be considered ($A_3 = A$, $A_1 = A_2 = 0$). After a brief outline of the isogeometric discretisation, the numerical properties of IGA are compared to XFEM using one of the demonstration problems described in Section 2.7. In the case of IGA NURBS basis functions are applied in order to exactly represent the geometry of the circular inclusion while Lagrangian polynomials used with XFEM can only approximate the circular interface.

6.2.1 Discretisation

Geometry

Similar to the standard finite element approach, the domain $\Omega = \bigcup\limits_{I=1}^{n_{\mathrm{e}}} \Omega_{I\mathrm{e}}$ is discretised by a number of n_{e} Bézier elements $\Omega_{I\mathrm{e}}$. The geometric map of a two-dimensional finite element domain Ω_{e} from the parametric domain to the physical domain according to equation (6.11)

is defined by

$$\mathbf{x}(\boldsymbol{\xi}) = \sum_{I=1}^{p_1+1} \sum_{J=1}^{p_2+1} R_{IJ}^{\mathrm{e}}(\boldsymbol{\xi}) \underline{\mathbf{x}}_{IJ}^{\mathrm{e}} \tag{6.21}$$

based on $(p_1 + 1) \times (p_2 + 1)$ bivariate NURBS basis functions R_{IJ}^{e} and their associated control points $\hat{\mathbf{x}}_{IJ}^{\mathrm{e}}$. Bézier extraction based on an element local extraction operator $\underline{\underline{\mathbf{C}}}_{\mathrm{e}}$ [17] allows to express the geometry representation

$$\mathbf{x}\left(\bar{\boldsymbol{\xi}}\right) = \underline{\underline{\mathbf{x}}}_{\mathrm{e}}^{T} \underline{\underline{\mathbf{W}}}_{\mathrm{e}} \underline{\underline{\mathbf{C}}}_{\mathrm{e}} \frac{\mathbf{B}_{\mathrm{e}}\left(\bar{\boldsymbol{\xi}}\right)}{W\left(\bar{\boldsymbol{\xi}}\right)} \tag{6.22}$$

in terms of Bernstein polynomials similar to equation (6.19). This facilitates a direct geometrical map between the physical and parent domain where numerical integration is carried out. The quadrature of the weak form involves the Jacobian of the geometrical map

$$\mathrm{d}x_1 \mathrm{d}x_2 = \left| \frac{\partial \mathbf{x}\left(\bar{\boldsymbol{\xi}}\right)}{\partial \bar{\boldsymbol{\xi}}} \right| \mathrm{d}\bar{\xi}_1 \mathrm{d}\bar{\xi}_2 = |\underline{\underline{\mathbf{J}}}_{\mathrm{e}}| \mathrm{d}\bar{\xi}_1 \mathrm{d}\bar{\xi}_2 = J \mathrm{d}\bar{\xi}_1 \mathrm{d}\bar{\xi}_2 \, . \tag{6.23}$$

An isogeometric finite element formulation for the stationary magnetic field problem is obtained from the discretisation of the weak form (3.5) introduced in Chapter 3. Following the idea of isogeometric analysis, the same functions which represent the geometry of the element (6.22) are used to approximate the potential

Magnetic BVP

$$A^h\left(\bar{\boldsymbol{\xi}}\right) = \underline{\mathbf{A}}_{\mathrm{e}}^{T} \underline{\underline{\mathbf{W}}}_{\mathrm{e}} \underline{\underline{\mathbf{C}}}_{\mathrm{e}} \frac{\mathbf{B}_{\mathrm{e}}\left(\bar{\boldsymbol{\xi}}\right)}{W\left(\bar{\boldsymbol{\xi}}\right)} \, . \tag{6.24}$$

The vector $\underline{\mathbf{A}}_{\mathrm{e}}$ contains the control values of the magnetic potential, i.e. discrete values at control points associated to the element. However, as the spline-based approximation will generally be non-interpolatory, the control values do not represent physical values of the magnetic potential at the geometric location of the control points. The Bézier extraction algorithm is practically implemented in a shape function routine to compute a vector $\underline{\mathbf{N}}_A$ operating on the control values which allows to rewrite the approximation of the magnetic potential

$$A^h\left(\bar{\boldsymbol{\xi}}\right) = \underline{\mathbf{N}}_A\left(\bar{\boldsymbol{\xi}}\right) \underline{\mathbf{A}}_{\mathrm{e}} \tag{6.25}$$

in a form similar to standard FEM. In the same manner, the magnetic induction is related to the control values of the potential by

$$\mathbf{B}^h\left(\bar{\boldsymbol{\xi}}\right) = \underline{\underline{\mathbf{B}}}_A\left(\bar{\boldsymbol{\xi}}\right) \underline{\mathbf{A}}_{\mathrm{e}} \tag{6.26}$$

with the matrix $\underline{\underline{\mathbf{B}}}_A$ representing a discrete version of the definition of the vector potential (2.35). The form of the global system of equations that results from the isogeometric discretisation is therefore exactly the same as for a Lagrangian FEM and reads

$$\underline{\underline{\mathbf{K}}}_A \underline{\mathbf{A}} = \underline{\mathbf{P}}_A + \underline{\mathbf{J}} \, . \tag{6.27}$$

All changes due to the spline-based approximation are essentially contained in an adapted shape function routine. The non-interpolary nature of the spline basis may, however, require some consideration during the application of non-homogeneous boundary conditions. The coefficient matrix and the vector of equivalent currents are obtained from assembling the

contributions of all n_e elements defining the domain Ω

$$\underline{\underline{\mathbf{K}}}_A = \bigcup_{I=1}^{n_\mathrm{e}} \int_{\Omega_{I\mathrm{e}}} \underline{\underline{\mathbf{B}}}_A^T \underline{\underline{\mathbf{C}}}_A \underline{\underline{\mathbf{B}}}_A \, \mathrm{d}V \tag{6.28}$$

$$\underline{\mathbf{P}}_A = \bigcup_{I=1}^{n_\mathrm{e}} \left[\int_{\Omega_{I\mathrm{e}}} \underline{\mathbf{N}}_A^T j \, \mathrm{d}V + \int_{\partial\Omega_{I\mathrm{e}}} \underline{\mathbf{N}}_A^T \hat{k} \, \mathrm{d}S \right] . \tag{6.29}$$

The vector $\underline{\mathbf{J}}$ allows for the application of discrete currents at control points.

Magneto-mechanical BVP
The discretisation of the domain Ω used in the mechanical pass is the same as for the magnetic problem with the following isogeometric approximation of the displacement field

$$\mathbf{u}^h\left(\bar{\boldsymbol{\xi}}\right) = \underline{\underline{\mathbf{N}}}_u\left(\bar{\boldsymbol{\xi}}\right) \underline{\mathbf{u}}_\mathrm{e} . \tag{6.30}$$

The vector $\underline{\mathbf{u}}_\mathrm{e}$ contains the control values of the displacement associated to the considered element. A matrix representation of the infinitesimal strain-displacement relation is given by

$$\underline{\boldsymbol{\varepsilon}}^h\left(\bar{\boldsymbol{\xi}}\right) = \underline{\underline{\mathbf{B}}}_u\left(\bar{\boldsymbol{\xi}}\right) \underline{\mathbf{u}}_\mathrm{e} \tag{6.31}$$

with the operator matrix $\underline{\underline{\mathbf{B}}}_u$ involving partial derivatives of the shape functions. Applying these approximations to the weak form (3.6) results in the global system of equations for the magneto-mechanical problem considering a one-sided coupling due to magnetic stresses

$$\underline{\underline{\mathbf{K}}}_u \, \underline{\mathbf{u}} = \underline{\mathbf{P}}_u + \mathbf{F} \tag{6.32}$$

with

$$\underline{\underline{\mathbf{K}}}_u = \bigcup_{I=1}^{n_\mathrm{e}} \int_{\Omega_{I\mathrm{e}}} \underline{\underline{\mathbf{B}}}_u^T \underline{\underline{\mathbf{C}}}_u \underline{\underline{\mathbf{B}}}_u \, \mathrm{d}V \tag{6.33}$$

$$\underline{\mathbf{P}}_u = \bigcup_{I=1}^{n_\mathrm{e}} \left[\int_{\Omega_{I\mathrm{e}}} \left(\underline{\underline{\mathbf{N}}}_u^T \rho \underline{\mathbf{f}} - \underline{\underline{\mathbf{B}}}_u^T \hat{\boldsymbol{\sigma}} \right) \mathrm{d}V - \int_{\partial\Omega_{I\mathrm{e}}} \underline{\underline{\mathbf{N}}}_u^T \hat{\underline{\mathbf{p}}} \, \mathrm{d}S \right] \tag{6.34}$$

and additional control point forces contained in the vector $\underline{\mathbf{F}}$.

6.2.2 Convergence Analysis

Introduction
Following the derivation of the isogeometric finite element formulation for the coupled magneto-mechanical field problem, its convergence behaviour will be investigated numerically and compared to XFEM. In Chapter 3 as well as in [KMG+13] the convergence of XFEM has been studied primarily for the magnetic field problem using the solution of Engel et al. [61]. Having at hand the analytical solution of the magneto-mechanical problem outlined in Section 2.7, convergence studies have been carried out for the coupled problem and purely magnetic or mechanical subproblems considering both discretisation approaches.
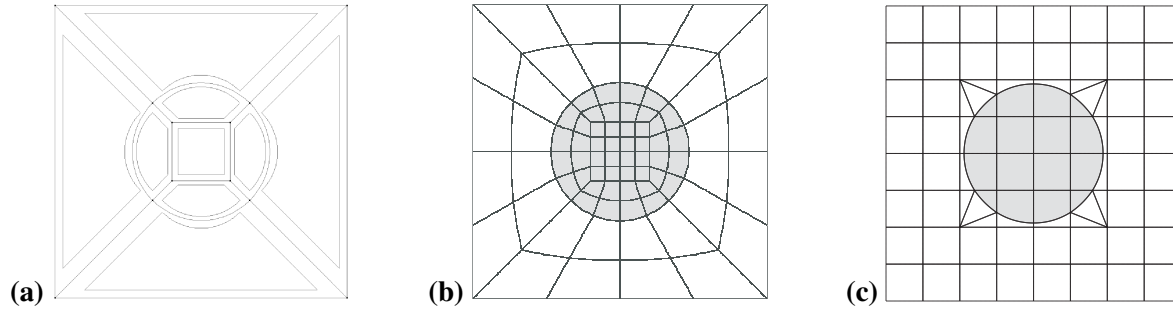
Figure 6.4: Isogeometric and XFEM discretisations used in the convergence analysis: **(a)** Definition of the geometry in terms of nine NURBS patches, **(b)** coarsest Bézier mesh (refinement level 1) considered in the analysis, and **(c)** XFEM mesh of Q8 elements. In addition, the used integration subdomains and the circular interface are depicted.

The investigated problem is given by a circular inclusion Ω^- of radius R which is embedded in an infinite matrix domain Ω^+, cf. Fig. 2.3 (b). Both domains can be magnetisable but are assumed to exhibit linear magnetic and mechanical material behaviour. For the present study, the parameters $\mu_{\mathrm{r}}^+ = 1$, $E^+ = 1 \times 10^9\,\mathrm{Pa}$, $\nu^+ = 0.3$, and $\mu_{\mathrm{r}}^- = 10$, $E^- = 1 \times 10^8\,\mathrm{Pa}$, $\nu^- = 0.4$ are used for inclusion and matrix, respectively. The numerical model comprises a square domain Ω of size $10\,\mathrm{m} \times 10\,\mathrm{m}$ containing a circular inclusion of radius $R = \frac{3}{4}\pi\,\mathrm{m}$. The exact solution of the problem derived in [195] is utilised to prescribe essential boundary conditions for the magnetic and mechanical problems. Based on the analytic solution which is able to represent a multitude of qualitatively different settings by varying the material and loading parameters, three subproblems will be analysed in the following:

Problem description

  (i) A stationary magnetic problem with a loading of $^\infty B = 1\,\mathrm{T}$,

  (ii) a coupled magneto-mechanical problem with $^\infty B = 1\,\mathrm{T}$ and $^\infty\sigma_{11} = {}^\infty\sigma_{22} = 0$, and

  (iii) a purely mechanical problem with $^\infty B = 0$ and $^\infty\sigma_{11} = {}^\infty\sigma_{22} = 3 \times 10^6\,\mathrm{Pa}$ which represents a biaxial tensile loading, cf. [204].

As outlined in Chapter 1, both discretisation methods are fundamentally different with respect to the representation of details of the modelled structure. The isogeometric approach uses a conforming mesh defined in terms of several NURBS patches which represent the geometry. The circular inclusion of the considered problem can be modelled exactly by quadratic NURBS. A total number of nine patches has been used to generate a convenient parametrisation of the geometry, Fig. 6.4 (a). The associated Bézier mesh of the first considered refinement level is shown in Fig. 6.4 (b). During the convergence study, each of the patches undergoes uniform h-refinement which ensures nestedness of the solution and yields meshes of $n_{\mathrm{e}} \in \{8, 16, 32, 64, 128, 256, 512\}$ elements. In contrast, XFEM uses a regular non-conforming mesh in combination with an implicit interface representation by level sets. For this convergence study, seven different discretisations with $n_{\mathrm{e}} = n \times n$ elements and $n \in \{8, 16, 32, 64, 128, 256, 512\}$ have been used. All computational results are obtained using the element local level set representation of the interface in combination with quadratic approximations (Q8 elements). The computational mesh with 8×8 Q8 elements is illustrated in Fig. 6.4 (c).

Discretisation
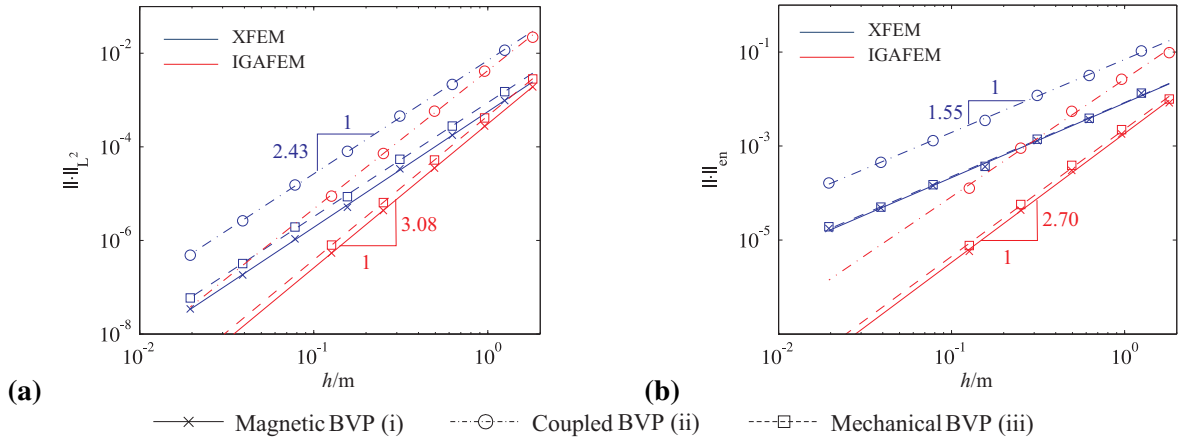
Figure 6.5: Convergence behaviour of the quadratic isogeometric finite element formulation (IGAFEM, solid lines) and XFEM (dashed lines) for the magnetic, coupled magneto-mechanical and mechanical problems as a function on the characteristic element size h: **(a)** L^2 norm, and **(b)** energy norm.

Discussion

The convergence behaviour for quadratic NURBS and XFEM in the L^2 and the energy norm is illustrated in Fig. 6.5. Monotonic convergence is obtained for both discretisation methods and all analysed problems. However, there is a significant difference between the isogeometric approach and XFEM regarding the overall error level and the convergence rate. While the isogeometric discretisations show optimal orders of convergence of almost exactly $p+1 = 3$ in the L^2 norm. The convergence behaviour in the energy norm even exceeds the theoretical optimal order of $p = 2$. The quadratic XFEM formulation convergences suboptimally which has already been reported in Section 3.4, in [KMG+13] as well as by Cheng and Fries [37]. This discrepancy is partly due to the exact geometry representation of the isogeometric approach. The rather poor convergence of the XFEM solutions is typically caused by small triangular integration subdomains which produce large errors and deteriorate the conditioning of the global system of equation. Eventually, it turns out that the appealing XFEM approach to mesh generation, whose advantages have been demonstrated with the generation of numerical models for random microstructures in the previous sections, is numerically far from optimal. The isogeometric approach features excellent numerical properties but requires conforming meshes which will be hard to obtain for solid three-dimensional problems.

Influence of problem type

While the order of convergence does not depend on the solved boundary value problem, a clear influence on the error level is observed. In terms of the L^2 norm, the error for the magnetic boundary value problem (i) is the smallest one, followed by the purely mechanical problem (iii). The displacement field of the coupled problem (ii) possesses the largest error. This applies to both discretisations. With respect to the energy norm, the error levels of the problems (i) and (iii) nearly coincide, while the one of (ii) is higher again. A reason for this apparently systematic error is to be seen in the realisation of the weak coupling in the magneto-mechanical case: At first the magnetic problem is solved. This approximate numerical solution enters the coupled mechanical subproblem by means of the pseudo-magnetic stress tensor which contains the first derivatives of the vector potential, i.e. the magnetic loads entering the magneto-mechanical problem are erroneous and cause the observed offset in the error levels.

7 Hybrid Isogeometric Finite Element and Boundary Element Formulation [MKMU14]

In this chapter a coupling of the Finite Element (FEM) and the Boundary Element Method (BEM) is proposed. The development is motivated from the characteristics of magnetic fields which are not only present in the material body but also in the surrounding free space. If a finite element approach is used, the free space domain has to be meshed in order to avoid truncation errors and to solve scatter problems, e.g. the analysis of electro-magnetic radiation resulting from electronic components. This meshing effort can be avoided by BEM whose integral formulation inherently deals with infinite domains. As the BEM is very limited regarding the modelling of heterogeneous structures as well as material non-linearities, a coupling of both methods is pursued in the following. Motivation

FEM is used in this coupled approach to model heterogeneous materials or components that may exhibit non-linear magnetic and mechanical behaviour. The BEM accounts for the surrounding free space. Both methods are coupled on the boundary of the finite element domain. Due to this hybrid approach, no meshing of the free space is necessary and truncation errors are avoided for problems to be solved on open, infinite or semi-infinite domains. Once the solution for the magnetic problem is obtained by the hybrid formulation, FEM is used to solve the magneto-mechanical field problem with one-sided coupling in a subdomain of the magnetic problem. Here, the hybrid method is applied in conjunction with spline-based approximations to form a hybrid isogeometric FEM/BEM approach which offers efficient discretisations and an exact representation of typical engineering geometries. Hybrid approach

This chapter is outlined as follows. After a short review of the Isogeometric Boundary Element Method (IGABEM), a boundary integral formulation for the magnetic field problem is developed. Subsequently, the coupling of IGABEM with the Isogeometric Finite Element Method (IGAFEM) is outlined and the numerical properties of the proposed approach in terms of errors and convergence rates are investigated. Results obtained from discretisations based on NURBS and Lagrangian polynomials are compared using the first demonstration problem described in Section 2.7. Eventually, the simulation of magnetically induced deformations of an elliptic sample representing a generic, magnetoactive material that consists of magnetisable particles embedded in a polymeric matrix with non-linear viscoelastic constitutive behaviour. Outline

7.1 Isogeometric Boundary Element Method

The idea of IGABEM was first mentioned in [41]. Early contributions focus on the modelling of potential-flow problems [169] and structural shape optimisation [128]. In order to handle the dense coefficient matrices of BEM efficiently even for large models, Takahashi and Matsumoto [206] combined IGABEM with the Fast Multipole Method to solve problems of Laplace type. Scott et al. [184] used T-splines to eliminate shortcomings in the smoothness of NURBS-based geometry representations. The idea of partition-of-unity IGABEM

based enrichments was recently transferred to IGABEM by Peake et al. [162]. As BEM requires only the boundary of objects to be meshed, it is even more attractive in combination with isogeometric analysis. Computer aided design models only describe the boundary of objects. This surface representation has to be converted into a three-dimensional solid model in the case of IGAFEM which is one of the key challenges in isogeometric analysis. This problem is avoided for BEM and the method has therefore been applied to elastostatic analysis by Simpson et al. [191, 192].

7.2 Hybrid Approach – Coupling IGAFEM and IGABEM

Hybrid methods

Despite being advantageous for infinite or semi-infinite domains and the attractive combination with IGA, boundary integral methods have restrictions regarding the representation of non-linear material behaviour, especially for materials models that involve internal constitutive variables, cf. Section 2.6. While certain approaches for non-linear isotropic [21] and anisotropic [164, 219] elastic and linear viscoelastic [76, 175] material models exist, the consideration of more complex non-linear constitutive relations remains cumbersome – not to say impossible – due to the requirement of an appropriate fundamental solution. In order to allow for the modelling of complex components, which involve non-linear material models, and the surrounding free space, FEM and BEM can be coupled to combine the adavantages of both approaches. An early attempt for such a hybrid modelling strategy has been presented by Fredkin and Koehler [69] for computing scatter fields. Applications to electric field problems can be found in [66]. Recent contributions by Daveau and Menad [45], Pusch and Ostrowski [172], Bruckner et al. [24], Fritze et al. [72] as well as Peters et al. [166] discuss various direct coupling techniques for conforming and non-conforming discretisations. Here, the hybrid FEM/BEM method is applied in conjunction with spline-based approximations to form a hybrid IGAFEM/IGABEM approach.

Solution procedure

The infinite domain Ω_∞ is decomposed into two separate parts Ω_{BEM} and Ω_{FEM}, Fig. 7.1. The domain Ω_{FEM} involves the heterogeneous material body with arbitrarily complex material behaviour while the domain Ω_{BEM} models the free space surrounding the material. Both domains have the common boundary $\Gamma = \partial\Omega = \partial\Omega_{\mathrm{FEM}} = \partial\Omega_{\mathrm{BEM}}$ which represents the surface of the material body. In this way no meshing of the free space is necessary. This approach is applied to the model magneto-mechanical problems according to Chapter 2 assuming small deformations and a one-sided coupling. That is, magnetically induced deformations result from attractive or repulsive interactions between the particles modelled in terms of magnetic stresses. The following staggered solution procedure is used:

(i) *Hybrid IGAFEM/IGABEM* is applied to compute the magnetic field in Ω_∞, i.e. within and outside the magnetisable body.

(ii) *IGAFEM* is used to simulate magneto-mechanical interactions in the magnetisable body which covers Ω_{FEM}. During this pass magnetic loads according to step (i) are applied.

Moreover, the domain Ω_{BEM} is assumed to be free of mechanical stresses and the magneto-mechanical problem (ii) can be solved by only FEM or IGAFEM, respectively. Nevertheless, magnetic loads that result from the exterior of the domain Ω_{FEM} are considered in terms of magnetic surface tractions on Γ which are also obtained from the solution of the magnetic field problem in step (i).
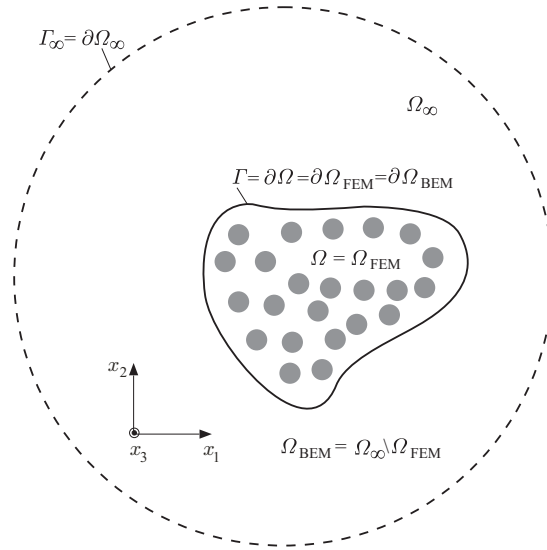
Figure 7.1: Modelling problems on infinite or semi-infinite domains Ω_∞ using a hybrid approach that couples FEM and BEM on the common boundary Γ. This boundary can be fictitious but will often coincide with the boundary $\partial\Omega$ of a material body or device Ω in the open domain Ω_∞. While FEM can be used to model heterogeneous materials with complex history dependent constitutive relations in Ω_{FEM}, BEM is utilised to account for fields in the free space Ω_{BEM}.

7.3 Hybrid Isogeometric Discretisation of the Magnetic Boundary Value Problem

In this section a hybrid formulation for the stationary magnetic problem is developed. Emphasis is placed on the isogeometric discretisation of the boundary, the derivation of the boundary integral equation, and the discrete system of equations. Subsequently, IGABEM is coupled to IGAFEM which requires some changes to the formulation outlined in Section 6.2.

Introduction

7.3.1 Boundary Discretisation

While the domain Ω_{FEM} is divided into a number of n_{e} finite elements Ω_{e}, cf. Fig. 6.2, the boundary Γ is split into $n_{\tilde{\mathrm{e}}}$ boundary elements $\Gamma_{\tilde{\mathrm{e}}}$, Fig. 7.2

Geometric map

$$\Gamma = \bigcup_{I=1}^{n_{\tilde{\mathrm{e}}}} \Gamma_{I\tilde{\mathrm{e}}} \,. \tag{7.1}$$

As in the two-dimensional case, elements are defined by unique non-zero intervals of the knot vector. The geometry of the boundary element $\Gamma_{\tilde{\mathrm{e}}}$ is a NURBS curve according to equation (6.8)

$$\mathbf{x}(\psi) = \sum_{k=1}^{p+1} R_{I,p}(\psi)\, \underline{\mathbf{x}}_I^{\tilde{\mathrm{e}}} \tag{7.2}$$
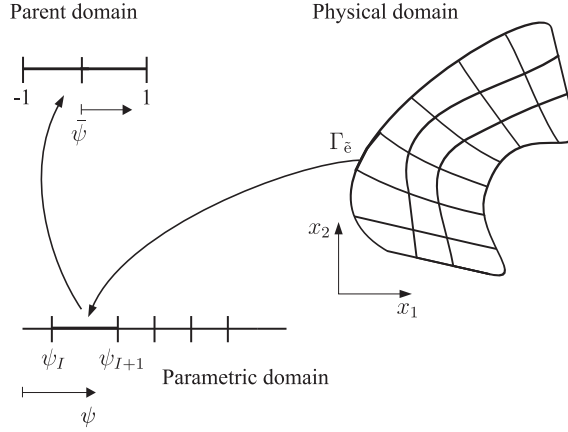
Figure 7.2: Isogeometric discretisation of the boundary of a NURBS patch and three sets of Cartesian coordinates describing the physical, parametric and parent domains.

defined in terms of $p+1$ univariate NURBS basis functions $R_{I,p}(\psi)$ and control point coordinates associated to the element $\Gamma_{\tilde{e}}$. Using Bézier extraction, the basis functions are expressed in terms of Bernstein polynomials that are functions of the parent domain coordinate $\bar{\psi}$

$$\mathbf{x}\left(\bar{\psi}\right) = \underline{\mathbf{x}}_{\tilde{e}}^{T} \underline{\underline{\mathbf{W}}}_{\tilde{e}} \underline{\underline{\mathbf{C}}}_{\tilde{e}} \frac{\mathbf{B}_{\tilde{e}}\left(\bar{\psi}\right)}{W\left(\bar{\psi}\right)} \,. \tag{7.3}$$

Quadrature of the boundary integral formulation is performed in the parent domain and the geometric mapping between the physical and parent domain requires the determinant of the Jacobian of the geometric map to be considered

$$\mathrm{d}\Gamma_{\tilde{e}} = \sqrt{\left(\frac{\mathrm{d}x_1^{\tilde{e}}(\bar{\psi})}{\mathrm{d}\bar{\psi}}\right)^2 + \left(\frac{\mathrm{d}x_2^{\tilde{e}}(\bar{\psi})}{\mathrm{d}\bar{\psi}}\right)^2}\,\mathrm{d}\bar{\psi} = J_{\tilde{e}}\mathrm{d}\bar{\psi}\,. \tag{7.4}$$

7.3.2 Isogeometric Boundary Element Formulation

Poisson problem

In the linear magnetic case $B_i = \mu H_i$, the stationary magnetic field problem described by equations (2.30) and (2.31) can be represented in terms by the Poisson type partial differential equation

$$A_{,ii} = -\mu\,j \tag{7.5}$$

for which a detailed derivation of the boundary integral equation can be found in [77]. In order to obtain the typical structure of the discrete BEM equations, the normal derivative of the magnetic potential is defined by $Q = A_{,i}n_i$ and jump conditions (2.32) as well as (2.33) across an interface Γ can be recast in the form

$$[\![A]\!] = 0 \tag{7.6}$$

$$\left[\!\!\left[\frac{Q}{\mu}\right]\!\!\right] = -k\,. \tag{7.7}$$
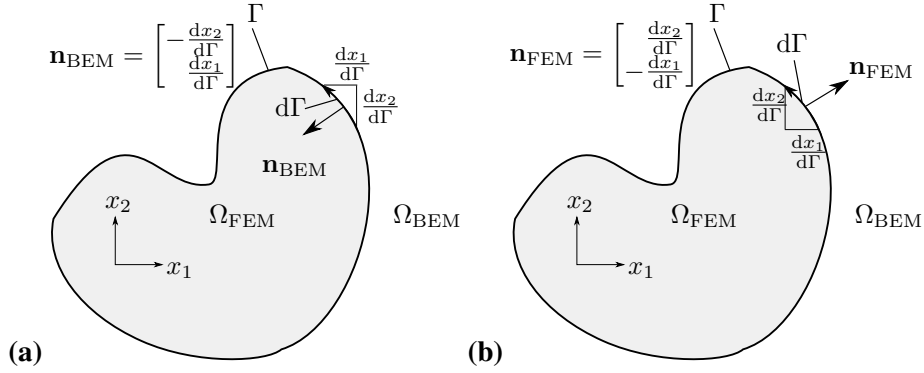
Figure 7.3: Definitions of the outward unit normal vectors: **(a)** $\mathbf{n}_{\text{BEM}}$, and **(b)** $\mathbf{n}_{\text{FEM}}$.

A corresponding boundary integral formulation of the stationary magnetic field problem is derived by multiplying (7.5) with a test function $A^*(\mathbf{x}, \mathbf{x}')$ which satisfies

Boundary integral equation

$$A^*_{,ii} = -\delta(\mathbf{x}, \mathbf{x}'), \tag{7.8}$$

with the Dirac distribution δ. Integrating over the domain Ω_{BEM}, applying integration by parts twice and using Gauss' theorem yields the boundary integral equation for the two-dimensional stationary magnetic field problem to be solved on the open, infinite domain Ω_{BEM}

$$A(\mathbf{x}') = \int\limits_{\Gamma} A^*(\mathbf{x}, \mathbf{x}')Q(\mathbf{x}) - Q^*(\mathbf{x}, \mathbf{x}')A(\mathbf{x})\, \mathrm{d}S + \mu \int\limits_{\Omega_{\text{BEM}}} A^*(\mathbf{x}, \mathbf{x}')j(\mathbf{x})\, \mathrm{d}V\,. \tag{7.9}$$

In the equation above $Q = A_{,i}n_i^{\text{BEM}}$ is the normal derivative of the magnetic potential A with the outward unit normal vector $\mathbf{n}_{\text{BEM}}$ of the BEM domain, Fig. 7.3 (a). The fundamental solution A^* of the magnetic potential obtained from (7.8) and its normal derivative Q^* are given by

$$A^*(r) = -\frac{1}{2\pi}\ln r, \quad Q^*(r) = A^*_{,i}n_i^{\text{BEM}} = -\frac{1}{2\pi r}\frac{\partial r}{\partial n_{\text{BEM}}} \tag{7.10}$$

with the Euclidean distance $r = |\mathbf{x} - \mathbf{x}'|$ between source $\mathbf{x}'$ and field point $\mathbf{x}$.

It is important to mention that terms in the boundary integral equation (7.9) related to the fictitious boundary Γ_∞, cf. Fig. 7.1,

Boundary integral for Γ_∞

$$\lim_{r \to \infty}\left[\int\limits_{\Gamma_\infty} A^*(\mathbf{x}, \mathbf{x}')Q(\mathbf{x}) - Q^*(\mathbf{x}, \mathbf{x}')A(\mathbf{x})\, \mathrm{d}S\right] = 0 \tag{7.11}$$

cancel each other out in two dimensions. In the three-dimensional case, each of the terms in (7.11) approaches zero for $r \to \infty$ [20]. As a consequence, Γ_∞ never has to be considered explicitly nor discretised and no boundary conditions have to be assigned.

Using the boundary integral equation (7.9), the magnetic potential can be computed for any point in the domain Ω_{BEM} once the potential and its normal derivative are known on Γ. In this work, the missing boundary values will be computed by collocation which is, however, not the only discretisation strategy for generating a system of equations. Problems in this procedure arise from the fact that the source point $\mathbf{x}'$ is restricted to the interior of Ω_{BEM} and

Collocation
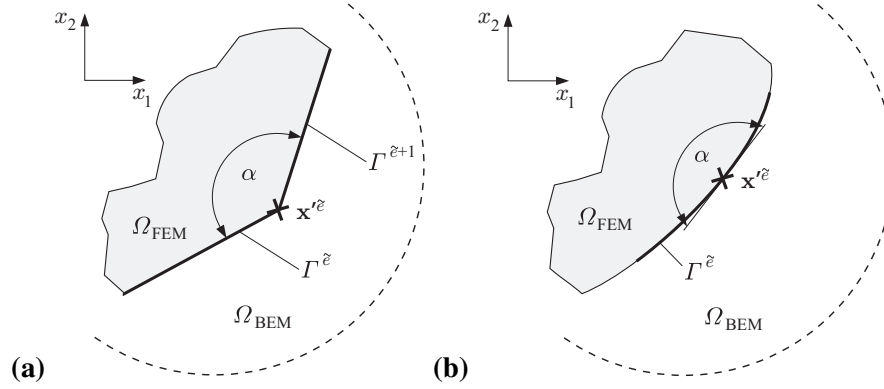
Figure 7.4: Definition of the planar angle α for **(a)** straight C^0-continuous boundary elements, and **(b)** for C^1-continuous boundary elements or integration points inside elements ($\alpha = 180°$, $c = 0.5$).

can approach a point on the boundary Γ only in a limit sense. From an implementation point of view, collocation with points on Γ will lead to singular integrals in (7.9) which require special treatment as explained in more detail in [MKMU14]. This results in the modified integral equation valid to compute values on Γ

$$c(\mathbf{x}')A(\mathbf{x}') + \oint_\Gamma Q^*(\mathbf{x}, \mathbf{x}')A(\mathbf{x})\,\mathrm{d}\Gamma - \int_\Gamma A^*(\mathbf{x}, \mathbf{x}')Q(\mathbf{x})\,\mathrm{d}S = \mu_{\mathrm{BEM}} \int_{\Omega_{\mathrm{BEM}}} A^*(\mathbf{x}, \mathbf{x}')j(\mathbf{x})\,\mathrm{d}V$$

(7.12)

where c is a free term coefficient defined by

$$c(\mathbf{x}') = \begin{cases} 1 - \frac{\alpha}{2\pi} & \text{for } \mathbf{x}' \in \Gamma \\ 1 & \text{for } \mathbf{x}' \in \Omega_{\mathrm{BEM}} \\ 0 & \text{for } \mathbf{x}' \notin \Gamma, \mathbf{x}' \notin \Omega_{\mathrm{BEM}} \end{cases}$$

(7.13)

with the planar angle α according to Fig. 7.4. The symbol $\oint$ indicates that the first integral in (7.12) – which is strongly singular (singularity at $r = 0$) – is evaluated in the Cauchy Principal Value limiting sense.

Discrete boundary Integral equation

A discrete form of the boundary integral equation which forms the basis for IGABEM is finally obtained from utilising univariate approximations of the magnetic potential and its normal derivative

$$A^h\left(\bar{\psi}\right) = \underline{\mathbf{N}}_A\left(\bar{\psi}\right)\underline{\mathbf{A}}_{\tilde{\mathrm{e}}} \tag{7.14}$$

$$Q^h\left(\bar{\psi}\right) = \underline{\mathbf{N}}_Q\left(\bar{\psi}\right)\underline{\mathbf{Q}}_{\tilde{\mathrm{e}}}. \tag{7.15}$$

Similar to two-dimensional case of Section 6.2.1, equation (6.25), the above vector-matrix notation of the approximations is implemented in terms of a modified shape function routine that is on the framework of Bézier extraction suitable for both, B-spline and NURBS.

The resulting discrete boundary integral equation is given by

$$c(\mathbf{x}')\underline{\mathbf{N}}_A\left(\bar{\psi}'\right)\underline{\mathbf{A}}_{\bar{\tilde{e}}} + \bigcup_{I=1}^{n_{\tilde{e}}}\left(\oint_{\Gamma_{I\tilde{e}}} Q^*(\mathbf{x}(\bar{\psi}),\mathbf{x}')\underline{\mathbf{N}}_A(\bar{\psi})J_{\tilde{e}}(\bar{\psi})\mathrm{d}\bar{\psi}\right)\underline{\mathbf{A}}_{\tilde{e}} \qquad (7.16)$$

$$-\bigcup_{I=1}^{n_{\tilde{e}}}\left(\int_{\Gamma_{I\tilde{e}}} A^*(\mathbf{x}(\bar{\psi}),\mathbf{x}')\underline{\mathbf{N}}_Q(\bar{\psi})J_{\tilde{e}}(\bar{\psi})\mathrm{d}\bar{\psi}\right)\underline{\mathbf{Q}}_{\tilde{e}}$$

$$= \mu\sum_{K=1}^{n_J} J_K A^*(\mathbf{x}_K,\mathbf{x}') \ .$$

In the equation above $\underline{\mathbf{A}}_{\tilde{e}}$ and $\underline{\mathbf{Q}}_{\tilde{e}}$ represent the control values of the magnetic potential and its normal derivative associated to the boundary element $\Gamma_{\tilde{e}}$, $\bar{\psi}'$ denotes the coordinate of the collocation point in the parent space, and $\bar{\tilde{e}}$ indicates the element containing the collocation point $\bar{\psi}'$. The first term in equation (7.16) takes into account that the rational basis functions are not interpolatory at the collocation coordinate $\bar{\psi}'$. For the right-hand side it is assumed, that a number of n_J concentrated current sources J_K act at field points $\mathbf{x}_K$ in Ω_{BEM}

$$j(\mathbf{x}) = \sum_{K=1}^{n_J} J_K \delta(\mathbf{x} - \mathbf{x}_K) \qquad (7.17)$$

which is a reasonable choice to model the demonstration problems presented in Section 7.4.

As previously mentioned, collocation which was already applied by Simpson [192] in the framework of IGABEM, is used to finally set up a system of equations to compute the unknown values of A and Q on Γ. The source points in the parametric space are defined by

<div align="right">System of equations</div>

$$\bar{\psi}'_I = \frac{\bar{\psi}_{I+1} + \bar{\psi}_{I+2} + \ldots + \bar{\psi}_{I+p}}{p} \ \text{for } I = 1, 2, \ldots, n-1 \qquad (7.18)$$

which yields a corresponding collocation point for each control point. Collocation at $\bar{\psi}'$ produces one line of the system of equations

$$\underline{\underline{\mathbf{H}}}\,\underline{\mathbf{A}}_{\mathrm{BEM}} + \underline{\underline{\mathbf{G}}}\,\underline{\mathbf{Q}}_{\mathrm{BEM}} = \underline{\mathbf{A}}_S \ . \qquad (7.19)$$

In equation (7.19) the vectors $\underline{\mathbf{A}}_{\mathrm{BEM}}$ and $\underline{\mathbf{Q}}_{\mathrm{BEM}}$ contain the control values of the potential and its normal derivative while the coefficient matrices $\underline{\underline{\mathbf{H}}}$ and $\underline{\underline{\mathbf{G}}}$ result from the quadrature of the integrals in (7.16). The vector $\underline{\mathbf{A}}_S$ exists due to currents in the domain Ω_{BEM} according to (7.17).

Special treatment has to be taken for the integration of the integrals in (7.16). If the collocation point $\bar{\psi}'$ does not lie in the element $\tilde{e}$ over which integration is performed, the integral is regular. In case that the collocation point lies in the element which is integrated, a method proposed by Guiggiani [84, 83] is applied to calculate the resulting strongly singular integral and the coordinate transformation proposed by Telles [207] for the weakly singular integral – for more details see the appendix of May et al. [MKMU14]. The number of integration points used is given explicitly in the numerical studies in section 7.4. Regular and nearly singular integrals are treated in the same manner.

<div align="right">Singular integrals</div>

7.3.3 Coupling of the Finite Element and Boundary Element Formulations

Reformulation of IGAFEM

In order to compute the magnetic potential in the domain Ω_∞, the IGAFEM approach of Section 6.2 has to be coupled to the present IGABEM formulation taking into account the interactions between the two domains Ω_{BEM} and Ω_{FEM}. They are given by the jump conditions according to equations (7.6) and (7.7) which hold on the interface Γ. The system of equations (6.27) has to be slightly altered to accomodate the jump condition (7.7). Equation (6.27) was derived from a weak form that considers current density boundary conditions $\hat{k}$, i.e. the jump condition (7.7) has already been evaluated assuming that Γ is an external boundary. A weak form which allows for a coupling of the domains Ω_{BEM} and Ω_{FEM} reads

$$\int\limits_{\Omega_{\text{FEM}}} \frac{1}{\mu_{\text{FEM}}} B_i \delta B_i \, \mathrm{d}V - \int\limits_{\Omega_{\text{FEM}}} j \delta A \, \mathrm{d}V - \int\limits_{\Gamma} \frac{1}{\mu_{\text{FEM}}} Q \delta A \, \mathrm{d}S = 0 \qquad (7.20)$$

and requires an approximation of the normal derivative Q on the edges of the finite elements representing the interface Γ. In view of the aspired coupling of IGAFEM and IGABEM, the same approximation (7.15) which is used for the boundary elements $\Gamma_{\tilde{e}}$

$$Q^h(\bar{\psi}) = \underline{\mathbf{N}}_Q(\bar{\psi}) \underline{\mathbf{Q}}_{\text{FEM}}^{\tilde{e}} \qquad (7.21)$$

is applied here. In equation (7.21) $\underline{\mathbf{Q}}_{\text{FEM}}^{\tilde{e}}$ are the control values of the normal derivative of the magnetic potential at the control points associated to the edge $\Gamma_{\tilde{e}}$ of a finite element Ω_{e}. Consequently, the discrete IGAFEM formulation now reads

$$\underline{\underline{\mathbf{K}}}_A \, \underline{\mathbf{A}}_{\text{FEM}} - \underline{\underline{\mathbf{T}}} \, \underline{\mathbf{Q}}_{\text{FEM}} = \underline{\mathbf{P}}_A, \qquad (7.22)$$

with the coefficient matrix $\underline{\underline{\mathbf{K}}}_A$ defined by equation (6.28). Since currents on the boundary are assumed to be zero in order to simplify the coupling procedure, the vector of equivalent nodal currents

$$\underline{\mathbf{P}}_A = \bigcup_{I=1}^{n_{\text{e}}} \int\limits_{\Omega_{Ie}} \underline{\mathbf{N}}_A^T \, j \, \mathrm{d}V \qquad (7.23)$$

only accounts for contributions due to body current densities. In addition, the approximation of Q results in the matrix

$$\underline{\underline{\mathbf{T}}} = \bigcup_{I=1}^{n_{\text{e}}} \int\limits_{\Gamma_{I\tilde{e}}} \frac{1}{\mu_{\text{FEM}}} \underline{\mathbf{N}}_A^T \underline{\mathbf{N}}_Q^{\tilde{e}} \, \mathrm{d}S \,. \qquad (7.24)$$

Boundary control values

The vectors $\underline{\mathbf{A}}_{\text{BEM}}$, $\underline{\mathbf{Q}}_{\text{BEM}}$ and $\underline{\mathbf{Q}}_{\text{FEM}}$ involve values at the same control points because the IGAFEM/-BEM approximations (7.14), (7.15) and (7.21) used for A and Q on the boundary Γ are identical. In contrast, the vector $\underline{\mathbf{A}}_{\text{FEM}}$ contains values from all control points of the domain Ω_{FEM}. As illustrated in Fig. 7.5, the representation of the geometry and the element approximation of the magnetic potential (6.25) in the finite element domain Ω_e

$$\mathbf{x}^h\left(\bar{\boldsymbol{\xi}}\right) = \underline{\underline{\mathbf{N}}}\left(\bar{\boldsymbol{\xi}}\right) \underline{\mathbf{x}}_{\text{e}} = \underline{\underline{\mathbf{N}}}^{\text{i}}\left(\bar{\boldsymbol{\xi}}\right) \underline{\mathbf{x}}_{\text{e,i}} + \underline{\underline{\mathbf{N}}}^{\text{b}}\left(\bar{\boldsymbol{\xi}}\right) \underline{\mathbf{x}}_{\text{e,b}} \qquad (7.25)$$

$$A^h\left(\bar{\boldsymbol{\xi}}\right) = \underline{\mathbf{N}}_A\left(\bar{\boldsymbol{\xi}}\right) \underline{\mathbf{A}}_{\text{FEM}}^{\text{e}} = \underline{\mathbf{N}}_A^{\text{i}}\left(\bar{\boldsymbol{\xi}}\right) \underline{\mathbf{A}}_{\text{FEM}}^{\text{e,i}} + \underline{\mathbf{N}}_A^{\text{b}}\left(\bar{\boldsymbol{\xi}}\right) \underline{\mathbf{A}}_{\text{FEM}}^{\text{e,b}} \qquad (7.26)$$

can be split into control values $\underline{\mathbf{A}}_{\text{FEM}}^{\text{e,i}}$ associated to the interior of the element and control values $\underline{\mathbf{A}}_{\text{FEM}}^{\text{e,b}}$ associated to its boundary. As $\underline{\mathbf{N}}_A^{\text{e,i}} = \underline{\mathbf{0}}$ for points on the element edge which
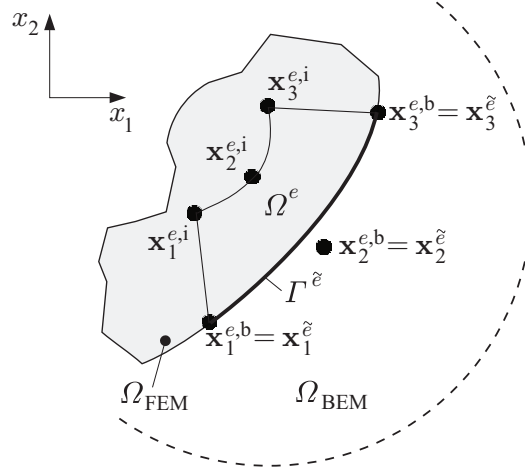
Figure 7.5: Decomposition of geometry representation and approximation into contributions from control points $\mathbf{x}_I^{e,i}$ associated to the interior of the element domain Ω_e and $\mathbf{x}_J^{e,b}$ associated to its boundary which are identical to the control points $\mathbf{x}_J^{\tilde{e}}$ of the boundary element $\Gamma_{\tilde{e}}$.

corresponds to the boundary element $\Gamma_{\tilde{e}}$, only the control values $\underline{\mathbf{A}}^{e,b}$ have influence on the approximation of A on Γ. Consequently, equation (7.26) reduces to

$$A^e\left(\bar{\boldsymbol{\xi}}\right)\big|_\Gamma = \underline{\mathbf{N}}_A^b\left(\bar{\boldsymbol{\xi}}\right)\underline{\mathbf{A}}_{\mathrm{FEM}}^{e,b} = \underline{\mathbf{N}}_A(\bar{\psi})\underline{\mathbf{A}}_{\mathrm{FEM}}^{e,b} \tag{7.27}$$

which is identical to the approximation in the boundary element $\Gamma_{\tilde{e}}$ given by equation (7.14).

From the discussion above it follows, that due to matching IGAFEM and IGABEM approximations along the boundary Γ, the jump conditions (7.6) and (7.7) can be satisfied by conditions for the control values of IGAFEM and IGABEM, respectively,

Coupling of control values

$$\underline{\mathbf{A}}_{\mathrm{FEM}}\big|_\Gamma = \underline{\mathbf{A}}_{\mathrm{BEM}} \tag{7.28}$$

$$\frac{1}{\mu_{\mathrm{FEM}}|_\Gamma}\underline{\mathbf{Q}}_{\mathrm{FEM}} = -\frac{1}{\mu_{\mathrm{BEM}}}\underline{\mathbf{Q}}_{\mathrm{BEM}}\;. \tag{7.29}$$

The negative sign in equation (7.29) results from the opposite direction of the normal vectors $\mathbf{n}_{\mathrm{FEM}}$ and $\mathbf{n}_{\mathrm{BEM}}$, cf. Fig. 7.3, and no surface current density k is applied. Eventually, the following system of equations

$$\begin{bmatrix} \underline{\underline{\mathbf{K}}}_A & \frac{\mu_{\mathrm{FEM}}|_\Gamma}{\mu_{\mathrm{BEM}}}\underline{\underline{\mathbf{T}}} \\ \tilde{\underline{\underline{\mathbf{H}}}} & \underline{\underline{\mathbf{G}}} \end{bmatrix} \begin{bmatrix} \underline{\mathbf{A}}_{\mathrm{FEM}} \\ \underline{\mathbf{Q}}_{\mathrm{BEM}} \end{bmatrix} = \begin{bmatrix} \underline{\mathbf{P}}_A \\ \underline{\mathbf{A}}_S \end{bmatrix} \tag{7.30}$$

which can be solved for the unknowns $\underline{\mathbf{A}}_{\mathrm{FEM}}$ and $\underline{\mathbf{Q}}_{\mathrm{BEM}}$ is obtained. The matrix $\tilde{\underline{\underline{\mathbf{H}}}}$ contains the entries of the matrix $\underline{\underline{\mathbf{H}}}$ in a special order because it operates on $\underline{\mathbf{A}}_{\mathrm{FEM}}$ and not on the subset of boundary values $\underline{\mathbf{A}}_{\mathrm{BEM}}$.
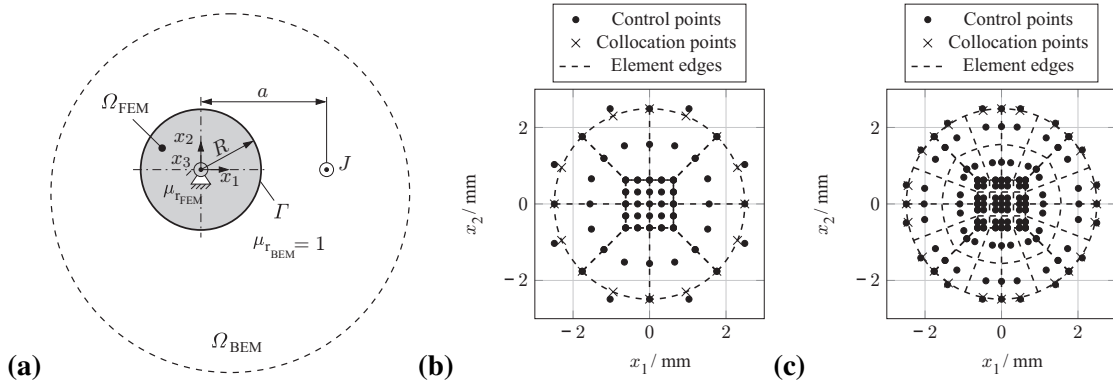
Figure 7.6: Hybrid model of the demonstration problem according to Fig. 2.3 (a): **(a)** rigid cylinder of radius R with relative magnetic permeability $\mu_{r_{FEM}}$; in free space $\mu_{r_{BEM}} = 1$. At distance a from its centre, a conducting wire carries the current J, **(b)** initial mesh for the magnetisable cylinder, and **(c)** mesh after applying uniform h-refinement with the collocation points on the boundary Γ for the IGAFEM/-BEM coupling

7.4 Demonstration

Introduction

The formulation presented the previous sections is used to simulate two different magneto-mechanical problems below. In the first example, based on the demonstration problem of Fig. 2.3 (a), outlined in Section 2.7, numerical properties of the hybrid formulation are studied in terms of error norms and convergence rates for the magnetic field problem. The accuracy of the predicted magneto-mechanical coupling effect is analysed by the relative error of a magnetic force acting on a magnetisable inclusion fixed in free space due to an inhomogeneous magnetic field. In the second example magnetostricitive effects are investigated in a heterogeneous magnetoactive material. The sample consists of magnetisable particles embedded in a polymer matrix with typical strain rate dependent constitutive behaviour modelled by a non-linear viscoelastic material model [116] underlining the usefulness and variability of the proposed hybrid approach. The two-dimensional problems are assumed to be homogeneous in the x_3-direction. Due to the considered one-sided coupling, the numerical analyses of the magnetic and magneto-mechanical problems are performed consecutively, starting with the magnetic field problem. As previously outlined, the magnetic loads are then computed from the obtained solution and applied in the mechanical pass.

7.4.1 Convergence Analysis

Problem description

The hybrid numerical model of the first demonstration problem according to Section 2.7 is illustrated in Fig. 7.6. For the computations the same material properties as in Chapter 3 are used. While the infinite domain Ω_∞ is considered for the magnetic case and therefore solved using the hybrid approach, only the subdomain Ω_{FEM} is of interest for the mechanical analysis. It is assumed that the mechanical stresses in the surrounding free space vanish. Since no additional mechanical surface tractions are applied, all boundary loads are purely magnetic. In order to prevent rigid body motions, the displacements of the centre of the cylinder are set to zero.
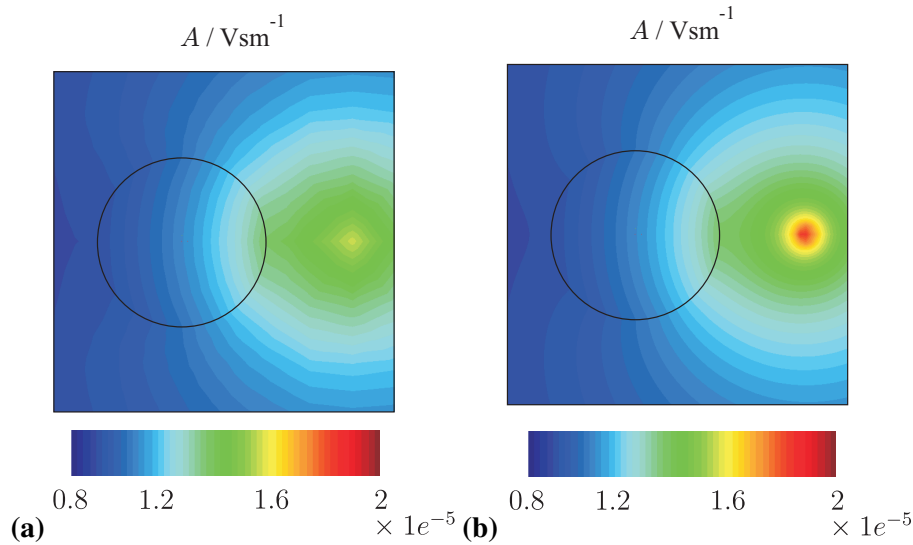
Figure 7.7: Contour plot of the magnetic potential obtained from the numerical solution of the stationary magnetic boundary value problem illustrated in Fig. 7.6: solutions obtained using the NURBS discretisation with a refinement level of **(a)** 1, and **(b)** 4. The outline of the cylinder is indicated by a black line.

Starting from the NURBS representation of the magnetisable cylinder with the order $p_1 = p_2 = p = 2$ illustrated in Fig. 7.6 (b), uniform h-refinement has been applied to study the convergence. The first refinement level is shown in Fig. 7.6 (c). In the same manner NURBS of order $p = 3$ have been examined. Numerical integration was performed using the same number of Gauss points for both, NURBS and Lagrangian dicretisations of equal order. In detail, 8 integration points have been used for regular boundary integrals, 20 for weakly singular ones and strongly singular kernels have been integrated using a number of p^2 sample points.

Mesh refinement

Contour plots of the magnetic potential are depicted in Fig. 7.7. The solution has been obtained using a second-order NURBS approximation with the refinement levels of 1 and 4, respectively. It is noted that already the coarse NURBS approximation with only 121 control points is capable of describing the principal characteristics of the solution of the stationary magnetic field problem, e.g. the flux lines entering the highly permeable cylinder at angle of approximately 90 degrees. Furthermore, Fig. 7.8 shows a contour plot of the two non-vanishing components of the magnetic induction. Both components are continuous in regions where they align with the normal vector of the cylinder surface which demonstrates the proper handling of the jump conditions.

Contour plots

Results of the convergence study are presented for the error of the potential in the L^2 norm and the energy norm for both, the domain Ω_{FEM} and the boundary Γ, Fig. 7.9. Additionally, the relative error for the force has been computed in order to assess the quality of the solution of the coupled magneto-mechanical field problem. From Fig. 7.9 it can be seen that Lagrangian and NURBS-based discretisations show a monotonic convergence behaviour although very coarse NURBS meshes are not within the range of asymptotic convergence. The convergence rates given in the error plots have therefore been computed using only the three finest meshes. It is noted, that Lagrangian approximations provide rates of convergence that are close to the optimal order for both, the L^2 and the energy norm. As expected, the NURBS-based modelling outperforms the Lagrangian polynomials in terms of the overall

Convergence study

B_1/T B_2/T

-0.002 0.002
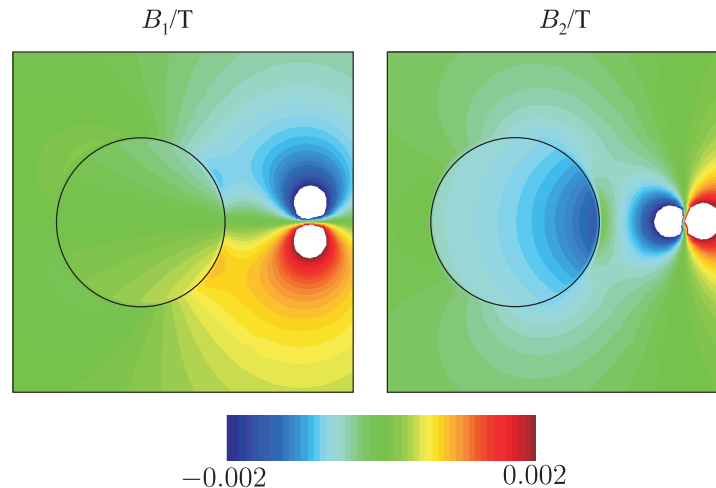
Figure 7.8: The two non-vanishing components of the magnetic induction. The outline of the cylinder is indicated by a black line. Regions with a high magnitude, e.g. the area near the conducting wire, have been blanked out in order to properly illustrate the field near the cylinder.

error level. The convergence rates obtained for IGA are also significantly higher than the optimal values which was not observed to this extent in the convergence study performed for IGAFEM in Section 6.2.2. This effect may originate from the improved continuity of the boundary representation. The relative error of the resulting force $|\Delta F_1|$ seems actually less affected by the type of basis functions as both approximations produce almost the same error levels and convergence rates. Possible explanations are that the force represents an integral quantity and that the solution of the coupled magneto-mechanical problem is affected by results from the solution of the stationary magnetic field problem.

7.4.2 Heterogeneous Magnetoactive Material in an External Field

Problem description

The second example illustrates the modelling of magnetostriction by the hybrid IGAFEM/-BEM approach. It considers an elliptic sample which consists of magnetisable particles embedded in a soft polymeric matrix, Fig. 7.10. Similar to the periodic unit cell in Chapter 4, a simple two-dimensional arrangement of three particles is considered. To allow for magnetically induced deformations of the sample while preventing rigid body motions, the displacements of a set of control points on the horizontal axis of symmetry have been constrained, Fig. 7.10 (a). The NURBS mesh used in the entire analysis is given in Fig. 7.10 (b).

Magnetic loads

The magnetic stimulus is provided by a coil which is represented by several conducting wires in the two-dimensional setting. These wires carry opposite currents $J = \pm 2$A and generate an almost homogeneous external magnetic field $\bar{\mathbf{B}}$. However, the local fields induced by the magnetisation of the particles will result in attractive or repulsive interactions between the particles. These particle-particle interactions generate an observable magnetostriction of the elliptic sample. Two principal loadings are considered. The horizontal orientation of the coil generates a magnetic field $\bar{\mathbf{B}} = \begin{bmatrix} \bar{B}_1, & 0 \end{bmatrix}^T$, red in Fig. 7.10 (a), while the vertical arrangement leads to $\bar{\mathbf{B}} = \begin{bmatrix} 0, & \bar{B}_2 \end{bmatrix}^T$, blue in Fig. 7.10 (a).
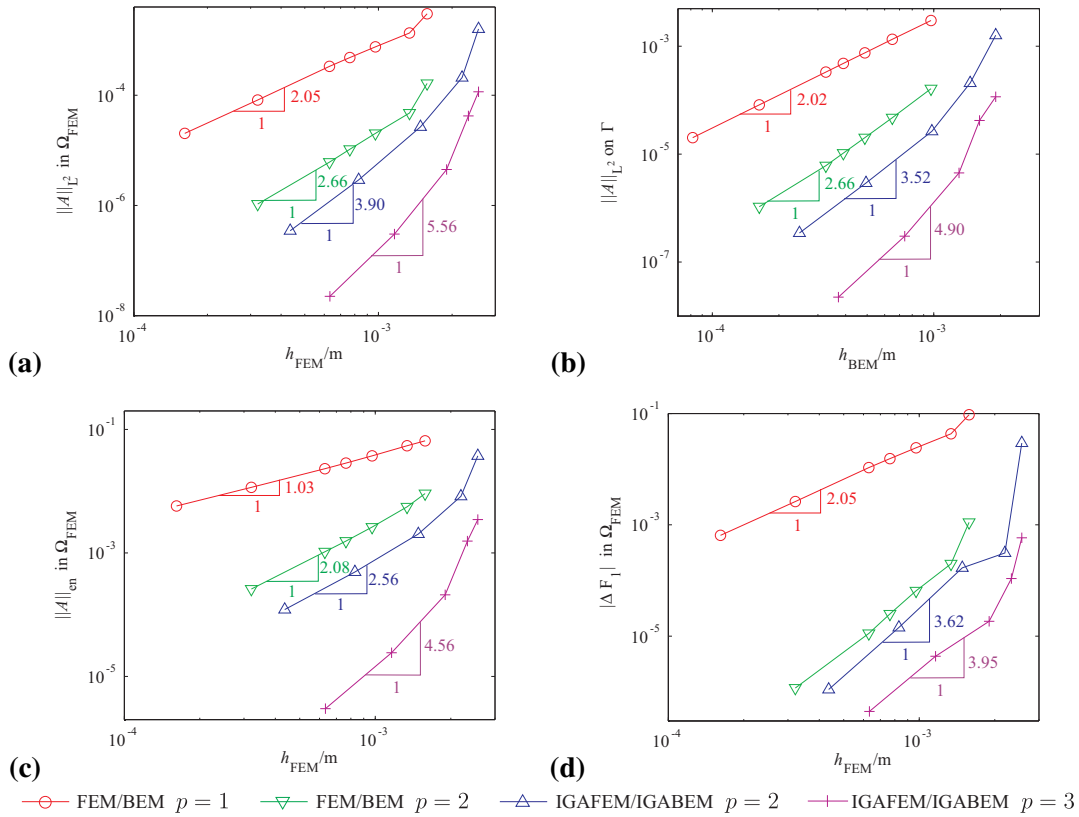
Figure 7.9: Results of the convergence analysis: **(a)** error $||A||_{L^2}$ in the domain Ω_{FEM}, **(b)** error $||A||_{L^2}$ on the boundary Γ, **(c)** error $||A||_{\mathrm{en}}$ in the domain Ω_{FEM}, and **(d)** relative error $|\Delta F_1|$ of the resulting force per unit length acting on the cylinder as a function of the maximum characteristic element size h of the domain Ω_{FEM} and the boundary Γ, respectively.
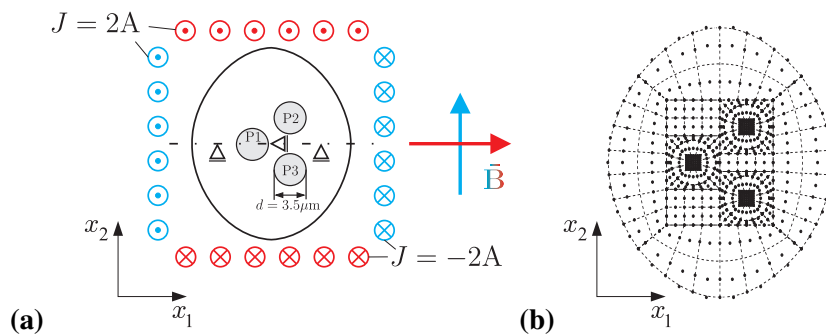
Figure 7.10: Elliptic sample of a magnetoactive material consisting of magnetisable particles and a polymeric matrix: **(a)** model arrangement with two possible external magnetic fields, horizontal (red) or vertical (blue), and **(b)** initial NURBS mesh used for analysis.

Table 7.1: Material parameters of the viscoelastic matrix.

E^{eq}	ν	E^{ov}	τ	s_0
0.2 MPa	0.4	1 MPa	10 s	0.15 MPa

Material behaviour

The particles are assumed to show a linear isotropic magnetisation behaviour with the relative permeability $\mu_r^{\mathrm{P}} = 1 \times 10^3$. The polymer matrix is non-magnetisable, $\mu_r^{\mathrm{M}} = 1$. The linearity of the stationary magnetic field problem allows for its solution in a single loadstep. In contrast, the magneto-mechanical field problem exhibits physical non-linearities due to the considered non-linear strain rate dependence which is typical for polymers. Therefore, it is solved iteratively in a Newton-Raphson scheme using several load steps. The mechanical behaviour is formulated in terms of the pseudo-mechanical stress $_{\mathrm{E}}\boldsymbol{\sigma}$. While the particles are modelled isotropic linear elastic ($E^{\mathrm{P}} = 2.1 \times 10^5\,\mathrm{MPa}$, $\nu^{\mathrm{P}} = 0.3$), a non-linear viscoelastic material model with a stress dependent viscosity [116] is used to represent the polymeric matrix. It consists of a linear elastic equilibrium relation and a non-linear viscoelastic overstress branch. The fundamental relations are given by

$$_{\mathrm{E}}\boldsymbol{\sigma} = {_{\mathrm{E}}\boldsymbol{\sigma}}^{\mathrm{eq}} + {_{\mathrm{E}}\boldsymbol{\sigma}}^{\mathrm{ov}}, \qquad {_{\mathrm{E}}\boldsymbol{\sigma}}^{\mathrm{eq}} = \mathbf{E}^{\mathrm{eq}}\boldsymbol{\varepsilon}, \tag{7.31}$$

$$_{\mathrm{E}}\dot{\boldsymbol{\sigma}}^{\mathrm{ov}} + \frac{1}{\tilde{\tau}}\,{_{\mathrm{E}}\boldsymbol{\sigma}}^{\mathrm{ov}} = \mathbf{E}^{\mathrm{ov}}\dot{\boldsymbol{\varepsilon}}, \quad \tilde{\tau} = \tau \exp\left(-\frac{\|{_{\mathrm{E}}\boldsymbol{\sigma}}^{\mathrm{ov}}\|}{s_0}\right). \tag{7.32}$$

In these constitutive equations, $_{\mathrm{E}}\boldsymbol{\sigma}$ is the pseudo-mechanical stress, and $_{\mathrm{E}}\boldsymbol{\sigma}^{\mathrm{eq}}$ and $_{\mathrm{E}}\boldsymbol{\sigma}^{\mathrm{ov}}$ are its equilibrium and strain rate dependent overstress parts, respectively. $\mathbf{E}^{\mathrm{eq}}$ and $\mathbf{E}^{\mathrm{ov}}$ are fourth-order elasticity tensors whose elements are computed from the material parameters E^{eq}, E^{ov}, and ν. The load dependent viscosity is taken into account by an overstress dependent relaxation time $\tilde{\tau}$. A set of material parameters has been chosen in order to account for a soft polymer matrix, Tab. 7.1.

Simulation

The time frame of the magneto-mechanical simulation has been set to $t \in [0,\,200]$s. Starting from an undeformed stress-free configuration, the magnetic field quantities known from the previous solution of the magnetic field are gradually applied in 20 equidistant time increments until $t = 100$ s. This is followed by 20 additional increments covering another 100 seconds. During this time the magnetic field is kept constant and the viscoelastic characteristics of the polymer results in an ongoing motion of the particles due to creep deformations of the matrix.

Results

The magnetic potential as well as the deformation of the sample at the end of the simulation are illustrated in Fig. 7.11 for both orientations of the magnetic field $\bar{\mathbf{B}}$. It can be seen that the magnetically induced attractive or repulsive interactions of the particles cause either an elongation or contraction of the sample, i.e. a magnetostrictive effect can be observed. The deformation behaviour is in agreement with the numerical results for effective macroscopic actuation stresses in Chapter 4. Displacement-time ($u_{x_2} - t$) curves that illustrate the vertical motion of the particle centres for both orientations of the magnetic field are plotted in Fig. 7.12. While the vertical position of particle (P1) remains constant due to the symmetry of the arrangement, the upper (P2) and lower (P3) particles attract or repel each other depending on the orientation of the magnetic field. In correspondence to the previously described loading, two time domains can be identified. In the first (grey domain), the displacement of the particles increases progressively with the magnetic field. In the second (white domain), the magnetic field and therefore the magnetic forces remain constant. The ongoing deforma-
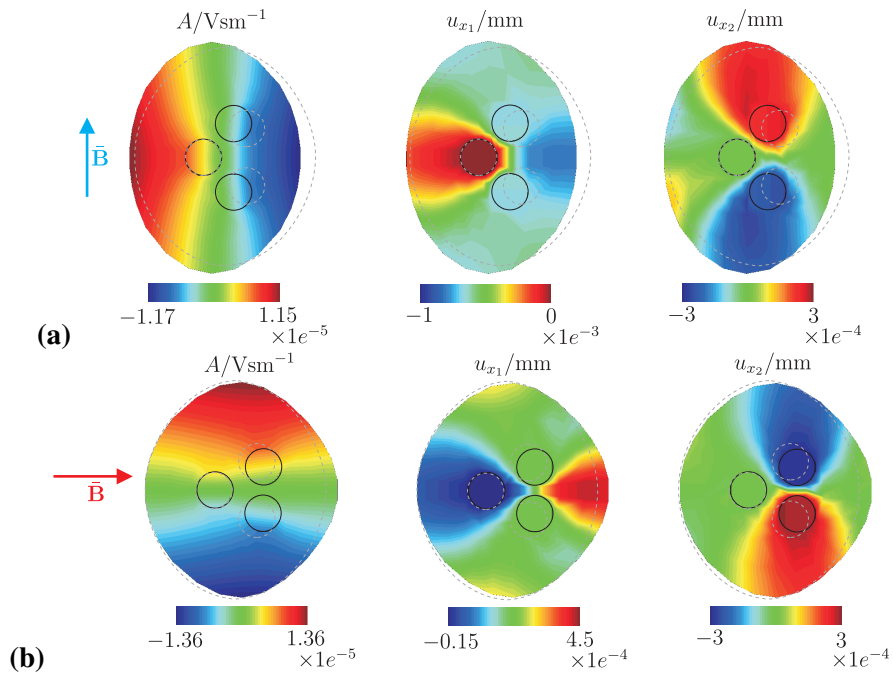
Figure 7.11: Local magnetic fields and magnetically induced deformation of an elliptic sample for **(a)** a vertically, and **(b)** a horizontally aligned magnetic field $\bar{\mathbf{B}}$. The dashed grey lines illustrate the original undeformed configuration, while the solid black lines show the position of the particles at the end of the simulation.

tion is caused by creep effects in the viscoelastic matrix material and approaches a state of equilibrium.
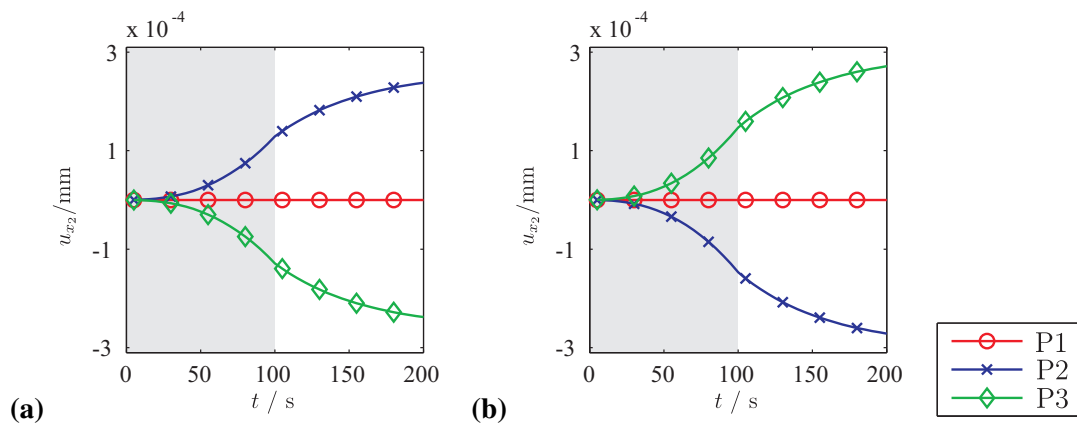
Figure 7.12: Displacement-time curves of the particle centres for **(a)** a vertical, and **(b)** a horizontal orientation of the magnetic field. Two time regimes can be identified. In the first (grey region), the displacement increases progressively due to the increasing magnetic field. In the second (white region), the deformation continues to increase at a constant magnetic field due to creep effects in the viscoelastic matrix.

7.5 Conclusion

In this chapter isogeometric analysis has been utilised to solve two-dimensional stationary magnetic and coupled magneto-mechanical field problems. The magnetic problem was handled by a hybrid IGAFEM/-BEM approach. While IGAFEM was used to model the magnetisable body, IGABEM accounted for the infinite domain representing the free space. As a consequence, truncation errors are avoided and no meshing of the free space was required. The subsequent solution of the magneto-mechanical field problem was obtained from applying IGAFEM to discretise the domain of the magnetisable body which allows for inelastic material behaviour. Magnetic contributions to the total stress as well as to the surface traction acting on this body were obtained from the solution of the stationary magnetic field problem provided by the hybrid IGAFEM/-BEM method. Compared to discretisations based on Lagrangian polynomial shape functions the isogeometric approach was proved to be more efficient.

8 Isogeometric Phase-Field Modelling of Structural Evolution Processes [KMdB16]

In the first chapter of this work sharp and diffuse interface models have been introduced. Owing to the classical continuum formulation of the underlying boundary value problems, only sharp interface representations were used in the preceding chapters. With the diffuse interface model being a fundamental part of the phase-field method, the Cahn-Hilliard model [29, 30] will be considered as an illustrative example for the diffuse approach below. The Cahn-Hilliard model was originally derived to describe the spinodal decomposition of binary mixtures but has later been used in more complex phase-field models. A difficulty regarding the solution of phase-field models including the Cahn-Hilliard model is that they typically involve spatial differential operators that are higher than second-order. Therefore, standard finite elements based on C^0-continuous Lagrangian polynomial shape functions do not provide converging solutions when directly applied to the phase-field equation. Starting with the work of Gómez [80] a new approach has emerged which combines phase-field models with spline-based approximations. The higher-order continuity of splines allows for a direct discretisation of the weak forms as explained below. In this way isogeometric analysis enables an accurate and efficient resolution of steep gradients that can occur when higher-order derivatives are introduced.

<div align="right">Motivation</div>

Phase-field models have become a powerful tool for the modelling of phase transformations and morphological changes in different fields of physics as well as materials and engineering science. Compared to sharp interface models their advantage is that topological changes are avoided, since interfaces are treated in a diffuse manner which is achieved through a parameter which varies continously. This phase-field parameter accounts for the different material phases and/or the concentration of the different components. Such an approach allows to fully capture the physics of the individual interfaces without the need to explicitly track them. Typical applications include the modelling and simulation of solidification processes, spinodal decomposition, coarsening of precipitate phases, shape memory effects, re-crystallisation, and dislocation dynamics [36, 60, 143, 197]. Phase-field models have been successfully applied to model tumor growth [91, 218, 226], and image impainting [14]. The phase-field approach has also been used to model crack propagation [93, 123, 138, 140, 194]. Diffuse interface representations can also be of interest to predict microstructural changes under external fields [198, 122]. They are therefore considered in this work.

<div align="right">Phase-field models</div>

This chapter is organised as follows: Section 8.1 will briefly review the derivation of the Cahn-Hilliard equation. In Section 8.2, two different finite element formulations for the numerical solution of the Cahn-Hilliard problem, i.e. a mixed form and a direct approach, are discussed. These formulations are compared and their numerical properties are analysed in terms of error norms and convergence rates in Section 8.3. Eventually, it will be shown that both formulations provide statistically similar results for two exemplary demonstration problems in Section 8.4.

<div align="right">Outline</div>

8.1 Cahn-Hilliard Model of Spinodal Decomposition

Free energy

The governing equation of the Cahn-Hilliard model can be derived from a concentration dependent free energy density $f(c)$. In order to incorporate gradients and interfacial energy terms, a truncated Taylor series expansion of $f(c)$ with respect to c

$$\bar{f}(c) = f(c) + L_i c_{,i} + K_{ij} c_{,i} c_{,j} + \dots \tag{8.1}$$

is employed. Since $L_i = 0$ for symmetry reasons, and $K_{ij} = \lambda \delta_{ij}$ for isotropic systems, the truncated free energy can be written as

$$\bar{f}(c) = f(c) + \lambda c_{,i}^2 . \tag{8.2}$$

Here, λ is the interface parameter that governs the thickness of the diffuse interface. Integration over the domain Ω yields the total Ginsburg-Landau free energy functional

$$\mathcal{F} = \mathcal{F}_{\text{bulk}} + \mathcal{F}_{\text{int}} = \int\limits_{\Omega} \left(f(c) + \lambda c_{,i}^2 \right) \ \mathrm{d}V \tag{8.3}$$

which contains two contributions, a configurational or bulk energy $\mathcal{F}_{\text{bulk}}$, and an interface energy $\mathcal{F}_{\text{int}}$. It is actually the interface energy term which leads to the fourth-order derivatives in the phase-field approaches.

Chemical potential

The chemical potential follows as variational derivative of the free energy density

$$\mu = \frac{\delta \bar{f}}{\delta c} = \frac{\partial \bar{f}}{\partial c} - \left(\frac{\partial \bar{f}}{\partial c_{,i}} \right)_{,i} = f'(c) - \lambda c_{,ii} \quad \text{with} \quad (\cdot)' = \frac{d(\cdot)}{dc} . \tag{8.4}$$

It is the thermodynamical driving force which governs the structural evolution process and is therefore used in the constitutive equation defining the concentration flux

$$J_i = -M(c) \mu_{,i} . \tag{8.5}$$

This equation involves the mobility $M(c)$ as a concentration dependent material property.

Cahn-Hilliard equation

The Cahn-Hilliard equation is finally obtained from considering the balance of mass (2.18) in the form

$$\frac{dc}{dt} = \frac{\partial c}{\partial t} = -J_{i,i} . \tag{8.6}$$

Combining equations (8.5) and (8.6) yields the fourth-order Cahn-Hilliard equation

$$\frac{\partial c}{\partial t} = \left[M(c) \left(f'(c) - \lambda c_{,kk} \right)_{,i} \right]_{,i} \tag{8.7}$$

which is valid in the domain Ω. To fully define the boundary value problem of structural evolution, two sets of boundary conditions and an intial condition for the concentration field $c\left(x_k, t\right)$ are required, cf. Section 8.2.

Mobility

As it can be seen from equation (8.7), the evolution process depends on the interaction of bulk and interfacial energy terms. Their ratio is governed by the interface parameter λ. The mobility $M(c)$ characterises the ability for diffusion processes. Mainly two different choices for the mobility $M(c)$ are considered in the literature: (i) $M = \text{const.}$ or (ii) $M = Dc(1-c)$.
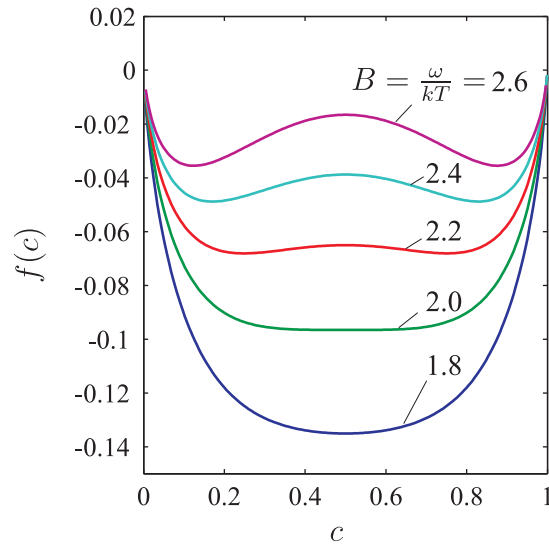
Figure 8.1: Plot of the free energy density function (8.8) as a function of $B = \frac{\omega}{kT}$: A double well shape is observed for ratios $B > 2$.

The latter is known as degenerate mobility and restricts diffusion processes primarily to the interface zones, because $M(c)$ is significantly lower in domains of pure phases than across the interface which is assumed to be a more realistic assumption than a constant value.

Whether decomposition occurs depends on the free energy

$$f(c) = A\left[c\ln(c) + (1-c)\ln(1-c) + Bc(1-c)\right] . \tag{8.8}$$

Double well potential

Its pararameters $A = NkT$ and $B = \omega/kT$ depend on the absolute temperature T, the number of molecules per unit volume N, Boltzmann's constant k, and a parameter ω related to the mixing enthalpy. For $B > 2$, the chemical free energy is non-convex, Fig. 8.1. Its two wells drive phase separation into domains whose concentrations are defined by the minima of $f(c)$. They are called binodal points. For $B \leq 2$ the free energy has a single well which leads to homogeneously distributed phases. Decomposition is only observed for certain temperature ranges, i.e. when the temperature decreases, mixtures with a concentration in between the two spinodal points become unstable [201]. Only isothermal processes with $B > 2$ are considered here.

8.2 Finite Element Formulation

As a consequence of the fourth-order spatial derivatives in the Cahn-Hilliard equation (8.7), the corresponding weak form will involve second-order partial derivatives. To obtain converging solutions, a direct discretisation will require at least C^1 inter-element continuity of the used approximations. Lagrangian polynomials that provide only C^0 continuity can therefore not be applied directly. Consequently, three major alternative approaches to the finite element discretisation of the Cahn-Hilliard equation have been pursued:

Spatial discretisation

(i) *Mixed formulation:* The fourth-order equation is decomposed into a coupled system of two second-order partial differential equations [4, 59]. Since the corresponding weak

forms will contain only first-order derivatives, the need for higher-order continuity across element boundaries is avoided and C^0-continuous Lagrangian interpolations can be applied.

(ii) *Discontinuous Galerkin:* The application of this method was proposed in [229]. A slightly different approach by Wells et al. [225] combines features of continuous and discontinuous Galerkin methods as outlined in [62], i.e. it uses a lower-order continuity of the basis functions than actually required by the weak form. Hence, C^0-continuous Lagrangian basis functions are applicable and the first-order inter-element continuity is weakly enforced by Nitsche's method.

(iii) *Direct discretisation:* The weak form of the Cahn-Hilliard equation is discretised by elements that provide at least C^1 continuity. Approaches include Hermite elements [33, 201] as well as isogeometric discretisations [80, 132].

Discussion These different discretisation strategies come along with certain advantages and drawbacks. The solution of the coupled system can lead to stability issues [201] which motivated the development of the direct discretisation approach. Zhang et al. [232] have presented a quantitative comparison of the coupled formulation with quadratic Lagrangian polynomials and the direct approach with C^1-continuous cubic Hermite elements. It was observed that both solution schemes deliver optimal convergence rates. Since different polynomial orders have been used with both methods, a direct comparison of error levels and convergence rates is however not possible. Therefore, a ratio of accuracy vs. computational costs has been investigated with similar results for both procedures. Despite the promising results obtained for the Hermitean elements, one has to keep in mind that there are only few elements with C^1 continuity in two dimensions and none for three-dimensional problems. Moreover, both formulations involve degrees of freedom in addition to the primary field variable c. The only approach avoiding them is the continuous/discontinuous Galerkin formulation [225] but it requires a change of the data structure due to the weak enforcement of the C^1 continuity across element boundaries. Besides this, the penalty parameter has to be carefully chosen in order to avoid instabilities or accuracy issues, respectively. In this work, isogeometric analysis, cf. Chapter 6, will be applied to the spatial discretisation of the Cahn-Hilliard equation which was first proposed by Gómez et al. [80]. Different from all previous approaches it offers higher-order continuity without introducing additional degrees of freedom. In Section 8.2.1, the mixed formulation as well as the direct discretisation of the fourth-order partial differential equation will be briefly outlined. All equations are given for a concentration dependent mobility $M(c)$ and the most general case of boundary conditions. Both formulations have been implemented and are employed in a comparative convergence analysis in Section 8.3.

8.2.1 Spatial Discretisation

Approximation As outlined in Section 6.1.2, Bézier extraction facilitates the incorporation of isogeometric analysis into any existing finite element code by simply replacing the shape function routines. Therefore, a finite element point of view can be adopted for both FEM and IGAFEM. The analysis domain Ω is discretised by a set of n_e either standard or Bézier finite elements $\Omega = \bigcup_{I=1}^{n_e} \Omega_{Ie}$. In addition, Lagrangian and spline-based approximations of a generalised primary field variable $u = \{c, \mu\}$, and its spatial derivatives in each element domain Ω_e are given by

$$u = \underline{\mathbf{N}}\,\underline{\mathbf{u}}, \quad u_{,k} = \underline{\underline{\mathbf{B}}}\,\underline{\mathbf{u}}, \quad u_{,kk} = \underline{\underline{\mathbf{B}}}'\underline{\mathbf{u}} \tag{8.9}$$

with $\underline{\mathbf{N}}$, $\underline{\underline{\mathbf{B}}}$, and $\underline{\underline{\mathbf{B}}}'$ row vector or matrix representations of the element shape functions and their corresponding first- and second-order spatial derivatives. All nodal or control point degrees of freedom are contained in the column vector $\underline{\mathbf{u}}$. Following a standard Ritz or Galerkin approach, the same approximations will be used for the weight functions.

In the mixed formulation approach, the fourth-order Cahn-Hilliard equation is split into a system of two second-order partial differential equations

$$\frac{\partial c}{\partial t} = (M(c)\mu_{,i})_{,i} \tag{8.10}$$

$$\mu = f' - \lambda c_{,ii} \,. \tag{8.11}$$

This is accomplished by introducing the chemical potential μ, cf. equation (8.4), as an additional primary field variable. The corresponding weak form of the system is obtained by multiplying the equations (8.10) and (8.11) by test functions w and v, respectively. Integration by parts and applying Gauss' theorem eventually lead to

$$\int_\Omega \frac{\partial c}{\partial t} w \,\, \mathrm{d}V + \int_\Omega M(c)\mu_{,i}w_{,i} \,\, \mathrm{d}V = \int_{\partial\Omega} M(c)\mu_{,i}n_i w \,\, \mathrm{d}S \tag{8.12}$$

$$\int_\Omega \mu v \,\, \mathrm{d}V - \int_\Omega f'(c) v \,\, \mathrm{d}V - \int_\Omega \lambda c_{,i} v_{,i} \,\, \mathrm{d}V = - \int_{\partial\Omega} \lambda c_{,i} n_i v \,\, \mathrm{d}S \,. \tag{8.13}$$

The right hand sides of equations (8.12) and (8.13) allow for the identification of the corresponding boundary conditions

$$c = g_1 \quad \text{on} \quad \partial\Omega_{1_g} \vee \mu_{,i}n_i = h_1 \quad \text{on} \quad \partial\Omega_{1_h} \tag{8.14}$$

$$\mu = g_2 \quad \text{on} \quad \partial\Omega_{2_g} \vee c_{,i}n_i = h_2 \quad \text{on} \quad \partial\Omega_{2_h} \,. \tag{8.15}$$

The parts of the boundary with essential or natural boundary conditions satisfy $\partial\Omega_{i_g} \cup \partial\Omega_{i_h} = \partial\Omega$ and $\partial\Omega_{i_g} \cap \partial\Omega_{i_h} = \varnothing$. Due to the presence of a time derivative which accounts for the temporal evolution of the concentration field an appropriate initial condition

$$c(x_k, t = 0) = c_0(x_k) \quad \text{in} \quad \Omega \tag{8.16}$$

is required. Initial values $\mu(x_k, t = 0)$ of the potential that are consistent with $c(x_k, t = 0)$ are computed from equation (8.11).

As exclusively homogeneous essential and natural as well as periodic boundary conditions are used in this work, the boundary integrals in equations (8.12) and (8.13) vanish and will therefore be omitted in the remainder. Inserting the approximations (8.9) into the weak form and taking into consideration the arbitrariness of the control point values of the test functions, yields the following non-linear system of equations for each element Ω_e:

$$\underline{\mathbf{r}}^c = \int_{\Omega_\mathrm{e}} \underline{\mathbf{N}}^T \underline{\mathbf{N}} \, \underline{\dot{\mathbf{c}}} \, \mathrm{d}V + \int_{\Omega_\mathrm{e}} \underline{\underline{\mathbf{B}}}^T M(c) \underline{\underline{\mathbf{B}}} \, \underline{\boldsymbol{\mu}} \, \mathrm{d}V = \underline{\mathbf{0}} \tag{8.17}$$

$$\underline{\mathbf{r}}^\mu = \int_{\Omega_\mathrm{e}} \underline{\mathbf{N}}^T \underline{\mathbf{N}} \, \underline{\boldsymbol{\mu}} \, \mathrm{d}V - \int_{\Omega_\mathrm{e}} \underline{\mathbf{N}}^T f'(c) \, \mathrm{d}V - \int_{\Omega_\mathrm{e}} \underline{\underline{\mathbf{B}}}^T \lambda \underline{\underline{\mathbf{B}}} \, \underline{\mathbf{c}} \, \mathrm{d}V = \underline{\mathbf{0}} \,. \tag{8.18}$$

Here, $\underline{\mathbf{r}}^c$ and $\underline{\mathbf{r}}^\mu$ represent the residuals, while $\underline{\dot{\mathbf{c}}} = \partial \underline{\mathbf{c}} / \partial t$ replaces the partial derivative with

respect to time. Because the connection between $\underline{\dot{c}}$ and $\underline{c}$ is determined by the employed time integration scheme presented in section 8.2.2, equations (8.17) and (8.18) are often referred to as the semidiscrete weak form.

Direct discretisation

Following the same lines, the corresponding weak form for the direct discretisation is obtained from taking the weighted residual (test function w) of equation (8.7). Using integration by parts, the weak form

$$\int_\Omega \left(\frac{\partial c}{\partial t} w + M(c) f'_{,i}(c) w_{,i} + M_{,i}(c) \lambda c_{,kk} w_{,i} + M(c) \lambda c_{,kk} w_{,ii} \right) \, \mathrm{d}V = \ldots$$

$$\ldots = \int_{\partial\Omega} M(c) \left(f'(c) - \lambda c_{,kk} \right)_{,i} w n_i \, \mathrm{d}S + \int_{\partial\Omega} M(c) \lambda c_{,kk} w_{,i} n_i \, \mathrm{d}S \tag{8.19}$$

ensues. The boundary conditions

$$c = g_1 \quad \text{on} \quad \partial\Omega_{1_g} \vee \left(f'(c) - \lambda c_{,kk} \right)_{,i} n_i = \mu_{,i} n_i = h_1 \quad \text{on} \quad \partial\Omega_{1_h} \tag{8.20}$$

$$c_{,i} n_i = g_2 \quad \text{on} \quad \partial\Omega_{2_g} \vee c_{,kk} = h_2 \quad \text{on} \quad \partial\Omega_{2_h} \tag{8.21}$$

can be identified from the boundary integrals forming the right hand side of the weak form (8.19). While the set of conditions found for $\partial\Omega_1$ match equation (8.14), a permutation of the essential g_2 and natural h_2 boundary conditions can be observed for $\partial\Omega_2$. However, the second set of boundary conditions is equivalent to (8.15) as the condition $c_{,kk} = h_2$ in combination with g_1 corresponds to a given value for the chemical potential μ. The parts of the boundary with essential or natural boundary conditions satisfy $\partial\Omega_{i_g} \cup \partial\Omega_{i_h} = \partial\Omega$ and $\partial\Omega_{i_g} \cap \partial\Omega_{i_h} = \varnothing$.

Semidiscrete equations

Taking into account the special choice of homogeneous or periodic boundary conditions that lead to vanishing boundary integrals in equation (8.19), the semidiscrete form of the direct approach reads

$$\underline{r} = \int_{\Omega_e} \underline{N}^T \underline{N} \, \underline{\dot{c}} \, \mathrm{d}V + \int_{\Omega_e} \underline{\underline{B}}^T M(c) f''(c) \underline{\underline{B}} \, \underline{c} \, \mathrm{d}V + \ldots$$

$$\ldots + \int_{\Omega_e} \underline{\underline{B}}^T \lambda M'(c) \underline{B}' \underline{c} \underline{\underline{B}} \, \underline{c} \, \mathrm{d}V + \int_{\Omega_e} \underline{B}'^T \lambda M(c) \underline{B}' \underline{c} \, \mathrm{d}V = \underline{0} \tag{8.22}$$

with $\underline{r}$ the residual vector.

8.2.2 Temporal Discretisation

Generalised-α method

For the temporal discretisation it is necessary to apply an efficient but accurate time integration algorithm. In order to achieve an optimal ratio of high- and low-frequency dissipation, Chung and Hulbert [38] introduced the generalised-α method. In case of linear, first-order differential equations in time having the form $\underline{r}\,(\underline{u}, \underline{\dot{u}}) = \underline{0}$, the method is given by the set of

equations

$$\underline{\mathbf{0}} = \underline{\mathbf{r}} \left(\underline{\mathbf{u}}_{n+\alpha_{\mathrm{f}}}, \underline{\dot{\mathbf{u}}}_{n+\alpha_{\mathrm{m}}} \right) \tag{8.23}$$

$$\underline{\mathbf{u}}_{n+1} = \underline{\mathbf{u}}_n + \Delta t_n + \gamma \Delta t_n \left(\underline{\dot{\mathbf{u}}}_{n+1} - \underline{\dot{\mathbf{u}}}_n \right) \tag{8.24}$$

$$\underline{\mathbf{u}}_{n+\alpha_{\mathrm{f}}} = \underline{\mathbf{u}}_n + \alpha_{\mathrm{f}} \left(\underline{\mathbf{u}}_{n+1} - \underline{\mathbf{u}}_n \right) \tag{8.25}$$

$$\underline{\dot{\mathbf{u}}}_{n+\alpha_{\mathrm{m}}} = \underline{\dot{\mathbf{u}}}_n + \alpha_{\mathrm{m}} \left(\underline{\dot{\mathbf{u}}}_{n+1} - \underline{\dot{\mathbf{u}}}_n \right) . \tag{8.26}$$

Here, $\Delta t_n = t_{n+1} - t_n$ represents the current time step size, while the constants α_{f}, α_{m} and γ are algorithmic parameters controlling numerical dissipation. For an unconditionally stable, second-order accurate time integration scheme, they can be expressed in terms of a single parameter ρ_∞ [105]

$$\alpha_{\mathrm{f}} = \frac{1}{1 + \rho_\infty} \quad , \quad \alpha_{\mathrm{m}} = \frac{3 - \rho_\infty}{2(1 + \rho_\infty)} \quad \text{and} \quad \gamma = \frac{1}{2} + \alpha_{\mathrm{m}} - \alpha_{\mathrm{f}} . \tag{8.27}$$

A good performance of the algorithm can be achieved by setting $\rho_\infty = 0.5$ [80, 105]. It is noted that for $\alpha_{\mathrm{f}} = \alpha_{\mathrm{m}} = \gamma = 1$, the generalised-$\alpha$ method contains the implicit Euler method as a special case.

The non-linear governing equation $\underline{\mathbf{r}} \left(\underline{\mathbf{u}}_{n+\alpha_{\mathrm{f}}}, \underline{\dot{\mathbf{u}}}_{n+\alpha_{\mathrm{m}}} \right) = \underline{\mathbf{0}}$ has to be linearised in order to solve for the field variable $\underline{\mathbf{u}}_{n+1}$ at time t_{n+1} starting from given values $\underline{\mathbf{u}}_n$ and $\underline{\dot{\mathbf{u}}}_n$ at time t_n. Different from [80, 105] the linearisation is taken with respect to $\underline{\mathbf{u}}_{n+1}$ which leads to the tangent stiffness matrix

Linearisation

$$\underline{\underline{\mathbf{K}}} = \frac{\partial \underline{\mathbf{r}} \left(\underline{\mathbf{u}}_{n+\alpha_{\mathrm{f}}}, \underline{\dot{\mathbf{u}}}_{n+\alpha_{\mathrm{m}}} \right)}{\partial \underline{\mathbf{u}}_{n+1}} = \alpha_{\mathrm{f}} \frac{\partial \underline{\mathbf{r}} \left(\underline{\mathbf{u}}_{n+\alpha_{\mathrm{f}}}, \underline{\dot{\mathbf{u}}}_{n+\alpha_{\mathrm{m}}} \right)}{\partial \underline{\mathbf{u}}_{n+\alpha_{\mathrm{f}}}} + \frac{\alpha_{\mathrm{m}}}{\gamma \Delta t_n} \frac{\partial \underline{\mathbf{r}} \left(\underline{\mathbf{u}}_{n+\alpha_{\mathrm{f}}}, \underline{\dot{\mathbf{u}}}_{n+\alpha_{\mathrm{m}}} \right)}{\partial \underline{\dot{\mathbf{u}}}_{n+\alpha_{\mathrm{m}}}} . \tag{8.28}$$

The factors that precede the derivatives with respect to $\underline{\mathbf{u}}_{n+\alpha_{\mathrm{f}}}$ and $\underline{\dot{\mathbf{u}}}_{n+\alpha_{\mathrm{m}}}$ result from the relations (8.23)-(8.26).

Starting from an initialisation of the solution vector

Iterative solution

$$\underline{\mathbf{u}}_{n+1}^0 = \underline{\mathbf{u}}_n \tag{8.29}$$

$$\underline{\dot{\mathbf{u}}}_{n+1}^0 = \frac{\gamma - 1}{\gamma} \underline{\dot{\mathbf{u}}}_n , \tag{8.30}$$

a Newton-Raphson algorithm based on the linearised system of equations

$$\underline{\underline{\mathbf{K}}}^{(i)} \Delta \underline{\mathbf{u}}_{n+1}^{(i)} = \underline{\mathbf{r}}^{(i)} \left(\underline{\mathbf{u}}_{n+\alpha_{\mathrm{f}}}, \underline{\dot{\mathbf{u}}}_{n+\alpha_{\mathrm{m}}} \right) \tag{8.31}$$

is used to determine the update of the field variable $\Delta \underline{\mathbf{u}}_{n+1}^i$. Herein, the superscript i denotes the current iteration. After each iteration the field variables are updated

$$\underline{\mathbf{u}}_{n+1}^{(i)} = \underline{\mathbf{u}}_{n+1}^{(i-1)} + \Delta \underline{\mathbf{u}}_{n+1}^{(i)} \tag{8.32}$$

$$\underline{\dot{\mathbf{u}}}_{n+1}^{(i)} = \underline{\dot{\mathbf{u}}}_{n+1}^{(i-1)} + \frac{1}{\gamma \Delta t_n} \Delta \underline{\mathbf{u}}_{n+1}^{(i)} \tag{8.33}$$

and convergence criteria related to the norms of the residual $\underline{\mathbf{r}} \left(\underline{\mathbf{u}}_{n+\alpha_{\mathrm{f}}}, \underline{\dot{\mathbf{u}}}_{n+\alpha_{\mathrm{m}}} \right)$ and of the change in $\underline{\mathbf{u}}_{n+1}$ are checked.

As the processes involved in spinodal decomposition proceed at different time scales, an adaptive time stepping scheme has to be adopted for an efficient numerical solution. In this work, the algorithm proposed by Gómez et al. in [80] is employed. Since the generalised-α (GA) method contains the backward Euler (BE) method as a special case, it is possible to produce second-order accurate results $\underline{\mathbf{u}}_{n+1}^{\mathrm{GA}}$ as well as first-order accurate results $\underline{\mathbf{u}}_{n+1}^{\mathrm{BE}}$ in order to estimate the local error from

$$\varepsilon = \frac{\left\| \underline{\mathbf{u}}_{n+1}^{\mathrm{GA}} - \underline{\mathbf{u}}_{n+1}^{\mathrm{BE}} \right\|_{\infty}}{\left\| \underline{\mathbf{u}}_{n+1}^{\mathrm{GA}} \right\|_{\infty}} \ . \tag{8.34}$$

By setting an admissible tolerance $\varepsilon^{\mathrm{adm}}$ and a safety factor θ with preferably $\theta < 1$ [193], the new step size $\Delta t_n^{\mathrm{new}}$ can be computed from the current one $\Delta t_n^{\mathrm{old}}$ according to

$$\Delta t_n^{\mathrm{new}} = \left(\frac{\theta \varepsilon^{\mathrm{adm}}}{\varepsilon} \right)^{\frac{1}{2}} \Delta t_n^{\mathrm{old}} \ . \tag{8.35}$$

This elementary error control allows to keep ε close to $\varepsilon^{\mathrm{adm}}$. If the estimated error of a computed solution exceeds the chosen tolerance, the current time step is rejected and recomputed with an adapted step size. In the present simulations, a tolerance $\varepsilon^{\mathrm{adm}} = 10^{-3}$ and a safety coefficient $\theta = 0.85$ have been used.

8.3 Convergence Analysis

In this section the numerical properties of the presented finite element formulations will be compared in terms of a quantitative analysis of error levels and convergence rates for different approximations:

(i) *Mixed formulation:* first- and second-order Lagrangian polynomials, and second- to fourth-order B-splines,

(ii) *Direct discretisation:* second- to fourth-order B-splines.

As there is no analytical solution available, the technique of manufactured solutions [117, 232], is utilised. The general idea is to use an arbitrary function as analytic reference solution. Since this function will not fulfill the governing differential equations exactly, the resulting residual has to be added to the right hand side of the discrete system of equations. Due to the non-linearity of the problem, optimal convergence rates available for the linear case can only serve as an indicator. However, as there are no discontinuities and a smooth free energy functional is used, these rates should be recovered fairly well.

8.3.1 Manufactured Solution Approach

Herein, a manufactured solution is employed that varies harmonically with respect to space and time. Taking α, β, and δ as constants, it is described by

$$\hat{c}(x_k, t) = \cos \left(\alpha \pi x_1 \right) \cos \left(\beta \pi x_2 \right) \cos \left(\delta \pi t \right) \ . \tag{8.36}$$

In order to handle concentrations $c \in [-1, 1]$ which are possible with the solution (8.36), the polynomial free energy function

$$f(c) = \frac{1}{4}(1 - c^2)^2 \tag{8.37}$$

is used instead of equation (8.8). Evaluating the Cahn-Hilliard equation (8.7) for the manufactured solution (8.36) and assuming a constant mobility yields

$$\frac{\partial \hat{c}}{\partial t} - \left[M \left(f'(\hat{c}) - \lambda \hat{c}_{,kk} \right)_{,i} \right]_{,i} = Q(x_k, t) \tag{8.38}$$

with the residual

$$Q(x_k, t) = -\cos(\alpha \pi x_1) \cos(\beta \pi x_2) \left\{ \delta \pi \sin(\delta \pi t) + M \pi^2 \cos(\delta \pi t) \cdot \ldots \right. \tag{8.39}$$
$$\ldots \cdot \left[\alpha^2 + \beta^2 - \lambda \pi^2 \left(\alpha^2 + \beta^2 \right)^2 + 3 \cos^2(\delta \pi t) \cdot \ldots \right.$$
$$\ldots \cdot \left(\alpha^2 \cos^2(\beta \pi x_2) \left(2 \sin^2(\alpha \pi x_1) - \cos^2(\alpha \pi x_1) + \ldots \right. \right.$$
$$\left. \left. \left. \ldots + \beta^2 \cos^2(\alpha \pi x_1) \left(2 \sin^2(\beta \pi x_2) - \cos^2(\beta \pi x_2) \right) \right) \right] \right\} .$$

In the convergence studies carried out for the spatial and the temporal discretisation this residual $Q(x_k, t)$ represents an external body load which is completely defined in terms of the manufactured solution (8.36).

For the convergence analysis, a set of boundary conditions has to be defined. Analytical values $\hat{c}$ are prescribed on the boundary $\partial \Omega$. In isogeometric analysis, the non-interpolary nature of the basis functions does not allow to directly assign analytical values of the concentration or chemical potential to the control point values. Instead, a transformation procedure is employed to compute the control point values [223]. For the mixed form the zero flux boundary condition $c_{,i} n_i = 0$ which is compatible to $\hat{c}$ for $\alpha, \beta = 1, 2, \ldots n$ is utilised in addition to prescribing $\hat{c}$. **Boundary conditions**

In the direct discretisation approach $c_{,i} n_i = 0$ is an essential condition which requires some consideration, i.e. it is not sufficient to prescribe control values at control points associated to the immediate boundary of the domain. Instead, two consecutive rows or columns of control points in the vicinity of the boundary have to be considered. Due to the geometric map $x_k(\xi_l)$ between the physical and parametric domain, the boundary $\partial \Omega$ of the physical domain is represented in terms of one varying parametric coordinate $\xi_{\partial \Omega}$ with the second coordinate being constant. Therefore, homogeneous conditions on the normal derivative of the concentration reduce to **Strong imposition of zero flux condition**

$$\frac{dc}{d\xi_{\partial \Omega}} \left(\xi_1^{\partial \Omega} \right) = \frac{dc}{d\xi_{\partial \Omega}} (\xi_{n+p+1}^{\partial \Omega}) = 0 . \tag{8.40}$$

For a univariate, open knot vector spline basis the relations

$$\frac{dc}{d\xi_{\partial \Omega}}(\xi_1^{\partial \Omega}) = (c_2 - c_1) \frac{dN_2(\xi_{\partial \Omega})}{d\xi_{\partial \Omega}}(\xi_1^{\partial \Omega}) = 0 \tag{8.41}$$

$$\frac{dc}{d\xi_{\partial \Omega}}(\xi_{n+p+1}^{\partial \Omega}) = (c_{n-1} - c_n) \frac{dN_{n+p+1}(\xi_{\partial \Omega})}{d\xi_{\partial \Omega}}(\xi_{n+p+1}^{\partial \Omega}) = 0 \tag{8.42}$$

hold. Hence, the homogeneous essential zero flux condition can be imposed by setting the
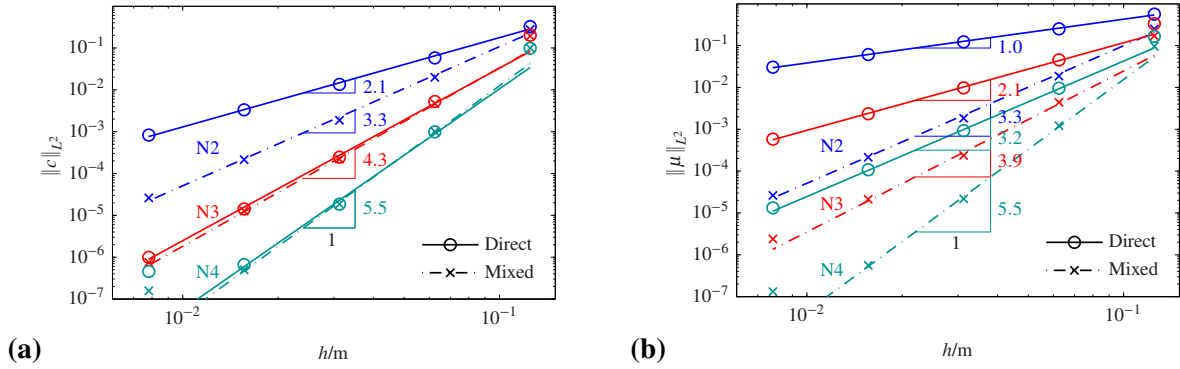
Figure 8.2: Quantitative comparison between the mixed formulation and the direct discretisation of the Cahn-Hilliard equation for second-order (N2), third-order (N3), and fourth-order (N4) B-splines: **(a)** L^2 error of the concentration c, and **(b)** L^2 error of the chemical potential μ as function of the element size h. In case of the direct discretisation μ is computed from $\mu = f'(c) - \lambda c_{,kk}$. Therefore, the error is governed by the H^2 error norm of the concentration field c.

control variables to $c_1 = c_2$ and $c_{n-1} = c_n$. It can be observed that due to the homogeneity of the boundary condition, there is no influence of the derivatives of the basis functions. This, however, does not hold for the case for periodic boundary conditions discussed in Section 8.4.

8.3.2 Convergence Analysis for the Spatial Discretisation

Mixed vs. direct formulation

All results of this study have been obtained using the following set of parameters: $\lambda = 0.1\,\mathrm{J\,m^{-1}}$, $M = 500\,\mathrm{m^3\,s\,kg^{-1}}$, $\alpha = \beta = 6$, and $\delta = \frac{2}{3}$. Five meshes of a unit square domain Ω with $2^n \times 2^n$ elements ($n = 3 \ldots 7$) have been considered. The focus is first put on a comparison of the performance of the mixed formulation and the direct discretisation of the Cahn-Hilliard equation. Results of isogeometric finite element analyses are shown in Fig. 8.2. The L^2 error of the concentration field in Fig. 8.2 (a) shows a monotonic convergence for both formulations. For the mixed formulation, convergence rates are obtained which are similar to the optimal value of h^{p+1} valid for linear problems with p the order of the approximation. The results of the direct discretisation approach match the mixed formulation in terms of error levels and convergence rates for the third-order and the fourth-order approximations. For the second-order shape functions a lower convergence rate is observed for the direct approach. This is in accordance with theoretical findings for higher-order differential operators, see the discussion in Section 8.3.3.

Chemical potential

For the chemical potential μ in Fig. 8.2 (b), the two formulations are fundamentally different. The mixed approach uses the same order of approximation for c and μ and, hence, provides the same accuracy and convergence behaviour for both variables. For the direct discretisation, the chemical potential $\mu = f'(c) - \lambda c_{,kk}$ is computed from the primary field variable which involves second-order derivatives. The error of the chemical potential is therefore governed by the H^2 error norm of the concentration field c, for which an optimal convergence rate of $p - 1$ is expected in the linear case. It is almost identically recovered by the numerical convergence study of Fig. 8.2 (b).

Efficiency

In Fig. 8.3 the same information is plotted as a function of the total number of degrees of freedom. It illustrates the fact that the direct discretisation requires less degrees of freedom
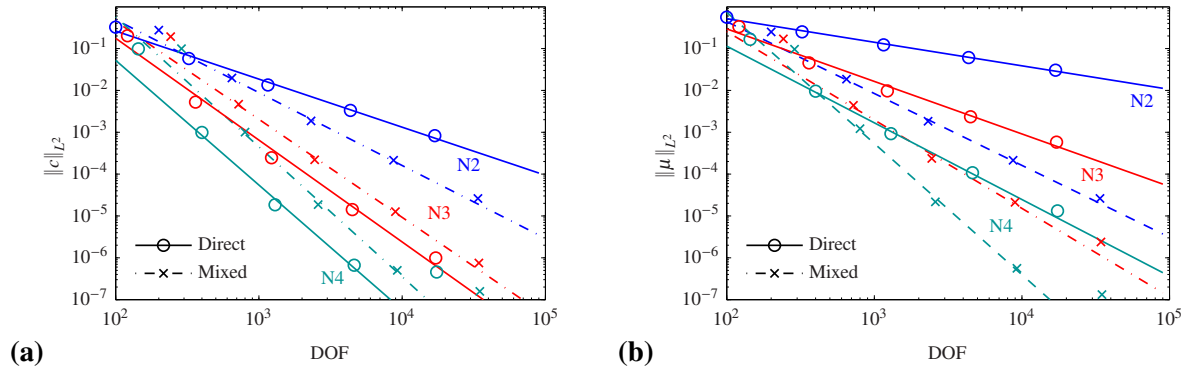
(a) **(b)**

Figure 8.3: Quantitative comparison between the mixed formulation and the direct discretisation of the Cahn-Hilliard equation for second-order (N2), third-order (N3), and fourth-order (N4) B-splines as function of the total number of degrees of freedom (DOF): **(a)** L^2 error norm of the concentration c, and **(b)** L^2 error norm of the chemical potential μ.
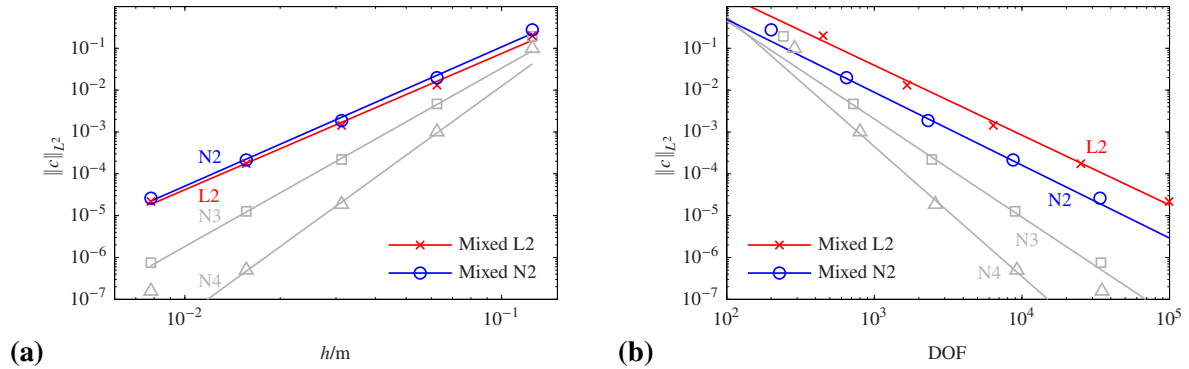

(a) **(b)**

Figure 8.4: Quantitative comparison of the error $||c||_{L^2}$ between the mixed formulation discretised by quadratic Lagrangian polynomials (L2) and B-splines (N2). In addition, cubic B-splines (N3) and quartic B-splines (N4) are plotted: **(a)** L^2 error with respect to element size h, and **(b)** with respect to the total number of degrees of freedom (DOF).

to obtain a given level of accuracy. Indeed, it involves only half the number of degrees of freedom compared to the mixed formulation to achieve the same accuracy of the concentration field c, see Fig. 8.3 (a). The less accurate approximations of the chemical potential illustrated in Fig. 8.3 (b) are of minor importance.

Although the main motivation to apply isogeometric analysis in this case is the requirement of C^1-continuous approximations, it is also competitive when used in the mixed formulation. Fig. 8.4 demonstrates that spline basis functions are more efficient than Lagrangian polynomials considering the total number of degrees of freedom. Moreover, the L^2 error converges at similar rates for both variants.

FEM vs. IGAFEM (mixed)

8.3.3 Convergence Analysis for Higher-Order Linear Partial Differential Equations

The preceding convergence study of the non-linear Cahn-Hilliard equation revealed a peculiar convergence behaviour for quadratic splines in the L^2 error norm, i.e. an order of convergence of approximately p rather than the expected value of $p + 1$. In fact, an a priori error estimate for linear, second-order and higher-order partial differential equations can be
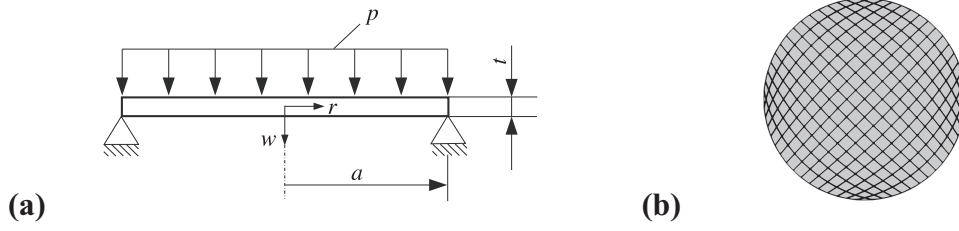
A priori error estimates

Figure 8.5: Simply supported circular Kirchhoff plate of radius a, thickness t and linear elastic material behaviour E, ν loaded by a constant pressure p: **(a)** problem definition, and **(b)** single patch isogeometric mesh in the physical domain.

derived using the Aubin-Nitsche argument [203, 205]

$$\|u - u_h\|_{H^\sigma} \le C_\sigma h^\beta \|u\|_{H^r} \tag{8.43}$$

with u_h the approximate solution of the primary field variable u. It turns out that the optimal order of convergence

$$\beta = \min\{\delta - \sigma, 2(\delta - m)\} \quad \text{with} \quad \delta = \min\{p + 1, r\} \tag{8.44}$$

depends not only on the order of approximation p, and on the error norm H^σ, but also on the order of the partial differential equation, $2m$. For a linear fourth-order differential equation ($m = 2$) and the infinitely continuous reference solution $r = \infty$, cf. equation (8.36), the optimal orders of convergence are

$$\|u - u_h\|_{H^0 \equiv L^2} \le C_0 h^{\min\{p+1,\, 2(p-1)\}} \|u\|_{H^r} \,, \tag{8.45}$$

$$\|u - u_h\|_{H^1} \le C_1 h^{\min\{p,\, 2(p-1)\}} \|u\|_{H^r} \,, \tag{8.46}$$

$$\|u - u_h\|_{H^2} \le C_2 h^{\min\{p-1,\, 2(p-1)\}} \|u\|_{H^r} \,. \tag{8.47}$$

For $p = 2$ these equations show that the error in the L^2 and H^1-norms actually converges with the same order of $\beta = 2$, which is in good agreement with the results of the preceding study.

Circular plate   In order to demonstrate that the results of equations (8.45)-(8.47) can be recovered exactly for linear partial differential equations, an additional convergence study has been carried out for the linear fourth-order problem of a simply supported circular Kirchhoff plate according to Fig. 8.5. It is noted that this example involves a singular geometric map, see Figure 8.5 (b). The isotropic plate of radius a, thickness t, and stiffness $K = \frac{Et^3}{12(1-\nu^2)}$, with E Young's modulus and ν Poisson's ratio, is loaded by a constant pressure p, see Fig. 8.5 (a). The static problem is governed by

$$Kw_{,kkll} - p = 0 \,. \tag{8.48}$$

The rotationally symmetric analytical reference solution

$$w(r) = \frac{pa^4}{64K} \frac{5 + \nu}{1 + \nu} - \frac{pa^2}{32K} \frac{3 + \nu}{1 + \nu} r^2 + \frac{p}{64K} r^4 \tag{8.49}$$

for the subsequent convergence study is a function of the radius $r = 0 \ldots a$. The corresponding numerical solution is given in Fig. 8.6 (a).
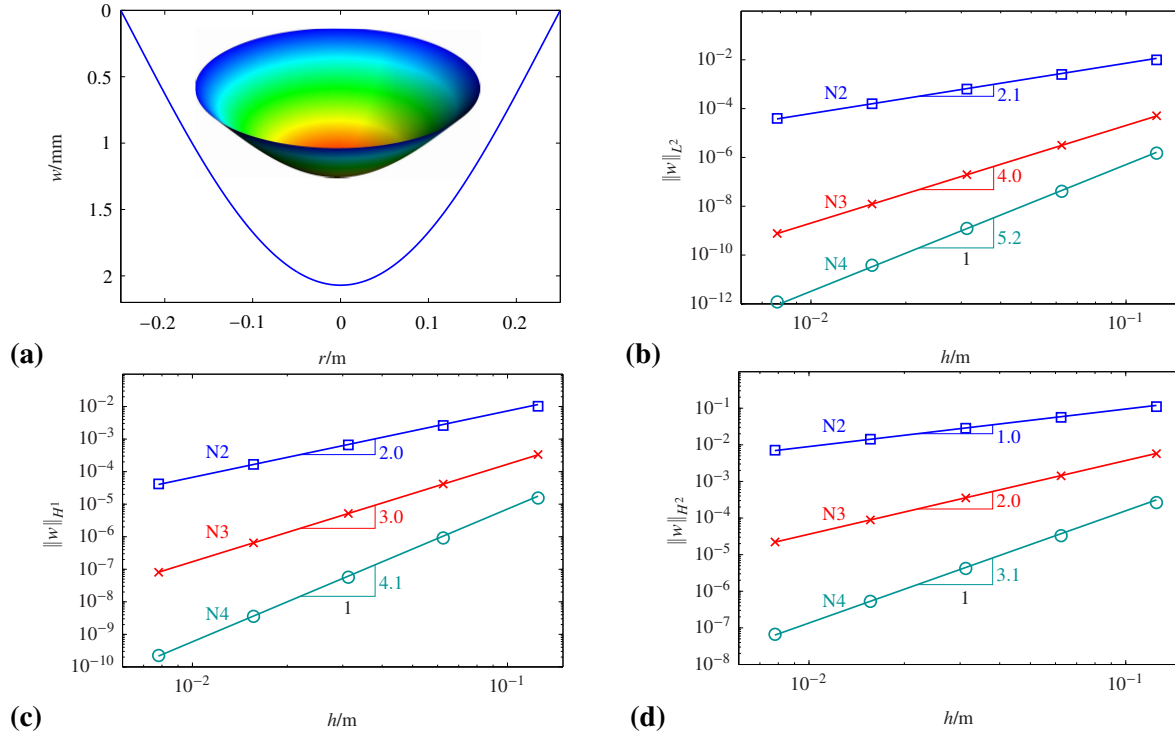
Figure 8.6: Quantitative convergence analysis for a circular Kirchhoff plate for second-order (N2), third-order (N3), and fourth-order (N4) NURBS: **(a)** Shape of the deformed plate with maximum deflection $w_{\max} = 2.07\,\text{mm}$ obtained for $E = 2.1 \times 10^5\,\text{MPa}$, $\nu = 0.3$, $a = 250\,\text{mm}$, $t = 10\,\text{mm}$, $p = 0.16\,\text{MPa}$, **(b)** L^2 norm, **(c)** H^1 norm, and **(d)** H^2 norm for the error in the deflection w.

The h-refinement analysis considers $2^n \times 2^n$ elements, with $n = 1, 2, \dots 8$, and NURBS approximations of the orders two, three, and four. The error for the deflection is given in Fig. 8.6 in terms of the L^2, H^1, and H^2 norms and is in agreement with the analytical findings. A similar behaviour has been found in qualitative convergence studies for plates and shells in [119, 120]. It is noted that no negative effect of the singular geometry map on the convergence behaviour could be observed.

Numerical analysis

8.3.4 Convergence Analysis for the Temporal Discretisation

The application of higher-order time integration schemes is essential for an efficient simulation of the structural evolution described by the Cahn-Hilliard equation. Jansen et al. [105] have proved that the generalised-α method provides second-order accuracy in time for linear problems. With regard to the adaptive time stepping scheme presented in Section 8.2.2, it is important that this also holds for non-linear problems. For this reason, a convergence analysis has been performed for the temporal discretisation. In order to avoid interference with the spatial discretisation error, the parameters of the manufactured solution have been chosen as $\alpha = \beta = 1$ and $\delta = \frac{2}{3}$ while the unit square domain is discretised by 128×128 elements using cubic B-splines ($p = 3$). The mobility and the interface parameters are set to $M = 1\,\text{m}^3\,\text{s}\,\text{kg}^{-1}$ and $\lambda = 0.1\,\text{J}\,\text{m}^{-1}$, respectively. Considering a total time of $t = 0.5\,\text{s}$, equation (8.38) is solved five times in 2^n time steps ($n = 0 \dots 4$). The convergence behaviour of different temporal discretisations is shown in Fig. 8.7. Results for
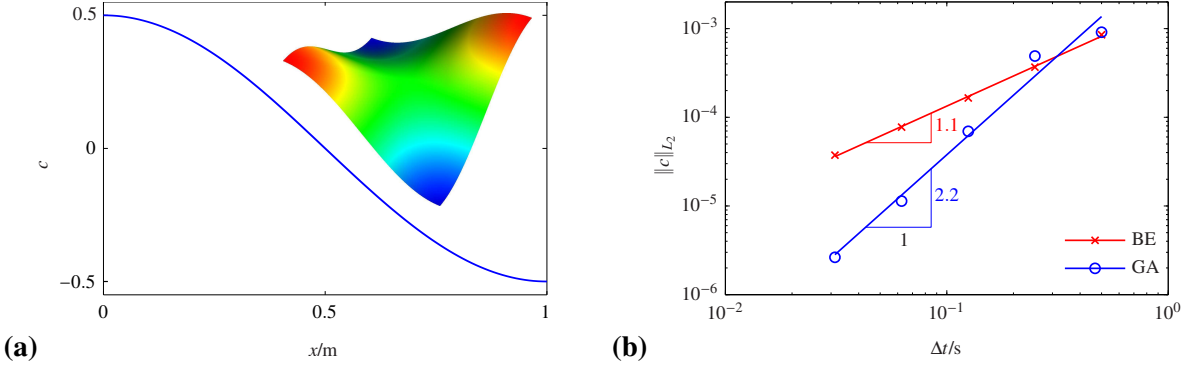
Generalised-α vs. implicit Euler

(a)

(b)

Figure 8.7: Quantitative comparison of time integration via the backward Euler (BA) and the generalised-α method (GA): **(a)** plot of the adapted manufactured solution according to equation (8.36) with parameters $\alpha = \beta = 1$, and $\delta = \frac{2}{3}$ to avoid the influence of the spatial discretisation error, and **(b)** convergence of the L^2 error norm of the concentration field c with respect to the time increment Δt.

the generalised-α method are complemented by those for the implicit Euler method. For both methods, the convergence rates match the optimal value Δt^p, as can be observed for the L^2 error norm of the concentration c. As a result, the accuracy obtained by the generalised-α method is significantly higher for reasonable sizes of the time step. Therefore, the error control according to equation (8.35) should be effective.

8.4 Simulation of Structural Evolution Processes

Introduction

In the following examples the predictions of the mixed formulation and the direct discretisation will be compared for the spinodal decomposition of a binary system. As the different stages of the structural evolution can be identified by the free energy and its individual parts, special attention is paid to them. Starting from an initial concentration distribution in which small perturbations promote the evolution of the system, each problem is considered until a steady state is reached. The course of the decomposition is influenced by the initial concentration distribution. Considering the averaged concentration in a small region $\tilde{c}$, different morphologies can occur [80, 227]. While $\tilde{c} = 0.5$ leads to deeply interconnected phases, values of $\tilde{c} \neq 0.5$ favor one phase and result in nucleation phenomena. Moreover, the choice of a degenerate mobility

$$M(c) = Dc\,(1 - c) \tag{8.50}$$

with a positive constant D has a significant influence on the coarsening behaviour of the system, as it prevents the evolution of pure phases. In the simulation, the domain of interest has been taken as $1\,\mathrm{m} \times 1\,\mathrm{m}$ and is discretised into 128×128 elements with a cubic B-spline basis ($p = 3$). Considering a free energy according to equation (8.8), the following set of parameters is assumed: $A = 3000\,\mathrm{J}$, $B = 3$, $D = 1\,\mathrm{m}^3\,\mathrm{s}\,\mathrm{kg}^{-1}$, $\lambda = 1\,\mathrm{J}\,\mathrm{m}^{-1}$.

Periodic boundary conditions

Depending on the discretisation, the imposition of periodic boundary conditions intended for the subsequent simulation requires some consideration. In the mixed formulation, the periodicity of the two primary field variables c and μ can be imposed by constraining their control values at opposite edges of the boundary, i.e. by setting $c_1 = c_n$ and $\mu_1 = \mu_n$. For the direct discretisation periodicity has to be ensured for the concentration c and its normal derivative $c_k n_k$. The direct imposition of these conditions is achieved by setting
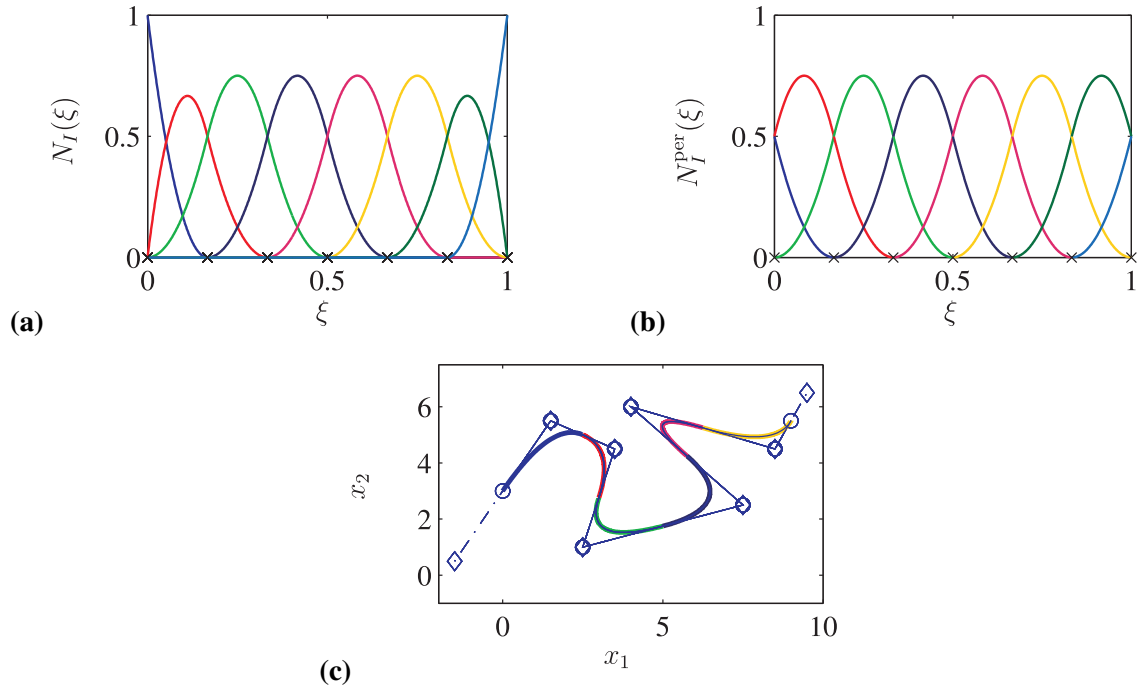
Figure 8.8: Generation of a periodic spline basis via periodic Bézier extraction according to [132]: **(a)** original spline basis ($p = 2$), **(b)** modified periodic spline basis, and **(c)** representation of the B-spline curve of Fig. 6.1 in terms of the original (thin solid blue line) as well as periodic spline basis (coloured thick solid lines). For the considered polynomial order $p = 2$, the positions of original $\underline{\mathbf{P}}$ ($\circ$) and periodic control points $\underline{\mathbf{P}}^{\mathrm{per}}$ ($\diamond$) are different only for the first and last control points.

$c_I^{\mathrm{per}} = c_{n-p+I}^{\mathrm{per}}$ for $I = 1 \ldots p$ and the periodic basis functions

$$\underline{\boldsymbol{N}}^{\mathrm{per}}(\bar{\xi}) = \underline{\underline{\mathbf{T}}}^{\mathrm{per}} \underline{\boldsymbol{N}}(\bar{\xi}) = \underline{\underline{\mathbf{T}}}^{\mathrm{per}} \underline{\underline{\mathbf{C}}} \boldsymbol{M}(\bar{\xi}) = \underline{\underline{\mathbf{C}}}^{\mathrm{per}} \underline{\boldsymbol{M}}(\bar{\xi}) \tag{8.51}$$

with the periodic transformation matrix $\underline{\underline{\mathbf{T}}}^{\mathrm{per}}$ and the periodic Bézier extraction operator $\underline{\underline{\mathbf{C}}}^{\mathrm{per}}$ [132], cf. Fig. 8.8. As the basis transformation should not affect the geometry representation

$$\mathbf{x}(\xi) = \underline{\mathbf{P}}^T \underline{\mathbf{N}}(\xi) = \underline{\mathbf{P}}^{\mathrm{per}T} \underline{\mathbf{N}}^{\mathrm{per}}(\xi) \,, \tag{8.52}$$

a new set of control point coordinates

$$\underline{\underline{\mathbf{P}}}^{\mathrm{per}} = \underline{\underline{\mathbf{T}}}^{-T} \underline{\underline{\mathbf{P}}} \tag{8.53}$$

for the periodic basis has to be computed. Fig. 8.8 (c) exemplarily shows the representation of the B-spline curve introduced in Fig. 6.1 in terms of the new periodic basis of order $p = 2$. Different colors indicate the contributions of the various Bézier elements.

8.4.1 Random Concentration Distribution

Firstly, an initially stochastic concentration distribution $c = \tilde{c} + r$ is considered with mean value $\tilde{c} = 0.63$ and standard deviation $r = 0.005$. Since $\tilde{c}$ is a constant, the characteristics of

Problem
definition

(a) $t = 2.851 \times 10^{-6}$ s   (b) $t = 7.364 \times 10^{-6}$ s   (c) $t = 4.036 \times 10^{-5}$ s

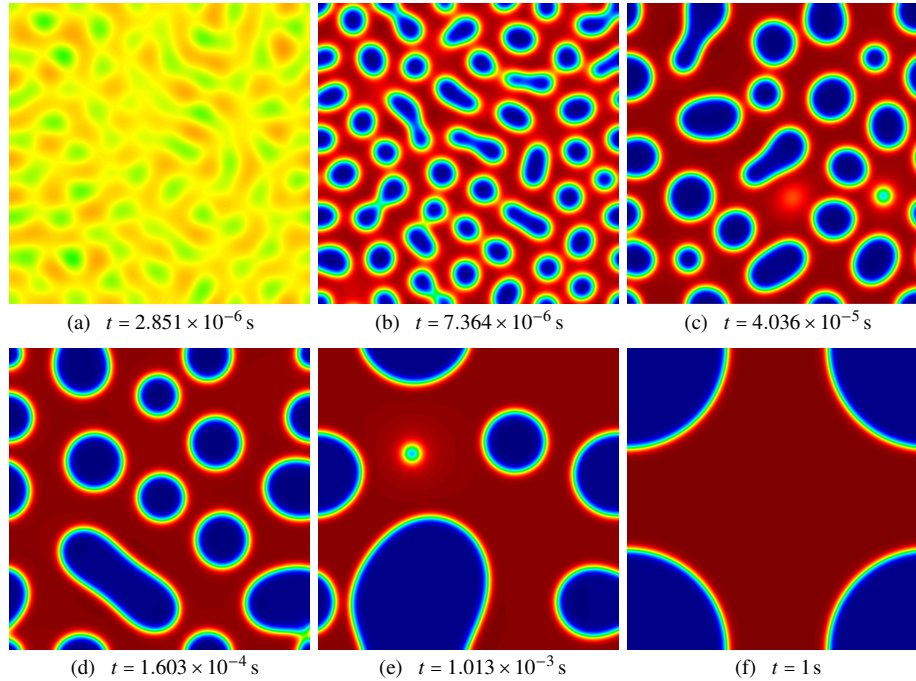(d) $t = 1.603 \times 10^{-4}$ s   (e) $t = 1.013 \times 10^{-3}$ s   (f) $t = 1$ s

Figure 8.9: Spinodal decomposition from a random concentration distribution with $\tilde{c} = 0.63$: temporal evolution of an initially stochastic concentration distribution into phases of different composition.

the evolution will be the same, locally and globally. In view of the above considerations and taking into account that periodic boundary conditions are applied, it is anticipated that in the steady state only one circular inclusion remains.

Temporal evolution

Figure 8.9 shows the progress of the structural evolution. From its initial concentration distribution the system separates into two phases whose composition is determined by the minima of the bulk free energy (8.8) which are called binodal points. This process is very fast and leads to a considerable reduction of the bulk free energy as can be seen in Figure 8.10 (a), which presents the temporal evolution of $\mathcal{F}$ and its individual parts $\mathcal{F}_{\mathrm{bulk}}$ and $\mathcal{F}_{\mathrm{int}}$. The figure also shows that the formation of interfacial regions is accompanied by an increase of the gradient energy – the instant of time where $\mathcal{F}_{\mathrm{int}}$ reaches its maximum value therefore marks the end of the decomposition. Subsequently, the evolution is dominated by coarsening which takes place over several orders of magnitude of time. In this process, the inclusions interact locally in order to minimise the gradient energy by reducing the number while increasing their characteristic length. Each decline of $\mathcal{F}_{\mathrm{int}}$ in Figure 8.10 (a) is related to such an interaction. The circular shape of the single inclusion that results is an outcome of the minimisation procedure.

Validation

Figure 8.10 (a) reveals that the total free energy decreases monotonically during the structural evolution. This is a basic property of the Cahn-Hilliard model, because $\mathcal{F}$, characterised by equation (8.3), is a Lyapunov functional. Moreover, conservation of mass is used to derive the Cahn-Hilliard equation. As a consequence, the average concentration $\tilde{c}$ calculated by numerical integration should remain constant throughout the simulation. In compliance with this requirement, the variation in the temporal evolution of $\tilde{c}$ in Fig. 8.10 (a) is not noticeable. Essentially the same characteristics of $\mathcal{F}$ and $\tilde{c}$ are found for the mixed formulation and the direct discretisation.
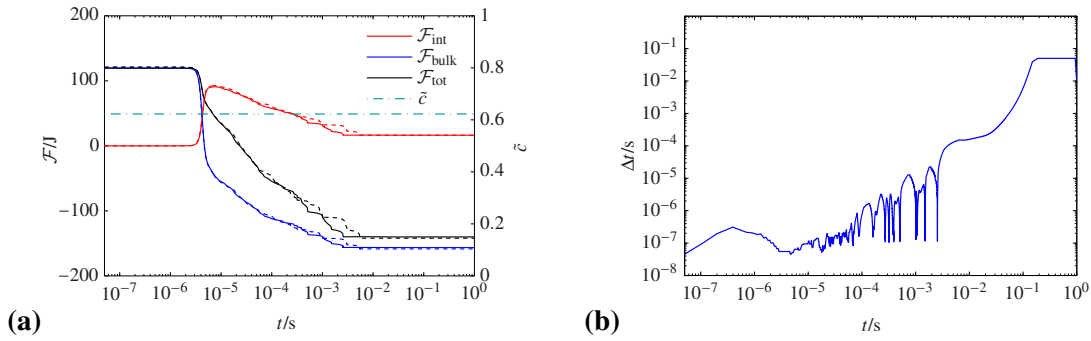
Figure 8.10: Spinodal decomposition from a stochastic concentration distribution with $\tilde{c} = 0.63$: **(a)** temporal evolution of $\tilde{c}$ and $\mathcal{F}$ compared for the direct (solid lines) and mixed (dashed lines) formulation of the Cahn-Hilliard equation, and **(b)** evolution of the adaptively controlled time step.

An important feature of the simulation is the adaptive time stepping scheme. According to Fig. 8.10 (b) the step size Δt ranges from $\Delta t = 5 \times 10^{-8}$ s to $\Delta t = 5 \times 10^{-2}$ s. This can only be achieved if the time step increases when the evolution shows low activity and decreases in case of larger structural changes. For this reason, every major decrease in the size of Δt corresponds to a variation of the systems structure. This is particularly obvious when comparing Figures 8.9 (c) – 8.9 (e) to Fig. 8.10 (b). A total of 2042 time steps were needed to complete the simulation. On top of that 253 steps, which is fewer than 12 %, have been rejected in order to keep the estimated error close to the chosen tolerance $\varepsilon^{\mathrm{adm}}$. With an average of 4 Newton iterations per time step the computational effort is significantly lower than in an approach with constant step size while the results are comparable to those presented in [80, 227] for a second-order accurate time integration.

Adaptive time stepping

8.4.2 Linear Concentration Distribution

The purpose of the second example is to show the evolution of different morphologies as a function of the local average concentration $\tilde{c}$. Therefore, an initial distribution $c = \tilde{c} + r$ is considered, with $-0.005 \leq r \leq 0.005$, which represents a random perturbation to promote the evolution of the system. Herein, $\tilde{c} = x_1$, $0 \leq x_1 \leq 1$, is a concentration which varies linearly in the x_1-direction. For this reason, regions with different characteristics of the evolution should develop that can be distinguished clearly [81]. As the average of the concentration is $\tilde{c} = 0.5$ and homogeneous Neumann boundary conditions are applied, the steady state of the system is expected to consist of two phases of an equilibrium composition, separated by a straight interface at $x_1 = 0.5$ m.

Problem definition

The progress of the evolution is depicted in Fig. 8.11 for six representative times. Again, the period of time needed for the separation process is very short. In contrast to the first example, the separation process emanates from regions where $\tilde{c} \approx 0.5$, because the degenerate mobility (8.50) reaches its maximum value at this concentration. Hence, an interconnected pattern evolves around $x_1 = 0.5$ m, while nucleation of one phase into the other is the dominant mechanism if the local average concentration differs considerably from $\tilde{c} = 0.5$. Since the mobility decreases with an increasing level of decomposition, the structural evolution at the boundaries with $x_1 = 0$ m and $x_1 = 1$ m hardly exists.

Temporal evolution

(a) $t = 2.918 \times 10^{-6}$ s (b) $t = 5.705 \times 10^{-6}$ s (c) $t = 2.181 \times 10^{-5}$ s

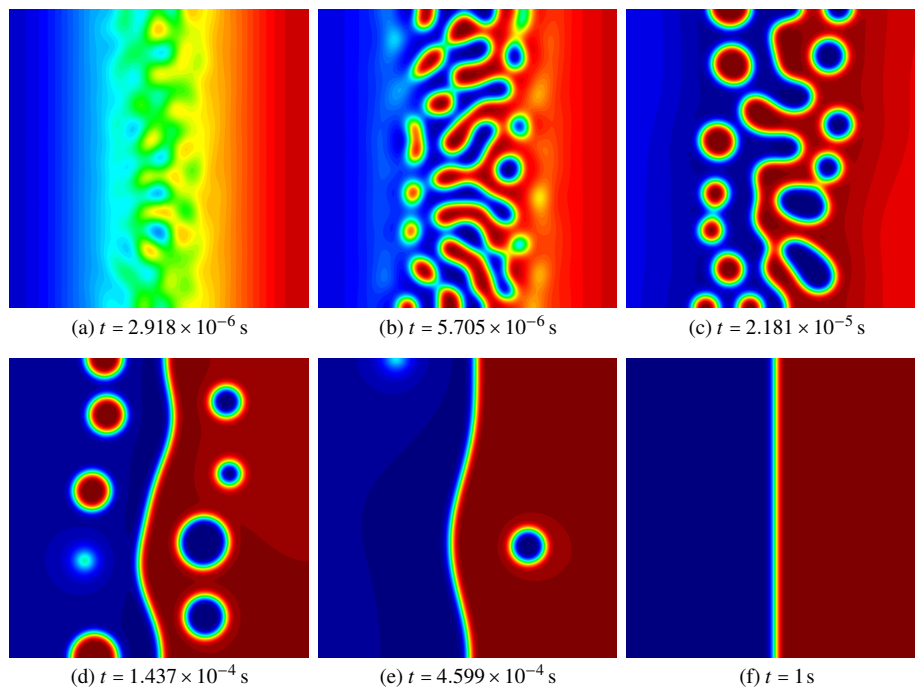(d) $t = 1.437 \times 10^{-4}$ s (e) $t = 4.599 \times 10^{-4}$ s (f) $t = 1$ s

Figure 8.11: Spinodal decomposition from a linear, randomly perturbed concentration distribution with $\tilde{c} = 0.5$: temporal evolution of the initial concentration field into two phases separated by a straigth interface.

Validation

Similar to the example presented in Section 8.4.1 the formation of interfacial areas leads to an increase of the gradient energy $\mathcal{F}_{\text{int}}$, Fig. 8.12. The minimisation of $\mathcal{F}_{\text{int}}$ via coarsening prevails at the later stages of the evolution. While the bands forming the interconnected pattern broaden, the characteristic length of the interacting inclusions increases. Once again, every decrease in the free energy corresponds to a significant change of the structure of the system which is evident when comparing Figures 8.11 (c) – 8.11 (e) to the temporal evolution of $\mathcal{F}$ depicted in Fig. 8.12. Eventually, the shape of the remaining interface is optimised – the curved transition zone located at $x_1 = 0.5$ m develops into a straight line. In compliance with the theoretical aspect of $\mathcal{F}$ being a Lyapunov functional, the total free energy decreases monotonically. Furthermore, the average of the concentration $\tilde{c}$ shows no variation during the entire simulation, which implies that the finite element model of the Cahn-Hilliard equation fulfills the basic requirements. A comparison of the times needed by the system to reach a steady state reveals another influence of the initial condition. Different from the example shown in Section 8.4.1, the structural evolution advances much faster which is mainly caused by a smaller region of activity in the current example. The phenomenon is also in agreement with the findings in [80] where the coarsening process for deeply interconnected phases is shown to be much smoother than for droplet-type morphologies.

8.5 Conclusion

In this chapter a detailed convergence analysis of the Cahn-Hilliard phase-field model has been presented. Two different discretisations of the model have been analysed within the framework of isogeometric analysis. Due to the lack of an analytic reference solution, the
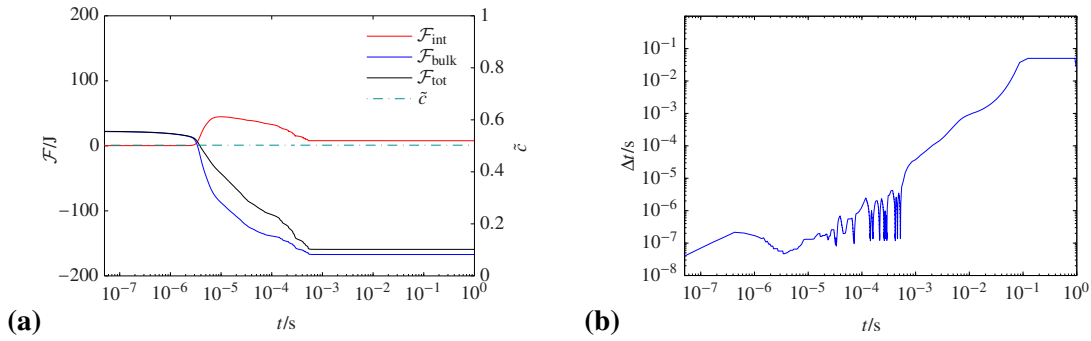
Figure 8.12: Spinodal decomposition from a linear, randomly perturbed concentration distribution with $\tilde{c} = 0.5$: **(a)** temporal evolution of $\tilde{c}$ and $\mathcal{F}$, and **(b)** evolution of the adaptively controlled time step.

method of manufactured solutions has been adopted. With respect to the spatial discretisation, convergence rates are obtained that match analytical error estimates available for linear problems. Irrespective of the problem, the direct discretisations of higher-order partial differential equations provide superior efficiency compared to mixed formulations. However, optimal convergence rates are only obtained if approximations of sufficient order are utilised. Further investigations on the convergence behaviour of the generalised-α method justify the application of an adaptive time stepping scheme based on elementary error control. Two numerical examples of spinodal decomposition have been used to compare the physical predictions of the mixed formulation and direct discretisation approach and to validate the latter.

9 Adaptive Isogeometric Phase-Field Modelling [HMK16]

As it was shown in the preceding chapter, the phase-field method provides a convenient way to model structural evolution processes because interfaces are represented fully implicitly in terms of an order parameter field. The accurate approximation of these field variables however requires highly refined meshes. If fixed grids are used, practical applications will cause tremendous numerical costs which limits the applicability of the approach. Therefore, local adaptive mesh refinement and coarsening procedures are required to improve the numerical efficiency of finite element discretisations of phase-field models.

Isogeometric analysis seems to be an ideal discretisation technique to be combined with adaptivity features as already the coarsest mesh provides an exact geometry representation which is preserved during refinement. Consequently, tedious interaction with an underlying geometry model is avoided. However, if B-splines or NURBS are considered as a basis, their tensor product nature will prohibit a purely local refinement within a single NURBS patch. Local refinement with these bases would require the subdivision of the analysis domain into several patches which can then be refined uniformly [41, 109]. In addition, the continuity across patches will only be C^0 which is not sufficient for the direct discretisation of higher-order differential equations as the Cahn-Hilliard model presented in the previous chapter.

Three major approaches to overcome the restrictive tensor product structure have been developed:

  (i) *T-splines* introduced by Sederberg [187, 188] result from the insertion of extra vertices into the tensor product mesh. This produces so called T-junctions which are comparable to hanging nodes in the standard FEM. T-splines were firstly used to represent complex and watertight geometries. Bazilevs et al. [5] introduced T-splines into isogeometric analysis. Recent contributions have focussed on analysis suitable T-splines which ensure the linear independence of the basis [129, 137, 186]. Local refinement based on T-splines is presented in [54, 183].

  (ii) *Locally refined (LR) B-splines* have been presented by Dokken et al. [53]. They are in some way dual to T-splines, i.e. tensor product B-splines are locally refined by the insertion of knot line segments instead of extra vertices. The properties of LR-B-splines have been analysed by Bressan [22] and first applications to adaptive isogeometric analysis can be found in [108].

  (iii) *Hierarchical splines* use basis functions defined by knot vectors of different levels of nested meshes that result from sucessive uniform h-refinement. They were introduced by Forsey and Bartels [68] already in 1988. With the recent works of Vuong et al. [220, 221], Schillinger [176], Gianelli et al. [79], and Scott et al. [185] hierarchical B-splines have been further developed to meet the requirements of isogeometric analysis. Recent applications are presented in [177, 178].
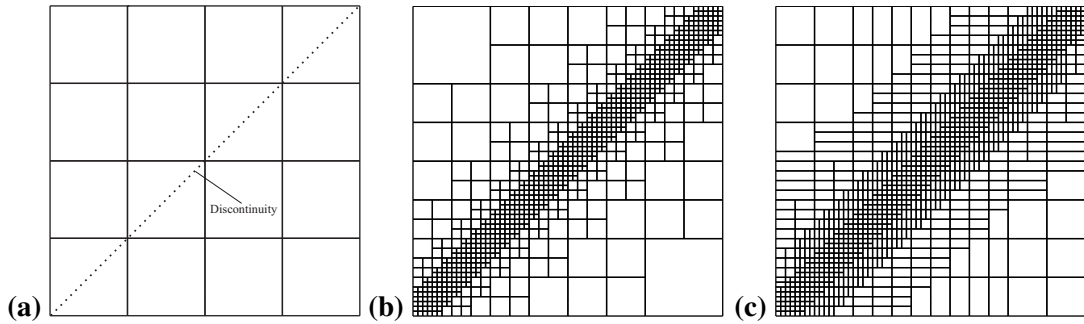
Figure 9.1: Two approaches to local mesh refinement in IGA: **(a)** initial mesh with an interal layer/discontinuity, **(b)** local mesh refinement using hierarchical splines, and **(c)** T-splines.

In particular T-splines and hierarchical B-splines have been utilised to facilitate adaptive isogeometric analysis. Local mesh refinement with both approaches is illustrated in Fig. 9.1 for the benchmark case of a sharp internal layer. Since ensuring linear independence imposes restrictions on the T-spline mesh, the refinement will not be as local as with hierarchical splines, cf. Fig. 9.1. Despite their deficit regarding locality, local refinement of T-splines is essential for complex engineering geometries which cannot be respresented conveniently by B-splines or NURBS. The hierarchical approach to refinement has been generalised to T-splines by Evans et al. [64] which provides a highly localised refinement strategy for complex geometries.

Outline
In this chapter adaptive local refinement will be applied to the isogeometric analysis of phase-field models. As a consequence of the typically used simple unit square domains, hierarchical refinement strategies are employed in conjunction with B-splines. Firstly, a local refinement procedure based on hierarchical B-splines will be outlined in Section 9.1. This introduction exploits the one-dimensional case to present the construction of a hierarchical basis and to illustrate modifications which are useful for analysis. For the selection of active basis functions an element based approach similar to [185] is applied. Section 9.2 presents a new way to assemble the hierarchical system of equations based on Bézier extraction. It will be shown that this novel procedure produces the truncated hierarchical basis [79] without the need to explicitly compute the hierarchical basis. Eventually, the numerical properties of the approach will be analysed. In Section 9.3, adaptive local refinement and coarsening based on hierarchical splines will be used for the isogeometric analysis of the Cahn-Hilliard phase-field model introduced in Chapter 8.

9.1 Univariate Hierarchical B-Splines

Assumptions
In this section the foundations of local refinement and coarsening using hierarchical splines are outlined. In contrast to many works a finite element viewpoint is used as it allows for the straight forward identification of active elements and the associated basis functions. Furthermore, it is easily combined with Bézier extraction. Without loss of generality only B-splines are considered. The hierarchical basis consists of splines of only one polynomial degree and strong conditions on the boundaries of different hierarchy levels are assumed [221], i.e. elements of two consecutive levels are not allowed to overlap.
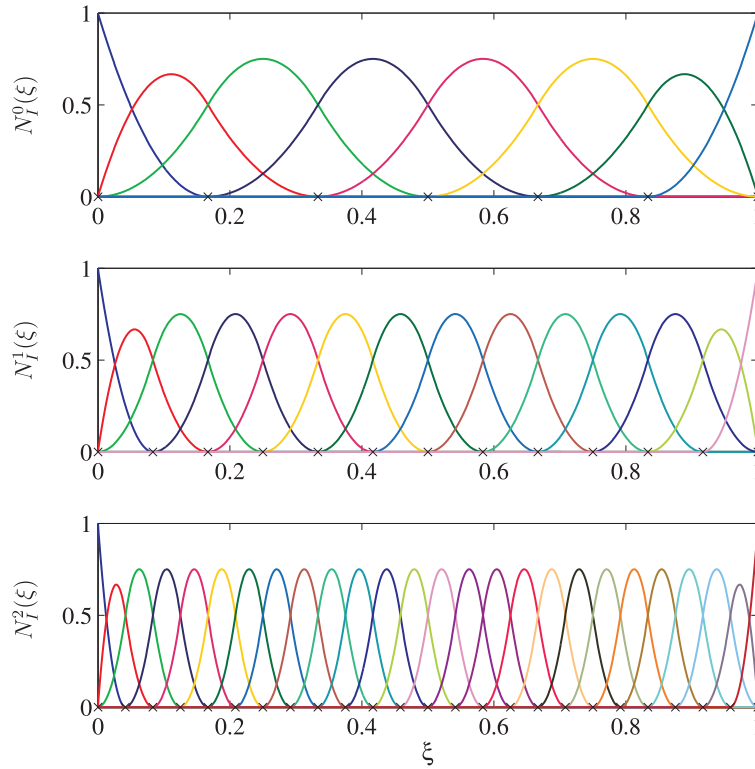
Figure 9.2: Multi-level univariate B-spline basis defined by multi-level nested knot vectors, $n = 3, p = 2$, knots are indicated by the symbol $\times$.

9.1.1 Multi-Level Basis and Multi-Level Mesh

As a simple univariate example consider a unit domain $\Omega : x \in [0, 1]$. A hierarchy of n knot vectors $\underline{\Xi}^\ell, \ell = 0 \ldots n - 1$ is created by successive uniform h-refinement within the domain Ω starting from the knot vector $\underline{\Xi}^0$ of the coarsest mesh ($\ell = 0$). The resulting knot vectors are nested, i.e. $\underline{\Xi}^\ell \subset \underline{\Xi}^{\ell+1}$, and each knot vector $\underline{\Xi}^\ell$ defines a set of B-spline basis functions $\underline{\mathbf{N}}^\ell = \{N_{I,p}^\ell\}_{I=1}^{n^\ell}$ of degree p. The approximation spaces $\mathcal{N}^\ell$ of each level are spanned by the vectors of basis functions $\underline{\mathbf{N}}^\ell$. The h-refinement is accomplished via uniform knot insertion and results in a new spline space $\mathcal{N}^{\ell+1}$ with more B-splines and therefore more flexibility than the original spline space. It contains the original spline space as a subspace, i.e. $\mathcal{N}^\ell \subset \mathcal{N}^{\ell+1}$. Therefore, any spline in the original space can also be represented in terms of the B-splines in the refined space. An examplary three-level basis is illustrated in Fig. 9.2 for the case $p = 2$.

Multi-level basis

The basis functions of two consecutive levels are related by

Refinement operator

$$\underline{\mathbf{N}}^\ell = \underline{\underline{\mathbf{M}}}^{\ell,\ell+1} \underline{\mathbf{N}}^{\ell+1} \qquad (9.1)$$

with $\underline{\underline{\mathbf{M}}}$ the subdivision, knot insertion or refinement operator [183]. From the two-scale relation (9.1) it can be seen that the coarse basis (level ℓ) can be fully expressed as a linear combination of basis functions of the finer level $\ell+1$. The individual entries of the refinement

operator are the coefficients of this linear combination and can be computed from recursion formulae. A corresponding algorithm developed by Casciola and Romani [32] for open, non-uniform knot vectors with repeated knots is used in this work. Refinement operators for two non-consecutive levels are obtained according to

$$\underline{\mathbf{N}}^I = \underline{\underline{\mathbf{M}}}^{I,J}\underline{\mathbf{N}}^J = \prod_{\ell=I}^{J-1} \underline{\underline{\mathbf{M}}}^{\ell,\ell+1}\underline{\mathbf{N}}^J \ . \tag{9.2}$$

The relations between basis functions translate directly into transformation rules for control point values $\underline{\mathbf{P}}$ if the same curve $\mathbf{x}$ is to be represented in terms of a refined basis

$$\mathbf{x} = \left(\underline{\mathbf{P}}^\ell\right)^T \underline{\underline{\mathbf{M}}}^{\ell,\ell+1} \underline{\mathbf{N}}^{\ell+1} \tag{9.3}$$

$$\underline{\mathbf{P}}^{\ell+1} = \left(\underline{\underline{\mathbf{M}}}^{\ell,\ell+1}\right)^T \underline{\mathbf{P}}^\ell. \tag{9.4}$$

In addition to the basis functions, the nested knot vectors define a multi-level element structure. According to the framework of Bézier extraction, cf. Section 6.1.2, a number of n_{e}^ℓ elements $\Omega_I^{\mathrm{e},\ell}$ are defined by non-zero intervals of the knot vectors on the individual hierarchy level ℓ. The union of elements on each level covers the analysis domain $\Omega = \bigcup_{I=1}^{n_{\mathrm{e}}^\ell} \Omega_I^{\mathrm{e},\ell}$. Assuming that two consecutive levels result from a uniform refinement splitting each coarse knot interval into two fine scale intervals, a hierarchy of nested elements is obtained. In this tree-like element structure each parent element on level ℓ possesses two children on level $\ell + 1$ in the one-dimensional case. Every element on level ℓ is associated to $p + 1$ basis functions in $\underline{\mathbf{N}}^\ell$ which will facilitate an element-based refinement procedure outlined later in this section.

9.1.2 Hierarchical Basis – Selection of Active Basis Functions and Elements

In the hierarchical approach to local refinement, basis functions from the vector $\underline{\mathbf{N}}^\ell$ of different levels ℓ are combined into the vector of hierarchical basis functions $\underline{\mathbf{N}}_{\mathrm{h}}$ which spans the hierarchical basis space $\mathcal{H}$. However, building the hierarchical basis cannot be accomplished by simply adding basis functions from finer hierarchy levels to the coarse scale basis. This would result in the loss of linear independence because coarse level basis functions are linear combinations of the fine-scale functions according to equation (9.1). Therefore, coarse level basis functions have to be removed from the approximation space. To facilitate the implementation of hierachical splines into the existing framework which uses Bézier extraction, an element-based approach to the proper selection of active basis functions will be outlined in the following. In this way, typical FE procedures for evaluating error measures and marking elements for refinement or coarsening, respectively, can be seamlessly transferred to the framework of isogeometric analysis.

The element-based selection of active basis functions for the hierarchical approximation uses two essential definitions which are examplarily illustrated in Fig. 9.3 which results from the three-level basis of Fig. 9.2 by the following procedure:

(i) *Active elements:* By some criterion elements of different hierarchy levels have to be chosen to discretise the analysis domain. The elements of this set are called active elements. As it can be seen in Fig. 9.3 (a) where active elements are marked in green, the union of these elements fully covers the domain Ω without any overlap. The active

elements represent the finest possible hierarchy level at a considered position in the mesh. They are therefore the leafs of the tree-like element structure and also referred to as *leaf elements* [185].

(ii) *Active basis functions $\mathcal{A}^\ell$ of level ℓ:* Each of the active elements is associated to a number of $p + 1$ basis functions. On each level ℓ these functions form a set $\mathcal{A}_a^\ell$ plotted in colour in Fig. 9.3 (a). However, to ensure a linearly independent basis not all of these functions can contribute to the hierarchical approximation, i.e. attention has to be paid to basis functions whose support overlaps with the domains of active elements on higher or lower hierarchy levels. In this context, the definition of two subsets is convenient:

   a) *Basis functions below active elements $\mathcal{A}_{ba}^\ell$:* To ensure a linear independent hierarchical approximation, basis functions in $\mathcal{A}_a^{\ell+1}$ that have support below an active element of level ℓ cannot contribute to the hierarchical basis. Functions belonging to these sets $\mathcal{A}_{ba}^\ell$ are plotted by dotted coloured lines in Fig. 9.3 (a). The subscript *ba* indicates *below active* elements.

   b) *Basis functions above active elements $\mathcal{A}_{aa}^\ell$:* In a similar fashion the support of basis functions in $\mathcal{A}_e^\ell$ will intersect the domains of active elements on level $\ell + 1$. They form the set $\mathcal{A}_{aa}^\ell$ and contribute actively to the hierarchical approximation. Corresponding functions are indicated in Fig. 9.3 (a) by dashed coloured lines.

A linearly independent, i.e. analysis suitable, hierarchical basis $\mathcal{H}$ is therefore defined by

$$\mathcal{A}^\ell = \mathcal{A}_{ba}^\ell \setminus \mathcal{A}_a^\ell \,. \tag{9.5}$$

It is depicted in Fig. 9.3 (b). As this basis does not possess the partion of unity property[1], Giannelli et al. [79] propose the scaling and truncation of basis functions in the set $\mathcal{A}_{aa}^\ell$ which results in the truncated hierarchical basis, Fig. 9.3 (c).

9.2 Implementation of Truncated Hierarchical B-Splines using Bézier Extraction

In the preceding section, procedures for selecting the elements and basis functions which contribute to the hierarchical approximation have been introduced. In the following, an implementation of the truncated hierarchical B-spline basis will be outlined which does not require to carry out the truncation and scaling operations explicitly. Instead, the basis is obtained from Bézier extraction performed for the multi-level basis, i.e. for all active elements or functions in the sets $\mathcal{A}_a^\ell$, respectively. The required scaling and trunction are accomplished in terms of a hierachical subdivision operator. This procedure consists of three steps:

 (i) At first the element matrices of all active elements are computed without considering information on whether the basis function contributes to the hierarchical basis or not. This ensures the applicability of standard Bézier extraction.

(ii) Once element matrices for all active elements of one level ℓ have been obtained, they are assembled to form sub-systems for each hierarchy level.

---

[1]*Remark:* Although the hiearchical basis in Fig. 9.3 (b) does not form a partition of unity it is able to represent constant fields and is therefore a valid basis as explained in [185].
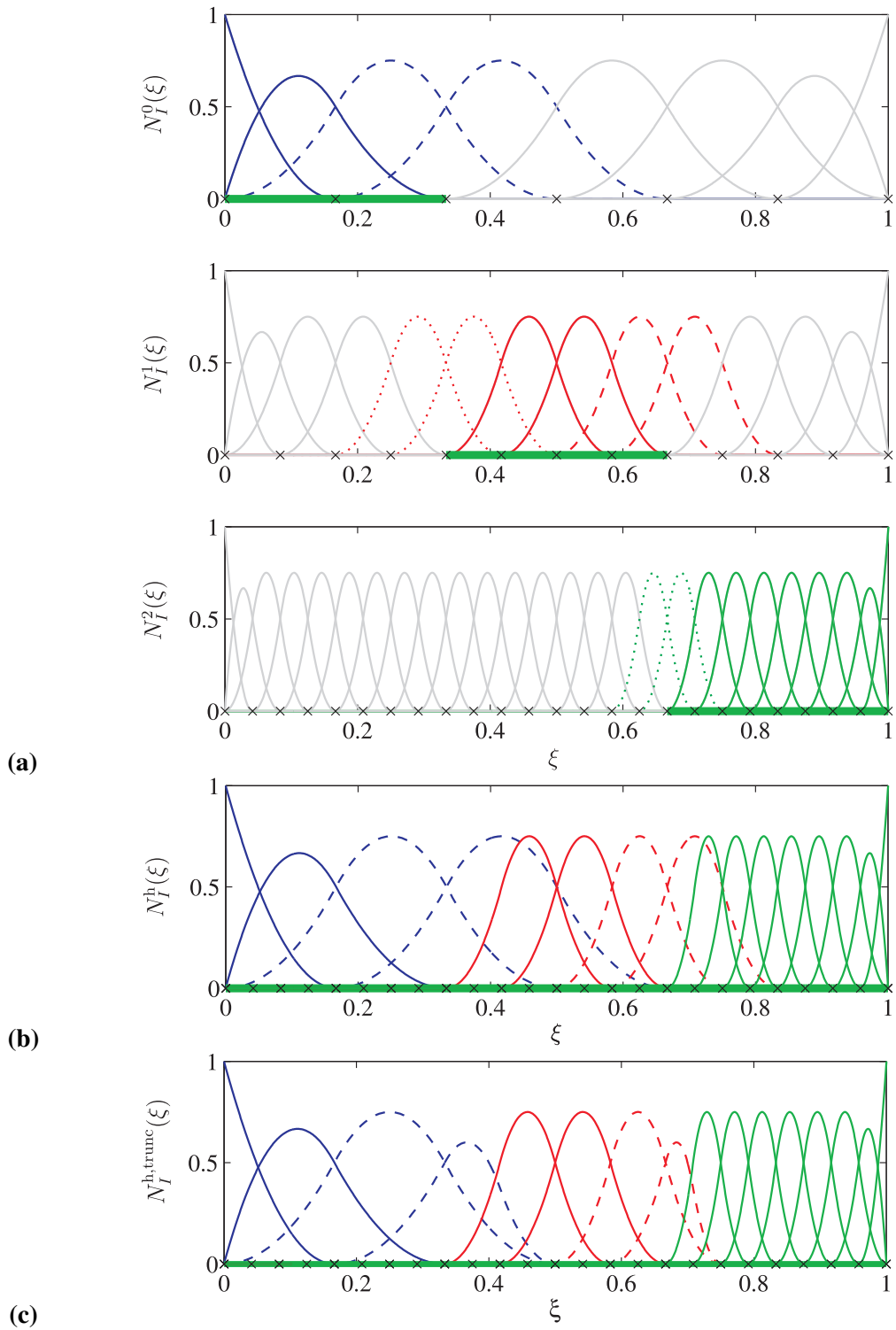
Figure 9.3: Hierarchical approximation ($n = 3$ levels of hierarchy) and differents sets of basis functions: **(a)** $\mathcal{A}_{\mathrm{a}}^{\ell}$ – basis functions belonging to active elements (all coloured lines), $\mathcal{A}_{\mathrm{ba}}^{\ell}$ – basis functions below active elements (dotted lines), and $\mathcal{A}_{\mathrm{aa}}^{\ell}$ – basis functions supported by inactive elements (dashed lines), **(b)** the basis functions of the hierarchical basis $\mathcal{H}$, and **(c)** the truncated hierarchical basis [79] which results from the scaling and truncation of basis functions in the sets $\mathcal{A}_{\mathrm{aa}}^{\ell}$.

(iii) Finally, these sub-systems are combined to form the global system of equations. This process is accomplished by a transformation matrix $\underline{\underline{\mathbf{M}}}_h$ which can be identified as a hierarchical subdivision operator, i.e. simple matrix multiplication ensures that only basis functions in $\mathcal{H}$ contribute to the approximation.

9.2.1 Assembly of Global System of Equations

The operations carried out in steps (i) and (ii) are standard procedures in isogeometric analysis. Using Bézier extraction outlined in Section 6.1.2 the B-spline basis is mapped onto a unique set of Bernstein polynomials which act as shape functions of the Bézier elements. Then numerical quadrature is applied to obtain the coefficient matrices of all active elements. The matrices of active elements of each hierarchy level ℓ are assembled into sub-systems of equations

Multi-level systems of equations

$$\underline{\underline{\mathbf{K}}}^\ell \underline{\mathbf{u}}^\ell = \underline{\mathbf{F}}^\ell \tag{9.6}$$

with $\underline{\mathbf{u}}^\ell$ and $\underline{\mathbf{F}}^\ell$ column vectors containing the control values of generalised degrees of freedom and the associated generalised forces. Their length is $n^\ell \cdot n_{\mathrm{DOF}}$ where n^ℓ is the total number of basis functions or control points on level ℓ, and n_{DOF} is the degree of freedom at each control point. Consequently, $\underline{\underline{\mathbf{K}}}^\ell$ is a square matrix of size $[n^\ell \cdot n_{\mathrm{DOF}} \times n^\ell \cdot n_{\mathrm{DOF}}]$. The sub-systems of the individual levels ℓ can be arranged into a system of multi-level equations

$$\underbrace{\begin{bmatrix} \underline{\underline{\mathbf{K}}}^0 & \underline{\underline{\mathbf{0}}} & \cdots & \underline{\underline{\mathbf{0}}} \\ \underline{\underline{\mathbf{0}}} & \underline{\underline{\mathbf{K}}}^1 & & \\ \vdots & & \ddots & \\ \underline{\underline{\mathbf{0}}} & & & \underline{\underline{\mathbf{K}}}^{n-1} \end{bmatrix}}_{\underline{\underline{\mathbf{K}}}} \underbrace{\begin{bmatrix} \underline{\mathbf{u}}^0 \\ \underline{\mathbf{u}}^1 \\ \vdots \\ \underline{\mathbf{u}}^{n-1} \end{bmatrix}}_{\underline{\mathbf{u}}} = \underbrace{\begin{bmatrix} \underline{\mathbf{F}}^0 \\ \underline{\mathbf{F}}^1 \\ \vdots \\ \underline{\mathbf{F}}^{n-1} \end{bmatrix}}_{\underline{\mathbf{F}}} . \tag{9.7}$$

In the multi-level system of equations (9.7) individual levels are not linked to each other. This interconnection will be introduced in the following by a hiearchical refinement operator $\underline{\underline{\mathbf{M}}}_h$. It acts as a transformation matrix on the multi-level system

Hierarchical system of equations

$$\underline{\underline{\mathbf{K}}}_h = \underline{\underline{\mathbf{M}}}_h \underline{\underline{\mathbf{K}}} \underline{\underline{\mathbf{M}}}_h^T \tag{9.8}$$

$$\underline{\mathbf{F}}_h = \underline{\underline{\mathbf{M}}}_h \underline{\mathbf{F}} \tag{9.9}$$

which results in the hierarchical system of equations

$$\underline{\underline{\mathbf{K}}}_h \underline{\mathbf{u}}_h = \underline{\mathbf{F}}_h . \tag{9.10}$$

The sparsity pattern of the refinement operator $\underline{\underline{\mathbf{M}}}_h$ is shown in Fig. 9.4 (b) while the population of the resulting coefficient matrix $\underline{\underline{\mathbf{K}}}_h$ is plotted in Fig. 9.4 (c). It is noted that in order to reduce memory requirements, efficient matrix libaries with adjusted indexing should be used to avoid zero rows and columns in the multi-level as well as the hiearchical system matrices and in the refinement operator. A more efficient, condensed matrix representation is illustrated in Fig. 9.4 (d). The matrix $\underline{\underline{\mathbf{K}}}$ of the hierarchical basis according to Fig. 9.3 possesses the sparsity pattern illustrated in Fig. 9.4 (a). Empty spaces in the characteristic band structure result from inactive elements on each level.
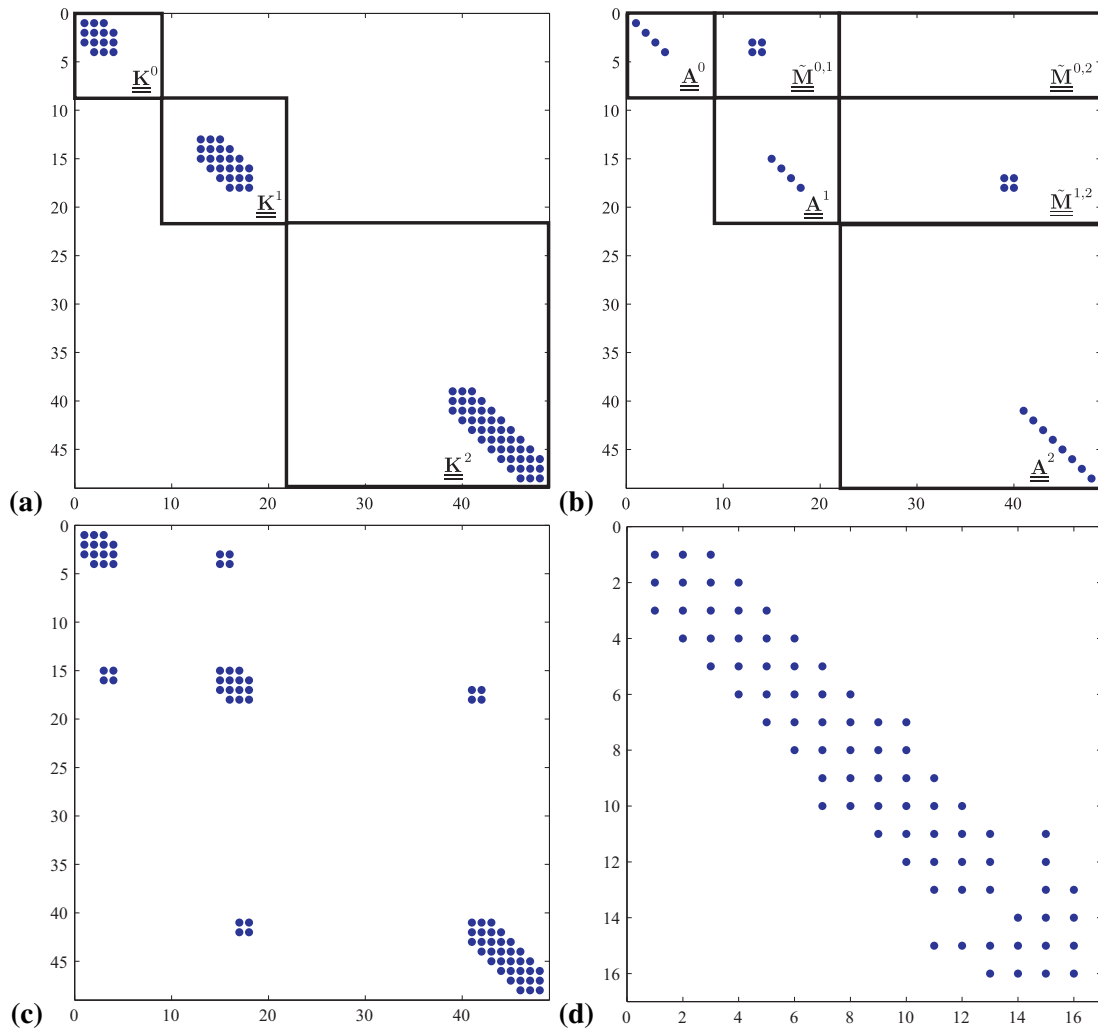
Figure 9.4: Sparsity patterns of the coefficient matrices and the hierarchical refinement operator: **(a)** multi-level coefficient matrix $\underline{\underline{K}}$ with clear separation of the different levels ℓ, **(b)** hiearchical refinement operator $\underline{\underline{M}}_h$ with entries on the diagonal resulting from the activity indicators $\underline{\underline{A}}^\ell$ and off-diagonal elements due to $\underline{\underline{\tilde{M}}}^{I,J}$, **(c)** hierarchical coefficient matrix $\underline{\underline{K}}_h$, and **(d)** rearranged hiearchical coefficient matrix $\underline{\underline{K}}_h$.

9.2.2 Hierarchical Refinement Operator and Equivalence to the Truncated Hierarchical Basis

As indicated by Fig. 9.4 (b), the hierarchical refinement operator $\underline{\underline{M}}_h$ is an upper triangular matrix. Its elements are given by

$$
\underline{\underline{M}}_h = \begin{bmatrix} \underline{\underline{A}}^0 & \underline{\underline{\tilde{M}}}^{0,1} & \underline{\underline{\tilde{M}}}^{0,2} & \dots & \underline{\underline{\tilde{M}}}^{0,n-1} \\ & \underline{\underline{A}}^1 & \underline{\underline{\tilde{M}}}^{1,2} & \dots & \underline{\underline{\tilde{M}}}^{1,n-1} \\ & & \underline{\underline{A}}^2 & \dots & \underline{\underline{\tilde{M}}}^{2,n-1} \\ & \underline{\underline{0}} & & \ddots & \\ & & & & \underline{\underline{A}}^{n-1} \end{bmatrix} .
\tag{9.11}
$$

It has to transfer the contributions from all active shape functions of the multi-level to the hierarchical system of equations. This is accomplished in terms of an activity indicator matrix for each level

$$
A^\ell_{(II)} = \begin{cases} 1 & \text{for} \quad N^\ell_I \in \mathcal{A}^\ell \\ 0 & \text{else} \end{cases} \quad \text{and} \quad A^\ell_{IJ} = 0 \text{ for } I \neq J .
\tag{9.12}
$$

In addition, it can be observed that basis functions belonging to active elements but not to the hierarchical basis, i.e. the functions in the sets $\mathcal{A}^\ell_{ba}$, have been used during the integration of the coefficient matrices of hierarchy levels $\ell > 1$. The contribution of these basis functions on level $\ell + 1$ has to be mapped to active shape functions of level ℓ, i.e. those in the set $\mathcal{A}^\ell_{aa}$. The relation between these shape functions is given in terms of the refinement operator according to equation (9.1). Since these are the only transformations required, a modified refinement operator

$$
\tilde{M}^{\ell,\ell+1}_{IJ} = \begin{cases} M^{\ell,\ell+1}_{IJ} & \text{for} \quad N^\ell_I \in \mathcal{A}^\ell_{aa} \wedge N^{\ell+1}_J \in \mathcal{A}^{\ell+1}_{ba} \\ 0 & \text{else} \end{cases}
\tag{9.13}
$$

is used in $\underline{\underline{M}}_h$.

Although the hierarchical basis is never computed explicitly in the present approach, it can be shown that the resulting approximation is identical to the truncated hierarchical basis [79, 92], cf. Fig. 9.3 (c). This basis varies from the hierarchical set of basis functions, Fig. 9.3 (b), in terms of the contribution of some active basis functions in the sets $\mathcal{A}^\ell_{aa}$, i.e. the functions plotted as dashed coloured lines in Fig. 9.3 (a). The correspondence of the present approach and the truncated basis in [79, 221] results from the procedure used to compute the coefficient matrices and from the mapping of contributions of basis functions in $\mathcal{A}^{\ell+1}_{ba}$ to those in $\mathcal{A}^\ell_{aa}$. In order to understand this effect, the basis functions N^0_3 and N^0_4 according to Fig. 9.3 (a) are to be considered as an illustrative example, Fig. 9.5.

During the multi-level Bézier extraction, standard extraction operators are computed for each active element and numerical integration is carried out subsequently. This has two major implications:

(i) All basis functions supported in an active element will be considered during quadrature irrespectively of the fact if they are part of the hierarchical basis.

(ii) The contribution of basis functions on level ℓ is limited to the domains of active ele-
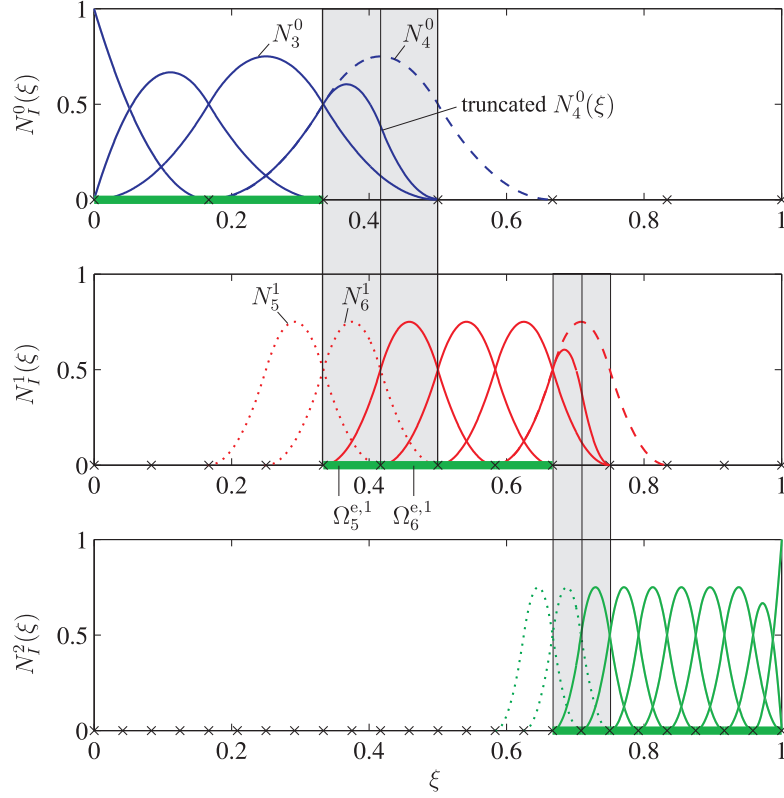
Figure 9.5: Relation of the hierarchical refinement operator to the truncated hierarchical B-spline basis of Gianelli et al. [79]: When the hierarchical system is build using the operator $\underline{\underline{\mathbf{M}}}_{\mathrm{h}}$, contributions of the active basis functions N_3^0 and N_4^0 are expressed in terms of N_5^1 and N_6^1. The limitation of their support to $\Omega_5^{\mathrm{e},1}$ and $\Omega_6^{\mathrm{e},1}$ results in the truncation and scaling of N_4^0 which is identical to the truncated hierarchical basis in [79]. Hence the hiearchical basis possesses the partition of unity property.

ments, i.e. the integrated domain.

That is, the basis functions N_1^0 to N_4^0 fully add to the coefficient matrix $\underline{\underline{\mathbf{K}}}^0$ during quadrature of the active elements $\Omega_1^{\mathrm{e},0}$ and $\Omega_2^{\mathrm{e},0}$. However, the remainder of the support of N_3^0 and N_4^0 on the coarsest level $\ell = 0$ is not considered during numerical integration as it is not covered by an active element. Instead, integration continues with the elements $\Omega_5^{\mathrm{e},1}$ and $\Omega_6^{\mathrm{e},1}$. In these two elements, the basis functions N_5^1 and N_6^1, which are not part of the hierarchical basis, contribute to the coefficient matrix $\underline{\underline{\mathbf{K}}}^1$.

Effect of $\underline{\underline{\mathbf{M}}}_{\mathrm{h}}$

Eventually, the hierarchical refinement operator will account for the activity of the basis functions and recover the correct support of active basis functions. The matrix elements resulting from N_5^1 and N_6^1 are mapped onto those due to N_3^0 and N_4^0. In this way the contribution of the active basis functions N_3^0 and N_4^0 in the domains $\Omega_5^{\mathrm{e},1}$ and $\Omega_6^{\mathrm{e},1}$ is taken into account. As the support of N_5^1 and N_6^1 is limited to these two active elements on level $\ell = 1$, the support domain of N_4^0 is truncated which also results in a scaling of the basis function. The result is identical to the proposal in [79]. Therefore, the presented approach provides approximations that possess the partition of unity property. As a consequence, the control point polygon will be a convex hull to any B-spline curve represented in terms of the truncated basis.
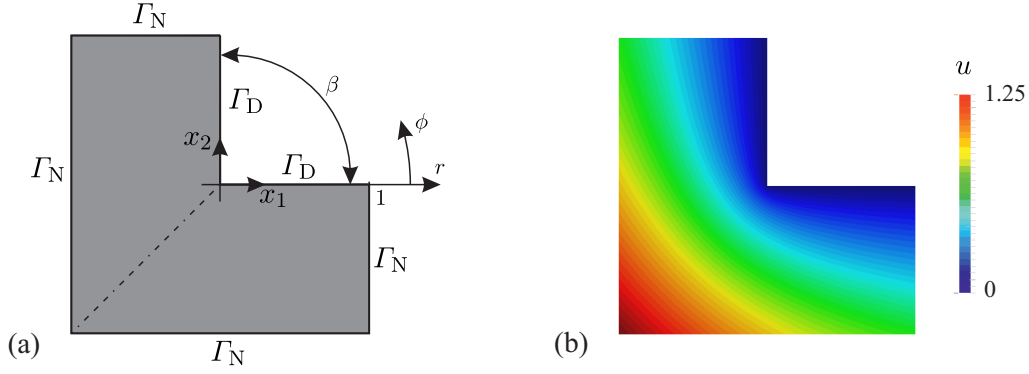
Figure 9.6: Laplace problem on an L-shaped domain: **(a)** domain modelled by two patches (C^0-continuous patch boundary indicated by dashed line) with boundary conditions, and **(b)** analytical solution.

9.2.3 Convergence Analysis

In this section a numerical example is considered to analyse the numerical properties of the presented refinement approach. The results of the adaptive local refinement algorithm are compared with results obtained from globally refined NURBS and given analytical solutions that are commonly used as benchmarks in adaptive IGA [54, 221]. Below, the Laplace problem

$$\Delta u = 0 \text{ in } \Omega \ , \ \bar{u} = 0 \text{ on } \Gamma_D \ , \ \frac{\partial \bar{u}}{\partial n} = g \text{ on } \Gamma_N \ , \tag{9.14}$$

is solved for the temperature u on a two-dimensional L-shaped domain Ω. The exact solution of the problem is given by

$$\bar{u} = r^{\frac{3}{2}} \sin \frac{2\phi - \pi}{3} \ . \tag{9.15}$$

On the Neumann boundary Γ_N, the exact heat flux $g = \partial \bar{u}/\partial n$ and on the Dirichtlet boundary Γ_D, homogeneous boundary conditions are applied. The definition of the boundary value problem is illustrated in Fig. 9.6.

The domain is modelled by two NURBS patches resulting in a C^0-continuous line, dashed in Fig. 9.6. Note that the L-shaped geometry could also be modelled by a C^1-continuous basis. But as already shown by Vuong [220], who used hierarchical B-splines to adaptively refine the mesh, the continuity of the approximation does not influence the convergence rates, neither for uniform nor for local refinement if the marking criterion is adjusted accordingly. Only an offset between the convergence curves can be found which implies that a C^1-continuous basis provides a better overall approximation.

The geometry of the problem leads to a singularity at the re-entrant corner. In this case classical convergence theory does not hold and the order of convergence with respect to the total number of degrees of freedom

$$k = -\frac{1}{2} \ \min \left(p, \frac{\pi}{2\pi - \beta} \right) \tag{9.16}$$

is governed by the angle β of the re-entrant corner. In the case of global h-refinement this leads to a convergence rate of $k = -1/3 \ \forall p$ for the L-shaped domain with $\beta = 90°$.
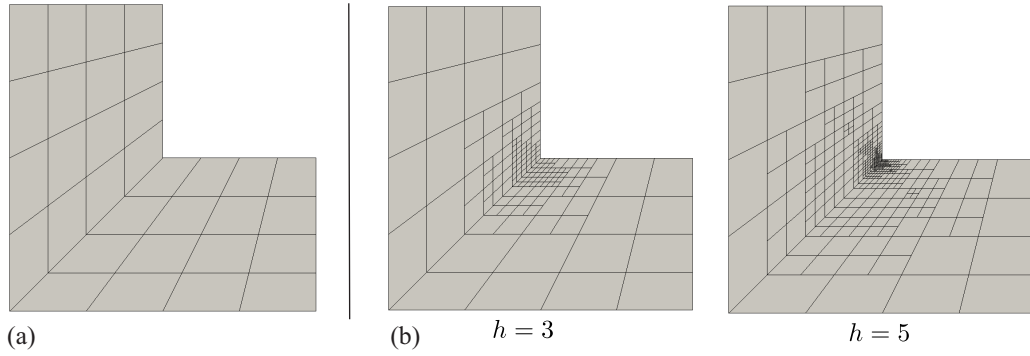
Figure 9.7: Bézier meshes for the Laplace problem: **(a)** initial mesh of 32 elements, and **(b)** adaptive mesh refinement resolves the corner singularity after $h = 3$ and $h = 5$ refinement steps.

Refinement criterion

The optimal order of convergence $k = -p/2$ can be recovered by local mesh refinement in the vicinity of the singularity. The adaptive refinement in this study is controlled by a measure for the element error and a treshold value θ. An element I whose error η_I exceeds the threshold ($\eta_I > \theta$) will be marked for refinement. Having at hand the reference solution (9.15), the H^1 norm of the error

$$\eta_I^2 = \|(\bar{u} - u)\|_{L^2} + \|\nabla(\bar{u} - u)\|_{L^2} \tag{9.17}$$

serves as a measure for η_I. The domain error $\eta^2 = \sum_I \eta_I^2$ is obtained as the sum over all elements. According to Dörfel et al. [54] two principal choices for the threshold can be used:

 (i) *Maximum error marking:* In this case the threshold

$$\theta = \alpha \cdot \max_I (\eta_I) \quad \text{with} \quad \alpha \approx 0.5 \tag{9.18}$$

is defined relative to the maximum element error. That is, those elements will be marked for refinement whose error exceeds $\alpha \cdot 100\,\%$ of the maximum element error in the mesh.

 (ii) *Quantile marking:* In the second major criterion the α-quantile of element errors defines the threshold

$$\theta = \alpha\text{-quantile}(\eta_I) \quad \text{with} \quad 0 < \alpha < 1. \tag{9.19}$$

All elements exceeding this error level will be refined, e.g. for $\alpha = 0.8$ the $20\,\%$ of elements with the largest error will be marked for refinement.

Analysis

The results presented below have been obtained for a quadratic and a cubic basis with an initial mesh of 32 elements, Fig. 9.7 (a), and $L = 6$ adaptive refinement steps. The mesh refinement is controlled by quantile marking with $\alpha = 0.8$. In Fig. 9.7 (b) meshes for the quadratic basis are given. It can be seen that the corner singularity is well detected within the refinement process. Figure 9.8 shows a comparison of the convergence for adaptive local and global mesh refinement. While the convergence of uniform h-refinement is governed by the singularity, i.e. the expected order of convergence of $k = -\frac{1}{3}$ is found, optimal orders of convergence are achieved for the quadratic ($k = -1$) and the cubic basis ($k = -1.5$) in the case of adaptive local refinement. This implies that the approach generates well graded meshes in the vicinity of the corner singularity.
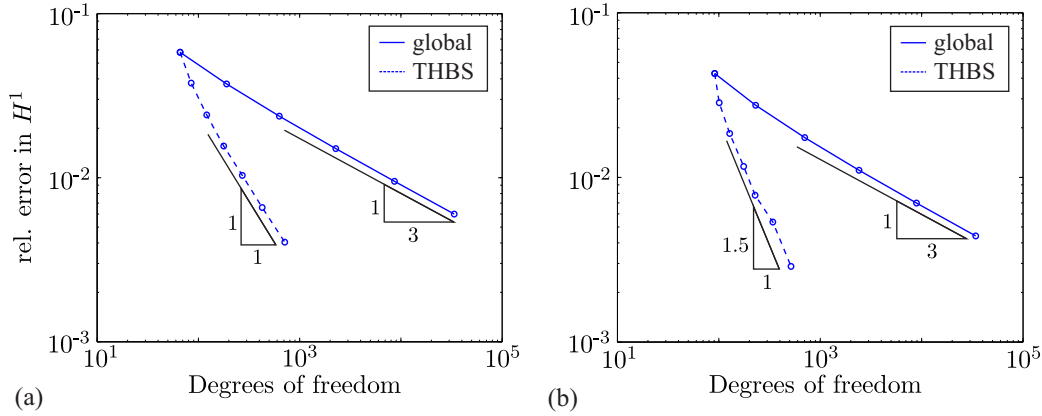
Figure 9.8: Convergence rates for the Laplace problem measured in the H^1 norm: As expected, local refinement improves the convergence rate to $k = -1$ for the quadratic **(a)** and to $k = -1.5$ for the cubic **(b)** basis.

9.3 Adaptive Isogeometric Analysis of the Cahn-Hilliard Model

In the following, the hierarchical refinement introduced and analysed in the preceding sections will be applied to the adaptive isogeometric analysis of the Cahn-Hilliard model presented in Section 8.1. Different from the convergence analysis of Section 9.2.3 where computations have been restarted from the initial state after each refinement step, the adaptive analysis of a typical structual evolution process will require the mapping of field quantities between the meshes of two consecutive time steps. While only refinement operations have been considered so far, the efficient analysis of decomposition processes necessitates the coarsening of the mesh. In Section 9.3.1 three suitable projection algorithms are introduced and compared. A demonstraction problem is presented in Section 9.3.2.

9.3.1 Projection of Field Quantities

Assume a solution ${}^t\underline{c}_h$ has been computed for the time increment t using the hierarchical basis ${}^t\mathcal{H}$ spanned by the set of basis functions ${}^t\underline{N}_h$. For the subsequent increment $t + \Delta t$, certain elements will be marked for refinement or coarsening. This results in the activation or deactivation of Bézier elements and their associated basis functions and control points. Therefore, the solution ${}^t\underline{c}_h$ has to be mapped to the new hierarchical basis ${}^{t+\Delta t}\mathcal{H}$ in order to generate a new initial solution vector ${}^{t+\Delta t}_0\underline{c}_h$ for the subsequent time step. If the hierarchical mesh ${}^{t+\Delta t}\mathcal{H}$ results from a refinement of ${}^t\mathcal{H}$, this mapping will always be exact because the fine scale basis functions are able to excatly represent the coarse scale solution. Consequently, new control variables

$$
{}^{t+\Delta t}_0\underline{c}^{\ell+1} = \left(\underline{\underline{M}}^{\ell,\ell+1}\right)^T {}^t\underline{c}^\ell \tag{9.20}
$$

can be obtained from a simple matrix operation which according to the two-scale relation (9.1) involves the subdivision operator $\underline{\underline{M}}^{\ell,\ell+1}$ relating two successive hierarchy levels ℓ and $\ell + 1$.

Contrarily, mapping the solution from level $\ell + 1$ to ℓ, which is required if the mesh has been coarsened during analysis, will generally introduce an approximation error as the coarse scale basis functions do not include the fine scale basis. Therefore, suitable projection meth-

Introduction

Refinement

Coarsening

ods are required. Three different approaches will be briefly reviewed and compared regarding the resulting discretisation error. The time increment is omitted for brevity of the notation:

(i) *Linear L^2 projection:* The aforementioned fact that the coarse scale basis does not contain the fine scale basis functions is reflected by the non-square structure of the subdivision operator $\underline{\underline{\mathbf{M}}}^{\ell,\ell+1}$. Therefore, a direct inversion of the two-scale relation (9.20) is not possible. However, a linear least square projection can be obtained from

$$\underline{\mathbf{c}}^\ell = \left(\underline{\underline{\mathbf{M}}}^{\ell,\ell+1}\right)^+ \underline{\mathbf{c}}^{\ell+1} \tag{9.21}$$

with $\left(\underline{\underline{\mathbf{M}}}^{\ell,\ell+1}\right)^+$ the *pseudo-inverse* of the subdivision operator defined by

$$\left(\underline{\underline{\mathbf{M}}}^{\ell,\ell+1}\right)^+ = \left[\underline{\underline{\mathbf{M}}}^{\ell,\ell+1} \left(\underline{\underline{\mathbf{M}}}^{\ell,\ell+1}\right)^T\right]^{-1} \underline{\underline{\mathbf{M}}}^{\ell,\ell+1} . \tag{9.22}$$

(ii) *Non-linear L^2 projection:* A generally more accurate result for the projection of the fine scale approximation $c^{\ell+1}(\mathbf{x})$ to the control values $\underline{\mathbf{c}}^\ell$ of a coarser level can be obtained from a standard L^2 projection. In this case the error between the fine and coarse scale approximations

$$\int_\Omega \left(c^\ell(\mathbf{x}) - c^{\ell+1}(\mathbf{x})\right)^2 \, dV = \int_\Omega \left(\underline{\mathbf{N}}^\ell\underline{\mathbf{c}}^\ell - \underline{\mathbf{N}}^{\ell+1}\underline{\mathbf{c}}^{\ell+1}\right)^2 \, dV = \min \tag{9.23}$$

is to be minimised which yields a system of equations for the computation of the coarse scale control variables.

(iii) *Bézier projection:* Bézier extraction has been combined with spline reconstruction techniques by Thomas et al. [209] to form a general method for the projection between modified, e.g. refined, coarsened, or degree-elevated spline bases. For the considered case of a projection from $J = 1 \ldots n_{\mathrm{m}}$ fine-scale elements $\Omega_J^{\mathrm{e},\ell+1}$ which are to be merged into a single coarse-scale element $\Omega_I^{\mathrm{e},\ell}$, Bézier projection consists of a sequence of matrix operations to compute the control values $\underline{\mathbf{c}}_I^\ell$ of the coarse level Bézier element

$$\underline{\mathbf{c}}_I^\ell = \underbrace{\left(\underline{\underline{\mathbf{R}}}_I^\ell\right)^T}_{\text{Reconstruction}} \underbrace{\sum_{J=1}^{n_{\mathrm{m}}} \phi_{IJ}\underline{\underline{\mathbf{G}}}^{-1} \underline{\underline{\mathbf{A}}}_J^{-T} \underline{\underline{\mathbf{G}}}}_{\text{Projection}} \underbrace{\left(\underline{\underline{\mathbf{C}}}_J^{\ell+1}\right)^T}_{\text{Extraction}} \underline{\mathbf{c}}_J^{\ell+1} \tag{9.24}$$

which are detailed in *Algorithm 4.3* of [209]. Firstly, the approximation in the fine-scale elements is localised, i.e. Bézier control variables, cf. Section 6.1.2, are obtained using the element-local Bézier extraction operators $\underline{\underline{\mathbf{C}}}_J^{\ell+1}$. These values are then projected onto the coarse Bézier element based on relations between the differently scaled Bernstein basis functions in the elements of the levels ℓ and $\ell+1$. According to Farouki [65] the relations are given in terms of the matrix $\underline{\underline{\mathbf{A}}}_J$ and the Gramian $\underline{\underline{\mathbf{G}}}$. For details see [209], equations (12)-(16). The contribution of each element J is weighted according to its volume fraction $\phi_{IJ} = \frac{\text{vol}(\Omega_J^{\mathrm{e},\ell+1})}{\text{vol}(\Omega_I^{\mathrm{e},\ell})}$. Eventually, the coarse-scale Bézier control variables are tranformed into control variables using the reconstruction operator $\underline{\underline{\mathbf{R}}}_I^\ell = \left(\underline{\underline{\mathbf{C}}}_I^\ell\right)^{-1}$. As the control value for a given function produced by Bézier
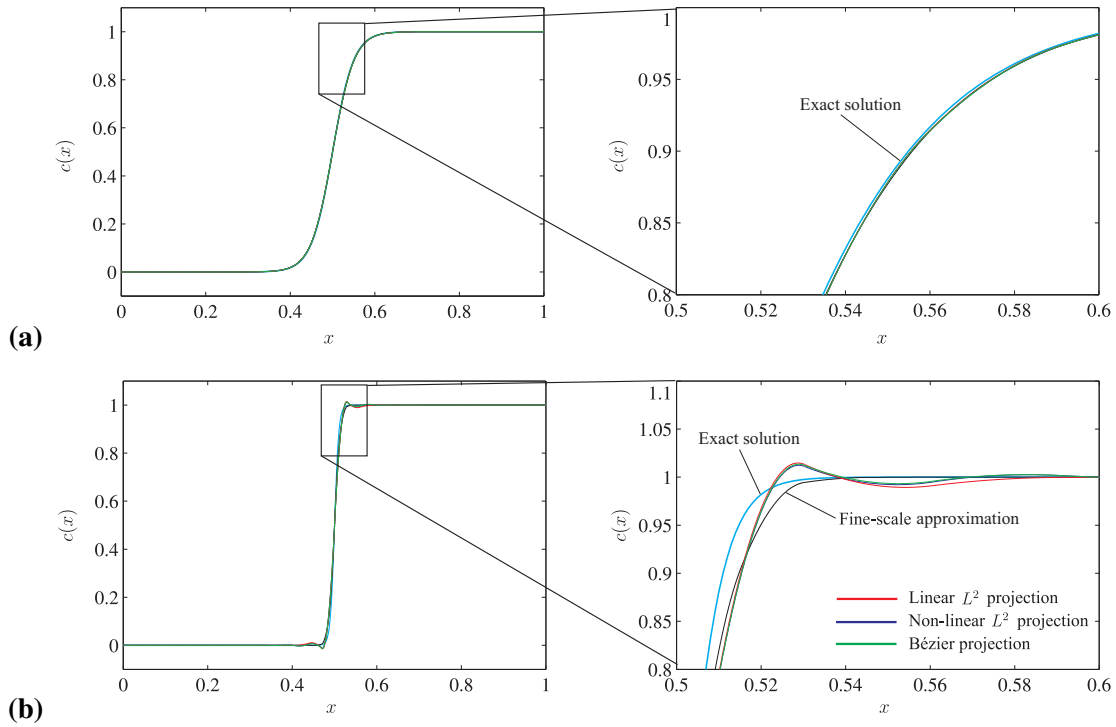
Figure 9.9: Comparison of three approaches to the projection of field quantities: (i) linear L^2 projection, (ii) non-linear L^2 projection, and (iii) Bézier projection [209] of a fine-scale approximation ($p = 2$, 64 elements) of $c(x)$ according to (9.26) to a coarse mesh of 32 elements ($p = 2$): **(a)** interface width $\varepsilon = 0.05\,\mathrm{m}$ which can be resolved by the coarse scale, and **(b)** increased projection error for a reduced interface thickness of $\varepsilon = 0.01\,\mathrm{m}$ which cannot be approximated by the coarse mesh.

projection will be different for each element in the support of the function, smoothing

$$c_A^\ell = \sum_{I \in \mathrm{supp}(N_A)} \omega_{AI} c_A^{I,\ell} \tag{9.25}$$

is required to generate a globally continuous approximation. In the equation above $c_A^{I,\ell}$ is the control value in $\underline{c}_I^\ell$ associated to the basis function N_A^ℓ.

Comparing these three principal approaches to the projection of control variables, it can be noted that both, linear least squares (i) and Bézier projection (iii), are quadrature free procedures which gives them the edge over the standard L^2 projection from a computational point of view. As the subdivision operators required to compute the pseudo-inverse are used in the implementation of the truncated hierarchical basis, the linear least square projection (i) is employed in the present implementation. In addition, it has to be remarked, that the approaches mentioned above do not have to be applied to a full hierarchy level. In order to increase their efficiency all transformations can be applied locally. Local L^2 projections are proposed by Jiang and Dolbow [107], and Bézier projection can be applied to any number of elements to be merged [209].

Discussion

In order to justify the choice of the linear L^2 projection (i) over Bézier projection (iii), the ac-

Accuracy

Table 9.1: L^2 error $||c||_{L^2}$ between fine- and coarse-scale approximations for three different projection methods.

Projection	$\varepsilon = 0.05\,\text{m}$	$\varepsilon = 0.01\,\text{m}$
(i) Linear L^2 projection	1×10^{-9}	1.724×10^{-7}
(ii) Non-linear L^2 projection	0.992×10^{-9}	1.711×10^{-7}
(iii) Bézier projection	1.097×10^{-9}	1.921×10^{-7}

curacy of the projection is analysed for a one-dimensional demonstration problem involving a highly localised concentration distribution

$$c(x) = \frac{1}{2} \left[1 + \tanh \left(\frac{x - x_{\text{int}}}{\varepsilon} \right) \right] \ . \tag{9.26}$$

Again ε is an adjustable interface width and the location of the interface is at $x_{\text{int}} = 0.5\,\text{m}$. Figure 9.9 shows the exact solution, the fine scale approximation, and projections to the coarse scale produced by the methods (i)-(iii) for two different values $\varepsilon = 0.05, 0.01\,\text{m}$. For the thick interface ($\varepsilon = 0.05\,\text{m}$), all curves are virtually identical by visual expection because the coarse level mesh can represent the exact solution. This is also confirmed by the numerical approximation error between the two levels

$$||c||_{L^2} = \int_{\Omega} \left(c^{\ell}(x) - c^{\ell+1}(x) \right)^2 \, dx \tag{9.27}$$

in the L^2 norm listed in Tab. 9.1. For the thin interface ($\varepsilon = 0.01\,\text{m}$) the projection to the coarse level results in larger approximation errors, Fig. 9.9 (b). As the interface cannot be resolved by the coarse level mesh all projection methods produce similar results with characteristic overshoots in the vicinity of the steepest gradient. Table 9.1 reveals similar errors for the linear and non-linear L^2 projections while a slightly increased error is found for Bézier projection.

9.3.2 Demonstration

Coarsening

The projection of field variables is now applied in conjunction with the adaptive hierarchical refinement strategy to track an evolving interface. As outlined in Section 8.4, the spinodal decomposition process of a binary system can be divided into two principal phases. The initial nucleation phase produces a large number of inclusions which then coalesce to form larger but fewer inclusions which minimises the interface energy. A fine mesh is required to capture the nucleation process and it has to be used until the mixture is fully decomposed. As this state corresponds to the maximum of the interface energy, the value $\mathcal{F}_{\text{int}}$ can serve as a criterion for the activation of adaptive mesh refinement. The process of coalescence leads to domains with virtually constant concentration which do not require fine meshes. Coarsening the mesh in these domains will therefore allow to reduce the total number of degrees of freedom. In conjunction with an adaptive time stepping scheme, the efficiency of the computations can be improved. However, as the shape and the position of inclusions will change significantly until the stationary state is achieved, cf. Fig. 8.9, previously coarsened domains of the mesh have to be refined again to properly track the moving interface.

$$t = 1 \times 10^{-5}\,\mathrm{s} \qquad t = 4.9 \times 10^{-4}\,\mathrm{s} \qquad t = 3.4 \times 10^{-3}\,\mathrm{s} \qquad t = 1\,\mathrm{s}$$
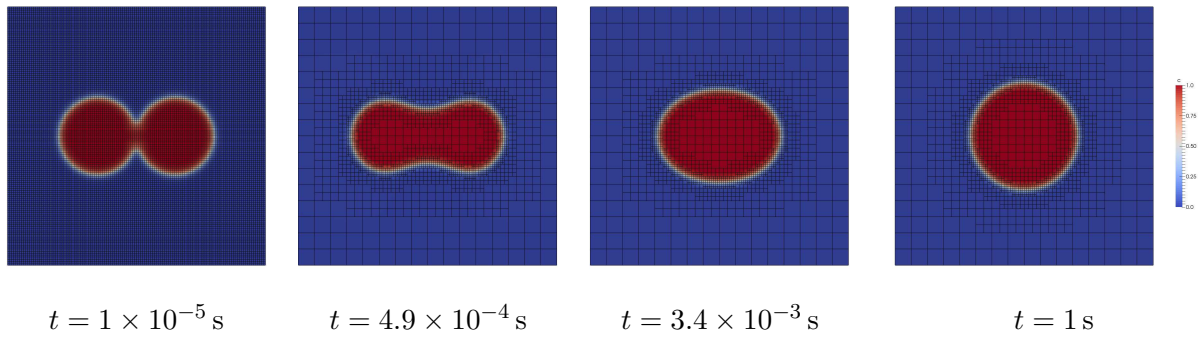
Figure 9.10: Simulation of two coalescing inclusions with an overall concentration $\tilde{c} \approx 0.14$: temporal evolution of the concentration field and adaptive mesh refinement/coarsening.

Below, two coalescing inclusions will be considered as a simplified preliminary demonstration problem. The initial configuration is defined by

<div align="right">Coalescing inclusions</div>

$$c(\mathbf{x}, t = 0) = 1 - \frac{1}{2}\sum_{I=1}^{2}\tanh\left(\frac{||\mathbf{x} - \mathbf{x}_c^I|| - R}{\sqrt{2}\varepsilon}\right) \tag{9.28}$$

with $x_{1c}^I = [0.35,\ 0.65]\,\mathrm{m}$ and $x_{2c}^I = [0.5,\ 0.5]\,\mathrm{m}$ the coordinates of the center points of two overlapping circular inclusions. A radius $R = 0.15\,\mathrm{m}$ that is identical for both inclusions and an interface thickness $\varepsilon = 1 \times 10^{-2}\,\mathrm{m}$ result in an overall concentration of $\tilde{c} \approx 0.14$. The mobility $M = 1\,\mathrm{m^3\,s\,kg^{-1}}$ was chosen to be constant and the interface parameter was set to $\lambda = 1 \times 10^{-2}\,\mathrm{J\,m^{-1}}$. Adaptive time stepping with an initial time step of $\Delta t_0 = 1 \times 10^{-5}\,\mathrm{s}$ has been applied during the solution. Figure 9.10 shows the temporal evolution of the concentration field in the interval $t \in [0,\ 1]\,\mathrm{s}$. Energy minimisation results in the complete coalescence of both inclusions. In the second part of this optimisation process, the oblate shape approaches a circular configuration.

In addition to the adaptive time stepping scheme, the analysis mesh has been refined in the vicinity of the interface and coarsened in domains of approximately constant concentration. A four-level hierarchical mesh was used and the solution starts from the finest resolution of 128×128 elements. An adaptation of the spatial discretisation is carried out in the first and every fifth increment. Mesh adaptivity is controlled in terms of the order parameter c, i.e. elements are selected for coarsening if $c_I \geq 0.95 \vee c_I \leq 0.05$ within an element Ω_{Ie}. Otherwise it is flagged for refinement. Additional constraints, e.g. that adjacent elements have to belong to two consecutive hierarchy levels and that elements can only be coarsened if all other children of the common parent element have been marked for coarsening, are imposed to ensure a well graded mesh. The hierarchical meshes which follow from these procedures are illustrated in Fig. 9.10.

<div align="right">Mesh adaptivity</div>

Figure 9.11 (a) presents a comparison of the energies and concentrations between a uniform and the hierarchical discretisation. It can be concluded that both uniform and adaptive meshing result in exactly the same physical behaviour. As a consequence of the lower number of active elements of approximately 2000 compared to 16384 in the uniform mesh, the solution time of the adaptive model, which includes time for mesh refinement and coarsening and the projection between different levels, is found to be less than one third of the time required for the solution using a uniform mesh, Fig. 9.11 (b).

<div align="right">Discussion</div>
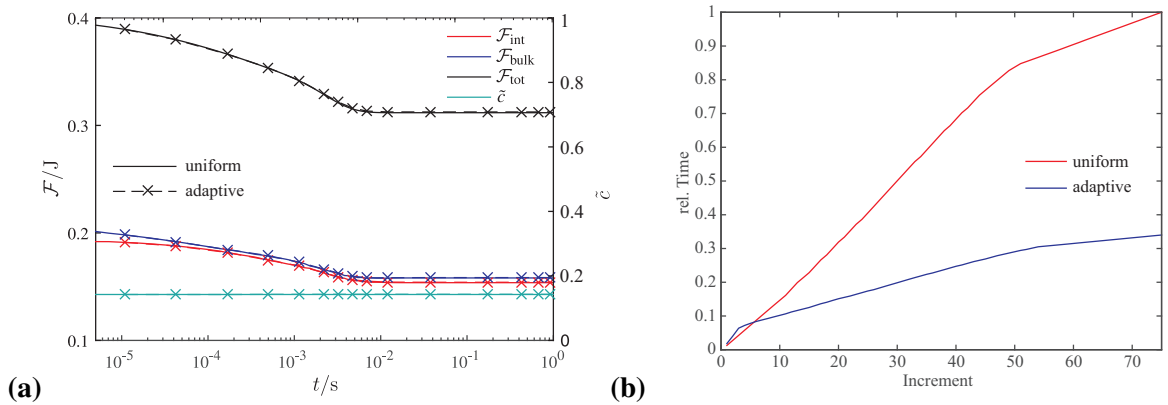
(a) t/s **(b)**

Figure 9.11: Temporal evolution of **(a)** the total concentration $\tilde{c}$ and different energy contributions $\mathcal{F}$. The adaptively refined and coarsened four-level hierarchical mesh (dashed lines) produces identical results compared to a uniform mesh (128×128 elements, solid lines), and **(b)** comparison of the total computation time.

$t = 1 \times 10^{-5}\,\mathrm{s}$ $t = 4.9 \times 10^{-4}\,\mathrm{s}$ $t = 3.4 \times 10^{-3}\,\mathrm{s}$ $t = 1\,\mathrm{s}$
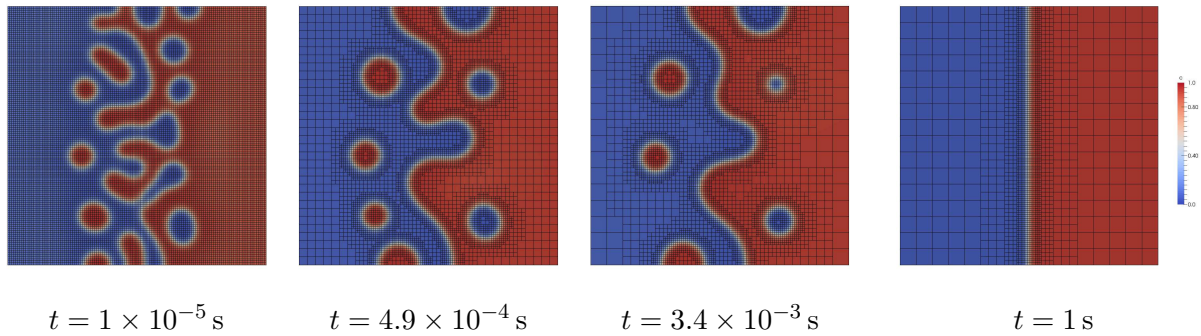
Figure 9.12: Spinodal decomposition from a linear, randomly perturbed concentration distribution with $\tilde{c} = 0.5$: temporal evolution of the initial concentration field into two phases separated by a straight interface and adaptively refined/coarsened mesh.

Linear concentration field

The purpose of the second example is to demonstrate the applicability of the approach to more complex distributions $c(\mathbf{x})$. To this end, the linearly varying initial distribution $c = x_1 + r$, with $0 \leq x_1 \leq 1$ and $-0.005 \leq r \leq 0.005$, already analysed in Section 8.4.2 is revisited here. During the first stage of the decomposition process new inclusions are generated. These newly formed inclusions are coarsened during the later stages of the evolution, Fig. 9.12. While the nucleation phase can only be captured by a highly refined uniform mesh, adaptive mesh refinement/coarsening will increase the efficiency of the computations during the latter phase. Adaptive meshing is therefore activated for $t \geq 1 \times 10^{-4}\,\mathrm{s}$, i.e. after the interfacial energy contribution has reached its maximum, Fig. 9.13 (a). Bézier elements are selected for refinement if $|\nabla c| \geq 0.5$ while they are flagged for coarsening otherwise. The restrictions on the refinement and coarsening mentioned above ensure well graded meshes. Snapshots of the temporal evolution of the microstructure and the associated adaptive mesh can be seen in Fig. 9.12.

Discussion

In order to allow for a quantitative comparison, Fig. 9.13 (a) shows the results for the temporal evolution of the concentration and various energies for both uniform and adaptive meshes. It can be observed, in particular from the detail plot, that both approaches produce almost
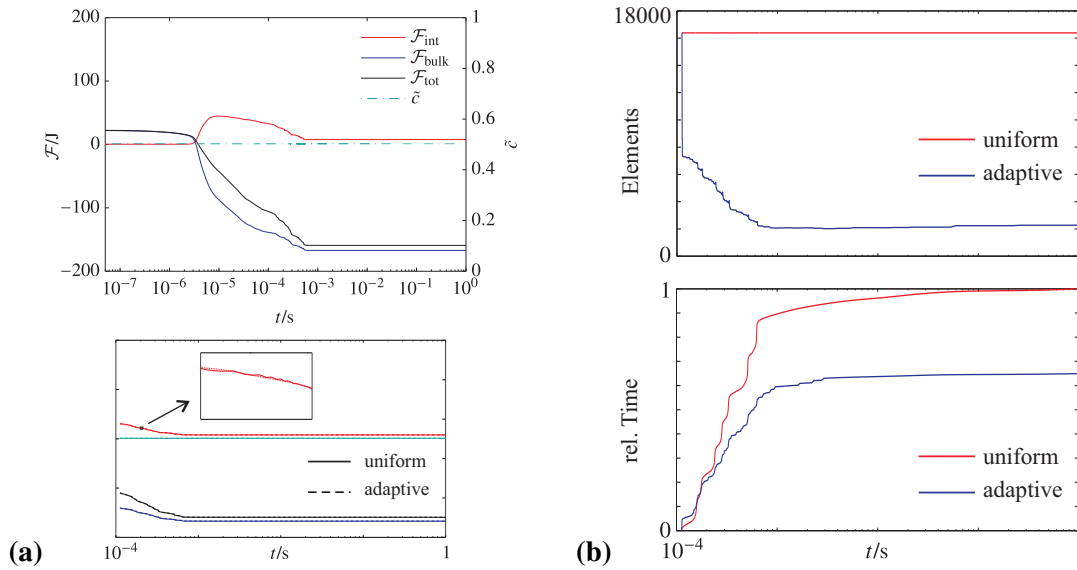
Figure 9.13: Spinodal decomposition from a linear, randomly perturbed concentration distribution with $\tilde{c} = 0.5$: **(a)** temporal evolution of $\tilde{c}$ and $\mathcal{F}$, and **(b)** evolution of the adaptively controlled time step.

identical results. In compliance with the theoretical aspect of $\mathcal{F}$ being a Lyapunov functional, the total free energy decreases monotonically. Furthermore, the average of the concentration $\tilde{c}$ is constant as expected for a conserved phase-field model described by the Cahn-Hilliard equation. However, the adaptive solution procedure significantly reduces the number of active elements compared to the uniform mesh. This results in a speed-up of the computation of almost factor two.

9.4 Conclusion

It has been shown that the adaptive isogeometric analysis of phase-field models provides identical predictions as highly refined uniform meshes, however, at significantly reduced computational costs. These preliminary results indicate that there is a great potential in adaptive isogeometric discretisations. Moreover, a novel approach to the implementation of hierarchical approximations has been introduced in this chapter. It is based on Bézier extraction and avoids the explicit computation of the hierarchical basis. As different levels of the hierarchical mesh are treated independently, standard procedures can be applied at each level. The communication between different levels is incorporated in terms of a hierarchical refinement operator and corresponding matrix operations. It was also shown that these procedures implicitly define the truncated hierarchical B-spline basis. The presented approach will therefore ensure linear independence and provide the partition of unity property. Future work will focus on the mapping of internal variables, the implementation of periodic hierarchical meshes, and the application to more complex distributions as well as to the adaptive isogeometric phase-field modelling of crack propagation.

10 Summary and Outlook

Industrial development processes as well as research in physics, materials and engineering science rely on computer modelling and simulation techniques today. Numerical challenges arising from these applications led to the development of new numerical methods and the continuous enhancement of existing approaches. With increasing computer power, computations are carried out on different scales ranging from the atomistic level to the macroscopic scale of engineering structures. Various modelling techniques, e.g. molecular dynamics, coarse grained approaches or finite element discretisations of continuum models, that are suitable for different scales can be combined into multi-scale techniques. They facilitate a prediction of the effective material or structural behaviour based on the local morphology and the properties of the individual constituents. This provides valueable insight into the structure-property relations which are of interest for any design process.

Modelling and simulation

In this work, it was assumed that the influence of the atomistic structure of the material at the considered scales can be neglected. Therefore, a phenomenological continuum approach has been applied in conjunction with two different representations of interfaces. In a continuum formulation, the physics of the problem to be solved is described in terms of partial differential equations for a certain set of field variables. The behaviour at interfaces is governed by jump conditions that occur during the transition from global to local forms of the balance equations. That is, classical continuum models use a *sharp interface* representation which requires the localisation of interfaces in the numerical models. In standard finite element discretisations this is achieved by conforming meshes, i.e. element edges with reduced continuity have to be aligned with the discontinuity. However, if the structure to be modelled changes with time, e.g. due to evolution processes in the material or the initiation and propagation of cracks, the sharp interface representation requires a topological update of the finite element mesh. Therefore, *diffuse interface* models which regularise the interface in terms of an additional field variable have been considered as an alternative. These models allow to decouple the localisation and representation of the discontinuity from the analysis mesh but fine discretisations are required to obtain reasonable solutions. If finite elements are to be applied, adaptive mesh refinement strategies are essential to limit the computational costs.

Interfaces and Discontinuities

With extended and isogeometric finite element discretisations two up-to-date modelling techniques have been considered in this work. At first, both methods have been applied to discretise sharp interface models and their numerical properties have been studied and compared. XFEM uses a non-conforming mesh and an implicit interface representation in terms of level sets. The physics at the interface is modelled by a local enrichment of the approximation. In order to improve its applicability, an element local level set representation was presented and procedures for the consistent handling of curved discontinuities have been investigated. Eventually an Update-Lagrangian formulation suitable for finite deformations was presented and differences to the standard formulation have been outlined. It was demonstrated that XFEM provides an ideal means to generate numerical models of random particulate microstructures. The regular XFEM mesh is also beneficial if periodic boundary conditions have to be applied. However, the flexibility of the approach comes at the cost of numerical accuracy. It was shown in two convergence studies that quadratic approximations provide

XFEM for sharp interface models

only suboptimal convergence rates. In comparison to both, standard and isogeometric finite elements, an increased error level is to be expected for XFEM. Despite its implicit interface representation in terms of the level set, the capability to model evolving discontinuities is limited as the division of elements into integration subdomains still represents a topological update.

IGA of sharp interface models The application of isogeometric discretisations to the modelling of sharp interfaces is very similar to the standard finite element method as a conforming mesh is required. Different from the standard approach, the adjustable continuity of the spline basis can be used to switch between different interface characteristics. That is, knot insertion could be used to transform a C^0-continuous material interface into an interface crack. Moreover, it could be shown that the method has excellent approximation properties. The spline-based approximation provides optimal convergence rates and is very efficient. Lower error levels have been found in comparison to the standard and extended FEM. As a consequence of the NURBS basis, geometric discretisation errors were avoided for the considered demonstration problems. This is of even greater advantage for macroscale computations because typical computer aided design geometry models can be used directly for structural analysis.

IGA of diffuse interface models A conceptually interesting approach results from the isogeometric discretisation of diffuse interface representations. The spline basis handles the high gradients of the order parameter in the vicinity of an interface very efficiently and it can provide the increased continuity required by higher-order differential operators. It was shown in this work that optimal orders of convergence can be achieved with a spline basis of sufficient order. To further increase the efficiency of isogeometric discretisations of diffuse interfaces, adaptive mesh refinement and coarsening techniques based on hierarchical splines have been developed. These procedures allow for an finite element point of view and avoid the explicit computation of the analysis suitable truncated hierarchical basis. The locally refined meshes were found to reduce the number of degrees of freedom required for a certain accuracy of the approximation significantly.

Comparison It is noted that the two combinations (i) XFEM + sharp interface model, and (ii) IGA + diffuse interface model, represent two fundamentally different approaches to the modelling of discontinuities. XFEM reduces the continuity of the approximation in terms suitable enrichment functions according to the discontinuity to be modelled. Instead diffuse models regularise the interface which requires an increased continuity that is provided by the spline-based approximation.

Modelling of MRE Except for the phase-field models which were considered to demonstrate the diffuse interface approach, the developed discretisation techniques have been applied to solve a coupled magneto-mechanical problem for particulate microstructures of MRE. In combination with a computational homogenisation approach these microscopic models allowed for the prediction of the effective coupled magneto-mechanical response of MRE. Moreover, finite element models of generic MRE microstructures have been coupled with a BEM domain that represents the surrounding free space in order to take into finite sample geometries. The macroscopic behaviour was analysed in terms of actuation stresses, magnetostrictive deformations, and the magnetorheological effect. The results obtained for different microstructures and various loadings have been found to be in qualitative agreement with experiments on MRE as well as analytical results. The presented results show in addition that there is no significant difference between the assumption of small or finite deformations in particular for a realistic non-linear magnetisation behaviour. However, MRE can undergo finite strains

due to mechanical loadings which cause significant changes to the internal structure. Taking into account these microstructural changes during the solution of the coupled magneto-mechanical field problem will require the application of the large deformation procedures presented here.

All of the discretisation techniques and models presented in this work have been implemented into a Matlab-based finite element code which provides further analysis features, e.g. thermo-mechanical coupling and several phase-field models for the simulation of crack propagation. This enables the adaptive isogeometric phase-field modelling of crack propagation. A possible future application that is interesting from a physical point of view is the simulation of the complex fracture behaviour of polymers under thermo-mechanical loadings. From a modelling point of view it is interesting to combine sharp and diffuse interface representations to improve the efficiency in comparison to a pure phase-field representation. Moreover, gradient damage models are very similar to phase-field models of crack propagation but they may resolve problems reported regarding the convergence of the phase-field approach with mesh refinement.

Bibliography

[1] H. Altenbach. *Kontinuumsmechanik*. Springer, 2012.

[2] J. Altenbach and H. Altenbach. *Einführung in die Kontinuumsmechanik*. Teubner, 1994.

[3] D. Bardzokas, M. Filshtinsky, and L. Filshtinsky. Mathematical Methods in Electro-Magneto-Elasticity. *Springer-Verlag, Berlin*, 2007.

[4] J. Barrett, J. Blowey, and H. Garcke. Finite Element Approximation of the Cahn–Hilliard Equation with Degenerate Mobility. *SIAM J. Numer. Anal.*, 37:286–318, 1999.

[5] Y. Bazilevs, V. Calo, J. Cottrell, J. Evans, T. Hughes, S. Lipton, M. Scott, and T. Sederberg. Isogeometric analysis using T-splines. *Comput. Methods Appl. Mech. Engrg.*, 199:229–263, 2010.

[6] Y. Bazilevs, V. Calo, T. Hughes, and Y. Zhang. Isogeometric fluid-structure interaction: theory, algorithms, and computations. *Comput. Mech.*, 43:3–37, 2008.

[7] Y. Bazilevs, V. Calo, Y. Zhang, and T. Hughes. Isogeometric Fluid-structure Interaction Analysis with Applications to Arterial Blood Flow. *Comput. Mech.*, 38:310–322, 2006.

[8] Y. Bazilevs, M.-C. Hsu, and M. Scott. Isogeometric fluid-structure interaction analysis with emphasis on non-matching discretizations, and with application to wind turbines. *Comput. Methods Appl. Mech. Engrg.*, 249–252:28–41, 2012.

[9] T. Belytschko, N. Moës, S. Usui, and C. Parimi. Arbitrary discontinuities in finite elements. *Int. J. Numer. Meth. Engng*, 50:993–1013, 2001.

[10] T. Belytschko, W. K. Liu, and B. Moran. *Nonlinear Finite Elements for Continua and Structures*. Wiley, 2000.

[11] T. Belytschko, C. Parimi, N. Moës, N. Sukumar, and S. Usui. Structured extended finite element methods for solids defined by implicit surfaces. *Int. J. Numer. Meth. Engng.*, 56:609–635, 2003.

[12] D. J. Benson, Y. Bazilevs, E. De Luycker, M.-C. Hsu, M. Scott, T. J. R. Hughes, and T. Belytschko. A generalized finite element formulation for arbitrary basis functions: From isogeometric analysis to XFEM. *Int. J. Numer. Meth. Engng.*, 83:765–785, 2010.

[13] D. Benson, Y. Bazilevs, M.-C. Hsu, and T. Hughes. A large deformation, rotation-free, isogeometric shell. *Comput. Methods Appl. Mech. Engrg.*, 200:1367–1378, 2011.

[14] A. L. Bertozzi, S. Esedoglu, and A. Gillette. Inpainting of Binary Images Using the Cahn-Hilliard Equation. *IEEE T. Image Process.*, 16:285–291, 2007.

[15] S. P. A. Bordas, S. Natarajan, P. Kerfriden, C. E. Augarde, D. R. Mahapatra, T. Rabczuk, and S. D. Pont. On the performance of strain smoothing for quadratic and enriched finite element approximations (XFEM/GFEM/PUFEM). *Int. J. Numer. Meth. Engng.*, 86:637–666, 2011.

[16] S. P. Bordas, T. Rabczuk, N.-X. Hung, V. P. Nguyen, S. Natarajan, T. Bog, D. M. Quan, and N. V. Hiep. Strain smoothing in FEM and XFEM. *Comput. Struct.*, 88:1419–1443, 2010.

[17] M. J. Borden, M. A. Scott, J. A. Evans, and T. J. R. Hughes. Isogeometric finite element data structures based on Bézier extraction of NURBS. *Int. J. Numer. Meth. Engng.*, 87:15–47, 2011.

[18] D. Borin, D. Günther, C. Hintze, G. Heinrich, and S. Odenbach. The level of cross-linking and the structure of anisotropic magnetorheological elastomers. *J. Magn. Mag. Mater.*, 324:3452–3454, 2012.

[19] M. C. Boyce and E. M. Arruda. Constitutive Models of Rubber Elasticity: A Review. *Rubber Chem. Technol.x*, 73:504–523, 2000.

[20] C. A. Brebbia, J. C. F. Telles, and L. C. Wrobel. *Boundary Element Techniques*. Springer, 1984.

[21] C. Brebbia and J. Dominquez. *Boundary Elements: An Introductory Course*. WIT Press, 1992.

[22] A. Bressan. Some properties of LR-splines. *Comput. Aided Geom. D.*, 30:778–794, 2013.

[23] I. A. Brigadnov and A. Dorfmann. Mathematical modeling of magneto-sensitive elastomers. *Int. J. Solids Struct.*, 40:4659–4674, 2003.

[24] F. Bruckner, C. Vogler, M. Feischl, D. Praetorius, B. Bergmair, T. Huber, M. Fuger, and D. Suess. 3D FEM–BEM-coupling method to solve magnetostatic Maxwell equations. *J. Magn. Mag. Mater.*, 324:1862–1866, 2012.

[25] J. Brummund. *Eine Notiz zur Ableitung von Sprungbedingungen und Feldgleichungen in einer Fläche aus den zughörigen Feldgleichungen im Raum mittels Distributionen und Anwendungen*. Personal Communication, 2013.

[26] A. Buffa, J. Rivas, G. Sangalli, and R. Vázquez. Isogeometric Discrete Differential Forms in Three Dimensions. *SIAM J. Numer. Anal.*, 49:818–844, 2011.

[27] A. Buffa, G. Sangalli, and R. Vázquez. Isogeometric analysis in electromagnetics: B-splines approximation. *Comput. Methods Appl. Mech. Engrg.*, 199:1143–1152, 2010.

[28] R. Bustamante. *Mathematical modelling of non-linear magneto- and electro-active rubber-like materials*. PhD thesis, University of Glasgow, 2007.

[29] J. W. Cahn. Phase Separation by Spinodal Decomposition in Isotropic Systems. *J. Chem. Phys.*, 42:93–99, 1965.

[30] J. W. Cahn and J. E. Hilliard. Free Energy of a Nonuniform System. I. Interfacial Free Energy. *J. Chem. Phys.*, 28:258–267, 1958.

[31] J. D. Carlson and M. R. Jolly. MR fluid, foam and elastomer devices. *Mechatronics*, 10:555–569, 2000.

[32] G. Casciola and L. Romani. *A general matrix representation for non-uniform B-spline subdivision with boundary control*. Technical report, University of Bologna, 2007.

[33] P. K. Chan and A. D. Rey. A numerical method for the nonlinear Cahn-Hilliard equation with nonperiodic boundary conditions. *Comput. Mater. Sci.*, 3:377–392, 1995.

[34] G. Chatzigeorgiou, A. Javili, and P. Steinmann. Unified magnetomechanical homogenization framework with application to magnetorheological elastomers. *Math. Mech. Solids*, 2012.

[35] L. Chen, T. Rabczuk, S. Bordas, G. Liu, K. Zeng, and P. Kerfriden. Extended finite element method with edge-based strain smoothing (ESm-XFEM) for linear elastic crack growth. *Comput. Methods Appl. Mech. Engrg.*, 209–212:250–265, 2012.

[36] L.-Q. Chen. Phase-field models for microstructure evolution. *Annu. Rev. Mater. Res.*, 32:113–140, 2002.

[37] K. W. Cheng and T.-P. Fries. Higher-order XFEM for curved strong and weak discontinuities. *Int. J. Numer. Meth. Engng.*, 82:564–590, 2010.

[38] J. Chung and G. M. Hulbert. A Time Integration Algorithm for Structural Dynamics With Improved Numerical Dissipation: The Generalized-α Method. *J. Appl. Mech.*, 60:371–375, 1993.

[39] B. D. Coleman and W. Noll. The thermodynamics of elastic materials with heat conduction and viscosity. *Arch. Ration. Mech. An.*, 13:167–178, 1963.

[40] E. Coquelle and G. Bossis. Magnetostriction and piezoresistivity in elastomers filled with magnetic particles. *J. Adv. Sci.*, 17:132–138, 2005.

[41] J. Cottrell, T. Hughes, and Y. Bazilevs. *Isogeometric Analysis: Toward Integration of CAD and FEA*. Wiley, Chichester, 2009.

[42] J. Cottrell, A. Reali, Y. Bazilevs, and T. Hughes. Isogeometric analysis of structural vibrations. *Comput. Methods Appl. Mech. Engrg.*, 195:5257–5296, 2006.

[43] K. Danas, S. Kankanala, and N. Triantafyllidis. Experiments and modeling of iron-particle-filled magnetorheological elastomers. *J. Mech. Phys. Solids*, 60:120–138, 2012.

[44] C. Dauxz, N. Moës, J. Dolbow, N. Sukumar, and T. Belytschko. Arbitrary branched and intersecting cracks with the extended finite element method. *Int. J. Numer. Meth. Engng*, 48:1741–1760, 2000.

[45] C. Daveau and M. Menad. Mixed FEM and BEM coupling for the three-dimensional magnetostatic problem. *Numer. Meth. Part. D. E.*, 19:443–462, 2003.

[46] L. C. Davis. Model of magnetorheological elastomers. *J. Appl. Phys.*, 85:3348–3351, 1999.

[47] R. de Borst, M. Crisfield, C. V. Verhoosel, and J. J. C. Remmers. *Non-linear Finite Element Analysis of Solids and Structures: Second edition*. Wiley, 2012.

[48] S. de Groot and L. Suttorp. *Foundations of Electrodynamics*. North Holland, 1972.

[49] L. De Lorenzis, I. Temizer, P. Wriggers, and G. Zavarise. A large deformation frictional contact formulation using NURBS-based isogeometric analysis. *Int. J. Numer. Meth. Engng.*, 87:1278–1300, 2011.

[50] E. De Luycker, D. J. Benson, T. Belytschko, Y. Bazilevs, and M. C. Hsu. X-FEM in isogeometric analysis for linear fracture mechanics. *Int. J. Numer. Meth. Engng.*, 87:541–565, 2011.

[51] G. Diguet, E. Beaugnon, and J. Y. Cavaillé. Shape effect in the magnetostriction of ferromagnetic composite. *J. Magn. Magn. Mater.*, 322:3337–3341, 2010.

[52] E. Dohmen, M. Boisly, D. Borin, M. Kästner, V. Ulbricht, M. Gude, W. Hufenbach, G. Heinrich, and S. Odenbach. Advancing Towards Polyurethane-Based Magnetorheological Composites. *Adv. Eng. Mater.*, 16:1270–1275, 2014.

[53] T. Dokken, T. Lyche, and K. F. Pettersen. Polynomial splines over locally refined box-partitions. *Comput. Aided Geom. D.*, 30:331–356, 2013.

[54] M. R. Dörfel, B. Jüttler, and B. Simeon. Adaptive isogeometric analysis by local h-refinement with T-splines. *Comput. Methods Appl. Mech. Engrg.*, 199:264–275, 2010.

[55] A. Dorfmann and R. W. Ogden. Nonlinear magnetoelastic deformations. *Q. J. Mech. Appl. Math.*, 57:599–622, 2004.

[56] K. Dréau, N. Chevaugeon, and N. Moës. Studied X-FEM enrichment to handle material interfaces with higher order finite element. *Comput. Methods Appl. Mech. Engrg.*, 199:1922–1936, 2010.

[57] A. Düster, J. Parvizian, Z. Yang, and E. Rank. The finite cell method for three-dimensional problems of solid mechanics. *Comput. Methods Appl. Mech. Engrg.*, 197:3768–3782, 2008.

[58] R. Echter, B. Oesterle, and M. Bischoff. A hierarchic family of isogeometric shell finite elements. *Comput. Methods Appl. Mech. Engrg.*, 254:170–180, 2013.

[59] C. Elliott, D. French, and F. Milner. A second order splitting method for the Cahn-Hilliard equation. *Numer. Math.*, 54:575–590, 1989.

[60] H. Emmerich. Advances of and by phase-field modelling in condensed-matter physics. *Adv. Phys.*, 57:1–87, 2008.

[61] A. Engel and R. Friedrichs. On the electromagnetic force on a polarizable body. *Am. J. Phys.*, 70:428–432, 2002.

[62] G. Engel, K. Garikipati, T. Hughes, M. Larson, L. Mazzei, and R. Taylor. Continuous/discontinuous finite element approximations of fourth-order elliptic problems in structural and continuum mechanics with applications to thin beams and plates, and strain gradient elasticity. *Comput. Methods Appl. Mech. Engrg.*, 191:3669–3750, 2002.

[63] A. Eringen and G. Maugin. *Electrodynamics of Continua I.* Springer New York, 1990.

[64] E. Evans, M. Scott, X. Li, and D. Thomas. Hierarchical T-splines: Analysis-suitability, Bézier extraction, and application as an adaptive basis for isogeometric analysis. *Comput. Methods Appl. Mech. Engrg.*, 284:1–20, 2015.

[65] R. T. Farouki. The Bernstein polynomial basis: A centennial retrospective. *Comput. Aided Geom. D.*, 29:379–419, 2012.

[66] J. Fetzer, S. Abele, and G. Lehner. Die Kopplung der Randelementmethode und der Methode der finiten Elemente zur Lösung dreidimensionaler elektromagnetischer Feldprobleme auf unendlichem Grundgebiet. *Electr. Eng.*, 76:361–368, 1993.

[67] G. Filipcsei, I. Csetneki, A. Szilágyi, and M. Zrínyi. Magnetic field-responsive smart polymer composites. *Adv. Polym. Sci.*, 206:137–189, 2007.

[68] D. R. Forsey and R. H. Bartels. Hierarchical B-spline Refinement. *SIGGRAPH Comput. Graph.*, 22:205–212, 1988.

[69] D. Fredkin and T. R. Koehler. Hybrid method for computing demagnetizing fields. *IEE T. Magn.*, 26:415–417, 1990.

[70] T.-P. Fries. A corrected XFEM approximation without problems in blending elements. *Int. J. Numer. Meth. Engng.*, 75:503–532, 2008.

[71] T.-P. Fries and T. Belytschko. The extended/generalized finite element method: An overview of the method and its applications. *Int. J. Numer. Meth. Engng.*, 84:253–304, 2010.

[72] D. Fritze, S. Marburg, and H.-J. Hardtke. FEM–BEM-coupling and structural–acoustic sensitivity analysis for shell geometries. *Comput. Struct.*, 83:143–154, 2005.

[73] E. Galipeau and P. Ponte Castañeda. The effect of particle shape and distribution on the macroscopic behavior of magnetoelastic composites. *Int. J. Solids Struct.*, 49:1–17, 2012.

[74] E. Galipeau and P. Ponte Castañeda. A finite-strain constitutive model for magnetorheological elastomers: Magnetic torques and fiber rotations. *J. Mech. Phys. Solids*, 61:1065–1090, 2013.

[75] E. Galipeau and P. Ponte Castañeda. Giant field-induced strains in magnetoactive elastomer composites. *Proc. R. Soc. A*, 469:1–12, 2013.

[76] L. Gaul and M. Schanz. A comparative study of three boundary element approaches to calculate the transient response of viscoelastic solids with unbounded domains. *Comput. Methods Appl. Mech. Engrg.*, 179:111–123, 1999.

[77] L. Gaul, M. Kögl, and M. Wagner. *Boundary Element Methods for Engineers and Scientists*. Springer, 2003.

[78] M. Geers, V. Kouznetsova, and W. Brekelmans. Multi-scale computational homogenization: Trends and challenges. *J. Comput. Appl. Math.*, 234:2175–2182, 2010.

[79] C. Giannelli, B. Jüttler, and H. Speleers. THB-splines: The truncated basis for hierarchical splines. *Comput. Aided Geom. D.*, 29:485–498, 2012.

[80] H. Gómez, V. M. Calo, Y. Bazilevs, and T. J. Hughes. Isogeometric analysis of the Cahn–Hilliard phase-field model. *Comput. Methods Appl. Mech. Engrg.*, 197:4333–4352, 2008.

[81] H. Gómez, A. Reali, and G. Sangalli. Accurate, efficient, and (iso)geometrically flexible collocation methods for phase-field models. *J. Comp. Phys.*, 262:153–171, 2014.

[82] X. Guan, X. Dong, and J. Ou. Magnetostrictive effect of magnetorheological elastomer. *J. Magn. Magn. Mater.*, 320:158–163, 2008.

[83] M. Guiggiani. Error indicators for adaptive mesh refinement in the boundary element method – a new approach. *Int. J. Numer. Meth. Engng.*, 29:1247–1269, 1990.

[84] M. Guiggiani and P. Casalini. Direct computation of Cauchy principal value integrals in advanced boundary elements. *Int. J. Numer. Meth. Engng.*, 24:1711–1720, 1987.

[85] D. Günther, D. Y. Borin, S. Günther, and S. Odenbach. X-ray micro-tomographic characterization of field-structured magnetorheological elastomers. *Smart Mater. Struct.*, 21:015005, 2012.

[86] G. Haasemann, M. Kästner, S. Prüger, and V. Ulbricht. Development of a quadratic finite element formulation based on the XFEM and NURBS. *Int. J. Numer. Meth. Engng.*, 86:598–617, 2011.

[87] Y. Han. *Mechanics of magneto-active polymers*. PhD thesis, Iowa State University, 2012.

[88] Y. Han, W. Hong, and L. E. Faidley. Field-stiffening effect of magneto-rheological elastomers. *Int. J. Solids Struct.*, 50:2281–2288, 2013.

[89] P. Haupt. On the mathematical modelling of material behavior in continuum mechanics. *Acta Mech.*, 100:129–154, 1993.

[90] P. Haupt. *Continuum Mechanics and Theory of Materials*. Springer, 2002.

[91] A. Hawkins-Daarud, K. G. van der Zee, and J. Tinsley Oden. Numerical simulation of a thermodynamically consistent four-species tumor growth model. *Int. J. Numer. Meth. Biomed. Engng.*, 28:3–24, 2012.

[92] P. Hennig. *Adaptive Isogeometric Modelling using T-splines and Hierarchical NURBS*. Master's thesis, TU Dresden, 2014.

[93] C. Hesch and K. Weinberg. Thermodynamically consistent algorithms for a finite-deformation phase-field approach to fracture. *Int. J. Numer. Meth. Engng*, 99:906–924, 2014.

[94] R. Hill. On constitutive macro-variables for heterogeneous solids at finite strain. *Proc. R. Soc. Lond. A.*, pages 131–147, 1972.

[95] F. Hirsch. *Bestimmung effektiver mikroskopischer Grenzflächeneigenschaften auf Basis einer Kohäsivzonenhomogenisierung*. Master's thesis, TU Dresden, 2015.

[96] S. J. Hollister and N. Kikuchi. Homogenization theory and digital imaging: A basis for studying the mechanics and design principles of bone tissue. *Biotechnol. Bioeng.*, 43:586–596, 1994.

[97] S. Hollister, J. Brennan, and N. Kikuchi. A homogenization sampling procedure for calculating trabecular bone effective stiffness and tissue level stress. *J. Biomech.*, 27:433–444, 1994.

[98]   G. Holzapfel. *Nonlinear Solid Mechanics - A Continuum Approach for Engineering.* Wiley, 2000.

[99]   T. Hughes, J. Cottrell, and Y. Bazilevs. Isogeometric analysis: CAD, finite elements, NURBS, exact geometry and mesh refinement. *Comput. Methods Appl. Mech. Engrg.*, 194:4135–4195, 2005.

[100] D. Ivaneyko, V. P. Toshchevikov, M. Saphiannikova, and G. Heinrich. Effects of particle distribution on the mechanical properties of magneto-sensitive elastomers in a homogeneous magnetic field. *Condens. Matter Phys.*, 15:33601:1–12, 2012.

[101] D. Ivaneyko, V. P. Toshchevikov, M. Saphiannikova, and G. Heinrich. Mechanical properties of magneto-sensitive elastomers in a homogeneous magnetic field: theory and experiment. *Macromol. Sy.*, accepted.

[102] D. Ivaneyko, V. Toshchevikov, M. Saphiannikova, and G. Heinrich. Mechanical properties of magneto-sensitive elastomers: unification of the continuum-mechanics and microscopic theoretical approaches. *Soft Matter*, 10:2213–2225, 2014.

[103] D. Ivaneyko, V. P. Toshchevikov, M. Saphiannikova, and G. Heinrich. Magneto-sensitive Elastomers in a Homogeneous Magnetic Field: A Regular Rectangular Lattice Model. *Macromol. Theory Simul.*, 20:411–424, 2011.

[104] J. Jackson. *Klassische Elektrodynamik.* Walter de Gruyter, Berlin, 4 edition, 2006.

[105] K. E. Jansen, C. H. Whiting, and G. M. Hulbert. A generalized-α method for integrating the filtered Navier–Stokes equations with a stabilized finite element method. *Comput. Methods Appl. Mech. Engrg.*, 190:305 – 319, 2000.

[106] A. Javili, G. Chatzigeorgiou, and P. Steinmann. Computational homogenization in magneto-mechanics. *Int. J. Solids Struct.*, 50:4197–4216, 2013.

[107] W. Jiang and J. E. Dolbow. Adaptive refinement of hierarchical B-spline finite elements with an efficient data transfer algorithm. *Int. J. Numer. Meth. Engng*, 102:233–256, 2015.

[108] K. A. Johannessen, T. Kvamsdal, and T. Dokken. Isogeometric analysis using LR B-splines. *Comput. Methods Appl. Mech. Engrg.*, 269:471–514, 2014.

[109] P. Kagan, A. Fischer, and P. Z. Bar-Yoseph. Mechanically based models: Adaptive refinement for B-spline finite element. *Int. J. Numer. Meth. Engng.*, 57:1145–1175, 2003.

[110] K. Kalina. *Formulierung und Implementierung eines Materialmodells für nichtlineare finite Viskoelastizität.* Student research project, TU Dresden, 2014.

[111] S. Kankanala and N. Triantafyllidis. On finitely strained magnetorheological elastomers. *J. Mech. Phys. Solids*, 52:2869–2908, 2004.

[112] P. Kanouté, D. Boso, J. Chaboche, and B. Schrefler. Multiscale Methods for Composites: A Review. 16:31–75–, 2009.

[113] M. Kästner. *Skalenübergreifende Modellierung und Simulation des mechanischen Verhaltens von textilverstärktem Polypropylen unter Nutzung der XFEM.* PhD thesis, TU Dresden, 2010.

[114] M. Kästner, G. Haasemann, and V. Ulbricht. Multiscale XFEM modelling and simulation of the inelastic material behaviour of textile-reinforced polymers. *Int. J. Numer. Meth. Engng*, 86:477–498, 2011.

[115] M. Kästner, S. Müller, and V. Ulbricht. XFEM Modelling of Inelastic Material Behaviour and Interface Failure in Textile-Reinforced Composites. *Proc. Mater. Sci.*, 2:43–51, 2013.

[116] M. Kästner, M. Obst, J. Brummund, K. Thielsch, and V. Ulbricht. Inelastic material behavior of polymers - Experimental characterization, formulation and implementation of a material model. *Mech. Mater.*, 52:40–57, 2012.

[117] D. Kay, V. Styles, and E. Süli. Discontinuous Galerkin Finite Element Approximation of the Cahn–Hilliard Equation with Convection. *SIAM J. Numer. Anal.*, 47:2660–2685, 2009.

[118] J. Keyak, J. Meagher, H. Skinner, and C. Mote Jr. Automated three-dimensional finite element modelling of bone: a new method. *J. Biomed. Eng.*, 12:389–397, 1990.

[119] J. Kiendl, Y. Bazilevs, M.-C. Hsu, R. Wüchner, and K.-U. Bletzinger. The bending strip method for isogeometric analysis of Kirchhoff–Love shell structures comprised of multiple patches. *Comput. Methods Appl. Mech. Engrg.*, 199:2403–2416, 2010.

[120] J. Kiendl, K.-U. Bletzinger, J. Linhard, and R. Wüchner. Isogeometric shell analysis with Kirchhoff–Love elements. *Comput. Methods Appl. Mech. Engrg.*, 198:3902–3914, 2009.

[121] V. Kouznetsova. *Computational homogenization for the multi-scale analysis of multiphase materials*. PhD thesis, TU Eindhoven, 2002.

[122] T. Koyama. Phase-field modeling of microstructure evolutions in magnetic materials. *Sci. Technol. Adv. Mat.*, 9:013006, 2008.

[123] C. Kuhn and R. Müller. A continuum phase field model for fracture. *Eng. Fract. Mech.*, 77:3625–3634, 2010.

[124] J. B. Lasserre. Integration on a Convex Polytope. *P. Am. Math. Soc.*, 126:2433–2441, 1998.

[125] J. B. Lasserre. Integration and Homogeneous Functions. *P. Am. Math. Soc.*, 127:813–818, 1999.

[126] G. Legrain, P. Cartraud, I. Perreard, and N. Moës. An X-FEM and level set computational approach for image-based modelling: Application to homogenization. *Int. J. Numer. Meth. Engng.*, 86:915–934, 2011.

[127] G. Legrain, N. Chevaugeon, and K. Dréau. High Order X-FEM and Levelsets for Complex Microstructures: Uncoupling Geometry and Approximation. *Comput. Methods Appl. Mech. Engrg.*, page http://dx.doi.org/10.1016/j.cma.2012.06.001., 2012.

[128] K. Li and X. Qian. Isogeometric analysis and shape optimization via boundary integral. *Comput. Aided Design*, 43:1427–1437, 2011.

[129] X. Li, J. Zheng, T. W. Sederberg, T. J. Hughes, and M. A. Scott. On linear independence of T-spline blending functions. *Comput. Aided Geom. D.*, 29:63–76, 2012.

[130] C. Linder, D. Rosato, and C. Miehe. New finite elements with embedded strong discontinuities for the modeling of failure in electromechanical coupled solids. *Comput. Methods Appl. Mech. Engrg.*, 200:141–161, 2011.

[131] G. Liu, K. Dai, and T. Nguyen. A Smoothed Finite Element Method for Mechanics Problems. *Comput. Mech.*, 39:859–877–, 2007.

[132] J. Liu, L. Dedè, J. A. Evans, M. J. Borden, and T. J. Hughes. Isogeometric analysis of the advective Cahn–Hilliard equation: Spinodal decomposition under shear flow. *J. Comp. Phys.*, 242:321–350, 2013.

[133] O. Lopez-Pamies, T. Goudarzi, and K. Danas. The nonlinear elastic response of suspensions of rigid inclusions in rubber: II – A simple explicit approximation for finite-concentration suspensions. *J. Mech. Phys. Solids*, 61:19–37, 2013.

[134] O. Lopez-Pamies, T. Goudarzi, and T. Nakamura. The nonlinear elastic response of suspensions of rigid inclusions in rubber: I – An exact result for dilute suspensions. *J. Mech. Phys. Solids*, 61:1–18, 2013.

[135] O. Lopez-Pamies and M. Idiart. An Exact Result for the Macroscopic Response of Porous Neo-Hookean Solids. *J. Elasticity*, 95:99–105, 2009.

[136] T. Martin and E. Cohen. Volumetric parameterization of complex objects by respecting multiple materials. *Comput. Graphics*, 34:187–197, 2010.

[137] S. May, J. Vignollet, and R. de Borst. The role of the Bézier extraction operator for T-splines of arbitrary degree: linear dependencies, partition of unity property, nesting behaviour and local refinement. *Int. J. Numer. Meth. Engng*, 2015.

[138] S. May, J. Vignollet, and R. de Borst. A numerical assessment of phase-field models for brittle and cohesive fracture: Γ-convergence and stress oscillations. *Eur. J. Mech. A-Solid.*, 2015.

[139] P. Metsch. Modellierung und Simulation gekoppelter magnetomechanischer Feldprobleme unter Berücksichtigung finiter Deformationen. Student research project, TU Dresden, 2013.

[140] C. Miehe, M. Hofacker, and F. Welschinger. A phase field model for rate-independent crack propagation: Robust algorithmic implementation based on operator splits. *Comput. Methods Appl. Mech. Engrg.*, 199:2765–2778, 2010.

[141] C. Miehe, B. Kiefer, and D. Rosato. An incremental variational formulation of dissipative magnetostriction at the macroscopic continuum level. *Int. J. Solids Struct.*, 48:1846–1866, 2011.

[142] C. Miehe, D. Rosato, and B. Kiefer. Variational principles in dissipative electro-magneto-mechanics: A framework for the macro-modeling of functional materials. *Int. J. Numer. Meth. Engng.*, 86:1225–1276, 2011.

[143] N. Moelans, B. Blanpain, and P. Wollants. An introduction to phase-field modeling of microstructure evolution. *Calphad*, 32:268–294, 2008.

[144] N. Moës, M. Cloirec, P. Cartraud, and J.-F. Remacle. A computational approach to handle complex microstructure geometries. *Comput. Methods Appl. Mech. Engrg.*, 192:3163–3177, 2003.

[145] N. Moës, J. Dolbow, and T. Belytschko. A finite element method for crack growth without remeshing. *Int. J. Numer. Meth. Engng.*, 46:131–150, 1999.

[146] J. Moraleda, J. Segurado, and J. LLorca. Finite deformation of incompressible fiber-reinforced elastomers: A computational micromechanics approach. *J. Mech. Phys. Solids*, 57:1596–1613, 2009.

[147] M. Moumnassi, S. Belouettar, E. Béchet, S. P. A. Bordas, D. Quoirin, and M. Potier-Ferry. Finite element analysis on implicitly defined domains: An accurate representation based on arbitrary parametric surfaces. *Comput. Methods Appl. Mech. Engrg.*, 200:774–796, 2011.

[148] S. Mousavi and N. Sukumar. Generalized Duffy transformation for integrating vertex singularities. *Comput. Mech.*, 45:127–140, 2010.

[149] S. Mousavi and N. Sukumar. Numerical integration of polynomials and discontinuous functions on irregular convex polygons and polyhedrons. *Comput. Mech.*, 47:535–554, 2011.

[150] S. E. Mousavi, H. Xiao, and N. Sukumar. Generalized Gaussian quadrature rules on arbitrary polygons. *Int. J. Numer. Meth. Engng.*, 82:99–113, 2010.

[151] S. Mousavi and N. Sukumar. Generalized Gaussian quadrature rules for discontinuities and crack singularities in the extended finite element method. *Comput. Methods Appl. Mech. Engrg.*, 199:3237–3249, 2010.

[152] S. Müller. *Modelling of inelastic material behaviour and failure of fibre reinforced polymers*. PhD thesis, TU Dresden, 2015.

[153] N. Mußchelischwili. Einige Grundaufgaben zur mathematischen Elastizitästheorie. *VEB Fachbuchverlag, Leipzig*, 1971.

[154] S. Natarajan, S. Bordas, and D. Roy Mahapatra. Numerical integration over arbitrary polygonal domains based on Schwarz–Christoffel conformal mapping. *Int. J. Numer. Meth. Engng.*, 80:103–134, 2009.

[155] S. Natarajan, D. R. Mahapatra, and S. P. A. Bordas. Integrating strong and weak discontinuities without integration subcells and example applications in an XFEM/GFEM framework. *Int. J. Numer. Meth. Engng.*, 83:269–294, 2010.

[156] V. P. Nguyen, R. Simpson, S. Bordas, and T. Rabczuk. An introduction to Isogeometric Analysis with Matlab implementation: FEM and XFEM formulations. *ArXiv e-prints*, 2012.

[157] R. W. Ogden. Large Deformation Isotropic Elasticity - On the Correlation of Theory and Experiment for Incompressible Rubberlike Solids. *P. Roy. Soc. Lond. A. Mat.*, 326:565–584, 1972.

[158] R. W. Ogden. Large Deformation Isotropic Elasticity: On the Correlation of Theory and Experiment for Compressible Rubberlike Solids. *P. Roy. Soc. Lond. A. Mat.*, 328:567–583, 1972.

[159] S. Osher and R. P. Fedkiw. Level Set Methods: An Overview and Some Recent Results. *J. Comp. Phys.*, 169:463–502, 2001.

[160] G. Paria. Magneto-Elasticity and Magneto-Thermo-Elasticity. *Adv. Appl. Mech.*, 10:73–112, 1966.

[161] K. Park, J. P. Pereira, C. A. Duarte, and G. H. Paulino. Integration of singular enrichment functions in the generalized/extended finite element method for three-dimensional problems. *Int. J. Numer. Meth. Engng.*, 78:1220–1257, 2009.

[162] M. Peake, J. Trevelyan, and G. Coates. Extended isogeometric boundary element method (XIBEM) for two-dimensional Helmholtz problems. *Comput. Methods Appl. Mech. Engrg.*, pages –.

[163] J. P. Pereira, C. A. Duarte, D. Guoy, and X. Jiao. hp-Generalized FEM and crack surface representation for non-planar 3-D cracks. *Int. J. Numer. Meth. Engng.*, 77:601–633, 2009.

[164] M. M. Perez and L. C. Wrobel. An Integral-Equation Formulation for Anisotropic Elastostatics. *J. Appl. Mech.*, 63:891, 1996.

[165] G. Pessot, P. Cremer, D. Y. Borin, S. Odenbach, H. Löwen, and A. M. Menzel. Structural control of elastic moduli in ferrogels and the importance of non-affine deformations. *J. Chem. Phys.*, 141, 2014.

[166] H. Peters, S. Marburg, and N. Kessissoglou. Structural-acoustic coupling on non-conforming meshes with quadratic shape functions. *Int. J. Numer. Meth. Engng*, 91:27–38, 2012.

[167] L. Piegl and W. Tiller. *The NURBS Book*. Springer, 1996.

[168] M.-J. Pindera, H. Khatam, A. S. Drago, and Y. Bansal. Micromechanics of spatially uniform heterogeneous media: A critical review and emerging approaches. *Compos. Part B-Eng.*, 40:349–378, 2009.

[169] C. Politis, A. I. Ginnis, P. D. Kaklis, K. Belibassakis, and C. Feurer. An isogeometric BEM for exterior potential-flow problems in the plane. In *2009 SIAM/ACM Joint Conference on Geometric and Physical Modeling*, pages 349–354, San Francisco, California, 2009. ACM.

[170] P. Ponte Castañeda and E. Galipeau. Homogenization-based constitutive models for magnetorheological elastomers at finite strain. *J. Mech. Phys. Solids*, 59:194–215, 2011.

[171] P. Ponte Castañeda and M. Siboni. A finite-strain constitutive theory for electro-active polymer composites via homogenization. *Int. J. Nonlinear Mech.*, 47:293–306, 2012.

[172] D. Pusch and J. Ostrowski. Robust FEM/BEM Coupling for Magnetostatics on Multiconnected Domains. *IEEE T. Magn.*, 46:3177–3180, 2010.

[173] V. Rochus, L. Van Miegroet, D. J. Rixen, and P. Duysinx. Electrostatic simulation using XFEM for conductor and dielectric interfaces. *Int. J. Numer. Meth. Engng.*, 85:1207–1226, 2011.

[174] R. Rojas-Díaz, N. Sukumar, A. Sáez, and F. García-Sánchez. Fracture in magneto-electroelastic materials using the extended finite element method. *Int. J. Numer. Meth. Engng.*, 88:1238–1259, 2011.

[175] M. Schanz. A boundary element formulation in time domain for viscoelastic solids. *Commun. Numer. Meth. Engng.*, 15:799–809, 1999.

[176] D. Schillinger. *The p- and B-spline versions of the geometrically nonlinear finite cell method and hierarchical refinement strategies for adaptive isogeometric and embedded domain analysis*. PhD thesis, TU München, 2012.

[177] D. Schillinger, L. Dedè, M. A. Scott, J. A. Evans, M. J. Borden, E. Rank, and T. J. Hughes. An isogeometric design-through-analysis methodology based on adaptive hierarchical refinement of NURBS, immersed boundary methods, and T-spline CAD surfaces. *Comput. Methods Appl. Mech. Engrg.*, 249–252:116–150, 2012.

[178] D. Schillinger, J. A. Evans, A. Reali, M. A. Scott, and T. J. Hughes. Isogeometric collocation: Cost comparison with Galerkin methods and extension to adaptive hierarchical NURBS discretizations. *Comput. Methods Appl. Mech. Engrg.*, 267:170–232, 2013.

[179] J. Schröder. *Homogenisierungsmethoden der nichtlinearen Kontinuumsmechanik unter Beachtung von Stabilitätsproblemen*. Habilitation, Universität Stuttgart, 2000.

[180] J. Schröder. Derivation of the localization and homogenization conditions for electro-mechanically coupled problems. *Comput. Mater. Sci.*, 46:595–599, 2009.

[181] G. Schubert. *Manufacture, Characterisation, and Modelling of Magneto-Rheological Elastomers*. PhD thesis, University of Glasgow, 2014.

[182] G. Schubert and P. Harrison. Large-strain behaviour of Magneto-Rheological Elastomers tested under uniaxial compression and tension, and pure shear deformations. *Polym. Test.*, 42:122–134, 2015.

[183] M. A. Scott, X. Li, T. W. Sederberg, and T. J. R. Hughes. Local Refinement of Analysis-Suitable T-Splines . *Comput. Methods Appl. Mech. Engrg.*, 213–216:206–222, 2012.

[184] M. Scott, R. Simpson, J. Evans, S. Lipton, S. Bordas, T. Hughes, and T. Sederberg. Isogeometric boundary element analysis using unstructured T-splines. *Comput. Methods Appl. Mech. Engrg.*, 254:197–221, 2013.

[185] M. Scott, D. Thomas, and E. Evans. Isogeometric spline forests. *Comput. Methods Appl. Mech. Engrg.*, 269:222–264, 2014.

[186] M. A. Scott, M. J. Borden, C. V. Verhoosel, T. W. Sederberg, and T. J. R. Hughes. Isogeometric finite element data structures based on Bézier extraction of T-splines. *Int. J. Numer. Meth. Engng.*, 88:126–156, 2011.

[187] T. W. Sederberg, J. Zheng, A. Bakenov, and A. Nasri. T-splines and T-NURCCs. *ACM Trans. Graph.*, 22:477–484, 2003.

[188] T. W. Sederberg, D. L. Cardon, G. T. Finnigan, N. S. North, J. Zheng, and T. Lyche. T-spline Simplification and Local Refinement. *ACM Trans. Graph.*, 23:276–283, 2004.

[189] M. Siboni and P. Ponte Castañeda. A magnetically anisotropic, ellipsoidal inclusion subjected to a non-aligned magnetic field in an elastic medium. *CR Mécanique*, 340:205–218, 2012.

[190] J. C. Simo and R. L. Taylor. Quasi-incompressible finite elasticity in principal stretches. continuum basis and numerical algorithms. *Comput. Methods Appl. Mech. Engrg.*, 85:273–310, 1991.

[191] R. Simpson, S. Bordas, H. Lian, and J. Trevelyan. An isogeometric boundary element method for elastostatic analysis: 2D implementation aspects. *Comput. Struct.*, 118:2–12, 2013.

[192] R. Simpson, S. Bordas, J. Trevelyan, and T. Rabczuk. A two-dimensional Isogeometric Boundary Element Method for elastostatic analysis. *Comput. Methods Appl. Mech. Engrg.*, 209–212:87–100, 2012.

[193] G. Söderlind. Automatic Control and Adaptive Time-Stepping. *Numer. Algorithms*, 31:281–310, 2002.

[194] R. Spatschek, E. Brener, and A. Karma. Phase field modeling of crack propagation. *Philos. Mag.*, 91:75–95, 2010.

[195] C. Spieler, M. Kästner, and V. Ulbricht. Analytic and numeric solution of a magneto-mechanical inclusion problem. *Arch. Appl. Mech.*, 2014.

[196] S. Stark, A. S. Semenov, and H. Balke. On the boundary conditions for the vector potential formulation in electrostatics. *Int. J. Numer. Meth. Engng*, 102:1704–1732, 2015.

[197] I. Steinbach. Phase-field models in materials science. *Model. Simul. Mater. Sc.*, 17:073001, 2009.

[198] I. Steinbach and M. Apel. The influence of lattice strain on pearlite formation in Fe–C. *Acta Mater.*, 55:4817 – 4822, 2007.

[199] P. Steinmann, M. Hossain, and G. Possart. Hyperelastic models for rubber-like materials: consistent tangent operators and suitability for Treloar's data. *Arch. Appl. Mech.*, 82:1183–1217, 2012.

[200] G. V. Stepanov, S. S. Abramchuk, D. A. Grishin, L. V. Nikitin, E. Y. Kramarenko, and A. R. Khokhlov. Effect of a homogeneous magnetic field on the viscoelastic behavior of magnetic elastomers. *Polymer*, 48:488–495, 2007.

[201] R. H. Stogner, G. F. Carey, and B. T. Murray. Approximation of Cahn–Hilliard diffuse interface models using parallel adaptive mesh refinement and coarsening with C1 elementsta. *Int. J. Numer. Meth. Engng.*, 76:636–661, 2008.

[202] M. Stolarska, D. L. Chopp, N. Moës, and T. Belytschko. Modelling crack growth by level sets in the extended finite element method. *Int. J. Numer. Meth. Engng*, 51:943–960, 2001.

[203] G. Strang and G. Fix. *An analysis of the finite element method.* Wellesley-Cambridge Press, 1973.

[204] N. Sukumar, D. Chopp, N. Moës, and T. Belytschko. Modeling holes and inclusions by level sets in the extended finite-element method. *Comput. Methods Appl. Mech. Engrg.*, 190:6183–6200, 2001.

[205] A. Tagliabue, L. Dedè, and A. Quarteroni. Isogeometric Analysis and error estimates for high order partial differential equations in fluid dynamics. *Comput. Fluids*, 102:277–303, 2014.

[206] T. Takahashi and T. Matsumoto. An application of fast multipole method to isogeometric boundary element method for Laplace equation in two dimensions. *Eng. Anal. Bound. Elem.*, 36:1766–1775, 2012.

[207] J. C. F. Telles. A self-adaptive co-ordinate transformation for efficient numerical evaluation of general boundary element integrals. *Int. J. Numer. Meth. Engng.*, 24:959–973, 1987.

[208] I. Temizer, P. Wriggers, and T. Hughes. Contact treatment in isogeometric analysis with NURBS. *Comput. Methods Appl. Mech. Engrg.*, 200:1100–1112, 2011.

[209] D. Thomas, M. Scott, J. Evans, K. Tew, and E. Evans. Bézier projection: A unified approach for local projection and quadrature-free refinement and coarsening of NURBS and T-splines with particular application to isogeometric design and analysis. *Comput. Methods Appl. Mech. Engrg.*, 284:55–105, 2015.

[210] S. Torquato. *Random Heterogeneous Materials: Microstructure and Macroscopic Properties.* Springer, 2002.

[211] C. Truesdell and W. Noll. *The Non-Linear Field Theories of Mechanics, Third Edition.* Springer, 2004.

[212] R. Vázquez and A. Buffa. Isogeometric Analysis for Electromagnetic Problems. *IEEE T. Magn.*, 46:3305–3308, 2010.

[213] G. Ventura. On the elimination of quadrature subcells for discontinuous functions in the eXtended Finite-Element Method. *Int. J. Numer. Meth. Engng.*, 66:761–795, 2006.

[214] C. V. Verhoosel and R. de Borst. A phase-field model for cohesive fracture. *Int. J. Numer. Meth. Engng*, 96:43–62, 2013.

[215] C. V. Verhoosel, M. A. Scott, R. de Borst, and T. J. R. Hughes. An isogeometric approach to cohesive zone modeling. *Int. J. Numer. Meth. Engng.*, 87:336–360, 2011.

[216] C. V. Verhoosel, M. A. Scott, T. J. R. Hughes, and R. de Borst. An isogeometric analysis approach to gradient damage models. *Int. J. Numer. Meth. Engng.*, 86:115–134, 2011.

[217] C. Verhoosel, G. van Zwieten, B. van Rietbergen, and R. de Borst. Image-based goal-oriented adaptive isogeometric analysis with application to the micro-mechanical modeling of trabecular bone. *Comput. Methods Appl. Mech. Engrg.*, 284:138–164, 2015.

[218] G. Vilanova, I. Colominas, and H. Gomez. Capillary networks in tumor angiogenesis: From discrete endothelial cells to phase?field averaged descriptions via isogeometric analysis. *Int. J. Numer. Meth. Biomed. Engng.*, 29:1015–1037, 2013.

[219] S. Vogel and F. Rizzo. An integral equation formulation of three dimensional anisotropic elastostatic boundary value problems. *J. Elasticity*, 3:203–216–, 1973.

[220] A.-V. Vuong. *Adaptive Hierarchical Isogeometric Finite Element Methods*. PhD thesis, TU München, 2012.

[221] A.-V. Vuong, C. Giannelli, B. Jüttler, and B. Simeon. A hierarchical approach to adaptive local refinement in isogeometric analysis. *Comput. Methods Appl. Mech. Engrg.*, 200:3554–3567, 2011.

[222] W. A. Wall, M. A. Frenzel, and C. Cyron. Isogeometric structural shape optimization. *Comput. Methods Appl. Mech. Engrg.*, 197:2976–2988, 2008.

[223] D. Wang and J. Xuan. An improved NURBS-based isogeometric analysis with enhanced treatment of essential boundary conditions. *Comput. Methods Appl. Mech. Engrg.*, 199:2425–2436, 2010.

[224] W. Wang, Y. Zhang, L. Liu, and T. J. R. Hughes. Trivariate solid T-spline construction from boundary triangulations with arbitrary genus topology. *Comput. Aided Design*, 45:351–360, 2013.

[225] G. N. Wells, E. Kuhl, and K. Garikipati. A discontinuous Galerkin method for the Cahn–Hilliard equation. *J. Comp. Phys.*, 218:860–877, 2006.

[226] S. M. Wise, J. S. Lowengrub, H. B. Frieboes, and V. Cristini. Three-dimensional multispecies nonlinear tumor growth – I: Model and numerical method. *J. Theor. Biol.*, 253:524 – 543, 2008.

[227] O. Wodo and B. Ganapathysubramanian. Computationally efficient solution to the Cahn-Hilliard equation: Adaptive implicit time schemes, mesh sensitivity analysis and the 3D isoperimetric problem. *J. Comp. Phys.*, 230:6037 – 6060, 2011.

[228] P. Wriggers. *Nichtlineare Finite-Element-Methoden*. Springer, 2001.

[229] Y. Xia, Y. Xu, and C.-W. Shu. Local discontinuous Galerkin methods for the Cahn–Hilliard type equations. *J. Comp. Phys.*, 227:472–491, 2007.

[230] D. Zäh and C. Miehe. Computational homogenization in dissipative electro-mechanics of functional materials. *Comput. Methods Appl. Mech. Engrg.*, 267:487–510, 2013.

[231] Y. Zhang, W. Wang, and T. J. R. Hughes. Solid T-spline construction from boundary representations for genus-zero geometry. *Comput. Methods Appl. Mech. Engrg.*, 249–252:185–197, 2012.

[232] Y. Zhang, W. Wang, and T. J. R. Hughes. Conformal solid T-spline construction from boundary T-spline representations. *Comput. Mech.*, 51:1051–1059, 2013.

[233] G. Y. Zhou and Z. Y. Jiang. Deformation in magnetorheological elastomer and elastomer-ferromagnet composite driven by a magnetic field. *Smart Mater. Struct.*, 13:309–316, 2004.

[234] A. Zubarev. Magnetodeformation of ferrogels and ferroelastomers. Effect of microstructure of the particles' spatial disposition. *Physica A*, 392:4824–4836, 2013.

[235] A. Y. Zubarev. On the theory of the magnetic deformation of ferrogels. *Soft Matter*, 8:3174–3179, 2012.